Thermal remote sensing of urban microclimates by means of time-sequential thermography

vorgelegt von
Dipl. Ing. Fred Meier
aus Berlin

Von der Fakultät VI – Planen Bauen Umwelt
der Technischen Universität Berlin
zur Erlangung des akademischen Grades
Doktor der Naturwissenschaften
Dr. rer. nat.

genehmigte Dissertation

Promotionsausschuss:

Vorsitzender:	Prof. Dr. Gerd Wessolek
Gutachter:	Prof. Dr. Dieter Scherer
Gutachter:	Prof. Dr. Eberhard Parlow

Tag der wissenschaftlichen Aussprache: 16.03.2011

Berlin 2011
D 83

Table of contents

List of manuscripts

The dissertation is presented in cumulative form and consists of four individual manuscripts, which are referred to by their corresponding Roman numerals in the text. All manuscripts are completely reproduced in Appendix A-D. Two manuscripts are published. The others are submitted and still in the review process.

Published manuscripts

I Meier, F., Scherer, D., Richters, J. and Christen, A. (2010): Atmospheric correction of thermal infrared imagery of the 3-D urban environment acquired in oblique viewing geometry. *Atmospheric Measurement Techniques Discussions*, 3, 5671–5703. doi:10.5194/amtd-3-5671-2010.

II. Meier, F., Scherer, D. and Richters, J. (2010): Determination of persistence effects in spatio-temporal patterns of upward long-wave radiation flux density from an urban courtyard by means of Time-Sequential Thermography. *Remote Sensing of Environment*, 114, 21-34.

Submitted manuscripts

III Meier, F. and Scherer, D. (2010): Spatial and temporal variability of urban tree canopy temperature during summer 2010 in Berlin, Germany. Submitted to *Theoretical and Applied Climatology*.

IV Christen, A., Meier, F. and Scherer, D. (2010): High-frequency fluctuations of surface temperatures in an urban environment. Submitted to *Remote Sensing of Environment*.

Acknowledgements

At this point I would like to thank the following people who have contributed significantly to the success of this work.

I would like to express my deep and sincere gratitude to Prof. Dr. Dieter Scherer. His understanding, encouraging and personal guidance have provided the best basis for the present thesis. He let me participate in a number of fruitful discussions, excursions, expeditions and scientific conferences. Without his support I would not be so enthusiastic about the scientific issues of urban climatology and thermal remote sensing.

I wish to express my warm and sincere thanks to Dr. Jochen Richters, Prof. Dr. Andreas Christen and Prof. Dr. Eberhard Parlow for their co-supervision, motivation and support in pursuing my PhD thesis.

Many thanks to all colleagues at the chair of climatology for creating such a friendly place where it is a pleasure to work. I cordially thank Marco Otto for reviewing all my manuscripts, his support with numerous and helpful comments, as a discussion partner and friend. Special thanks go to Hartmut Küster who helped substantially to set up and maintain the meteorological and thermography experimental sites. I am grateful to Roman and Fabi for discussing various scientific issues and for finding quick and reliable solutions for many practical problems.

I am immensely grateful to my parents and my wife Sabi. Her lovely support always encouraged me. I am also grateful to all my friends, especially Olli for reviewing my manuscripts and all for being there and helping me to keep perspective.

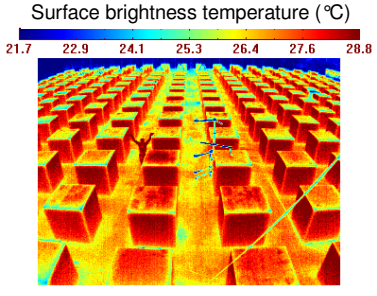

Thank you very much!

Abstract

Surface temperature is an important variable for studies of the urban atmosphere. It directly controls emission of thermal-infrared (TIR) radiation, is central to the energy balance of the surface, modulates the air temperature of the adjacent urban atmosphere, helps to determine the internal climate of buildings and affects the comfort of city dwellers. TIR remote sensing techniques can significantly contribute to urban climatology because TIR imagery provide time-synchronised spatially distributed data of upward long-wave radiation, which is an important component of the surface radiation budget. Furthermore, it is possible to retrieve the surface temperature from observed radiance via Planck's law under consideration of atmospheric influences and the non-blackbody properties of surfaces. However, applications of TIR remote sensing in urban climatology are difficult because of the complex structure of the surface-atmosphere interface.

This contribution demonstrates the potential of ground-based TIR remote sensing using an industrial-type thermography camera system mounted on building roofs in order to study urban microclimates. Thermography allows a simultaneous sampling of spatial and temporal changes of surface temperatures by recording a time-series of thermal images referred to as time-sequential thermography (TST). In this context, an adequate data pre-processing chain was developed. The chain includes a comprehensive atmospheric correction procedure, which works on a pixel-by-pixel basis considering explicitly the three-dimensional form of the urban environment and resulting differences in the line-of-sight due to an oblique viewing geometry.

The thesis answers the question in which way individual elements of the urban surface interact with the adjacent atmosphere. The results from a study of an urban courtyard microclimate clearly demonstrate the influence of shadow and thermal properties of surface materials on thermal patterns, which can persist from several minutes to hours leading to nocturnal thermal anisotropy. The microclimate of urban trees revealed clear differences between tree genera and strong spatio-temporal variability of canopy temperature. The results show that canopy temperature depends on tree genus, leaf size, degree of sealing around the tree and atmospheric conditions especially vapour pressure deficit. Tree-specific canopy temperature in response to the urban environment is essential for comprehensive research concerning the energy and water balance of individual trees. With knowledge from these studies, it is then possible to evaluate the function of urban trees and to optimise the benefits of trees in urban environments. The use of a high sampling frequency (1 Hz) in TST

observations allows for the extraction of information on the dynamic response of the surface energy balance induced by atmospheric turbulence and thermal properties of surface materials. Further, high-frequency thermography enables the visualization of turbulent motions.

Zusammenfassung

In der Erforschung des Stadtklimas ist die Temperatur urbaner Oberflächen von großer Bedeutung. Die Oberflächentemperatur beeinflusst direkt die langwellige Ausstrahlung, sie ist von zentraler Bedeutung für die Energiebilanz einer Oberfläche, moduliert die Lufttemperatur in der oberflächennahen städtischen Atmosphäre, beeinflusst das Innenraumklima von Gebäuden und den thermischen Komfort der Stadtbewohner. Die Thermalfernerkundung kann einen erheblichen Beitrag zur Erforschung des Stadtklimas leisten. Thermalbilder liefern zeitsynchrone und räumlich verteilte Daten der langwelligen Ausstrahlung einer Oberfläche. Zudem ist es möglich, die Oberflächentemperatur aus der beobachteten langwelligen Ausstrahlung abzuleiten unter Berücksichtigung der Emissionseigenschaft der observierten Oberfläche und der atmosphärischen Einflüsse auf das Signal.

Die vorliegende Arbeit widmet sich der Analyse urbaner Mikroklimate mit Hilfe meteorologischer Messungen und insbesondere thermaler Bildzeitreihen aufgenommen mit einer industriellen Thermographie Kamera, welche dauerhaft auf dem Dach eines Hochhauses in Berlin installiert wurde bzw. für kürzere Perioden auch andernorts zum Einsatz kam. In diesem Zusammenhang wurden eine Datenprozessierungskette und ein Dekompositionsschema für thermale Bildzeitreihen entwickelt. Zentrales Element der Datenprozessierung ist die Atmosphärenkorrektur. Diese erfolgt pixelbasiert und berücksichtigt ausdrücklich die dreidimensionale Form der Stadtoberfläche, die Schrägsicht der Kamera und die daraus resultierenden unterschiedlichen Sichtwinkel und Abstände zwischen Kamera und Oberfläche.

Die vorliegende Arbeit widmet sich der Frage, inwieweit einzelne Bestandteile der städtischen Oberfläche z.B. Bäume, Wände oder Dächer mit dem Untergrund und der bodennahen Atmosphäre energetisch interagieren. Die Ergebnisse der Mikroklimaanalyse eines Innenhofes zeigen deutlich den Einfluss der Verschattung und der thermischen Materialeigenschaften auf die Oberflächentemperatur. Hierbei erstreckt sich die Persistenz thermischer Muster von wenigen Minuten bis hin zu Stunden und sollte insbesondere bei der Interpretation und Analyse nächtlicher Thermalbilder beachtet werden.

Die Ergebnisse der Mikroklimaanalyse städtischer Bäume zeigen deutliche Unterschiede zwischen den Gattungen sowie eine ausgeprägte raumzeitliche Variabilität der Baumkronentemperatur. Diese Temperaturmuster korrelieren mit den baumphysiologischen Eigenschaften der untersuchten Bäume insbesondere der Blattgröße, der Ausrichtung der

Blätter und der Regulation der Spaltöffnungen (Stomata). Sie sind zudem eine Folge des Anteils versiegelter Flächen am Standort und der atmosphärischen Bedingungen, insbesondere dem Sättigungsdefizit des Wasserdampfgehalts in der Atmosphäre. Die beobachteten Unterschiede sind unerlässlich für eine umfassende Erforschung der Energie- und Wasserbilanz von Stadtbäumen. Diese weiterführenden Arbeiten würden dann die Möglichkeiten der Bewertung und Optimierung des Nutzens von Bäumen im städtischen Umfeld erweitern.

Insbesondere die Anwendung einer hohen zeitlichen Auflösung (Bildaufnahmerate = 1 Hz) eröffnet neue Perspektiven in der Anwendung der Thermografie für stadtklimatologische Fragen. Die raumzeitlichen Beobachtungen der Oberflächentemperatur und deren Zerlegung in thermale Muster, Trends und Fluktuation unter Verwendung zeitlicher und räumlicher Mittelwertoperatoren liefern Informationen über den Energieaustausch zwischen Oberfläche und Umgebung d. h. das dynamische Verhalten der Energiebilanz als Reaktion auf die atmosphärische Turbulenz, die dreidimensionale Struktur der Stadt und den thermischen Eigenschaften der Oberflächenmaterialien.

Die Thermographie kann einen wichtigen Beitrag in der Erforschung des Stadtklimas leisten. Insbesondere durch die hohe räumliche und zeitliche Auflösung der prozessierten Daten in Kombination mit meteorologischen Messungen und einer dreidimensionalen Beschreibung der beobachteten Oberflächen.

1. Introduction

Although cities themselves form a very small fraction of the global surface area, the urban environment affects a considerable portion of the global population. Today fifty percent of the population lives in cities or urban agglomerations (UN 2010). Urbanisation is set to continue i.e. by 2050 the global percentage of urban dwellers is projected to reach 70.1 % and in the case of Europe to 84.3 % (UN 2010). Understanding the urban climate and its anthropogenic modifications is therefore of great interest in the creation of a healthy and comfortable environment to which an increasing amount of urban dwellers are exposed.

Urbanisation has led to distinct landscape changes, which typically involved the substantial replacement of natural cover by materials, which are generally impermeable and have distinct thermal and radiative properties. Moreover, this new landscape has a unique geometry associated with building form and arrangement that generates atmospheric turbulence and interferes with radiative exchange processes. These landscape changes and anthropogenic emissions affect the exchange of heat, mass and momentum between the surface and the atmosphere resulting in the development of an urban climate that deviates from the surrounding non-urbanised areas (Landsberg 1981, Oke 1988). One of the most distinct alterations is the characteristic warmth of urban areas compared to their surroundings referred to as the urban heat island (UHI), which is one of the best-documented anthropogenic climate modifications (Arnfield 2003).

The concept of scale is important to understand the phenomena of urban climate (Oke 1984). The thesis answers the question in which way individual elements of the urban surface interact with the adjacent atmosphere. This leads to a microscale perspective. Every surface and object has its own microclimate. Typical scales extend from < 1 m to hundreds of metres (Oke 2006). 'Surface and air temperature may vary by several degrees in very short distances, even millimetres, and airflow can be greatly perturbed by even small objects' (Oke 2006, p. 3). The urban surface is a patchwork of vertical and horizontal elements, such as buildings that consist of walls and roof facets, each with a differing time-varying exposure to short- and long-wave radiation and ventilation (Arnfield 1990; Kobayashi and Takamura 1994; Blocken and Carmeliet 2004). Moreover, there are sealed surfaces (Asaeda et al., 1996; Anandakumar 1999), irrigated gardens and lawns (Oke 1979; Suckling 1980; Spronken-Smith et al. 2000) and trees (Oke 1989; Grimmond et al. 1996; Kjelgren and Montague 1998). Single surface facets (microscale γ) may be aggregated hierarchically to define the urban canyon (microscale β). Urban canyons and roofs of adjacent buildings define city blocks (microscale α), which in turn scale up to neighbourhoods (localscale), land-use zones (mesoscale γ)

and, ultimately, the entire city (mesoscale β) and urban region (mesoscale α) (Oke 1984, Orlanski 1975). This work focuses mainly on the microscale.

The next two sections describe briefly the linkage between surface climate processes and thermal remote sensing, state of research and problems in the application of remote sensing data arising from surface heterogeneity as well as constraints of TIR data derived from satellite and airborne platforms.

1.1 Thermal remote sensing of urban climates

Radiation in the thermal-infrared (TIR) part of the electromagnetic spectrum observable via TIR sensors is an essential variable both in the radiation budget and the energy balance of land-surfaces. Surface temperature directly controls emission of TIR radiation but is also the result of energy exchange processes between the atmosphere and bordering surfaces. Knowledge of the surface energy balance is fundamental in understanding surface climate processes (Oke 1987, Monteith and Unsworth 2008). The net radiation (Q*) either as surplus or deficit at the surface obeys the law of energy conservation through the surface energy balance (cf. Oke 1996, Eq. 2.8):

$$Q^* + Q_F = Q_E + Q_H + Q_G + Q_P + Q_B + Q_A, \quad (1)$$

where the terms to the right are the flux densities: Q_E for convective latent heat, Q_H for convective sensible heat, Q_G for conductive heat in the substrate, Q_P for photosynthetic energy uptake or release, Q_B for heat stored in the air or biomass, and Q_A for net horizontal heat advection. Energy produced by humans (Q_F) is also available in urban areas. In practice, Q_P and Q_B are very small in comparison to other terms in Eq. 1. Garai et al. (2010) estimated biomass heat storage in a walnut orchard to be 9 % of nighttime and 1 % of daytime Q* using a ground-based TIR remote sensing approach. Further terms can enter the energy balance equation for instance heat associated with melting and freezing of snow and ice (Lemonsou et al. 2008).

Long-term tower measurements using pyranometers and pyrgeometers have shown the large contribution of upward long-wave radiation ($^{\uparrow}E_{LW}$) to Q^* in urban environments (e.g. Christen and Vogt, 2004), which is fully comprised of the following radiation flux densities:

$$Q^* = {}^{\downarrow}E_{SW} + {}^{\uparrow}E_{SW} + {}^{\downarrow}E_{LW} + {}^{\uparrow}E_{LW}, \quad (2)$$

where $^{\downarrow}E_{SW}$ is downward short-wave radiation (global radiation), $^{\uparrow}E_{SW}$ is upward short-wave radiation (reflection) and $^{\downarrow}E_{LW}$ is downward long-wave radiation originated from the surface surrounding environment (sky, building walls).

Thermal remote sensing techniques can significantly contribute to the field of urban climatology because TIR imagery provides time-synchronised spatially distributed data of $^{\uparrow}E_{LW}$ at various spatial and temporal scales depending on recording frequency and measurement platform. Further, it is possible to retrieve surface temperature from observed $^{\uparrow}E_{LW}$ via Planck's law under consideration of atmospheric influences and non-blackbody properties of land-surfaces (Dash et al. 2002; Quattrochi and Luvall 2003). The convective (Q_H, Q_E) and conductive heat fluxes (Q_G) can be mathematically expressed in terms of surface temperature (Carlson et al. 1981, Bonan 2008). However, modelling of these fluxes using TIR remote sensing data requires a careful definition of the observed surface and determination of surface temperatures especially in complex urban environments (Voogt and Grimmond 2000).

TIR remote sensing approaches have been widely applied in urban climate studies (Voogt and Oke 2003; Weng 2009) and served as an important part of several field campaigns in comprehensive urban climate studies like BUBBLE (Rotach et al. 2005), ESCOMPOTE (Mestayer et al. 2005) and CAPITOUL (Masson et al. 2008). Many studies have used TIR remote sensing to examine urban thermal patterns and their relation to surface characteristics (e.g. Roth et al. 1989; Streutker 2002; Weng et al. 2006) partly supported by multispectral techniques (e.g. Gallo et al. 1993; Dousset and Gourmelon 2003). In some ways, satellite-derived UHI are largely an artefact of low spatial resolution, and the term ‘surface temperature patterns’ is more meaningful than surface urban heat island (SUHI) (Nichol 1996), which is often used in order to differentiate between atmospheric heat islands e.g. in the urban canopy layer (UCL) defined by screen-level air temperature and surface heat islands (Oke 1995). One topic addressed by TIR studies is the relation between atmospheric heat islands and SUHI using a combination of remote sensing data, air temperature observations (e.g. Eliasson 1992; Nichol 1996; Ben-Dor and Saaroni 1997) and urban atmospheric models (e.g. Henry et al. 1989; Hafner and Kidder 1999). A further topic is the analysis of the spatial distribution of radiation balance components and the partition of Q* into sensible, latent and conductive heat fluxes (e.g. Carlson et al. 1981; Parlow 2003; Rigo and Parlow 2007; Xu et al. 2008). Voogt and Oke (2003, Table 1) present an extensive overview of studies that have applied thermal remote sensing data in order to study the urban climate.

1.2 Spatial and temporal heterogeneity

The unavoidable trade-off between spatial and temporal resolution inherent to satellite-based remote sensing, and the relatively high costs of airborne campaigns generate a significant problem for acquisition of spatially distributed TIR data at both high spatial and high temporal resolution. Satellite-based TIR remote sensing systems like NOAA-AVHRR or MODIS provide data several times per day but only at coarse spatial resolutions of 1 km and less, preventing their usage in microscale studies. Other satellite-based TIR sensors like ASTER and Landsat provide higher spatial resolutions between 60 and 120 m but only a coarse temporal resolution (e.g. 16 day repeat cycle for Landsat). However, the combination of several satellite sensors, e.g. MODIS, NOAA-AVHRR and Landsat is suitable to derive the daily course of $^{\uparrow}E_{LW}$ and can achieve good results in comparison with in-situ pyrgeometer measurements (Rigo et al. 2006). Airborne remote sensing systems are capable to provide TIR imagery of high spatial resolutions typically < 10 m (e.g. Eliasson 1992; Lagouarde et al. 2004). A large number of flight campaigns have been conducted over urban areas (e.g. Lagouarde et al. 2004; Voogt and Oke 1998a; Lagouarde and Irvine 2008), however only for short periods, often providing only a pair of day- and nighttime TIR imagery.

One of the central problems of TIR remote sensing is related to the field of view (FOV) and viewing angles of the employed sensors. Roth et al. (1989) suggest that spatio-temporal and quantitative differences between UHI and SUHI have their origin in the nature of the urban surface 'seen' by a TIR sensor, especially one at nadir view, giving a bird's eye or plan view of the city. In this case, roofs, treetops, roads and open horizontal areas are oversampled and vertical surfaces and areas below tree crowns are neglected (Roth et al. 1989). Voogt and Oke (1997) address this problem. They defined a 'complete urban surface temperature' representing the three-dimensional (3-D) nature of urban structures. They show that this temperature can exhibit significant deviations from airborne estimates of surface temperature at nadir and off-nadir viewing angles. This directional temperature variation is termed 'effective thermal anisotropy' (Voogt and Oke 2003) and has been directly observed through combination of ground-based and remote observations (Iino and Hoyano 1996; Voogt and Oke 1998a; Voogt and Oke 1998b; Nichol 1998; Soux et al. 2004; Lagouarde et al. 2004). The term 'effective' is used in order to indicate that anisotropy arises because of surface structure and temperature patterns, rather than the non-Lambertian behaviour of individual facets (Voogt 2008). Asano and Hoyano (1996) developed a spherical thermography technique to better sample the 3-D temperature structure of urban areas.

Voogt and Oke (2003) expect progress in the application of TIR remote sensing to the study of urban climates due to the availability of low cost, high-resolution portable TIR camera systems and

a more detailed representation of urban surfaces in the FOV. Ground-based remote sensing using TIR camera systems mounted on masts, towers or building roofs provide an alternative to airborne and satellite platforms. However, no long-term studies and no systematic analysis of high-frequency surface temperature observations have been reported for urban environments.

1.3 Objectives of the thesis

The principal goals of this dissertation are (i) to adapt a thermography camera system in order to study energy exchange processes at the surface-atmosphere interface in urban environments by recording time series of TIR images and (ii) to demonstrate its application. In more detail, this work addresses five specific objectives. The first and second objectives are dedicated to prerequisite conditions in order to use ground-based thermography in urban climate studies. All further objectives are dedicated to applications of ground-based thermography in order to study specific urban microclimates and energy exchange processes.

The first prerequisite concerns the continuous acquisition of TIR data over a long-term period of at least three years. The first objective is not primarily focused on an analysis of the entire TIR data record. Here, the focus is on the question of whether it is generally possible to use an industrial-type thermography system for continuous operation.

The second prerequisite concerns the post-processing chain handling raw data from the TIR camera system. The second objective of this thesis is to present a comprehensive atmospheric correction procedure for ground-based single-channel TIR sensors that works on a pixel-by-pixel basis considering the 3-D form of urban environments and resulting differences in the line-of-sight (LOS) due to an oblique viewing geometry (Paper I).

The third objective is to assess micro-scale thermal patterns concerning the persistence of thermal patterns inside an urban courtyard. Thermal persistence effects depend on thermal properties of surfaces. Therefore, this objective includes the development of an approach to determine thermal admittance of a concrete surface (Paper II).

The fourth objective is to estimate spatio-temporal variability of canopy temperature (T_C) and canopy-to-air temperature difference ($\Delta T_C = T_C - T_a$) of individual trees in an urban environment. This application of TST aims to quantify the dependency of spatio-temporal patterns of T_C and ΔT_C

on meteorological conditions, tree-specific (physiological) and urban site-specific characteristics (Paper III).

The fifth objective is to demonstrate the application of high-frequency thermography using a 1 Hz image acquisition rate in order to separate the forcing processes of surface temperature fluctuations on the one hand into Q^* and Q_G controlled by surface material and form, and on the other hand into Q_E and Q_H controlled by atmospheric turbulence (Paper IV).

2. Materials and Methods

The following section describes the observational, modelling and analysis framework of the thesis. Fig. 2, presented at the end of this section, depicts an integrative overview of all three frameworks. The thesis is conducted under the umbrella of the urban climate research program called 'Energy eXchange and Climates of Urban Structures and Environments' (EXCUSE) that intends to foster experimental and theoretical atmospheric research on quantification of energy as well as associated momentum and mass exchange processes in the urban boundary layer (Scherer 2005).

2.1 Observational framework

2.1.1 Time-Sequential Thermography

State of the art TIR cameras allow a simultaneous sampling of spatial and temporal changes of ${}^{\uparrow}E_{LW}$ and surface temperatures by recording a time-series (t) of thermal images ($\vec{x}_i$), where $\vec{x}_i$ represents each pixel and its spatial position with reference to image column and row index (x, y) or with reference to 3-D spatial coordinates (x, y, z). The resultant imagery ${}^{\uparrow}E_{TST}(\vec{x}_i, t)$ consists of equidistant images that can be considered as a spatio-temporal image-cube and is referred to as time-sequential thermography (TST, Hoyano et al. 1999). Paper I and Paper IV present an overview on the use of TST in urban environments and in agricultural and forest studies.

The TIR camera used is a VarioCam head (Infratec GmbH, Dresden, Germany). The spectral range of the camera's sensitivity is between 7.5 and 14.0 µm. The radiance detector type is an uncooled microbolometer. The detectors are arranged in a focal plane array (320 x 240 pixels) providing a thermal resolution of 0.08 K at 30 °C with an accuracy of 2 %. The camera's aperture is protected by a polyethylene foil with an estimated average transmissivity of $\tau_{foil} = 0.75$ in the sensitive range, which is considered in the radiance-to-temperature conversion part of the pre-processing chain (Paper I). The array is protected by an encapsulation (IP 65) and the camera is enclosed in an environmental enclosure that also hosts a heating and ventilation system to avoid strong temperature fluctuations.

2.1.2 Combination of TST and meteorological observations

The observational framework is a combination of TST records and meteorological measurements. Simultaneous measurements of radiation fluxes, air temperature, humidity, wind velocity and wind

speed inside or close to the FOV of the TIR camera are important in order to analyse the spatio-temporal patterns of surface temperatures in relation to atmospheric variables.

Steglitzer Kreisel

The study site for continuous acquisition of TIR and meteorological data over a long-term period is located in Berlin, Germany, in the Steglitz-Zehlendorf district (52°27'20''N, 13°19'12''E). The study site is characterised by a high fraction of vegetation and contrasting building densities. In the northern part, five to six-storey buildings enclosing courtyards are dominating, while the southern part include a park with mature trees and detached low and mid-rise residential houses. Detailed descriptions of building structure and trees are available in Paper IV (buildings) and Paper III (trees).

In particular, a platform on top of a high-rise building referred to as Steglitzer Kreisel carries the TIR camera system mounted on a boom at a height of 125 m above ground level (a.g.l.) and 3 m off the roof edge. During routine operation, the TIR camera records one image per minute. The one-minute recording frequency was used in all Papers except for Paper IV, which used a 1 Hz recording frequency. The camera system is equipped with a panning and tilting device that allows scanning of different FOV. However, a fixed camera position was used for acquisition of long-term TST data. The fixed camera position ensures a valid comparison between the multi-temporal imagery. The original FOV of the camera is 64° by 50° and covers an area of approximately 0.3 km^2. For the data analysis, the FOV was cropped to 57.5° by 44.7° in the data pre-processing chain (Paper I). Fig. 1 (left) depicts the mounted camera at the Steglitzer Kreisel study site. The fixed FOV is oriented towards northwest (325°) and inclined by 59° from the nadir angle. The sensor-target distance varies between 125 and 770 m due to the oblique view. This corresponds to a geometric resolution between 0.5 and 2.8 m for the instantaneous field of view (IFOV) of 3.6 mrad. The determination of the sensor-target distance for every pixel is important for the pre-processing chain and part of the modelling framework in this thesis.

Long-term meteorological measurements are installed at the roof of Steglitzer Kreisel. $\downarrow E_{SW}$ and $\downarrow E_{LW}$ (CM 3, and CG 3, Kipp & Zonen, Delft, Netherlands), T_a and RH (HMP45A, Vaisala, Vantaa, Finland) are measured in 5 sec intervals. Additionally a fast ultrasonic anemometer-thermometer (USA-1, Metek GmbH, Elmshorn, Germany) and hygrometer (Li-7500, Licor Inc., Lincoln, NK, USA) are installed at the same location. Within the FOV, in 300 m horizontal distance from the Steglitzer Kreisel at the campus of the Institute of Ecology (Rothenburgstraße), T_a and RH are measured at ground level (2 m) underneath a relatively open tree canopy and 3.5 m above an exposed 19 m pitched roof. Wind velocity and wind direction (Lambrecht GmbH, Göttingen,

Germany) were measured 4 m above the same roof. Further, one pyrometer measurement device (Heimann, KT15) was temporarily operated directly above the roof to obtain in-situ surface temperature for validation of the atmospheric correction procedure (Paper I, Fig. 2). The pyrometer is located 1 m offset from the roof and observes the roof under the same view zenith angle as the TIR camera.

Fig. 1: Photographs taken from the Steglitzer Kreisel roof (left) and from the Stilwerk roof (right) showing the study site and oblique viewing TIR camera mounted on a boom.

Stilwerk Experiment

In one case, TST was part of a local-scale urban climatology experiment including boundary layer meteorological measurements such as directly measured Q_H by the eddy-covariance method, T_a and *RH*. The experiment was conducted in Berlin, Germany, in the Charlottenburg-Wilmersdorf district, close to the city centre at Zoologischer Garten (52°30'22"N, 13°19'30"E). City structure is characterised by five to six-story block development. This experiment is called 'Stilwerk Experiment' according to the name of the shopping mall, whose roof provided a basis for measurement installations. Intensive experimental work was conducted between 20th April and 14th May 2007. The full description of the experimental setup and essential features in the FOV of the TIR camera looking inside the courtyard is given in Paper II. The mounted TIR camera and examined courtyard at the Stilwerk study site are depicted in Fig. 1 (right).

2.1.3 Definitions of surface temperatures

Accurate definitions of remotely sensed variables are important in order to understand precisely the information content of remotely sensed quantities and in which way they relate to surface properties (Voogt and Oke 2003). Becker and Li (1995) as well as Norman and Becker (1995) have carefully examined the definitions associated with TIR remote sensing of land-surfaces.

Here, the term brightness temperature (T_b) is used to describe the temperature derived from inversion of Planck's law for a TIR sensor operating in a given waveband. This temperature relates the radiance received by the TIR camera to a temperature without consideration of any process influencing the measured radiance along the path from the surface through the atmosphere to the sensor. This surface temperature is used in Paper IV and to simplify the symbol T is used. In Paper I, superscripts are used to differentiate between atmospherically corrected temperatures or not. The term T_b^{cam} describes uncorrected temperatures at camera position. The term T_b^{surf} is used in order to describe a surface temperature that has been corrected for atmospheric effects but not for surface emissivity effects. Radiometric temperatures (T_r) are those that have been corrected for atmospheric and surface emissivity effects (Voogt and Oke 2003). The study of the microclimate of urban trees (Paper III) analyses T_r of tree canopies. Hence, a canopy temperature (T_C) is an atmospherically and emissivity corrected surface temperature, which corresponds to the thermodynamic surface temperature, if the TIR pixel represents a homogeneous and isothermal surface but this is seldom the case, even the temperature of a single leaf shows spatial variability (Wigley and Clarke 1974).

2.2 Modelling framework

Radiative processes in the atmosphere between surface and sensor have an impact on remote sensing data. Atmospheric effects that alter the radiance observed by TIR sensors include absorption and emission primarily induced by water vapour, carbon dioxide and ozone. These atmospheric effects can lead to temperature differences between T_b^{cam} and T_b^{surf} of up to 10 K (Jacob et al. 2003).

Several methods are available to remove these atmospheric effects depending on sensor characteristics. The split window technique is useful for multi-channel sensors (Price 1984; Becker and Li 1990; Sobrino et al. 1991). Radiative transfer models coupled with atmospheric profile data on pressure, temperature and humidity are adequate for multi and single-channel sensors (Berk et al. 1998; Schmugge et al. 1998). While these methods are common for data derived from satellite

(Prata et al. 1995; Dash et al. 2002) or airborne platforms (Jacob et al. 2003; Lagouarde et al. 2004; Lagouarde and Irvine 2008), the need for atmospheric correction of ground-based TIR imagery acquired in oblique view is an open question insofar as the 3-D urban form is concerned.

The possible discrepancy between T_b^{cam} and T_b^{surf} is examined by a theoretical study using a fictitious urban experimental setup, a radiative transfer model and the spectral characteristics of the VarioCam provided by the manufacturer. In one case, the TIR camera would record a temperature difference of up to 3 K between two surfaces having equal T_b^{surf} (Paper I, Fig. 1). The results from this theoretical study emphasise the need to develop an atmospheric correction procedure that works on a pixel-by-pixel basis considering the 3-D urban form. The next two sections briefly describe the developed modelling approach in order to perform an adequate atmospheric correction of TST data.

2.2.1 Spatially distributed LOS geometry parameters

The oblique view of the camera and the 3-D form of the examined urban environment produce different LOS parameters for every TIR image pixel *j*. The LOS is fully described by the view zenith angle (θ_j) under which the camera observes the surface and by the height of the surface (z_j^{surf}). These parameters must be determined prior to the use of a radiative transfer model. The determination of spatially distributed LOS values is based on digital surface model (DSM) data, photogrammetry and 3-D computer vision techniques. The idea is to link the TIR image pixels to corresponding 3-D coordinates via geometrical transformations used in computer graphics (Foley and van Dam 1984) and based on camera interior and exterior orientation parameters.

At first, a 3-D building vector model and a digital ground model (DGM) of the study area were merged into a vector-based DSM. At present, the DSM does not include trees or any other vegetation. Therefore, the atmospheric correction of vegetative TIR pixels uses LOS parameters representing the nearest underlying ground, wall or roof surface. The origin of the DSM coordinate system was translated to the vanishing point of the perspective projection (fixed TIR camera position) in order to model the perspective projection of 3-D objects onto the two-dimensional (2-D) TIR image plane (Paper I, Eq. 8). The next step defines a view volume in order to realise the interior orientation of the camera. This is a frustum of a pyramid. Objects that fall within the view volume are projected toward the apex of the pyramid (viewpoint or eye position). Objects that are closer to the viewpoint appear larger because they occupy a proportionally larger amount of the view volume. The bounds of the view volume are described by the FOV of the TIR camera. The exterior and interior orientation was determined by using the optical centre point of the TIR image,

its spatial coordinates and 3-D rotations of the DSM around the horizontal and vertical axis (Paper I, Sec. 3.3).

2.2.2 Atmospheric correction procedure

The radiative transfer model MODTRAN 5.2 (MOD5) (Berk et al. 2005) is used to model spectral transmissivity (τ_λ) and upward atmospheric spectral radiance (L_λ^{atm}) between the surface and sensor under the assumption that surface emissivity is equal to unity. The basic idea is to model at-sensor radiances L_i^{MOD5} for a given range of surface brightness temperatures T_b^{MOD5} and LOS parameters in order to relate the observed at-sensor radiance L_i^{cam} under consideration of pixel-specific LOS values to an interpolated T_b^{surf} value. At-sensor radiances L_i^{MOD5} are obtained via integration over the spectral range of the TIR camera and adjusted to the normalised spectral response $f_i(\lambda)$ of the camera, where $f_i(\lambda)$ is a combination of sensor response and transmissivity of the lens and polyethylene protection foil. The following equation is used:

$$L_i^{MOD5} = \int_{7.5\mu m}^{14.0\mu m} d\lambda \; [B_\lambda(T_b^{surf})\tau_\lambda(\theta, z^{surf}) + L_\lambda^{atm}(\theta, z^{surf})] f_i(\lambda) \qquad (3)$$

This method requires accurate information about vertical distribution of T_a and RH in the atmosphere between surface and TIR camera. These values are derived from linearly interpolated atmospheric profiles of $T_a(z)$ and $RH(z)$ that are measured at two heights, i.e. at ground level (Rothenburgstraße) and at camera level (Steglitzer Kreisel). The flowchart of the complete atmospheric correction procedure is illustrated in Paper I (Fig. 4).

2.3 Analysis framework

2.3.1 Spatio-temporal decomposition

The basic approach of TST data analysis uses two averaging operators in order to separate trends, mean patterns and fluctuations. An overbar denotes the temporal averaging operator. For example, the temporal average of temperature $T(\vec{x}_i, t)$ of a single pixel is:

$$\overline{T} = \frac{1}{N}\sum_{t=0}^{N} T(t) \, . \qquad (4)$$

The temporal average applied to all image pixels or areas of interest (AOI) like a tree crown is a basic method to derive thermal patterns of $T(\vec{x}_i,t)$ or ${}^{\uparrow}E_{TST}(\vec{x}_i,t)$ indicating mean surface temperature or mean upward long-wave radiation for specific time intervals for instance daytime, nighttime, 24-hourly pattern, monthly patterns or an average diurnal course. An angle bracket denotes the spatial averaging operator. For example, the average temperature of a spatial subset or the entire image is:

$$\langle T \rangle = \frac{1}{N} \sum_{i=0}^{N} T(\vec{x}_i) \,. \tag{5}$$

The spatial averaging operator is modified in Paper III in the form of a median operator, in order to describe ΔT_C of tree-specific crowns. It is important to note that the spatial averaging operator does not equally weight surface areas due to the distorted image geometry (oblique view). This term is not equal to the spatially averaged complete surface temperature as defined by Voogt and Oke (1997). The deviations of pixels temperature from temporal or spatial averages of a region or the entire image are the next two important quantities in order to decompose the TST data into a (high-frequency) fluctuating part and a long-term mean part (temporal stability). All details of the proposed decomposition schemes are available in Paper IV, including useful temporal and/or spatial statistical parameters calculated from the decomposed terms.

2.3.2 Determination of persistence effects

The 3-D city structure generates a complex pattern of partially sunlit and shadowed surfaces in particular under cloudless conditions. Persistence in this contribution stands for a temporal stability of spatial TIR patterns. In a more general perspective, a thermal persistence effect is activated by a specific disturbance in the surface-atmosphere system. An important question is how long this disturbance is detectable in the system. The analysis of persistence effects is based upon the difference ΔE_{ref} between ${}^{\uparrow}E_{LW}$ from a shadowed (disturbed) surface and a non-shadowed (undisturbed) reference surface. The temporal mean (three-hourly and 24-hourly periods) of ΔE_{ref}, the standard deviation of ΔE_{ref} and the mean rate of change of ΔE_{ref} as well as the attenuation process of ΔE_{ref} in the course of time provide the basis for persistence analysis in Paper II.

2.3.3 Surface classification and 3-D data

The urban landscape is composed of a wide range of materials each having different climatic properties (radiative, thermal, moisture, aerodynamic) and structural arrangements (sizes, shapes and relationship to surrounding surfaces). The study of surface temperature patterns needs accurate information about surface characteristics. The correlation between climatic properties and thermal behaviour of a surface is a powerful tool in order to study energy exchange processes at the surface-atmosphere interface. Surface classifications based on physical surface properties and morphometry are preferred over functional land-use classifications (Voogt and Oke 2003).

Section 2.1.2 already presented descriptions of the surfaces in the FOV but a comprehensive analysis needs information on a pixel-by-pixel basis. Different surface classifications are used in order to address this issue. We can distinguish between manually classified surfaces and automatically classified surfaces using the linkage between TIR image pixel and corresponding DSM information (section 2.2). All investigated AOI in the courtyard study (Paper II) and all pixels in the FOV at the Steglitzer Kreisel site (Paper I, III, IV) were manually classified by visual (subjective) analysis or rectified (oblique) photos from the camera's location, the help of the 3-D building model and aerial photos. A tree crown mask consisting of 56 individual trees is used in Paper III (Fig. 1 and Fig. 2a) and four overarching form-based facet categories (roofs, walls, ground, trees) are used for the high-frequency TST study. These from-based categories are further separated into material classes (Paper IV, Fig. 1 and Table 3). The combination of camera's FOV and DSM attributes a height above ground, a slope and an azimuth to each building pixel. Vegetation is not resolved in the DSM, so information on tree crown geometry is not available.

Further used surface descriptions are leaf size and degree of sealing around the trunk. Leaf size was measured by a leaf area meter (Li-Cor Model 3100) for 20-50 leaves of 42 trees. The sealing map is available in a 2.5 m raster format (Senate Department for Urban Development 2007).

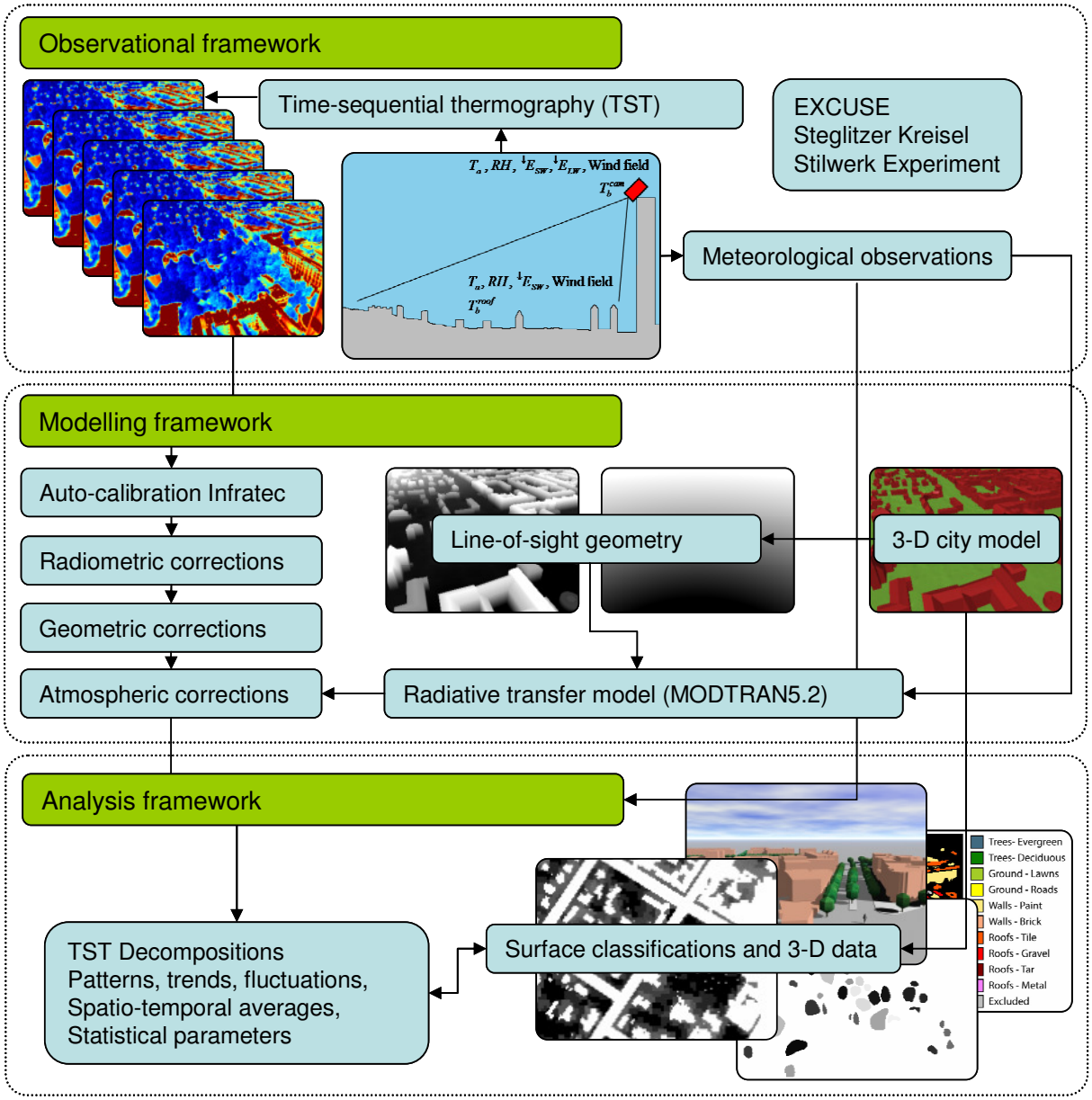

Fig. 2: Scheme of the observational, modelling and analysis framework of the thesis.

3. Time-sequential thermography and urban microclimates

The following section presents an integrative overview of the results of the thesis and relates them to relevant aspects of previous studies.

3.1 Availability of a long-term TST data set

The observation program at the Steglitzer Kreisel study site is a unique attempt to monitor upward long-wave radiation from urban surfaces at the microscale over a long-term period. This approach is also interesting because surface temperatures and long-wave radiation flux densities are generally seldom monitored at urban stations (Oke 2006). Further, TST provides spatially distributed data in contrast to spatially integrated measurements using pyrgeometers. The following Fig. 3 presents TST data availability for the last three years inclusive the denotation of periods where TST data was used for the thesis (Paper I, III and IV). Overall, the acquisition of TST data at the one-minute interval was very fruitful. TST data availability amounts to 83 %, 78 % and 82 % for the years 2008, 2009 and 2010 respectively.

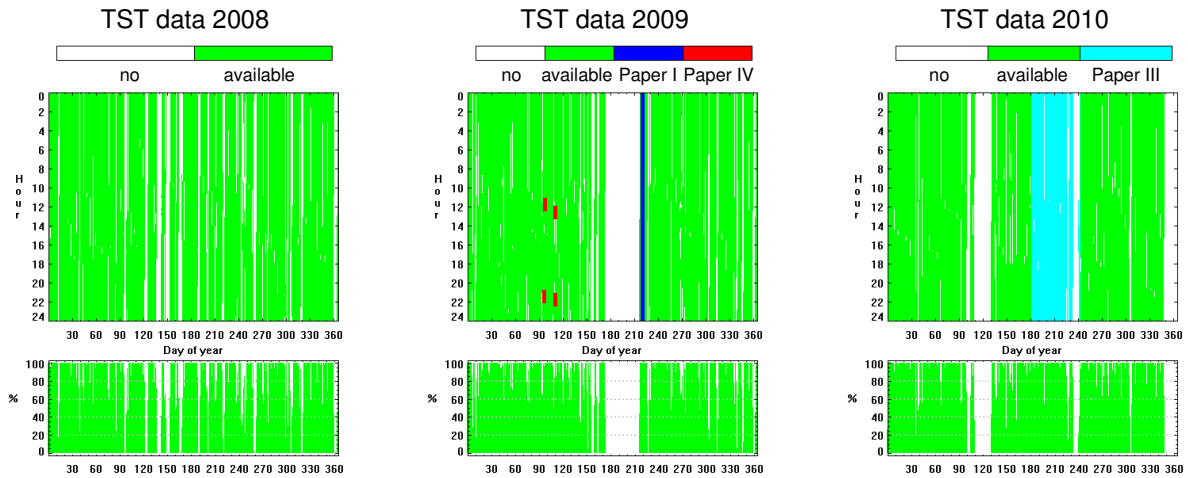

Fig. 3: Availability of time-sequential thermography (TST) data obtained by the VarioCAM camera at the long-term study site Steglitzer Kreisel for 2008 (left), 2009 (middle) and 2010 (right) inclusive denotation of periods where TST data was used for individuals Papers.

On two occasions the TIR camera systems was removed from the Steglitzer Kreisel for extended periods. At first for six weeks in summer 2009 in order to observe spatio-temporal patterns of surface temperatures at the COSMO scale model facility in Japan (Meier et al. 2009) and next for two weeks in spring 2010 in order to conduct an instrument comparison experiment in the garden of the Institute of Ecology (Paper I). Previous TST studies analysed data over one or two days (e.g.

Hoyano et al. 1999; Chudnovsky et al. 2004; Yang and Li 2009), while for this thesis for the first time a data set of two months was used (Paper III). The Steglitzer Kreisel TST dataset is the first one that covers several years.

3.2 Pre-processing chain of TST data

The developed pre-processing chain comprises four steps. At first, at-sensor radiance values (digital numbers, DN) are converted into T_b^{cam} for each pixel. Sensor case temperature is continuously monitored during the operation. Every minute (every 6 seconds for high-frequency TST runs, Paper IV) all microbolometer elements were homogenised using an inbuilt near to ideal blackbody (shutter) and sensor case temperature was stored in order to use the optimised radiance-to-temperature calibration parameters and to avoid drift effects. The calibration parameters for the TIR camera system were determined at the laboratory of the manufacturer using blackbody temperatures. It is possible to convert T_b^{cam} into at-sensor radiance L_i^{cam} by using the integral of the Planck equation at the sensors wavelengths and weighted by $f_i(\lambda)$ in order to do further corrections of TIR imagery based on radiance values. The camera is equipped with a wide-angle lens. This lens produces radiometric and geometric distortions, which are corrected in step two and three. Both corrections are described in detail in Paper I. Finally, the atmospheric correction is applied. It follows a more detailed presentation and discussion of the developed atmospheric correction procedure applied to a 24-hourly TST run (Paper I).

The results from the spatially distributed atmospheric correction procedure referred to as MLOS (multi line-of-sight) method in comparison with a simple approach using non-spatially distributed LOS parameters referred to as SLOS (single line-of-sight) method are presented in Fig. 4. The SLOS method is similar to the atmospheric correction method described above, but only one LOS parameter pair is used that represents the median of all θ_j and z_j^{surf} values in the FOV.

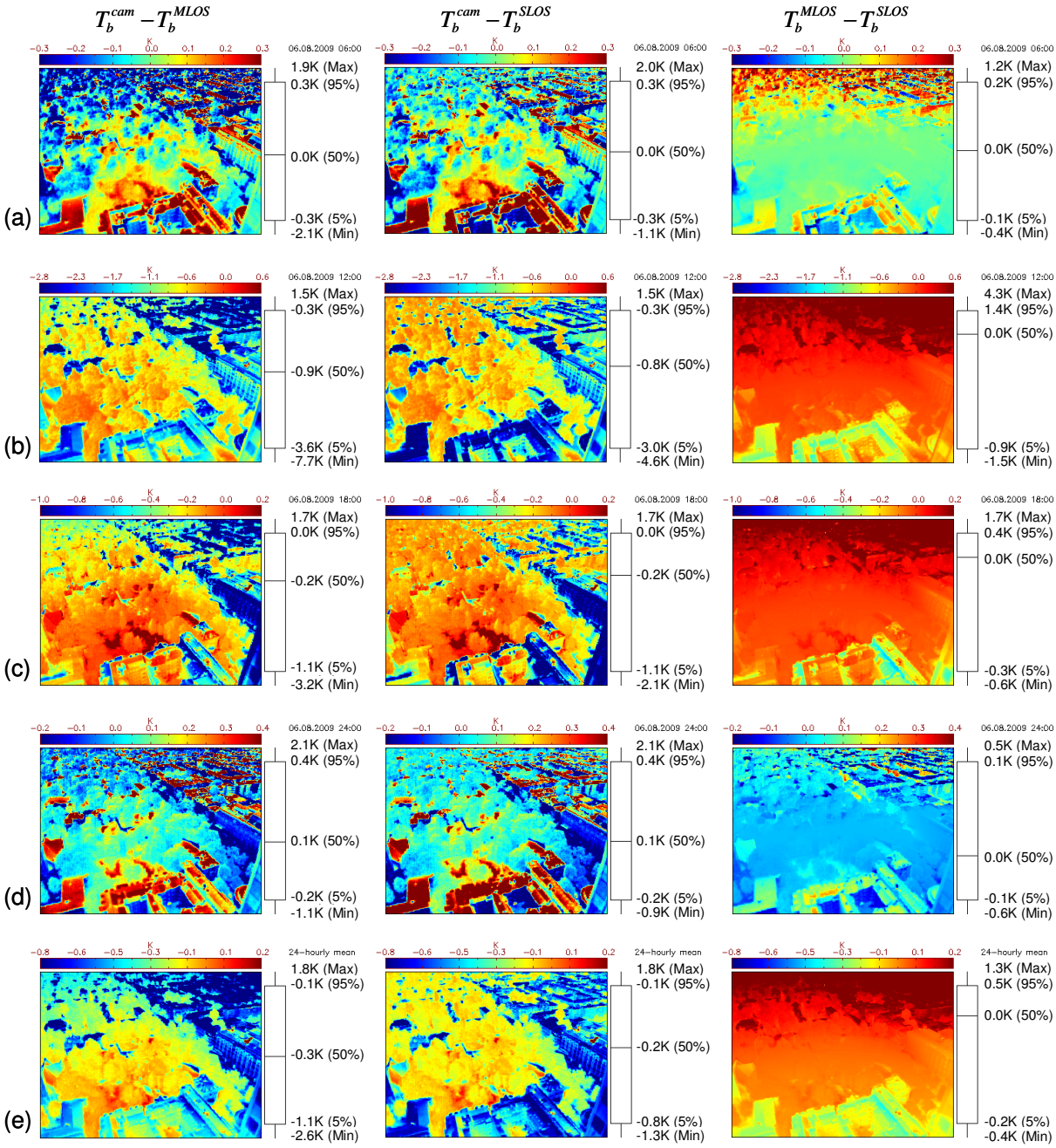

Fig. 4: Differences between T_b^{cam} and T_b^{MLOS} (left column), T_b^{cam} and T_b^{SLOS} (middle column) and between the two atmospheric correction methods ($T_b^{MLOS} - T_b^{SLOS}$, right column) for selected 30-minute periods during 8 August 2009 at 06:00 (a), 12:00 (b), 18:00 (c) and 24:00 (d) CET and the 24-hourly mean pattern (e) (Figure taken from Paper I, Appendix A, Fig. 7).

During daytime (Fig. 4b, 4c) at-sensor values (T_b^{cam}) are consistently lower than MLOS corrected temperatures (T_b^{MLOS}). There is a clear spatial gradient showing a greater difference for surfaces located further away from the TIR camera. This is particularly noticeable for very hot surfaces. For instance, underestimation of roof temperatures in the background amounts up to 7.7 K at 12:00. The

SLOS corrected temperatures (T_b^{SLOS}) also reveal a similar at-sensor underestimation depending on surface temperature (up to 4.6 K at 12:00). However, a spatial gradient as shown by the MLOS pattern is not visible. The comparison of both atmospheric correction methods (Fig. 4b, right column) shows a clear spatial gradient where the MLOS values are higher (up to 4.3 K) in the background and lower in the foreground (up to 1.5 K).

During nighttime and immediately after sunrise atmospheric effects are much lower than during daytime. At night, the TIR camera overestimates cold surfaces ($T_b^{surf} < T_a$) e.g. for roofs furthest away from sensor and underestimates hot surfaces ($T_b^{surf} > T_a$) in the case of roads and walls. The MLOS pattern (Fig. 4d, left column) reveals the clear dependency on LOS geometry. This spatial gradient is not visible in the SLOS pattern (Fig. 4d, middle column). However, the differences between MLOS and SLOS are very low (Fig. 4d, right column). The 24-hourly patterns are similar to the daytime patterns but with an overall lower magnitude.

The atmospherically corrected TIR data are in good accordance with in-situ surface temperature measurements. However, the roof selected for in-situ measurements is not strictly homogenous and shows microscale temperature variability, which is not detectable by the TIR image geometrical resolution.

The results show that atmospheric correction of ground-based TIR imagery of the 3-D urban environment acquired in oblique viewing geometry has to account for spatial variability of LOS. An accurate determination of urban surface temperatures via thermal remote sensing is important for sensible heat flux calculations (Voogt and Grimmond 2000) or the evaluation of surface heat island mitigation measures for instance the conversion of asphalt-covered parking areas to grass-covered ones (Takebayashi and Moriyama 2009).

Atmospherically corrected TST data are used in Paper III but not in Paper II due to short target-sensor distances in the experimental setup. The study of high-frequency fluctuations of surface temperatures applied also non-atmospherically corrected TST data but the effect on the analysed temperature fluctuations was estimated to be less than 10 %. The effect was estimated by using MOD5 and standard deviations of T_a and *RH* for the median LOS.

3.3 Urban microclimates

3.3.1 Microclimate of an urban courtyard

Courtyards are typical open spaces in Berlin and in other cities. With few exceptions (e.g. Hall et al. 1999; Mertens 1999; Shashua-Bar et al. 2006) urban courtyards have not received the same attention as the urban street canyon in urban climate research (Mills 2008).

Although there may exist considerable variations in courtyard geometry the results from the Stilwerk courtyard clearly demonstrate the strong influence of shadow and surface material on spatio-temporal patterns of ${}^{\uparrow}E_{LW}$. The history of shadow i.e. when shadow is present on the surface is important for the 24-hourly average of the mean difference (MD) between ${}^{\uparrow}E_{LW}$ from the courtyard surfaces (TST data) and ${}^{\uparrow}E_{LW}$ from the Stilwerk building roof (pyrgeometer). The 24-hourly pattern is used for the long-term persistence analysis. The thermal hot spot corresponds to the pavements, which received direct short-wave irradiance between 10:00 and 15:30 CET. The thermal cold spot corresponds to the shadowed part of the courtyard. The lime tree appears also as a cold spot due to transpiration (Q_E). The whole car park shows a slight gradient from the eastern to the western part. This thermal gradient is a persistence effect resulting from the history of shadow. The 24-hourly MD pattern and visualisations of shadow in the courtyard at 09:00, 12:00 and 18:00 CET are presented in Fig. 5.

The mean rate of change of ΔE_{ref} depends on shadow duration i.e. how long shadow has been present on the surface (Paper II, Fig. 7 and Table 2). However, this is not the case for vegetative surfaces, where T_a is very important for diurnal changes of surface temperature and ${}^{\uparrow}E_{LW}$ respectively (Oke 1987). This is in accordance with the results from the urban tree microclimate study (Paper III), which shows that shadow only produced short-term persistence effects for vegetation. The biomass of the vegetation is not able to store or conduct heat into ground in the same way as artificial surfaces. Therefore, changes of ${}^{\downarrow}E_{SW}$ particularly trigger changes of ${}^{\uparrow}E_{LW}$ and convective heat fluxes (Q_H and Q_E) depending on surface-to-air temperature difference and atmospheric vapour pressure deficit (VPD).

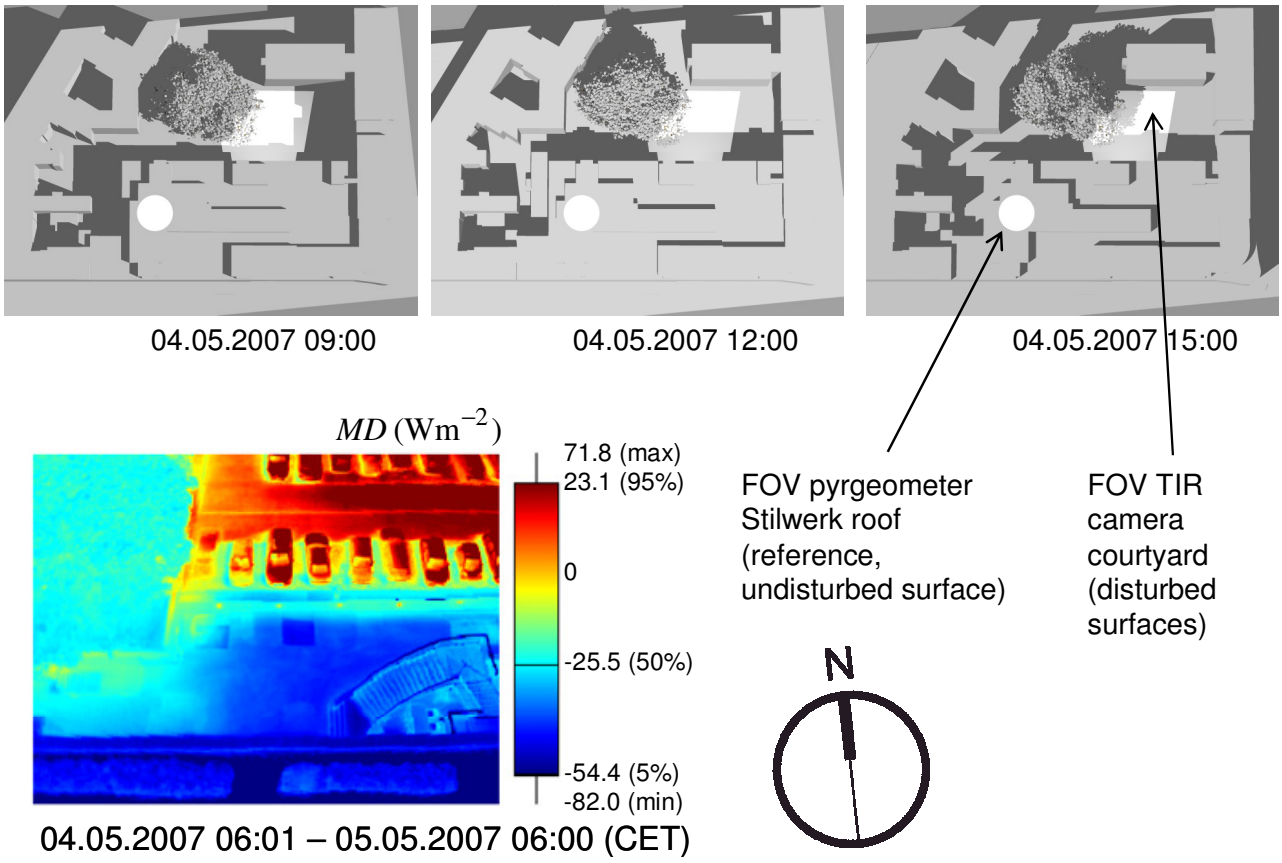

Fig. 5: Visualization of sunlit-shadow distribution in the radiative source areas of pyrgeometer roof (circle) and TST courtyard (trapeze) measurements at 12:00, 15:00 and 18:00 CET on 4th May (top) and spatio-temporal pattern of mean difference (MD) between upward long-wave radiation from the courtyard and upward long-wave radiation from the roof for a 24-hourly cycle (bottom).

Short-term persistence effects lead to the timescale of minutes and the estimation of surface thermal admittance for a concrete surface. After departure of a parked car, the parking space shows lower ${}^{\uparrow}E_{LW}$ in contrast to the surrounding area. This car shaped pattern is vanishing in the course of time. Comparison of the radiation balance of the two surfaces after car departure reveals that they differ only in respect to ${}^{\uparrow}E_{LW}$. Therefore, ΔE_{ref} is considered as the given heat flux responsible for the attenuation of the persistence effect. In other words, the temporarily shadowed (disturbed) surface should have a higher rate of change (ROC) of surface temperature (corrected for emissivity but not for atmospheric effects) in comparison to the reference surface close to it due to the lower upward long-wave radiation. The approach summarises the influence of further heat fluxes contributing to surface warming of the formerly shadowed surface in ΔQ_{res}, which is approximated to be constant. An appropriate thermal property controlling the heating or cooling rate of a surface to a given heat flux is the thermal admittance (μ), defined by the square root of thermal conductivity (k) and

volumetric heat capacity (C). The following equation (based on Zmarsly et al. 2002, p. 57) is used for the derivation of thermal admittance:

$$\Delta Q = \frac{2A\sqrt{\Delta t}}{\sqrt{\pi}} \cdot \mu \cdot \Delta T_s + \Delta Q_{res} = c \cdot \mu \cdot \Delta T_s + \Delta Q_{res}, \quad (6)$$

where ΔQ is defined as the ROC of ΔE_{ref}, multiplied by the constant measurement interval of 60 s. A is the active surface area set to unity (1 m^2). ΔT_s is defined as the ROC of the difference between surface temperatures of formerly shadowed surface and reference surface. T_s is derived from the original TST data using an emissivity value of 0.95. The relation between ΔT_s and ΔQ is shown in Paper II (Fig. 12). Finally, μ is obtained via linear regression using Eq. 6 and the data of the first 30 min of the persistence attenuation process. The derived μ values (2395 and 2464 J m^{-2} $s^{-0.5}$ K^{-1}) are in the range of literature values (Oke 1987; Stull 1988).

The radiation absorbed by a human is often the largest contributor to the human energy balance equation (Matzarakis et al. 2007; Kenny et al. 2008). Therefore, the persistence of spatio-temporal patterns of $^{\uparrow}E_{LW}$ influences also the spatio-temporal variation of thermal comfort within a courtyard (Mertens 1999).

3.3.2 Microclimate of urban trees

Trees form a significant part of urban vegetation. Their meteorological and climatological effects at all scales in urban environments make them a flexible tool for creating an urban landscape oriented to the needs of an urban dweller (Heisler 1986; Oke 1989).

The microclimate of individual urban trees was investigated in respect to their canopy temperature T_C and leaf-to-air temperature difference ΔT_C using T_a measured at 22.5 m above ground as reference (Rothenburgstraße). There have been no studies which characterise T_C over a wide range of trees, sites and atmospheric conditions in an urban environment, beyond those that have investigated temporal dynamics of several individual trees at different sites (e.g. Montague and Kjelgren 2004) or one-time T_C of more than 400 trees (Leuzinger et al. 2010). The used TST data covers a period of two months from 1st July to 31st August 2010. For the spatial analysis, 56 trees were selected. Among these, we found five genera (*Acer*, *Fagus*, *Quercus*, *Tilia* and *Populus*) and various conifers.

The results show that ΔT_C depends on tree genus, leaf size, degree of sealing around the tree and atmospheric conditions especially *VPD*. The average diurnal course of ΔT_C shows a consistently positive value for all trees. During the night, the range of ΔT_C was between 0.4 and 1.8 K, while ΔT_C varied between 1.5 and 5.2 K at noon (Paper III, Fig. 4). The time of diurnal maximum (ΔT_C at 11:00 and T_C at 13:00) does not coincide with the time of maximum T_a and *VPD* at 16:00 except for *Populus*. This genus showed lowest daytime ΔT_C but highest nighttime ΔT_C. Conifers and *Acer* trees showed maximum ΔT_C, and one individual reached more than 8 K at eight days in July and one day in August.

In the study of Leuzinger et al. (2010), also *Acer* trees showed the maximum ΔT_C (5 K). *Populus* (Körner et al .1979) and *Quercus* (Leuzinger and Körner 2007) reach high stomatal conductance values. During ample water supply, we can expect for these two genera high transpiration rates and lower ΔT_C values in comparison to other trees as indicated in the average diurnal course of genus-specific ΔT_C (Paper III, Fig. 8). The observed relationship between ΔT_C and *VPD* (Paper III, Fig. 6) indicates for *Populus* the classical feedback mechanism of stomatal control. The mechanism is sensitive to leaf water content and allows maintaining high rates of transpiration as long as the supply of water is sufficient (Körner 1985). All other trees show an increase of ΔT_C at lower *VPD*. This indicates the feedforward mechanism of stomatal control in response to increasing *VPD* in order to conserve soil water (Körner 1985). The hydraulic architecture of trees (ring-porous vs. diffuse-porous) is able to influence the stomatal regulation of transpiration in response to high *VPD* environments (Bush et al. 2008). However, in order to confirm stomatal regulation of transpiration and T_C, data of the variation of tree-specific stomatal conductance is useful. Leaf stomatal conductance was not measured during the study.

Leaf size and leaf shape influence the boundary layer thickness and for this reason the energy exchange by turbulence between leaf and atmosphere (Schuepp 1993). Lower T_C values can be attributed to smaller leaves. The thin flattened petioles of *Populus* cause leaves to flutter. This behaviour also reduces the boundary layer resistances (Grace 1978). However, the dynamic effects of wind (i.e. turbulent exchange) show spatial variability (Paper IV), which might cause lower temperatures even for crowns with big leaves.

The relationship between leaf size and ΔT_C is superimposed by the influence of the tree-specific location. This effect produces differences up to 2 K for *Acer* having similar leaf size. Trees surrounded by high amounts of sealed surfaces show consistently higher ΔT_C and T_C values partly in spite of smaller leaf size. During extreme high *VPD* (45 hPa) and T_a (36 °C) tree canopy temperature varied between 39 °C for park trees and 42 °C for city square trees. The following Fig. 6 shows the relation between leaf size and ΔT_C for an average daytime period (left) and the relation

between degree of sealing around the tree and ΔT_C for an average daytime (middle) and nighttime (right) period.

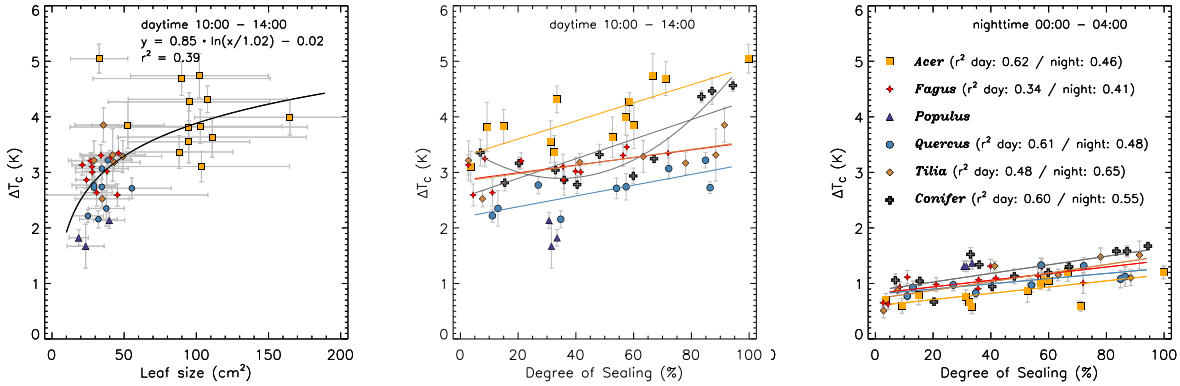

Fig. 6: Relation between leaf size and canopy-to-air temperature difference (ΔT_C) averaged for daytime (left) and relation between degree of sealing around the tree and ΔT_C averaged for daytime (middle) and nighttime (right). Horizontal error bars indicate ± standard deviations of leaf size (left) and vertical error bars indicate ± spatial standard deviations of ΔT_C within the crown.

Previous studies analysed the effect of urban ground cover on tree microclimate (Whitlow et al. 1992) and leaf temperatures (Kjelgren and Montague 1998; Montague and Kjelgren 2004; Mueller and Day 2005). This study confirms that trees over sealed surfaces exhibit consistently higher T_C due to interception of ${}^{\uparrow}E_{SW}$ and ${}^{\uparrow}E_{LW}$ from non-vegetative surfaces (Paper III). Higher leaf temperature enhances the leaf-to-air vapour pressure deficit and the relevance of stomatal control on transpiration (Kjelgren and Montague 1998; Celestian and Martin 2005). However, for short periods building shadow can reduce tree canopy temperature (Paper II). The interception of long-wave radiation during the night is one explanation for the observed nighttime temperature especially for the *Populus* canopy, which has predominantly vertical orientated leaves (Kucharik et al. 1998). This leads to a low sky-view factor and more interception of long-wave radiation in comparison to canopies having horizontally orientated leaves.

An interpretation of small differences in nighttime ΔT_C is complicated because air temperature is measured at one location at a height of 22.5 m, whereas the height of some trees is lower than the measurement height. Small trees especially *Acer* show lower nighttime temperatures (Paper III, Fig. 10, right). Besides the magnitude of nighttime temperature variability, it would be interesting to ask whether a greater respiration due to higher nighttime canopy temperature in urban environments contributes to a decline in net photosynthesis or not.

3.3.3 Forcing processes of surface temperature fluctuations

Surface temperatures of land-atmosphere interfaces fluctuate on scales of a few seconds to several minutes as indicated by occasional observations (e.g. Ballard et al. 2004). It is an open question how far these fluctuations are a response to high-frequency dynamics of turbulent energy exchange between surface and atmosphere. Paper IV applies the spatio-temporal decomposition scheme in order to decompose four 1 Hz TST runs recorded in April 2009 (day/night, leaves-on/leaves-off) into a fluctuating, high-frequency (< 20 min) and a long-term mean part (> 20 min).

Spatial differences in temporally averaged surface temperatures are related to facet materials, height above ground and azimuth of observed wall and roof surfaces (thermal anisotropy). During the day trees, lawns and shadowed surfaces experienced the lowest surface temperatures. In contrast, roofs, sunlit walls and street surfaces show highest surface temperatures. Mean temperatures of walls and roofs are significantly above T_a and generally increase with height (Paper IV, Figure 11a). Surfaces situated higher above ground received more direct ${}^{\downarrow}E_{SW}$ for a longer period of the day, which explains that mean surface temperature is significantly above T_a for roofs and higher walls. In contrast, lower surfaces are more likely in shadow and are below or at T_a.

During the night, roofs and lawns show lowest surface temperatures and are typically below T_a. In contrast, walls and road surfaces are warmest and are typically above T_a. Trees crowns are close to T_a. The same pattern was observed for other daytime periods (Paper I, Paper III). Mean surface temperatures decrease with height. Roofs are all significantly cooler than air temperatures, and their mean surface temperature generally decreases with height (Paper IV, Figure 11d). The influence of a reduced sky-view factor on the long-wave radiation exchange is suitable to explain higher temperatures of lower walls compared to higher walls. Notable are extraordinarily warm walls in narrow courtyards and walls in the denser part of the city (Paper IV, Fig 2 and Paper I, Fig 6d).

As urban form does not change over 20 min, sky-view factor, solar access and surface material can explain mean temperatures and warming/cooling rates, but not high-frequency fluctuations of surface temperatures.

Thermal patterns resulting from effective anisotropy are depicted in Paper IV (Fig. 13). Most building walls and roofs have an azimuth of 30º (NNE), 120º (ESE), 210º (SSW) or 300º (WNW) due to the rectangular street grid in the FOV. Walls with an azimuth towards WNW are not visible by the camera (which is pointing towards 325º). However, the camera can tangentially see roofs with an azimuth of around 300º that have a gentle slope. This applies mostly to the foreground of the FOV. While most NNE-facing walls are slightly below T_a in the daytime runs, walls facing ESE and SSW are 3-6 K warmer than T_a (Paper IV, Fig. 13a). For roofs, NNE-facing facets are coolest

and SSW-facing facets are warmest. The nighttime runs do not show any directional variability of roofs, while NNE-facing walls are about 1.5 K cooler in the evening than SSW-facing ones. Directional variation of surface temperature at night can be regarded as a long-term persistence effect originated from different radiation regimes during daytime. Lagouarde and Irvine (2008) found no effect of azimutal viewing direction for nighttime TIR observations and explained this 'by the fact that the distribution of street directions is rather uniform in the case of Toulouse'. Temperature fluctuations do not change significantly with azimuth for walls. Roofs show a clear anisotropy in the magnitude of fluctuations, where highest fluctuations are found on SSW-facing roofs and lowest on NNE-facing roofs (Paper IV, Fig. 13b).

A number of relationships were observed that link surface temperature fluctuations to the surface energy balance. (1) Surfaces with temperatures that were significantly different from T_a experienced the highest fluctuations (Paper IV, Fig. 14). (2) With increasing surface temperature above (below) T_a, fluctuations experienced a stronger negative (positive) skewness (Paper IV, Fig. 11). (3) Surface materials with low thermal admittance μ (lawns, vegetation) showed higher fluctuations than surfaces with high μ (walls, roads) (Paper IV, Fig. 16). (4) The emergence of leaves showed a measurable impact on high-frequency thermal behaviour where the leaves caused surface temperatures to fluctuate more compared to a leaves-off situation. (5) In many cases, observed fluctuations were coherent across several neighbouring pixels (Paper IV, Fig. 9 and Fig. 10). The evidence from (1) to (5) suggests that atmospheric turbulence and associated changes in Q_H and Q_E might be a significant control of surface temperature fluctuations at scales < 20 min.

4. Conclusions and outlook

At the beginning of this work, the question was whether it is possible to use an industrial-type thermography camera system for the study of urban microclimates. Now, three and a half years later, a huge dataset of continuously acquired TIR imagery and a comprehensive pre-processing chain are available. Overall, the acquisition of TST data from the roof of the Steglitzer Kreisel using a one-minute recording frequency was very fruitful. TST data availability amounts to 83 %, 78 % and 82 % for the years 2008, 2009 and 2010 respectively. This thesis shows that it is possible to use an industrial-type thermography camera system for continuous operation in general.

The second prerequisite condition in order to use ground-based thermography in urban climatological studies was related to the question how to perform an accurate pre-processing of TIR imagery acquired in oblique view, in particular how to remove atmospheric effects insofar as the 3-D urban form is concerned. The developed atmospheric correction method shows that the magnitude of atmospheric effects varies during a diurnal cycle and is particularly notable for surfaces showing a strong surface-to-air temperature difference. In the case study using TST data from 8th August 2009, the differences between uncorrected and corrected TIR imagery reach up to 7.7 K at noon. The use of non-spatially distributed LOS parameters for atmospheric corrections introduces a bias of up to 4.3 K at noon and up to 0.6 K at midnight (Paper I). However, some specific problems related to lens vignetting/narcissus effects are not completely solved (Paper I) and especially the analysis of high-frequency data identified considerable sensor noise that complicates the quantification of high-frequency fluctuations (Paper IV). The availability of a DSM model for the study area and the perspective projection of the 3-D objects onto the 2-D TIR image plane are essential to derive spatially distributed LOS parameters. At the same time, we have a detailed 3-D description of urban facets, which is critical in the progress of TIR remote sensing in urban environments as postulated by Voogt and Oke (2003). The available data of height, azimuth and slope for each building pixel in the FOV are the basis for quantification of relations between building geometry (urban structure) and thermal behaviour of the surface (Paper IV).

Further, the thesis demonstrates the potential of TST in order to study urban microclimates. The analysis of attenuation of persistence effects provides an opportunity to derive thermal admittance. It is necessary to carry out a controlled experiment using various urban materials in order to verify this method. The courtyard study (Paper II) and anisotropy analysis (Paper IV) reveal a basic phenomenon regarding the interpretation of nocturnal TIR images, because persistence effects and nocturnal anisotropy exist at night.

Although the description of vegetation inside the FOV still lacks information on 3-D geometry, the combination of TST, meteorological observations and 2-D surface descriptions (tree crown mask, degree of sealing, leaf size) reveal clear differences between tree genera and strong spatio-temporal variability of T_C (Paper III). Tree-specific T_C in response to the urban environment is essential for comprehensive research concerning the energy and water balance of individual trees. With knowledge from these studies, it is then possible to evaluate and optimise the benefits of trees in urban environments.

Further, the thesis underlines the potential of using high-frequency thermal remote sensing in energy balance and turbulence studies at complex land-atmosphere interfaces. Using high sampling frequencies in TST observations might allow for the extraction of information on the dynamic response of the surface energy balance to atmospheric turbulence, thermal properties of surface materials and visualization of turbulent motions (Paper IV).

The available long-term TST data set provides a basis for investigations on annual thermal behaviour of urban surfaces and holds the possibility to assess the accuracy of 3-D radiative exchange models and energy balance models developed for the complex urban environment. Further applications of TST should also address the role of the building envelope in sustainable urban design. TST and detailed physical descriptions of urban surfaces in the FOV may help to foster interdisciplinary research on the linkages between outdoor and indoor climates. On the long-term perspective, a complete inventory of all trees in the FOV should be available. Recently five trees were equipped with sap flux sensors in order to analyse linkages between canopy temperature and transpiration (stomatal response) in different urban settings and under various atmospheric conditions.

References

Anandakumar, K. (1999): A study on the partition of net radiation into heat fluxes on a dry asphalt surface. Atmospheric Environment 33, 3911 - 3918.

Asaeda, T., Ca, V. T. and Wake, A. (1996): Heat storage of pavement and its effect on the lower atmosphere. Atmospheric Environment 30, 413-427.

Asano, K., Hoyano, A. and Matsunaga, T. (1996): Development of an urban thermal environment measurement system using a new spherical thermography technique. Proceedings SPIE 2744, 620-631.

Arnfield, A. J. (1990): Street design and urban canyon solar access. Energy and Buildings 14, 117-131.

Arnfield, A. J. (2003): Two decades of urban climate research: a review of turbulence, exchanges of energy and water, and the urban heat island. International Journal of Climatology 23, 1-26.

Ballard, J. R., Smith, J. A., Koenig, G. G. (2004): Towards a high temporal frequency grass canopy thermal IR model for background signatures. Proceedings SPIE 5431, 251-259.

Becker, F. and Li, Z. L. (1990): Towards a local split window method over land surfaces. International Journal of Remote Sensing 11, 369-393.

Becker, F. and Li, Z.-L. (1995): Surface temperature and emissivity at various scales: Definition, measurement and related problems. Remote Sensing Reviews 12, 225-253.

Ben-Dor, E. and Saaroni, H. (1997): Airborne video thermal radiometry as a tool for monitoring microscale structures of the urban heat island. International Journal of Remote Sensing 18, 3039-3053.

Berk, A., Bernstein, L. S., Anderson, G. P., Acharya, P. K., Robertson, D. C., Chetwynd, J. H. and Adler-Golden, S. M. (1998): MODTRAN cloud and multiple scattering upgrades with application to AVIRIS. Remote Sensing of Environment 65, 367-375.

Berk, A., Anderson, G. P., Acharya, P. K., Bernstein, L. S., Muratov, L., Lee, J., Fox, M. J., Adler-Golden, S. M., Chetwynd, J. H., Hoke, M. L., Lockwood, R. B., Cooley, T. W. and Gardner, J. A. (2005):

MODTRAN5: a reformulated atmospheric band model with auxiliary species and practical multiple scattering options. Proceedings SPIE 5655, 88-95.

Bonan, G. (2008): Ecological Climatology. Concepts and Applications. Cambridge University Press, Cambridge.

Blocken, B. and Carmeliet, J. (2004): Pedestrian wind environment around buildings: Literature review and practical examples. Journal of Thermal Envelope and Building Science 28, 107-159.

Bush, S. E., Pataki, D. E., Hultine, K. R., West, A. G., Sperry, J. S. and Ehleringer, J. R. (2008): Wood anatomy constrains stomatal responses to atmospheric vapor pressure deficit in irrigated, urban trees. Oecologia 156, 13-20.

Carlson, T. N., Dodd, J. K., Benjamin, S. G. and Cooper, J. N. (1981): Satellite estimation of the surface energy balance, moisture availability and thermal inertia. Journal of Applied Meteorology 20, 67-87.

Celestian, S. B. and Martin, C. A. (2005): Effects of parking lot location on size and physiology of four southwest landscape trees. Journal of Arboriculture 31, 191-197.

Christen, A. and Vogt, R. (2004): Energy and radiation balance of a central European city. International Journal of Climatology 24, 1395-1421.

Chudnovsky, A., Ben-Dor, E. and Saaroni, H. (2004): Diurnal thermal behavior of selected urban objects using remote sensing measurements. Energy and Buildings 36, 1063-1074.

Eliasson, I. (1992): Infrared thermography and urban temperature patterns. International Journal of Remote Sensing 13, 869-879.

Dash, P., Göttsche, F.-M., Olesen, F.-S. and Fischer, H. (2002): Land surface temperature and emissivity estimation from passive sensor data: Theory and practice-current trends. International Journal of Remote Sensing 23, 2563-2594.

Dousset, B. and Gourmelon, F. (2003): Satellite multi-sensor data analysis of urban surface temperatures and landcover. Journal of Photogrammetry and Remote Sensing 58, 43-54.

Foley, J. D. and van Dam, A. (1984): Fundamentals of interactive computer graphics. Addison-Wesley Publishing Company, Reading.

Gallo, K. P., McNab, A. L., Karl, T. R., Brown, J. F., Hood, J. J. and Tarpley, J. D. (1992): The use of a vegetation index for assessment of the urban heat island effect. International Journal of Remote Sensing 14, 2223-2230.

Grace, J. (1978): The turbulent boundary layer over a flapping Populus leaf. Plant, Cell & Environment 1, 35-38.

Grimmond, C. S. B., Souch, C. and Hubble, M. D. (1996): Influence of tree cover on summertime surface energy balance fluxes, San Gabriel Valley, Los Angeles. Climate Research 6, 45-57.

Hafner, J. and Kidder, S. Q. (1999): Urban heat island modeling in conjunction with satellite-derived surface/soil parameters. Journal of Applied Meteorology 38, 448-465.

Hall, D. J., Walker, S. and Spanton, A. M. (1999): Dispersion from courtyards and other enclosed spaces. Atmospheric Environment 33, 1187-1203.

Heisler, G. M. (1986): Effects of individual trees on the solar radiation climate of small buildings. Urban Ecology 9, 337-359.

Henry, J. A., Dicks, S. E., Wetterqvist, O. F. and Roguski, S. J. (1989): Comparison of satellite, ground-based, and modeling techniques for analyzing the urban heat island. Photogrammetric Engineering and Remote Sensing 55, 69-76.

Hoyano, A., Asano, K. and Kanamaru, T. (1999): Analysis of the sensible heat flux from the exterior surface of buildings using time sequential thermography. Atmospheric Environment 33, 3941-3951.

Iino, A. and Hoyano, A. (1996): Development of a method to predict the heat island potential using remote sensing and GIS data. Energy and Buildings 23, 199-205.

Jacob, F., Gu, X. F., Hanocq, J. F., Tallet, N. and Baret, F. (2003). Atmospheric corrections of single broadband channel and multidirectional airborne thermal infrared data: application to the ReSeDA experiment. International Journal of Remote Sensing 24, 3269-3290.

Kenny, N., Warland, J., Brown, R. and Gillespie, T. (2008): Estimating the radiation absorbed by a human. International Journal of Biometeorology 52, 491-503.

Kjelgren, R. and Montague, T. (1998): Urban tree transpiration over turf and asphalt surfaces. Atmospheric Environment 32, 35-41.

Kobayashi, T. and Takamura, T. (1994): Upward longwave radiation from a non-black urban canopy. Boundary-Layer Meteorology 69, 201-213.

Körner, C., Scheel, J. A. and Bauer, H. (1979): Maximum leaf diffusive conductance in vascular plants. Photosynthetica 13, 45-82.

Körner, C. (1985): Humidity responses in forest trees - precautions in thermal scanning surveys. Archives for Meteorology, Geophysics, and Bioclimatology. Series B, Climatology, Environmental Meteorology, Radiation Research 36, 83-98.

Kucharik, C. J., Norman, J. M. and Gower, S. T. (1998): Measurements of leaf orientation, light distribution and sunlit leaf area in a boreal aspen forest. Agricultural and Forest Meteorology 91, 127-148.

Lagouarde, J.-P., Moreau, P., Irvine, M., Bonnefond, J. M., Voogt, J. A. and Solliec, F. (2004): Airborne experimental measurements of the angular variations in surface temperature over urban areas: case study of Marseille (France). Remote Sensing of Environment 93, 443-462.

Lagouarde, J.-P. and Irvine, M. (2008): Directional anisotropy in thermal infrared measurements over Toulouse city centre during the CAPITOUL measurement campaigns: First results. Meteorology and Atmospheric Physics 102, 173-185.

Lagouarde, J.-P., Henon, A., Kurz, B., Moreau, P., Irvine, M., Voogt, J. A. and Mestayer, P. (2010): Modelling daytime thermal infrared directional anisotropy over Toulouse city centre. Remote Sensing of Environment 114, 87-105.

Landsberg, H. E. (1981): The urban climate. International Geophysics Series, Vol. 28, Academic Press, New York.

Lemonsu, A., Belair, S., Mailhot, J., Benjamin, M., Chagnon, F., Morneau, G., Harvey, B., Voogt, J. A. and Jean, M. (2008): Overview and first results of the Montreal urban snow experiment 2005. Journal of Applied Meteorology and Climatology 47, 59-75.

Leuzinger, S. and Körner, C. (2007): Tree species diversity affects canopy leaf temperatures in a mature temperate forest. Agricultural and Forest Meteorology 146, 29-37.

Leuzinger, S., Vogt, R. and Körner, C. (2010): Tree surface temperature in an urban environment. Agricultural and Forest Meteorology 150, 56-62.

Masson, V., Gomes, L., Pigeon, G., Liousse, C., Pont, V., Lagouarde, J.-P., Voogt, J. A., Salmond, J., Oke, T. R., Hidalgo, J., Legain, D., Garrouste, O., Lac, C., Connan, O., Briottet, X., Lachérade, S. and Tulet, P. (2008): The Canopy and Aerosol Particles Interactions in TOulouse Urban Layer (CAPITOUL) experiment. Meteorology and Atmospheric Physics 102, 135-157.

Matzarakis, A., Rutz, F. and Mayer, H. (2007): Modelling radiation fluxes in simple and complex environments - application of the RayMan model. International Journal of Biometeorology 51, 323-334.

Meier, F., Richters, J., Scherer, D., Inagaki, A., Kanda, M. and Hagishima, A. (2009): Outdoor scale model experiment to evaluate the spatio-temporal variability of urban surface temperature. 28. Jahrestagung des AK Klima am KlimaCampus Hamburg, 30.10-01.11.2009, Poster, Tagungsband, 46.

Mertens, E. (1999): Bioclimate and city planning - open space planning. Atmospheric Environment 33, 4115-4123.

Mestayer, P. G., Durand, P., Augustin, P., Bastin, S., Bonnefond, J. M., Benech, B., Campistron, B., Coppalle, A., Delbarre, H., Dousset, B., Drobinski, P., Druilhet, A., Frejafon, E., Grimmond, C. S. B., Groleau, D., Irvine, M., Kergomard, C., Kermadi, S., Lagouarde, J.-P., Lemonsu, A., Lohou, F., Long, N., Masson, V., Moppert, C., Noilhan, J., Offerle, B., Oke, T. R., Pigeon, G., Puygrenier, V., Roberts, S., Rosant, J. M., Said, F., Salmond, J., Talbaut, M. and Voogt, J. A. (2005): The urban boundary-layer field campaign in Marseille (UBL/CLU-ESCOMPTE): Set-up and first results. Boundary-Layer Meteorology 114, 315-365.

Mills, G. (2008): Urban Climatology and its relevance to urban design. 25th Conference on Passive and Low Energy Architecture (PLEA), Dublin, Available online: http://architecture.ucd.ie/Paul/PLEA2008/content/papers/oral/PLEA_FinalPaper_ref_250.pdf [latest accessed January 4, 2011].

Montague, T. and Kjelgren, R. (2004): Energy balance of six common landscape surfaces and the influence of surface properties on gas exchange of four containerized tree species. Scientia Horticulturae 100, 229-249.

Monteith J. L. and Unsworth M. H. (2008): Principles of environmental physics. Academic Press, Oxford.

Mueller, E. C. and Day, T. A. (2005): The effect of urban ground cover on microclimate, growth and leaf gas exchange of oleander in Phoenix, Arizona. International Journal of Biometeorology 49, 244-255.

Nichol, J. E. (1996): High-resolution surface temperature patterns related to urban morphology in a tropical city: A satellite-based study. Journal of Applied Meteorology 35, 135-146.

Nichol, J. E. (1998): Visualisation of urban surface temperatures derived from satellite images. International Journal of Remote Sensing 19, 1639-164.

Norman, J. M. and Becker, F. (1995): Terminology in thermal infrared remote sensing of natural surfaces. Agricultural and Forest Meteorology 77, 153-166.

Oke, T. R. (1979): Advectively-assisted evapotranspiration from irrigated urban vegetation. Boundary-Layer Meteorology 17, 167-173.

Oke, T. R. (1984): Methods in Urban Climatology. In: Kirchhofer, W., Ohmura, A., and Wanner, H. (Ed.): Applied Geography. Zürcher Geografische Schriften 14, 19-29.

Oke, T. R. (1987): Boundary Layer Climates. Routledge, London.

Oke, T. R. (1988): The urban energy balance. Progress in Physical Geography 12, 471-508.

Oke, T. R. (1989): The micrometeorology of the urban forest. Philosophical Transactions of the Royal Society of London, Series B, Biological Sciences 324, 335-349.

Oke, T. R. (1995): The heat island of the urban boundary layer: characteristics, causes and effects. In: Cermak, J. E., Davenport, A. G., Plate, E. J. and Viegas, D. X. (Ed.): Wind climate in cities. NATO Science Series 277, Kluwer Academic Publishers, Dordrecht, 81-107.

Oke, T. R. (1997): Surface Climate Processes. In: Bailey, W. G., Oke, T. R. and Rouse, W. R. (Ed.): Surface Climates of Canada. McGill-Queen's University Press, Montreal, 21-43.

Oke, T. R. (2004): Initial guidance to obtain representative meteorological observations at urban sites. Instruments and methods of observation program. IOM Report No. 81, WMO/TD 1250, World Meteorological Organization, Geneva.

Orlanski, I. (1975): A rational subdivision of scales for atmospheric processes. Bulletin of the American Meteorological Society, 56, 527-530.

Parlow, E. (2003): The urban heat budget derived from satellite data. Geographica Helvetica 58, 99-111.

Prata, A. J., Caselles, V., Coll, C., Sobrino, J. A. and Ottlé, C. (1995): Thermal remote sensing of land surface temperature from satellites: Current status and future prospects. Remote Sensing Reviews 12, 175-224.

Price, J. C. (1984): Land surface-temperature measurements from the split window channels of the NOAA-7 Advanced Very High-Resolution Radiometer. Journal of Geophysical Research-Atmospheres 89, 7231-7237.

Quattrochi, D. A. and Luvall, J. C. (Ed.) (2003): Thermal remote sensing in land surface processes. CRC Press, Boca Raton.

Rigo, G., Parlow, E. and Oesch, D. (2006): Validation of satellite observed thermal emission with in-situ measurements over an urban surface. Remote Sensing of Environment 104, 201-210.

Rigo, G. and Parlow, E. (2007): Modelling the ground heat flux of an urban area using remote sensing data. Theoretical and Applied Climatology 90, 185-199.

Rotach, M. W., Vogt, R., Bernhofer, C., Batchvarova, E., Christen, A., Clappier, A., Feddersen, B., Gryning, S.-E., Martucci, G., Mayer, H., Mitev, V., Oke, T. R., Parlow, E., Richner, H., Roth, M., Roulet, Y.-A., Ruffieux, D., Salmond, J. A., Schatzmann, M. and Voogt, J. A. (2005): BUBBLE - An urban boundary layer meteorology project. Theoretical and Applied Climatology 81, 231-261.

Roth, M., Oke, T. R. and Emery, W. (1989): Satellite-derived urban heat islands from three coastal cities and the utilization of such data in urban climatology. International Journal of Remote Sensing 10, 1699-1720.

Scherer, D. (2005): Energy exchange and climates of urban structures and environments (EXCUSE). 4th German-Japanese Meeting on Urban Climatology, Tsukuba, Japan, November 30 - December 4, 2005.

Schmugge, T., Hook, S. J. and Coll, C. (1998): Recovering surface temperature and emissivity from thermal infrared multispectral data. Remote Sensing of Environment 65, 121-131.

Schuepp, P. H. (1993): Tansley Review No. 59 Leaf boundary-layers. New Phytologist 125, 477-507.

Senate Department for Urban Development (2007): Berlin digital environmental atlas 01.02 impervious soil coverage (sealing of soil surface). Data base: Urban and Environmental Information System (UEIS).

Shashua-Bar, L., Hoffman, M. E. and Tzamir, Y. (2006): Integrated thermal effects of generic built forms and vegetation on the UCL microclimate. Building and Environment 41, 343-354.

Sobrino, J. A., Coll, C. and Caselles, V. (1991): Atmospheric correction for land surface-temperature using NOAA-11 AVHRR Channel-4 and Channel-5. Remote Sensing of Environment 38, 19-34.

Soux, A., Voogt, J. A. and Oke T. R. (2004): A model to calculate what a remote sensor 'sees' of an urban surface. Boundary-Layer Meteorology 111, 109–132.

Spronken-Smith, R., Oke, T. R. and Lowry, W. (2000): Advection and the surface energy balance across an irrigated urban park. International Journal of Climatology 20, 1033-1047.

Streutker, D. R. (2002): A remote sensing study of the urban heat island of Houston, Texas. International Journal of Remote Sensing 23, 2595-2608.

Stull, R. B. (1988): An introduction to boundary layer meteorology. Kluwer Academic Publishers, Dordrecht.

Suckling, P. W. (1980): The energy-balance microclimate of a suburban lawn. Journal of Applied Meteorology 19, 606-608.

Takebayashi, H. and Moriyama, M. (2009): Study on the urban heat island mitigation effect achieved by converting to grass-covered parking. Solar Energy 83, 1211-1223.

United Nations (UN) Department of Economic and Social Affairs, Population Division (2010): World Urbanization Prospects: The 2009 Revision. Available online: http://esa.un.org/unpd/wup/index.htm [latest accessed December 12, 2010].

Voogt, J. A. (2008): Assessment of an urban sensor view model for thermal anisotropy. Remote Sensing of Environment 112, 482-495.

Voogt, J. A. and Oke, T. R. (1997): Complete urban surface temperatures. Journal of Applied Meteorology 36, 1117-1132.

Voogt, J. A. and Oke, T. R. (1998a): Effects of urban surface geometry on remotely sensed surface temperature. International Journal of Remote Sensing 19, 895-920.

Voogt, J. A. and Oke, T. R. (1998b): Radiometric temperatures of urban canyon walls obtained from vehicle traverses. Theoretical and Applied Climatology 60, 199-217

Voogt, J. A. and Grimmond, C. S. B. (2000): Modeling surface sensible heat flux using surface radiative temperatures in a simple urban area. Journal of Applied Meteorology 39, 1679-1699.

Voogt, J. A. and Oke, T. R. (2003): Thermal remote sensing of urban climates. Remote Sensing of Environment 86, 370-384.

Weng, Q. H., Lu, D. S. and Liang, B. Q. (2006): Urban surface biophysical descriptors and land surface temperature variations. Photogrammetric Engineering and Remote Sensing 72, 1275-1286.

Weng, Q. H. (2009): Thermal infrared remote sensing for urban climate and environmental studies: Methods, applications, and trends. Journal of Photogrammetry and Remote Sensing 64, 335-344.

Wigley, G. and Clark, J. A. (1974): Heat transport coefficients for constant energy flux models of broad leaves. Boundary-Layer Meteorology 7, 139-150.

Whitlow, T. H., Bassuk, N. L. and Reichert, D. L. (1992): A 3-year study of water relations of urban street trees. Journal of Applied Ecology 29, 436-450.

Xu, W., Wooster, M. J. and Grimmond, C. S. B. (2008): Modelling of urban sensible heat flux at multiple spatial scales: A demonstration using airborne hyperspectral imagery of Shanghai and a temperature-emissivity separation approach. Remote Sensing of Environment 112, 3493-3510.

Yang, L. and Li, Y. (2009): City ventilation of Hong Kong at no-wind conditions. Atmospheric Environment 43, 3111-3121.

Zmarsly, E., Kuttler, W. and Pethe, H. (2002): Meteorologisch-klimatologisches Grundwissen. Eine Einführung mit Übungen, Aufgaben und Lösungen. Ulmer, Stuttgart.

Appendix A: Atmospheric correction of thermal infrared imagery of the 3-D urban environment acquired in oblique viewing geometry

Meier, F., Scherer, D., Richters, J. and Christen, A. (2010): Atmospheric correction of thermal infrared imagery of the 3-D urban environment acquired in oblique viewing geometry. *Atmospheric Measurement Techniques Discussions*, 3, 5671–5703. doi:10.5194/amtd-3-5671-2010.

Status: Published

Own contribution:

- TST data acquisition
- Meteorological data collection
- Processing of TST data and meteorological data
- Handling of 3-D city model and DGM data
- Collection of ground control points
- Implementation of radiative transfer model software (with co-authors)
- Development of atmospheric correction procedure
- Analysis and interpretation of experimental and modelling results
- Validation and TIR sensor comparison
- Preparation of manuscript with all figures and tables and subsequently revision of the manuscript after comments and improvements of co-authors

Atmos. Meas. Tech. Discuss., 3, 5671–5703, 2010
www.atmos-meas-tech-discuss.net/3/5671/2010/
doi:10.5194/amtd-3-5671-2010

Atmospheric Measurement Techniques Discussions

Atmospheric correction of thermal-infrared imagery of the 3-D urban environment acquired in oblique viewing geometry

F. Meier[1], D. Scherer[1], J. Richters[2], and A. Christen[3]

[1]Technische Universität Berlin, Department of Ecology, Chair of Climatology, Rothenburgstraße 12, 12165 Berlin, Germany
[2]Lohmeyer Consulting Engineers GmbH & Co. KG, Karlsruhe, Germany
[3]University of British Columbia, Department of Geography & Atmospheric Science Program, Vancouver, Canada

Received: 7 October 2010 – Accepted: 29 November 2010 – Published: 13 December 2010

Correspondence to: F. Meier (fred.meier@tu-berlin.de)

Published by Copernicus Publications on behalf of the European Geosciences Union.

Abstract

This research quantifies and discusses atmospheric effects that alter the radiance observed by a ground-based thermal-infrared (TIR) camera mounted on top of a high-rise building in the city of Berlin, Germany. The study shows that atmospheric correction of ground-based TIR imagery of the three-dimensional (3-D) urban environment acquired in oblique viewing geometry has to account for spatial variability of line-of-sight (LOS) geometry. We present an atmospheric correction procedure that uses these spatially distributed LOS geometry parameters, the radiative transfer model MODTRAN 5.2 and atmospheric profile data derived from meteorological measurements in the field of view (FOV) of the TIR camera. The magnitude of atmospheric effects varies during the analysed 24-hourly period (8 August 2009) and is particularly notable for surfaces showing a strong surface-to-air temperature difference. The differences between uncorrected and corrected TIR imagery reach up to 7.7 K at 12:00. Atmospheric effects are biased up to 4.3 K at 12:00 and up to 0.6 K at 24:00, if non-spatially distributed LOS parameters are used.

1 Introduction

Surface temperature is a key variable in the study of energy and mass exchange at the surface-atmosphere interface. The combination of natural and anthropogenic three-dimensional (3-D) objects in urban areas results in strong spatial and temporal heterogeneity of surface temperatures of urban facets (Voogt and Oke, 1998; Lagouarde and Irvine, 2008; Lagouarde et al., 2010). Thermal-infrared (TIR) remote sensing approaches, which allow the derivation of surface temperatures, have been widely applied in urban climate studies (Voogt and Oke, 2003; Weng, 2009) and were part of several integrated field campaigns like BUBBLE (Rotach et al., 2005), ESCOMPOTE (Mestayer et al., 2005) and CAPITOUL (Masson et al., 2008).

With respect to urban climate research, low cost and high-resolution TIR camera systems mounted on towers or building roofs provide an alternative to airborne and satellite platforms (Voogt and Oke, 2003). Ground-based TIR remote sensing approaches were part of several studies addressing the energy exchange in urban areas. For instance, Hoyano et al. (1999) used time-sequential thermography (TST) for calculating sensible heat flux density at the building scale. In Tokyo, a TIR camera measured urban surface temperatures from the top of a high-rise building for derivation of a local-scale thermal property parameter (Sugawara et al., 2001). Further ground-based studies used TST for the assessment of thermal characteristics of various urban surfaces (Chudnovsky et al., 2004), to study spatio-temporal differences between surface and air temperature as an important boundary condition for ventilation of the urban canopy layer by buoyancy effects (Yang and Li, 2009), or to study spatio-temporal persistence of shadow effects and surface thermal admittance (Meier et al., 2010).

However, radiative processes in the atmosphere between surface and sensor have an impact on remote sensing data. In the TIR part of the electromagnetic spectrum, atmospheric effects that alter the radiance observed by the sensor include absorption and emission primarily induced by water vapour, carbon dioxide and ozone. These atmospheric effects can lead to temperature differences between true surface temperature and remotely sensed values recorded by the sensor larger than 10 K (Jacob et al., 2003).

Several methods are available to remove these atmospheric effects depending on sensor characteristics e.g. the split window technique for multi-channel sensors (Price, 1984; Becker and Li, 1990; Sobrino et al., 1991; Kerr et al., 1992) or the use of radiative transfer models coupled with atmospheric profile data on pressure, temperature and humidity adequate for multi and single-channel sensors (Berk et al., 1998; Schmugge et al., 1998; Richter and Schläpfer, 2002). While these methods are common for data derived from satellite (Prata et al., 1995; Dash et al., 2002) or airborne platforms (Jacob et al., 2003; Lagouarde et al., 2004; Lagouarde and Irvine, 2008), the need for atmospheric correction of ground-based TIR imagery acquired in oblique view is an

open question insofar as the 3-D urban form is concerned.

Only a few ground-based studies account for atmospheric effects. They include either the use of a radiative transfer model to determine a linear relation between observed and corrected surface temperature for target-sensor distances of selected region of interests (Sugawara et al., 2001) or the assumption of a global sensor-target distance and atmospheric transmission value (Yang and Li, 2009).

The objective of this paper is to present a comprehensive atmospheric correction procedure for ground-based single-channel TIR sensors that works on a pixel-by-pixel basis considering the 3-D form of the urban environment and resulting differences in line-of-sight (LOS) geometry due to an oblique viewing geometry. We give answers on how to derive view zenith angle (θ_j), surface height a.s.l. (z_j^{surf}) and sensor-target distances for every image pixel j. Further we quantify the magnitude of atmospheric effects on the TST data in the study area during a diurnal cycle using the atmospheric radiative transfer model MODTRAN 5.2 (MOD5) (Berk et al., 2005) coupled with profile data from temperature and humidity measurements in the field of view (FOV) of the TIR camera.

Section 2 describes the theoretical background and shows possible atmospheric effects on off-nadir TIR remote sensing in urban areas with the help of a fictitious experimental setup and MOD5 simulations. In the third section, we describe the study site, our experimental setup, pre-processing steps of TIR imagery, LOS parameter determination and the atmospheric correction procedure. Section 4 presents the spatial distribution of LOS parameters and atmospherically corrected TIR imagery during a diurnal cycle. In addition, we compare the results from the spatially distributed atmospheric correction procedure referred to as MLOS (multi line-of-sight) method with a simple approach using non-spatially distributed LOS parameters referred to as SLOS (single line-of-sight) method. Finally, we compare the originally TIR data and the results from the MLOS and SLOS approach with in-situ measurements acquired at one roof in the FOV.

2 Atmospheric effects on oblique TIR imagery in urban areas

This section describes the theoretical background of atmospheric effects on long-wave radiation and demonstrates these atmospheric effects with the help of a fictitious urban setup and radiative transfer simulations using MOD5.

2.1 Theoretical background

The radiance $L_i^{\text{cam}}(\theta_j, z_j)$ recorded in channel i of a ground-based TIR camera that observes a surface (image pixel j) having a certain height a.s.l. (z_j^{surf}) and under view zenith angle (θ_j), is the sum of the surface emission that is attenuated by the atmosphere, the upward radiance emitted by the atmosphere and the radiance from the environment for instance the sky or building walls that is reflected by the ground surface. Under the assumption that the surface is a Lambertian surface, we can write (cf. Sobrino et al., 1991):

$$L_i^{\text{cam}}(\theta_j, z_j^{\text{surf}}) = \int d\lambda f_i(\lambda)\epsilon_\lambda B_\lambda(T)\tau_\lambda(\theta_j, z_j^{\text{surf}}) + \int d\lambda f_i(\lambda) L_\lambda^{\text{atm}}(\theta_j, z_j^{\text{surf}}) + \int d\lambda f_i(\lambda)\frac{1-\epsilon_\lambda}{\pi}\tau_\lambda(\theta_j, z_j^{\text{surf}}) L_\lambda^{\text{envi}}, \quad (1)$$

where $f_i(\lambda)$ is the normalized spectral response of the TIR camera in channel i, ϵ is the surface spectral emissivity, B_λ is the spectral radiance from a blackbody at surface temperature T, and τ_λ is the spectral transmission of the atmosphere. The term L_λ^{atm} in Eq. (1) is the upward atmospheric spectral radiance and is given by:

$$L_\lambda^{\text{atm}}(\theta_j, z_j^{\text{surf}}) = \int_{z_j^{\text{surf}}}^{z^{\text{cam}}} dz B_\lambda(T_z)\frac{\delta\tau_\lambda(\theta_j, z^{\text{cam}}, z)}{\delta z}, \quad (2)$$

where $\tau_\lambda(\theta_j, z^{\text{cam}}, z)$ represents the spectral atmospheric transmittance between the altitude of the TIR camera z^{cam} e.g. on top of a high-rise building, and the altitude z that depends on how many atmospheric layers we consider in the radiative transfer model. If we consider only one atmospheric layer then z equals the height of the examined urban surface ($z = z_j^{\text{surf}}$) for instance the wall of the first floor that belongs to another high-rise building. The term T_z represents atmospheric temperature at level z.

L_λ^{envi} in Eq. (1) is the hemispherical value of the downward radiance originated from the environment (e.g. sky, building walls). In this study, the surface emissivity was assumed to unity and therefore we consider a surface brightness temperature (T_{b}). This assumption is motivated by the unknown spectral emissivity of the observed urban surfaces. Therefore, the at-sensor radiance $L_i^{\text{cam}}(\theta_j, z_j^{\text{surf}})$ for every pixel j is:

$$L_i^{\text{cam}}(\theta_j, z_j^{\text{surf}}) = \int d\lambda f_i(\lambda) B_\lambda(T_{\text{b}})\tau_\lambda(\theta_j, z_j^{\text{surf}}) + \int d\lambda f_i(\lambda) L_\lambda^{\text{atm}}(\theta_j, z_j^{\text{surf}}). \quad (3)$$

2.2 Quantification of atmospheric effects using MOD5 and a fictitious urban experimental setup

The aim of this section is to demonstrate the possible discrepancy ΔT_{b} between measured surface brightness temperature $T_{\text{b}}^{\text{cam}}$ by a single-channel TIR sensor and real surface brightness temperature $T_{\text{b}}^{\text{surf}}$ (Eq. 4).

$$\Delta T_{\text{b}} = T_{\text{b}}^{\text{cam}} - T_{\text{b}}^{\text{surf}} \quad (4)$$

For this purpose, we examine a fictitious urban experimental setup as depicted in Fig. 1a. The idea is to evaluate six vertical profiles of ΔT_{b} for two building walls A and B (both 150 m high) showing a homogenous $T_{\text{b}}^{\text{surf}}$ of 20 °C, 40 °C and 60 °C, respectively. Wall A is placed at a horizontal distance of 500 m from the observer and wall B at

a horizontal distance of 200 m. The camera position (z^{cam}) is 300 m above ground. The spectral characteristics of the single-channel TIR camera are adopted from our real experimental setup described in Sect. 3. This includes the TIR sensor response $f_i(\lambda)$ data, which is provided by the camera manufacturer. We calculate vertical profiles of ΔT_b in the following way. For T_b^{surf} given, the spectral blackbody radiance is calculated from the Planck equation. This spectral radiance $B_\lambda(T_b^{surf})$ is multiplied by the spectral transmission $\tau_\lambda(\theta, z^{surf})$ calculated from MOD5 and then added to $L_\lambda^{atm}(\theta, z^{surf})$ calculated from MOD5 for every θ and corresponding z^{surf} of the profile points derived from the given LOS geometry. In the next step, we multiply the simulated at-sensor spectral radiance by $f_i(\lambda)$ and integrate ($d\lambda$=20 nm, wavelengths increments of MOD5 runs) to get the band effective radiance L_i^{MOD5} for the given temperature T_b^{surf} of the wall. We can write:

$$L_i^{MOD5} = \int_{7.5\mu m}^{14.0\mu m} d\lambda [B_\lambda(T_b^{surf})\tau_\lambda(\theta, z^{surf}) + L_\lambda^{atm}(\theta, z^{surf})] f_i(\lambda). \quad (5)$$

The increment of z^{surf} amounts to 10 m. The atmosphere is considered as only one layer with a uniform air temperature (T_{air}) of 25 °C and a relative humidity (RH) of 45%. Finally, a temperature-radiance look-up table (LUT) can be generated to convert L_i^{MOD5} into T_b^{cam}. For a range of brightness temperatures (T_b^{LUT}=T_b^{surf}±15 K), we use the Plank equation within the sensor wavelengths and weighted by the sensor response $f_i(\lambda)$ to produce a band effective radiance for the LUT (L_i^{LUT}). The simulated L_i^{MOD5} is then compared to L_i^{LUT} and by an iterative approach using 0.1 K increments we selected the temperature whose associated integrated radiance in the LUT hat the smallest absolute difference with L_i^{MOD5}.

The evolution of vertical profiles of ΔT_b for wall A (black) and wall B (grey) as a function of LOS geometry and T_b^{surf} are displayed in Fig. 1b. The results show that ΔT_b depends on z^{surf}, θ and the difference between T_{air} and T_b^{surf}, which is important for

the relationship between atmospheric absorption and atmospheric emission. Cold surfaces (T_b^{surf}<T_{air}) enhance the impact of atmospheric emission, which induced an overestimation of T_b^{surf}. On the other hand, hot surfaces (T_b^{surf}>T_{air}) enhance the impact of atmospheric absorption, which induces an underestimation of T_b^{surf}, here by up to more than 7 K. The expanded range of θ for wall B leads to a clear vertical gradient of ΔT_b up to 1.2 K (T_b^{surf}=60 °C). In the case of wall A the vertical gradient of ΔT_b is only between 0.1 K (20 °C) and 0.5 K (60 °C). In the extreme case (T_b^{surf}=60 °C), the TIR camera records a temperature difference up to 3 K between the bottom of wall A and the top of wall B in spite of equal wall temperature.

The results from this theoretical study emphasise our motivation to develop an atmospheric correction procedure that works on a pixel-by-pixel basis considering the 3-D urban form.

3 Materials and method

In the following, we describe the experimental setup, data sets used, the calculation of LOS geometry parameters for every pixel of the TIR image and the atmospheric correction procedure.

3.1 Study site and experimental setup

The study site is located in Berlin (Germany) in the Steglitz-Zehlendorf district (52°27′ N, 13°19′ E). City structure is heterogenic and characterized by a five to six-storey block development, two storey residential houses, parks, trees, villas with gardens and one isolated high-rise building (see also Fig. 2a,b). This study is part of a research program called "Energy eXchange and Climates of Urban Structures and Environments (EXCUSE)" that focuses on quantification of energy, momentum and mass exchange processes in the urban boundary layer. In particular, a platform on top of the high-rise building carries a TIR camera system (InfraTec VarioCam head,

7.5–14.0 µm, 320×240 pixels) in order to record the spatial distribution of upward longwave radiation continuously. For details on technical specifications of the TIR camera system, please see Meier et al. (2010).

During routine operation, the TIR camera records one image per minute. The fixed camera position during this study ensures a valid comparison between the multitemporal imagery. The experimental setup is supplemented by meteorological measurements on top of the high-rise building (167 m a.s.l.), as well as near-ground instrumentation (66 m a.s.l., see also white circle in Fig. 2) within the FOV of the TIR camera in order to provide humidity and air temperature profile input data for MOD5. Measurement frequency is 5 s for air temperature ($T_{\mathrm{air}}^{66\mathrm{m}}$, $T_{\mathrm{air}}^{167\mathrm{m}}$), relative humidity ($\mathrm{RH}^{66\mathrm{m}}$, $\mathrm{RH}^{167\mathrm{m}}$) devices (Vaisala, HMP45A), which is the right sensor we used to measure air temperature and humidity and downward short-wave radiation ($^{\downarrow}E_{\mathrm{sw}}^{66\mathrm{m}}$, $^{\downarrow}E_{\mathrm{sw}}^{167\mathrm{m}}$) devices (Kipp & Zonen, CM3). Further, we installed one pyrometer measurement device (Heimann, KT15) directly above the roof to obtain in-situ surface brightness temperature ($T_{\mathrm{b}}^{\mathrm{roof}}$) for validation of the atmospheric correction procedure (Fig. 2c, white circle). The pyrometer is located 1 m offset from the roof and observes the roof under the same view zenith angle as the TIR camera.

3.2 Pre-processing, radiometric and geometric corrections of TIR imagery

The TIR camera system provides calibration metadata for each recorded image, derived from firmware calibration using laboratory blackbody temperatures. Depending on case temperature, the system generates calibration metadata in a user-defined frequency. The first step of image processing uses these internal calibration parameters for converting measured radiance (digital numbers, DN) into at-sensor brightness temperature $T_{\mathrm{b}}^{\mathrm{cam}}$ for each pixel. It is possible to convert $T_{\mathrm{b}}^{\mathrm{cam}}$ into at-sensor radiance L_i^{cam} by using the integral of the Planck equation at the sensors wavelengths and weighted by $f_i(\lambda)$ in order to do further corrections of TIR imagery based on radiance values.

3.2.1 Vignetting correction

Vignetting refers to the effect of radiance reduction towards the borders of a recorded image relative to its projection centre. The lens itself (aperture effect, pupil aberration) and the parameters of geometric projection of radiance on a non-spherical sensing element (Mitchell, 2010) can cause vignetting. The latter effect is often referred to as the "cosine fourth" law (e.g. Sands, 1973). It refers to the process that on a flat sensing element, uniform radiance is not causing uniform radiance as we move off-axis away from the centre of the image. Those effects are kept to a minimum through optimal design of the lens.

Following the procedure described in Mitchell (2010) we correct empirically for vignetting using a dataset with uniform radiance from a Lambertian source and assuming that the centre of the focal plane array records the correct radiance. We use a dataset with dense fog recorded by the TIR camera system operated at the same location. The dataset was obtained over two minutes on 20 January 2006 from 17:31 to 17:33 Central European Time (CET). Radiance was recorded at 1 Hz and averaged over 120 s to reduce sensor noise. Figure 3a illustrates that L_i^{cam} shows a distinct and symmetrical gradient from the centre of the image to the corner. The range 0.66 $\mathrm{W\,m^{-2}\,sr^{-1}}$ corresponds to a range in $T_{\mathrm{b}}^{\mathrm{cam}}$ of approx. 1.5 K. The radiance measured in a rectangular 6×6 pixel window in the centre of the image was assumed to be least affected by vignetting and selected as reference radiance L_i^{ref}. Figure 3a shows the differences ΔL (Eq. 6) for every pixel at row x and column y.

$$\Delta L = L_i^{\mathrm{cam}}(x,y) - L_i^{\mathrm{ref}} \tag{6}$$

There is a minor close to linear gradient observed between the top and bottom of the image (0.17 $\mathrm{W\,m^{-2}\,sr^{-1}}$) probably due to real atmospheric temperature distribution in the fog. The inclusion of the entire image in the calibration process ensured that this gradient does not affect the calibration. We used a third-order polynomial fit through ΔL of all pixels as a function of radial distance (Fig. 3b) in order to correct the radiance

for vignetting as a function of radial distance δ (in pixels) to the centre pixel:

$$\Delta L = -2.054 \times 10^{-7}\delta^3 + 6.587 \times 10^{-5}\delta^2 - 8.259 \times 10^{-3}\delta + 0.033 \quad (7)$$

The third-order polynomial correction reduces the differences across the image from a root mean square error (RMSE) of 0.37 W m^{-2} sr^{-1} to 0.12 W m^{-2} sr^{-1} (unexplained noise). The correction is assumed to be valid for difference radiances measured and has been applied to all imagery prior to geometric and atmospheric correction.

3.2.2 Geometric correction

The wide-angle lens that was used produced geometric deformations. These deformations were analysed by measuring a grid of metallic pins in a regular square pattern. We used the positions of the metallic pins to construct a Delaunay triangulation of a planar set of points. Then the geometrical deviations in x- and y-direction were interpolated for each image pixel. By using a nearest-neighbour technique, the TIR image pixels can be shifted to their real positions. After correction for lens deformation, the TIR image covers a FOV of 57.5° by 44.7°. Other experiments with TIR cameras using wide-angle lenses (e.g. Lagouarde et al., 2004) also reported such effects.

3.3 Spatially distributed line-of-sight (LOS) geometry determination

The determination of spatially distributed LOS geometry parameters is based on digital surface model (DSM) data, photogrammetry and 3-D computer vision techniques. The idea is to link the TIR image pixels to corresponding 3-D coordinates via geometrical transformations used in computer graphics (Foley and van Dam, 1984) based on camera interior and exterior orientation parameters.

At first, we merged the 3-D building vector model, which is available for Berlin in the CityGML format (Kolbe, 2009), and the digital ground model (DGM), which is available in 1 m resolution, into a vector-based DSM. At present, the DSM does not include trees or any other vegetation. Therefore, the atmospheric correction of vegetative TIR pixels

uses LOS parameters representing the nearest underlying ground, wall or roof surface. In order to model the perspective projection of 3-D objects onto the two-dimensional (2-D) TIR image plane, we translate the origin of the DSM coordinate system to the vanishing point of the perspective projection using the following Eq.:

$$\begin{pmatrix} x \\ y \\ z \end{pmatrix} = \begin{pmatrix} X_{\mathrm{DSM}} \\ Y_{\mathrm{DSM}} \\ Z_{\mathrm{DSM}} \end{pmatrix} - \begin{pmatrix} X_{\mathrm{VP}} \\ Y_{\mathrm{VP}} \\ Z_{\mathrm{VP}} \end{pmatrix}, \quad (8)$$

where x, y, z are the coordinates in the new camera reference system, X_{DSM}, Y_{DSM}, Z_{DSM} are the 3-D coordinates of a point in the originally DSM object space coordinate system and X_{VP}, Y_{VP}, Z_{VP} are the 3-D coordinates of vanishing point of the perspective projection, which is the fixed TIR camera position.

The next step defines a view volume in order to realise the interior orientation. In our perspective projection, this is a frustum of a pyramid. Objects that fall within the view volume are projected toward the apex of the pyramid (viewpoint or eye position). Objects that are closer to the viewpoint appear larger because they occupy a proportionally larger amount of the view volume than those that are farther away, in the larger part of the frustum. The bounds of the view volume are described by the FOV parameters of the wide-angle lens of the TIR camera after geometric correction.

The exterior orientation was determined by using the optical centre point (P_{o}) of the TIR image and its coordinates in the camera reference system (x_{o}, y_{o}, z_{o}). Then the view zenith angle (θ_{o}) between nadir viewing position and P_{o} was calculated (Eq. 9) to execute the first rotation of the DSM around the horizontal x-axis (West–East) of the camera reference system using θ_{o} and 3-D rotation matrix calculation (Foley and van Dam, 1984).

$$\tan(\theta_{\mathrm{o}}) = \frac{\sqrt{x_{\mathrm{o}}^2 + y_{\mathrm{o}}^2}}{|z_{\mathrm{o}}|} \quad (9)$$

The view azimuth angle (φ_o) between the horizontal y-axis (North–South) and P_o was calculated (Eq. 10) to execute the second rotation of the DSM around the vertical z-axis of the camera reference system.

$$\tan(\varphi_o) = \frac{x_o}{y_o} \tag{10}$$

The TIR camera was installed horizontally and allows no tilt around the horizontal y-axis. Hence, a third rotation around this y-axis is not necessary to navigate the DSM into the correct perspective of the TIR camera.

Further, we selected 12 ground control points (GCP) from the DSM data set in order to calculate the RMSE between LOS geometry values derived directly from x, y, z coordinates of GCP and corresponding pixel values of LOS geometry patterns.

3.4 Atmospheric correction procedure

The flowchart of the MLOS atmospheric correction procedure is illustrated in Fig. 4. We applied the workflow to 30-min averages of TIR and meteorological data. In order to analyse TST data representing a diurnal cycle, we processed 48 TIR images.

The integrated radiance at the sensor level (L_i^{MOD5}) was simulated for a range of surface brightness temperatures based on air temperature ($T_b^{MOD5} \in [T_{air}^{66m} - 5K, T_{air}^{66m} + 45K]$) with a 1 K step and a range of LOS parameters with a 5° step for θ and a 10 m step for z^{surf}, respectively. This set of input parameters provides a reasonable temperature and LOS resolution and takes into account the lower and upper limit of each parameter. The MOD5 atmospheric profile was divided into three levels between z^{surf} and z^{cam}. Therefore, we used linear interpolated atmospheric profile data $T_{air}(z)$ and RH(z) derived from the meteorological measurements. Up to now, we only used TIR data from clear-sky days and hence we did not use the cloud options of MOD5.

Overall, 2750 MOD5 runs were used to build-up a LUT for every 30-min interval. Since we know the LOS parameters (θ_j, z_j^{surf}) for every pixel j, it is possible to obtain

bilinear interpolated LUT values (L_j^{bilin}) on a pixel-by-pixel basis relating the 50 input values of T_b^{MOD5} to the simulated at-sensor radiances. Further, T_b^{cam} is converted into L_j^{cam} by using the integral of the Planck equation at the sensors wavelengths and weighted by $f_i(\lambda)$ to relate the measured at-sensor brightness temperature to simulated at-sensor radiance. Finally atmospherically corrected surface brightness temperature T_b^{surf} is obtained by linear interpolation using L_j^{cam} of jth pixel, L_j^{bilin} and T_b^{MOD5} (see also Fig. 4).

The SLOS atmospheric correction method is similar to the method described above, but only one LOS parameter pair is used that represents the median of all θ_j and the median of all z_j^{surf}. Please note, this simple LOS description is already a result of navigating the DSM into the 2-D TIR image projection and cannot be equated with θ_o and φ_o. The SLOS method only needs 50 MOD5 runs to do an atmospheric correction of one TIR image.

4 Results and discussion

This section presents the spatial distribution of LOS parameters and atmospherically corrected TIR imagery during a diurnal cycle and the 24-hourly average. Further, we show the difference between T_b^{cam} and the atmospheric corrections from MLOS (T_b^{MLOS}) and SLOS (T_b^{SLOS}) method and discuss the results from MLOS and SLOS atmospheric correction procedures in relation to in-situ surface brightness temperature (T_b^{roof}) and the magnitude of atmospheric effects in relation to sealed and non-sealed surfaces.

4.1 Line-of-sight (LOS) geometry

In the visualizations (Fig. 5), we scaled the values of LOS geometry between 95% percentile (maximum brightness) and 5% percentile (minimum brightness). Furthermore, all grey-scale bars have benchmarks for minimum, median (50%) and maximum value. The same visualisation approach is used for TIR imagery presented in Fig. 6.

The perspective projection of the 3-D DSM onto the 2-D image plane is visualized in Fig. 5a. Please note, a wall of the high-rise building carrying the TIR camera is not visible in Fig. 5a, but in the TIR image, we can see this wall in the lower right corner (Fig. 6). This DSM wall polygon object is not visualized, because it is too close to the viewpoint and it lies not fully in the view volume. Thus, the LOS parameters for this wall surface are biased. This surface is excluded from our further analysis. Figure 5b shows the spatial distribution of θ_j. The range amounts to 45.5° and is 2.5 times higher than in our fictitious experimental setup (Sect. 2). For the SLOS method, we used the median θ_j that amounts to 60.15°. The RMSE between view zenith angles θ_{GCP} derived from 3-D coordinates of the 12 GCP and the corresponding values in the LOS pattern amounts to 0.8°.

Figure 5c shows the spatial distribution of z_j^{surf}. The range amounts to 37.1 m, which is approximately 25% of the range in comparison to the fictitious experimental setup. The highest surfaces are the roofs of the five-storey buildings, the church and the roofs in the background located on a small hill. For the SLOS method, we used the median z_j^{surf} that amounts to 49.10 m. The RMSE for z_j^{surf} is 1.1 m. Overall, the atmospheric path length on the FOV varies between 125.8 m and 773.2 m and the RMSE is 2.9 m (Fig. 5d).

4.2 Diurnal cycle of multi line-of-sight (MLOS) atmospherically corrected TIR imagery

We present atmospherically corrected TST data from 8 August 2009 at 06:00 (Fig. 6a), 12:00 (Fig. 6b), 18:00 (Fig. 6c) and 24:00 CET (Fig. 6d). All time specifications refer to CET and the end of the 30-min averaging period. The 24-hourly mean pattern is presented in Fig. 6e and to facilitate interpretability a corresponding photograph of the study site is added (Fig. 6f).

During this day, clear sky conditions caused high downward short-wave irradiance with a maximum of 800 W m^{-2} around noon. The daily mean T_{air}^{66m} was 21.2 °C, the maximum value reached 26.1 °C at 17:00 and the minimum reached 16.5 °C at 05:00. During daytime, trees and shadowed surfaces have the lowest temperatures. In contrast, roofs, sunlit walls and street surfaces show the highest temperatures, for instance several roofs reaching more than 50 °C at 12:00 (Fig. 6b red coloured surfaces).

During night-time, TIR patterns are dominated by roofs and lawn showing the lowest temperatures and in contrast walls and sealed surfaces have the highest temperatures. The trees are in the medium range showing slightly higher temperatures than roof surfaces. In the 24-hourly mean pattern the order from low to high temperatures is as follows: shadowed lawn, trees, building walls, sealed surfaces and roofs (Fig. 6e).

4.3 Multi line-of-sight (MLOS) versus single line-of-sight (SLOS) approach

A visualization approach using fixed colour bars allows interpretation of differences in TIR patterns. Therefore, the values for image scaling (Fig. 7) are derived from all three TIR images showing the difference between T_b^{cam} and T_b^{MLOS} (left column), the difference between T_b^{cam} and T_b^{SLOS} (middle column) and the difference between the two atmospheric correction methods ($T_b^{MLOS} - T_b^{SLOS}$, right column), representing the same 30-min periods as in Fig. 6. The box on the right side of every image plot shows the range of individual image values in order to allow quantitative comparison.

During daytime (Fig. 7b,c) MLOS atmospheric correction reveals that at-sensor values are consistently lower than T_b^{MLOS}. There is a clear spatial gradient showing a greater difference for surfaces located further away from the TIR camera. This is particularly notable for very hot surfaces. For instance, underestimation of roof surfaces in the background reaches up to 7.7 K at 12:00. The SLOS method also reveals a similar at-sensor underestimation depending on surface temperature (up to 4.6 K at 12:00) but a spatial gradient is not visible. The comparison of both atmospheric correction methods (Fig. 7b, right column) shows a clear spatial gradient where the MLOS

values are higher (up to 4.3 K) in the background and lower in the foreground (up to 1.5 K).

During night-time and immediately after sunrise atmospheric effects are much lower than during daytime. The difference between T_b^{cam} and the two atmospheric correction methods at 24:00 only varies between −0.2 K (5% percentile) and 0.4 K (95% percentile). The TIR camera overestimates cold surfaces ($T_b^{surf} < T_{air}$) e.g. for roofs furthest away from sensor and underestimates hot surfaces ($T_b^{surf} > T_{air}$) in the case of roads and walls whereas the MLOS pattern (Fig. 7d, left column) reveals the clear dependency on atmospheric path length. This spatial gradient is not visible in the SLOS pattern (Fig. 7d, middle column). However, the differences between MLOS and SLOS are very low (Fig. 7d, right column). The 24-hourly patterns are similar to the daytime patterns but with an overall lower magnitude.

4.4 In-situ data comparison

The comparison between T_b^{roof} and the corresponding remote sensing data (roof pixel) shows that the in-situ temperatures are consistently higher than T_b^{cam} with the exception of a short period in the morning between 08:30 and 09:30 (Fig. 8). The difference between T_b^{roof} and T_b^{cam} is clearly reduced due to atmospheric correction, whereas the MLOS method produces a RMSE of 1.69 K and the SLOS method a RSME of 1.84 K (Fig. 9c,d). The deviation of the roof LOS geometry parameters (θ_j=70.1°, z_j^{surf}=60.5 m) from the SLOS input parameters used for MOD5 simulations caused the difference between MLOS and SLOS with a maximum of 0.9 K at 11:00 (Fig. 8b).

In our case, the comparison to in-situ data is critical, because the examined roof is not a strictly homogenous surface. The roof structure produces micro-scale temperature patterns due to tiles self-shadowing and shadow from the measurements installations. This is important for the small FOV (9°) of the in-situ KT15 device installed very close (1 m) to the pitched roof resulting in a target area of 0.03 m^2. If we consider the distance of 310 m between roof and TIR camera then the geometric resolution of a roof

pixel amounts to 1.1 m. Thus, the FOV of the in-situ measurements covers only 3% of the TIR camera pixel. The values between 08:30 and 09:30 are excluded from the correlation and RMSE analysis (Fig. 9b,c,d).

In April 2010, we moved the TIR camera from the high-rise building and conducted an instrument comparison experiment in the garden of our institute over a 10-day period using a homogenous wood plate as target surface. The data from this experiment reveals that the KT15 device in comparison to the TIR camera produces consistently higher values (Fig. 9a).

4.5 Atmospheric effects regarding sealed and non-sealed surfaces

Now, we use the atmospheric path length as a representative parameter of LOS geometry variability in order to discuss atmospheric effects for different urban surface types. The fictitious experimental setup and results presented in Sect. 4.3 reveal that the atmospheric correction is sensitive to the surface-to-air temperature difference. Hence, we discuss atmospheric effects at 12:00 for two surface types derived from image masks. That are sealed surfaces (roofs, walls and roads) to account for hot surfaces and 108 selected tree crowns, because we expect that tree surface temperature is close to air temperature (Oke, 1987; Leuzinger et al., 2010).

The atmospheric effects ($T_b^{cam} - T_b^{MLOS}$) relating to sealed surfaces are shown in Fig. 10a. The atmospheric correction clearly depends on the distance between TIR camera and sealed surface. If we use the SLOS method, this effect produces a strong bias (Fig. 10c). With distance less than 230 m, the atmospheric correction using the SLOS method would produce a warm bias (up to 1.5 K) and from a distance of 230 m to the maximum path length, a cold bias (up to 4.3 K) is expected.

The atmospheric effects relating to tree crowns are shown in Fig. 10b,d. The dependence on path length is present, but $T_b^{cam} - T_b^{MLOS}$ is in the range of 1 K for 95.2% of the tree crown pixels. The slope of a linear regression between atmospheric effect and atmospheric path length (Fig. 10b) is only −0.0014 K m^{-1}. Therefore, the influence of

incorrect tree LOS geometry parameters due to missing information in the DSM is negligible. The SLOS method produces only a small warm bias up to 0.1 K (5% percentile) and the cold bias is up to 0.4 K (95% percentile) (Fig. 10d). This quantification is based on the 5% and 95% percentile data, because the extreme values are prone to represent non-tree crown pixels due to the porous tree crown or due to falsely classified pixels during the creation of the tree crown mask by visual interpretation of photographs and TIR imagery.

5 Conclusions

The study shows that atmospheric correction of ground-based TIR imagery of the 3-D urban environment acquired in oblique viewing geometry has to account for spatial variability of LOS geometry. The combination of 3-D city models, DGM data and 3-D computer vision techniques allow a pixel-by-pixel determination of LOS geometry parameters used for atmospheric correction. In this study the magnitude of atmospheric effects is up to 7.7 K (Fig. 7b, left column) and particularly notable for surfaces showing a strong surface-to-air temperature difference which is typical for urban environments (Voogt and Oke, 2003). The 24-hourly mean pattern shows atmospheric effects up to 2.6 K (Fig. 7e, left column).The applied MLOS atmospheric correction method reveals that the magnitudes of atmospheric effects are biased up to 4.3 K at 12:00 (Fig. 7b, right column) and up to 0.6 K (Fig. 7d, right column) at 24:00, if only the median LOS parameters are used.

An accurate determination of urban surface temperatures via thermal remote sensing is important for sensible heat flux calculations (Voogt and Grimmond, 2000) or the evaluation of surface heat island mitigation measures for instance the conversion of asphalt-covered parking areas to grass-covered ones (Takebayashi and Moriyama, 2009). Atmospheric effects are small for vegetative, shadowed surfaces and trees, but even a 1 K difference can be important for the study of surface temperature variability in relation to tree species or location within the city (Kjelgren and Montague, 1998;

Leuzinger et al., 2010). The atmospherically corrected TIR data are in good accordance with in-situ surface temperature measurements acquired above one roof inside the FOV of the TIR camera. However, the roof selected for in-situ measurements is not strictly homogenous and shows micro-scale temperature variability, which is not detectable by the TIR image geometrical resolution. The completely atmospheric correction processing chain (encoded in IDL) inclusive the MOD5 simulations needs approximately 1 min computing time on a dual core personal computer. Therefore, a near real-time application of the MLOS atmospheric correction procedure is possible for a TIR image recording frequency lower than 1 min. Further studies will address the estimation of cloud base and horizontal visibility for the atmospheric correction of TIR imagery acquired at non-clear sky days.

Acknowledgements. We would like to thank our colleges at the Chair of Climatology (Technische Universität Berlin, Department of Ecology) for helping to set up and maintain the TIR camera measurement platform and the meteorological measurement sides, G. P. Anderson and A. Berk for valuable comments on using MODTRAN 5.2 and T. H. Kolbe for making available the 3-D building model dataset.

References

Becker, F. and Li, Z. L.: Towards a local split window method over land surfaces, Int. J. Remote Sens., 11, 369–393, 1990. 5673

Berk, A., Bernstein, L. S., Anderson, G. P., Acharya, P. K., Robertson, D. C., Chetwynd, J. H., and Adler-Golden, S. M.: MODTRAN cloud and multiple scattering upgrades with application to AVIRIS, Remote Sens. Environ., 65, 367–375, 1998. 5673

Berk, A., Anderson, G. P., Acharya, P. K., Bernstein, L. S., Muratov, L., Lee, J., Fox, M. J., Adler-Golden, S. M., Chetwynd, J. H., Hoke, M. L., Lockwood, R. B., Cooley, T. W., and Gardner, J. A.: MODTRAN5: a reformulated atmospheric band model with auxiliary species and practical multiple scattering options, Soc. Photo-Opt. Instru., 5655, 88–95, 2005. 5674

Chudnovsky, A., Ben-Dor, E., and Saaroni, H.: Diurnal thermal behavior of selected urban objects using remote sensing measurements, Energ. Buildings, 36, 1063–1074, 2004. 5673

Dash, P., Göttsche, F.-M., Olesen, F.-S., and Fischer, H.: Land surface temperature and emissivity estimation from passive sensor data: theory and practice-current trends, Int. J. Remote Sens., 23, 2563–2594, 2002. 5673

Foley, J. D. and van Dam, A.: Fundamentals of interactive computer graphics, in: The Systems Programming Series, 1 edition, Addison-Wesley Publishing Company, Reading, 1984. 5681, 5682

Hoyano, A., Asano, K., and Kanamaru, T.: Analysis of the sensible heat flux from the exterior surface of buildings using time sequential thermography, Atmos. Environ., 33, 3941–3951, 1999. 5673

Jacob, F., Gu, X. F., Hanocq, J. F., Tallet, N., and Baret, F.: Atmospheric corrections of single broadband channel and multidirectional airborne thermal infrared data: application to the ReSeDA experiment, Int. J. Remote Sens., 24, 3269–3290, 2003. 5673

Kerr, Y. H., Lagouarde, J. P., and Imbernon, J.: Accurate land surface temperature retrieval from AVHRR data with use of an improved split window algorithm, Remote Sens. Environ., 41, 197–209, 1992. 5673

Kjelgren, R. and Montague, T.: Urban tree transpiration over turf and asphalt surfaces, Atmos. Environ., 32, 35–41, 1998. 5689

Kolbe, T. H.: Representing and exchanging 3-D city models with CityGML, in: Lecture Notes in Geoinformation and Cartography, edited by: Lee, J. and Zlatanova, S., Springer, Berlin, 15–31, 2009. 5681

Lagouarde, J.-P. and Irvine, M.: Directional anisotropy in thermal infrared measurements over Toulouse city centre during the CAPITOUL measurement campaigns: first results, Meteorol. Atmos. Phys., 102, 173–185, 2008. 5672, 5673

Lagouarde, J. P., Moreau, P., Irvine, M., Bonnefond, J. M., Voogt, J. A., and Solliec, F.: Airborne experimental measurements of the angular variations in surface temperature over urban areas: case study of Marseille (France), Remote Sens. Environ., 93, 443–462, 2004. 5673, 5681

Lagouarde, J. P., Henon, A., Kurz, B., Moreau, P., Irvine, M., Voogt, J., and Mestayer, P.: Modelling daytime thermal infrared directional anisotropy over Toulouse city centre, Remote Sens. Environ., 114, 87–105, 2010. 5672

Leuzinger, S., Vogt, R., and Körner, C.: Tree surface temperature in an urban environment, Agr. Forest Meteorol., 150, 56–62, 2010. 5688, 5690

Masson, V., Gomes, L., Pigeon, G., Liousse, C., Pont, V., Lagouarde, J.-P., Voogt, J., Salmond, J., Oke, T., Hidalgo, J., Legain, D., Garrouste, O., Lac, C., Connan, O., Briottet, X., Lachrade, S., and Tulet, P.: The Canopy and Aerosol Particles Interactions in TOulouse Urban Layer (CAPITOUL) experiment, Meteorol. Atmos. Phys., 102, 135–157, 2008. 5672

Meier, F., Scherer, D., and Richters, J.: Determination of persistence effects in spatio-temporal patterns of upward long-wave radiation flux density from an urban courtyard by means of time-sequential thermography, Remote Sens. Environ., 114, 21–34, 2010. 5673, 5679

Mestayer, P. G., Durand, P., Augustin, P., Bastin, S., Bonnefond, J. M., Benech, B., Campistron, B., Coppalle, A., Delbarre, H., Dousset, B., Drobinski, P., Druilhet, A., Frejafon, E., Grimmond, C. S. B., Groleau, D., Irvine, M., Kergomard, C., Kermadi, S., Lagouarde, J. P., Lemonsu, A., Lohou, F., Long, N., Masson, V., Moppert, C., Noilhan, J., Offerle, B., Oke, T. R., Pigeon, G., Puygrenier, V., Roberts, S., Rosant, J. M., Said, F., Salmond, J., Talbaut, M., and Voogt, J.: The urban boundary-layer field campaign in Marseille (UBL/CLU-ESCOMPTE): set-up and first results, Bound.-Lay. Meteorol., 114, 315–365, 2005. 5672

Mitchell, H. B.: Image Fusion. Theories, Techniques and Applications, 1st edition, Springer, Berlin, 2010. 5680

Oke, T. R.: Boundary Layer Climates, 2nd edition, Routledge, London, 1987. 5688

Prata, A. J., Caselles, V., Coll, C., Sobrino, J. A., and Ottlé, C.: Thermal remote sensing of land surface temperature from satellites: Current status and future prospects, Remote Sens. Rev., 12, 175–224, 1995. 5673

Price, J. C.: Land surface temperature measurements from the split window channels of the NOAA-7 advanced very high-resolution radiometer, J. Geophys. Res.-Atmos., 89, 7231–7237, 1984. 5673

Richter, R. and Schläpfer, D.: Geo-atmospheric processing of airborne imaging spectrometry data, Part 2: atmospheric/topographic correction, Int. J. Remote Sens., 23, 2631–2649, 2002. 5673

Rotach, M., Vogt, R., Bernhofer, C., Batchvarova, E., Christen, A., Clappier, A., Feddersen, B., Gryning, S.-E., Martucci, G., Mayer, H., Mitev, V., Oke, T., Parlow, E., Richner, H., Roth, M., Roulet, Y.-A., Ruffieux, D., Salmond, J., Schatzmann, M., and Voogt, J.: BUBBLE – an urban boundary layer meteorology project, Theor. Appl. Climatol., 81, 231–261, 2005. 5672

Sands, P. J.: Prediction of vignetting, J. Opt. Soc. Am., 63, 803–805, 1973. 5680

Schmugge, T., Hook, S. J., and Coll, C.: Recovering surface temperature and emissivity from thermal infrared multispectral data, Remote Sens. Environ., 65, 121–131, 1998. 5673

Sobrino, J. A., Coll, C., and Caselles, V.: Atmospheric correction for land surface temperature using NOAA-11 AVHRR channel 4 and channel 5, Remote Sens. Environ., 38, 19–34, 1991. 5673, 5675
Sugawara, H., Narita, K., and Mikami, T.: Estimation of effective thermal property parameter on a heterogeneous urban surface, J. Meteorol. Soc. Jpn., 79, 1169–1181, 2001. 5673, 5674
Takebayashi, H. and Moriyama, M.: Study on the urban heat island mitigation effect achieved by converting to grass-covered parking, Sol. Energy, 83, 1211–1223, 2009. 5689
Voogt, J. A. and Grimmond, C. S. B.: Modeling surface sensible heat flux using surface radiative temperatures in a simple urban area, J. Appl. Meteorol., 39, 1679–1699, 2000. 5689
Voogt, J. A. and Oke, T. R.: Effects of urban surface geometry on remotely-sensed surface temperature, Int. J. Remote Sens., 19, 895–920, 1998. 5672
Voogt, J. A. and Oke, T. R.: Thermal remote sensing of urban climates, Remote Sens. Environ., 86, 370–384, 2003. 5672, 5673, 5689
Weng, Q. H.: Thermal infrared remote sensing for urban climate and environmental studies: methods, applications, and trends, ISPRS J. Photogramm., 64, 335–344, 2009. 5672
Yang, L. and Li, Y.: City ventilation of Hong Kong at no-wind conditions, Atmos. Environ., 43, 3111–3121, 2009. 5673, 5674

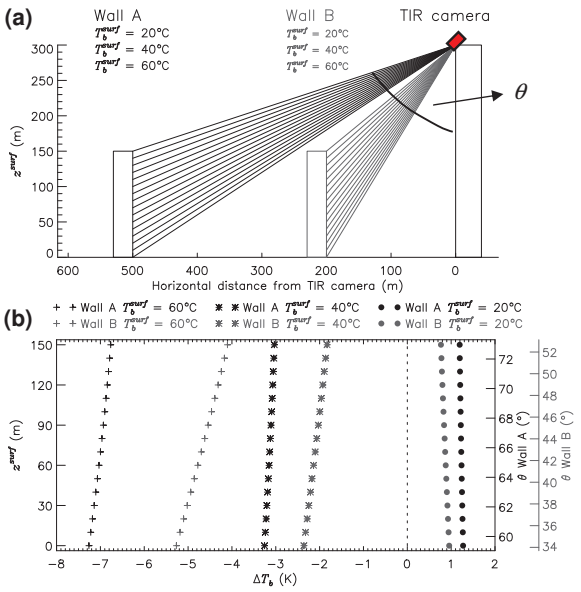

Fig. 1. **(a)** Scheme of the fictitious experimental setup and line-of-sight (LOS) geometry in order to demonstrate atmospheric effects on oblique TIR imagery in urban areas, **(b)** vertical profiles of ΔT_b for wall A (black) and wall B (grey) against wall height (z^{surf}) and corresponding view zenith angle (θ) for wall temperatures T_b^{surf} of 20 °C, 40 °C and 60 °C, respectively.

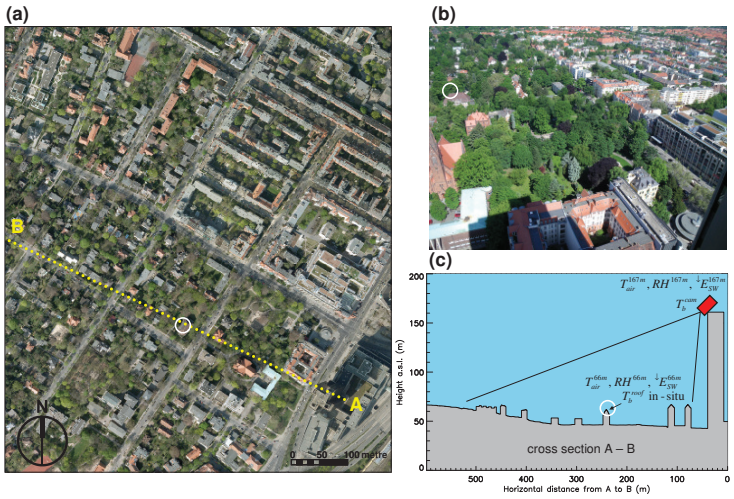

Fig. 2. **(a)** Aerial photo of the study site and ground meteorological measurement site (white circle) (aerial photo with permission of Berlin Department of Urban Development, Urban and Environmental Information System), **(b)** photograph showing approximately the FOV of TIR camera, **(c)** cross section A-B illustrates the experimental setup e.g. surface heights, location of TIR camera and in-situ measurements.

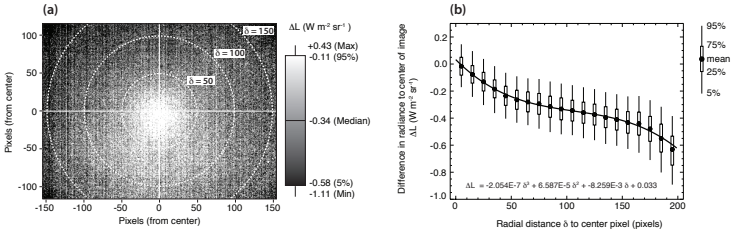

Fig. 3. Correction for vignetting: **(a)** Average difference in radiance (ΔL) to the radiance measured in a 6 × 6 pixel window in the centre of the image (L_i^{ref}) during the calibration run in dense fog on 20 January 2006, **(b)** correction derived for vignetting based on all pixels of the image.

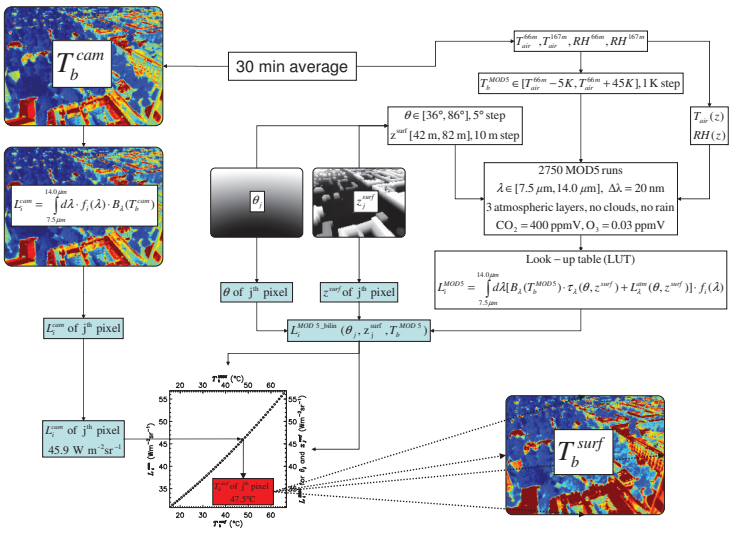

Fig. 4. Flowchart of the multi line-of-sight (MLOS) method on a pixel-by-pixel basis to remove atmospheric effects in off-nadir TIR imagery acquired in an urban environment.

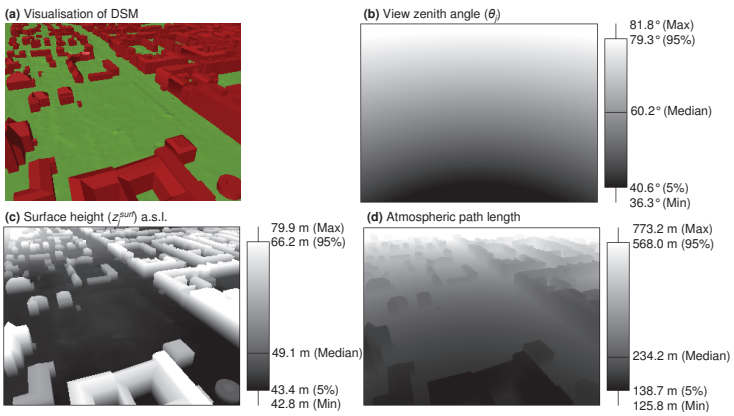

Fig. 5. Perspective projection of the DSM, spatial distribution of LOS geometry parameters: **(b)** view zenith angle θ_j, **(c)** surface height z_j^{surf} and **(d)** atmospheric path length.

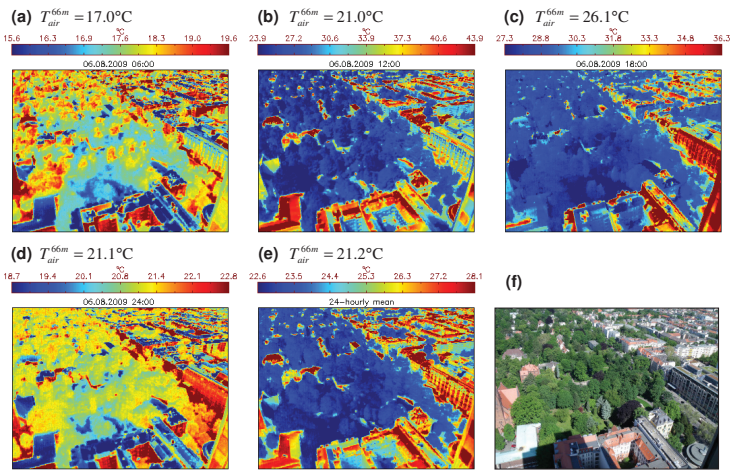

Fig. 6. Atmospherically corrected TIR imagery using the MLOS method for selected 30-min periods during 8 August 2009 at 06:00 **(a)**, 12:00 **(b)**, 18:00 **(c)** and 24:00 **(d)** CET, the 24-hourly mean pattern **(e)** and a photograph showing the FOV of TIR camera **(f)**.

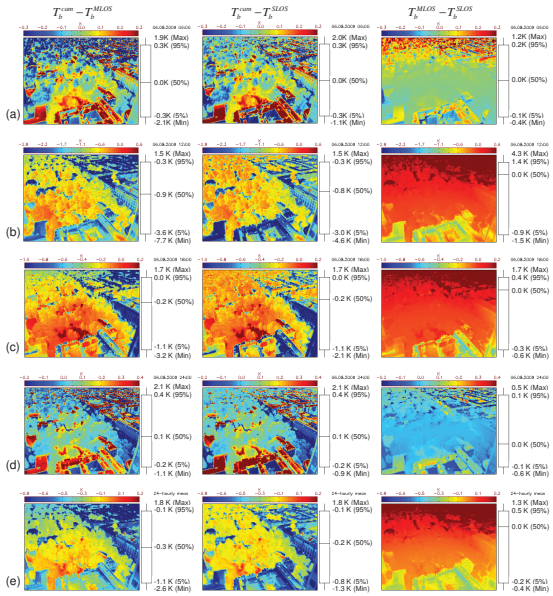

Fig. 7. Differences between T_b^{cam} and T_b^{MLOS} (left column), T_b^{cam} and T_b^{SLOS} (middle column) and between the two atmospheric correction methods ($T_b^{MLOS} - T_b^{SLOS}$, right column) for selected 30-min periods during 8 August 2009 at 06:00 **(a)**, 12:00 **(b)**, 18:00 **(c)** and 24:00 **(d)** CET and the 24-hourly mean pattern **(e)**.

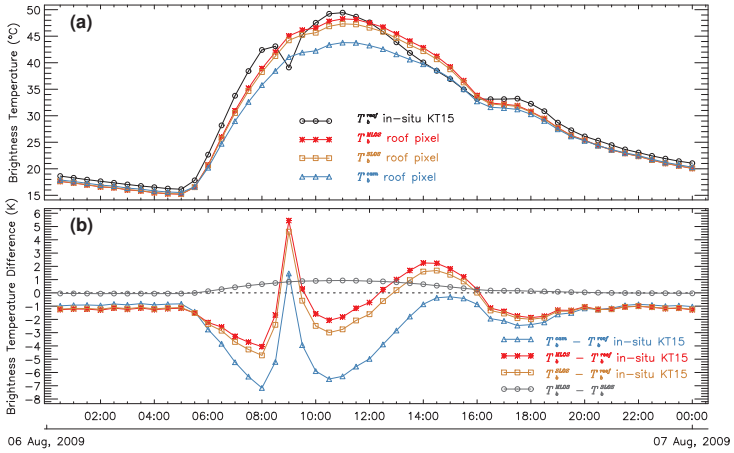

Fig. 8. **(a)** Diurnal variation of T_b^{roof} and corresponding TIR remote sensing data (roof pixel) (T_b^{cam}, T_b^{MLOS}, T_b^{SLOS}) during 8 August 2009, **(b)** temporal variability of difference between T_b^{roof} and corresponding TIR remote sensing data and difference between T_b^{MLOS} and T_b^{SLOS}.

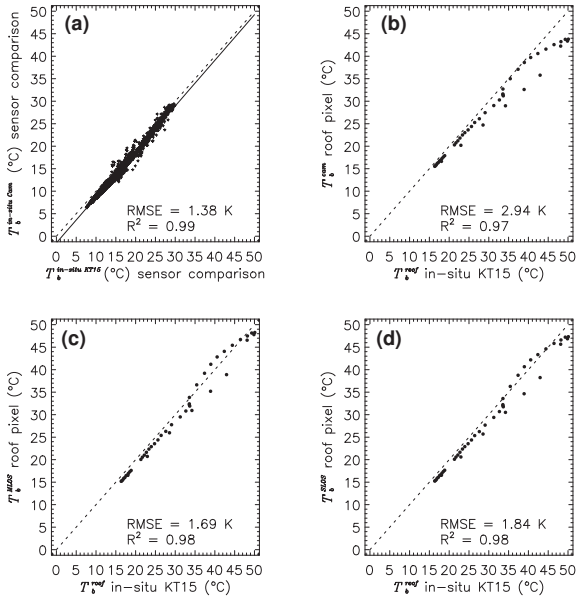

Fig. 9. **(a)** Instrument comparison over 10 days in April 2010 and plots of T_b^{roof} in-situ vs. the corresponding remote sensing data **(b)** T_b^{cam}, **(c)** T_b^{MLOS} and **(d)** T_b^{SLOS} during 8 August 2009.

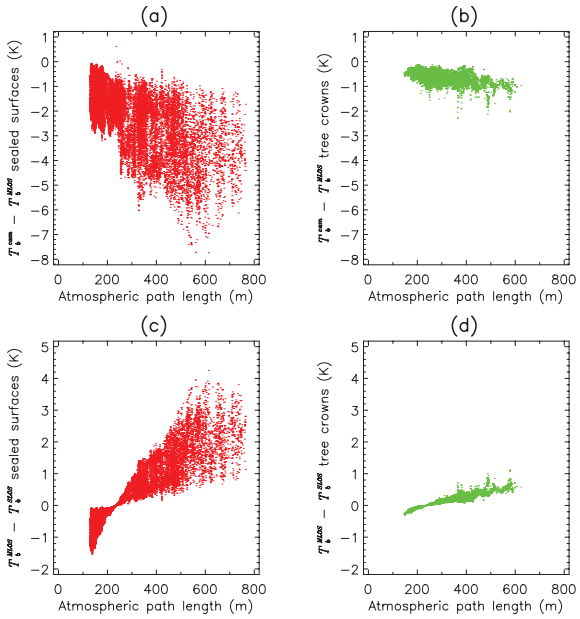

Fig. 10. Atmospheric path length vs. $T_b^{cam} - T_b^{MLOS}$ at 12:00 for **(a)** sealed surfaces and **(b)** tree crowns. Atmospheric path length vs. $T_b^{MLOS} - T_b^{SLOS}$ at 12:00 for **(c)** sealed surfaces and **(d)** tree crowns.

Appendix B: Determination of persistence effects in spatio-temporal patterns of upward long-wave radiation flux density from an urban courtyard by means of Time-Sequential Thermography

Meier, F., Scherer, D. and Richters, J. (2010): Determination of persistence effects in spatio-temporal patterns of upward long-wave radiation flux density from an urban courtyard by means of Time-Sequential Thermography. Remote Sensing of Environment, 114, 21-34.

Status: Published

Own contribution:

- Experimental design
- TST data acquisition
- Processing of TST data and meteorological data
- Analysis and interpretation of experimental results
- Definition of persistence effects and areas of interest
- Development of the method to derive surface thermal admittance
- Preparation of manuscript with all figures and tables and subsequently revision of the manuscript after comments and improvements of co-authors

Remote Sensing of Environment 114 (2010) 21–34

Contents lists available at ScienceDirect

Remote Sensing of Environment

journal homepage: www.elsevier.com/locate/rse

Determination of persistence effects in spatio-temporal patterns of upward long-wave radiation flux density from an urban courtyard by means of Time-Sequential Thermography

Fred Meier *, Dieter Scherer, Jochen Richters

Chair of Climatology, Department of Ecology, Technische Universität Berlin, Rothenburgstraße 12, D-12165 Berlin, Germany

ARTICLE INFO

Article history:
Received 24 February 2009
Received in revised form 31 July 2009
Accepted 4 August 2009

Keywords:
Time-Sequential Thermography
Persistence
Upward long-wave radiation
Shadow
Urban courtyard
Thermal admittance
Ground-based remote sensing
Spatio-temporal patterns

ABSTRACT

This research analyses upward long-wave radiation flux density from urban surfaces using a high-resolution thermal-infrared (TIR) camera and meteorological measurements in the city of Berlin, Germany. We report spatio-temporal patterns of the difference between upward long-wave radiation flux density from courtyard surfaces and the roof. For temporal analysis, the TIR camera recorded one TIR image per minute over a period of two days from 3rd to 5th May 2007. Three-hourly averaged thermal patterns show persistence effects due to shadow, sky-view factor (SVF) distribution in the courtyard, thermal properties of the surface materials, human activities and turbulence characteristics of the surface–atmosphere interface. The history of shadow influences the 24-hourly mean pattern. Shadow caused by temporarily parked cars results in a lower upward long-wave radiation flux density compared to the non-shadowed surface close to it. Immediately after car departure, this difference decreases. We propose a method to derive the thermal admittance of a concrete surface based on TIR data from this attenuation process. This study shows that ground-based high-resolution TIR imagery is highly suitable to investigate surface thermal properties and dynamic processes controlling thermal patterns within a complex three-dimensional (3D) urban structure.

1. Introduction

The urban surface reveals a complex three-dimensional (3D) structure creating strong micro-scale variations of upward long-wave radiation. These spatio-temporal patterns have several reasons e.g. different radiative and thermal properties of the individual urban surfaces, different radiation regimes depending on slope and aspect of the facets, including adjacency effects, multiple reflections, different sky-view factors (SVF) and shadows caused by objects in the immediate neighbourhood (Kobayashi & Takamura, 1994; Oke, 1987; Sugawara & Takamura, 2006; Voogt & Oke, 2003). Radiation in the thermal-infrared (TIR) part of the electromagnetic spectrum is an essential variable both in the radiation budget and the energy balance of the Earth's surface. Surface temperature directly controls emission of long-wave radiation but is also the result of energy exchange between atmosphere and bordering surfaces. Tower measurements using pyranometers and pyrgeometers have shown the large contribution of upward long-wave radiation to the surface radiation budget (e.g. Christen & Vogt, 2004).

1.1. Time-Sequential Thermography (TST)

The unavoidable trade-off between spatial and temporal resolution inherent to satellite-based remote sensing, and the relatively high costs of flight campaigns generate a significant problem for acquisition of spatially distributed TIR data at both high spatial and high temporal resolution. Higher spatial resolution data can be used to study changes in thermal patterns between daytime and nighttime at surface material level (Lo et al., 1997; Quattrochi & Ridd, 1994). The diurnal course of urban surface temperatures can be obtained by flight campaigns (Lagouarde et al., 2004; Voogt & Oke, 1998). The combination of several satellite sensors, e.g. MODIS, NOAA-AVHRR and Landsat-ETM is suitable to derive the diurnal course of upward long-wave radiation and can achieve good results in comparison with in-situ pyrgeometer measurements (Rigo et al., 2006). Ground-based remote sensing using TIR camera systems mounted on masts, towers or building roofs provides an alternative to airborne and satellite platforms. Voogt and Oke (2003) expect progress in urban climate research due to availability and application of low-cost, high-resolution portable TIR scanner systems. In Tokyo, a TIR camera system continuously measured urban surface temperatures for derivation of a town-scale thermal property parameter (Sugawara et al., 2001). At the building scale, Hoyano et al. (1999) used Time-Sequential Thermography (TST) for calculating sensible heat flux density. Thermal characteristics of various urban surfaces in Tel-Aviv

* Corresponding author. Tel.: +49 30 314 71324.
E-mail address: fred.meier@tu-berlin.de (F. Meier).

0034-4257/$ – see front matter © 2009 Elsevier Inc. All rights reserved.
doi:10.1016/j.rse.2009.08.002

were assessed using TST over a diurnal period at high spatial resolution by using a thermal video radiometer that captured images from a fixed position in a specific time interval (Chudnovsky et al., 2004).

1.2. Objectives

The general objective of this paper is to assess micro-scale urban surface thermal patterns concerning the persistence of thermal patterns inside an urban courtyard. In detail, we address the following two questions:

1.) How important is the history of shadow for upward long-wave radiation flux density from courtyard surfaces in relation to the diurnal cycle?
2.) Can we observe different persistence effects in spatio-temporal patterns of upward long-wave radiation flux density during daytime and nighttime hours?

Considering the assumption that thermal persistence effects depend on thermal properties of surfaces, we also discuss an approach to determine the thermal admittance of a concrete surface. For these purposes, we observe and analyse spatio-temporal variability of upward long-wave radiation flux density using an oblique viewing high-resolution TIR camera system capturing images at scales in the range of centimetres. We expect some variability in surface temperature due to emissivity differences at this micro-scale. Measurements of emissivity for all surfaces in the Field of View (FOV) are beyond the scope of this project. Therefore, this paper focuses on upward long-wave radiation. A further remaining problem of thermal remote sensing deals with directional variations of measured long-wave radiation, referred to as thermal anisotropy (e.g. Voogt, 2008). This aspect is not included in this paper.

1.3. Persistence phenomena in urban areas

The 3D city structure generates a complex pattern of partially sunlit and shadowed surfaces in particular under cloudless conditions. In a northern hemisphere square courtyard, the shadow always moves from West to East. In Fig. 1, the investigated courtyard is divided into a sunlit and a shadowed area, visible by sharp borders. The small treeless courtyards to the West are completely shadowed. Depending on shadow, different surfaces receive different short-wave irradiances. In a more general perspective, a thermal persistence effect is activated by a specific disturbance in the surface–atmosphere system. A question is how long is this disturbance detectable in the system? In urban areas, the disturbance is to be manifested in the 3D city structure or due to human activities like shadow for instance due to parked cars. The high-spatial resolution infrared image simulator OSIrIS reproduces the persistence of shadow effects in complex urban environments (Poglio et al., 2006). Within high-rise buildings, extensive shadow can produce sufficient surface cooling to induce an inversion of near-surface air temperature (Ruffieux et al., 1990). Other urban climate phenomena like the daytime cool island resulting partly from shadow effects (e.g. Erell & Williamson, 2007; Nichol, 2005). Impacts of shadow effects are also included in numerical simulations of interactions between the 3D urban surface and the atmosphere (e.g. Bruse & Fleer, 1998).

2. Methods

This section specifies the study site and the experimental setup, pre-processing steps of the TIR imagery and the basic idea and equations for determination of persistence effects.

2.1. Study site and experimental setup

The study site is located in Berlin (Germany) in the Charlottenburg–Wilmersdorf district close to the city centre Zoologischer Garten (City-West). City structure is characterized by five to six-story perimeter block development (see also Fig. 1). Previous investigations in Berlin concentrated on the relationship between land use data and surface temperature derived from Landsat data (Munier & Burger, 2001) or from airborne remote sensing (Kottmeier et al., 2007). Endlicher and

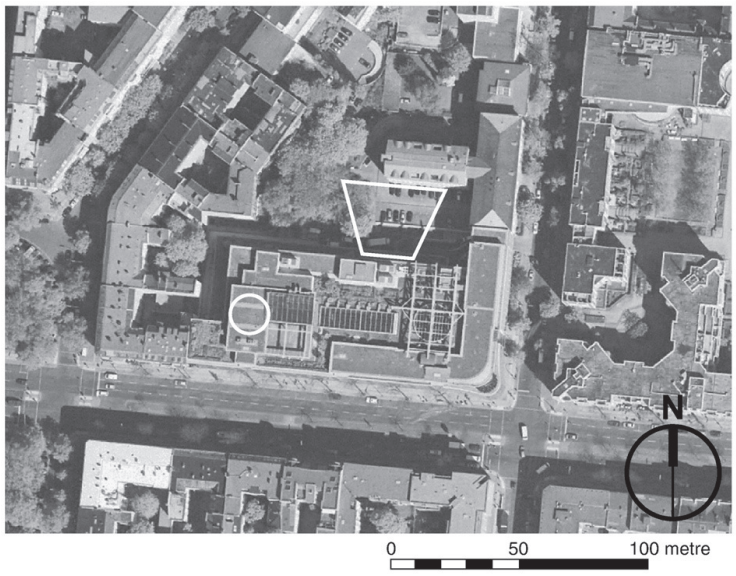

Fig. 1. Aerial photo of the study side and surrounding area in Berlin, district Charlottenburg–Wilmersdorf, with FOV of the TIR camera inside the investigated courtyard and FOV of the down-facing pyrgeometer (Kipp & Zonen, CNR1) on the Stilwerk building roof (aerial photo with permission of Berlin Department of Urban Development, Urban and Environmental Information System).

Lanfer (2003) articulate another interesting inter-relation between the thermal behaviour of urban surfaces and their influence on environmental conditions for plants and animals at the micro-scale. They pointed out that the urban heat island and heterogeneity in long-wave radiation regimes in cities lead to new biodiversity patterns particularly due to intrusion of non-native plants. Courtyards as a typical open space in Berlin were investigated with regard to spatial variations of thermal comfort, which depends on size and vertical building structure (Mertens, 1999).

This micro-scale TIR remote sensing study was part of a local-scale urban climatology experiment including boundary layer meteorological measurements such as directly measured sensible heat flux density, air temperature and humidity. We call it 'Stilwerk Experiment' according to the name of the shopping mall, whose roof provided a basis for measurement installations. Intensive experimental work was conducted between 20th April and 14th May 2007. Technical specifications of the TIR camera system are summarized in Table 1.

For spatial analysis, we selected an oblique viewing position from the roof. The TIR camera was oriented towards the North (354°) and inclined by 20° from the nadir angle. In the courtyard FOV the essential features (see numbering in Fig. 2) are one lime tree (1), a narrow green terrace (2), situated 9.4 m above street level, an asphalt loading zone (3) belonging to the department store and a car-park (4) belonging to the opposite building, separated by a small wall (5). The terrace consists of two small hedgerows, paving tiles and gravel. Concrete paving stones (4) and honeycomb-type paving stones with grass (6) cover the car-park area.

The geometric resolution of a pixel closer to the lens is higher than in the background due to of the oblique view. The geometric resolution changes from approx. 3.6 cm to 10.8 cm depending on distance between sensor and target. Here distance varies between approx. 10 m for the terrace pixels and approx. 30 m for the farthest car-park pixels. The TIR camera recorded one image per minute over a period of 48 h from 3rd to 5th May 2007. The fixed position ensures a valid comparison between the multi-temporal imagery on the same spatial basis and an accurate geometric co-registration respectively. All four components of the radiation balance were measured 2 m above the building roof. Measurement frequency of the device (Kipp & Zonen, CNR1) was 1 Hz and we used a 1 min averaging interval. Upward long-wave radiation from the roof FOV represents a mixed signal of components of the extensive green roof structure i.e. sedum, herbs, grass and a couple of concrete paving tiles (30 cm × 30 cm). During the TST operation period the substrate of the extensive green roof was very dry because of very low precipitation in April and the first half of May 2007.

2.2. Pre-processing, radiometric and geometric corrections steps of TIR imagery

The TIR camera system provides calibration metadata for each recorded image, derived from firmware calibration using laboratory blackbody temperatures. Depending on case temperature, the system generates calibration metadata in a user-defined frequency. The first step of image processing uses these internal calibration parameters for converting measured radiance into directional brightness temperatures (T_b) for each pixel. This assumes that the detected surface is a Lambertian blackbody. In order to avoid drift effects the internal image calibration file has to be updated in the same interval, or at higher frequency, than the measurement interval. If the system operates with an internal calibration frequency lower than the measurement interval then minor artificial jumps from one image acquisition to the next are possible resulting from unconsidered changes in case temperature.

Table 1
Technical specifications of the thermal-infrared (TIR) camera.

Camera manufacturer	InfraTec
Camera model	VarioCam® head
Spectral range	7.5 µm–14 µm
Detector type	Microbolometer Focal Plane Array (320 × 240 pixel), uncooled
Temperature resolution at 30 °C	Better than 0.1 K
Measurement accuracy	±2 K, ±2%
Lens	Standard wide-angle lens 12.5 mm
Field of View (FOV)	64° × 50°

Lens effects disturb TIR data. Experiments showed a clear 1.2 K difference of T_b from the centre of the TIR image to the corners. This lens effect was corrected by using a data set of dense fog and assuming isotropic distribution of radiance (Christen et al., 2006). Other experiments with TIR cameras using wide-angle lenses (Lagouarde et al., 2000, 2004) also reported such effects. They relate this problem to vignetting effects leading to reduced brightness in the periphery compared to the central part.

Lenses generally produce intrinsic geometric distortions. In our laboratory, these deformations have been analysed by measuring a grid of metallic pins in a regular square pattern. We used the positions of the metallic pins to construct a Delaunay triangulation of a planar set of points. Then the geometrical deviations in *x*- and *y*-direction were interpolated for each image pixel. By using a nearest-neighbour technique, the TIR image pixels can be shifted to their real positions. After correction for lens deformation, the TIR image covers a FOV of 57.5° by 44.7°.

We worked without an atmospheric correction procedure, due to short target-sensor distances in our experimental setup and therefore short atmospheric path lengths. Between adjacent surfaces, radiance differences caused by atmospheric effects are generally smaller than measurement errors. Finally, T_b was reconverted into long-wave radiation flux density via Stefan–Boltzmann law:

$$^{\uparrow}E_{TST}(\vec{x}_i,t) = \sigma T_b^4(\vec{x}_i,t), \quad (1)$$

where $\vec{x}_i$ represents each pixel and its spatial position in the courtyard, t is the acquisition time of the TIR image and σ is Stefan Boltzmann's constant. The resultant imagery $^{\uparrow}E_{TST}(\vec{x}_i,t)$ consists of 2880 TIR images that can be considered as a spatio-temporal image-cube.

2.3. Determination of persistence effects

Persistence in this paper means a temporal stability of spatial patterns of upward long-wave radiation flux density. The basic idea in order to determine persistence effects is to compare a temporarily disturbed surface with an undisturbed reference surface. We defined shadow as the disturbance. Simply because the building roof is always non-shadowed and in order to determine persistence effects in relation to the diurnal cycle, we selected the roof as a reference surface. The scenes in Fig. 3 show the shadow in the study area in three-hourly intervals during daytime on 4th May 2007. The highlighted area in the courtyard shows the FOV of the TIR camera during the TST investigation period. The highlighted circular area represents the 150° FOV of the down-facing pyrgeometer. The FOV of the TIR camera covers a complex shadow situation due to building walls and tree crown. The FOV on the roof is always non-shadowed.

Thus, we computed the difference between upward long-wave radiation from every courtyard pixel and upward long-wave radiation $^{\uparrow}E_{LW\_ROOF}(t)$ from the roof.

$$^{\uparrow}\Delta E(\vec{x}_i,t) = {}^{\uparrow}E_{TST}(\vec{x}_i,t) - {}^{\uparrow}E_{LW\_ROOF}(t) \quad (2)$$

Then we defined temporal stability for final persistence determination by computing a temporal average. The spatio-temporal patterns of mean difference (*MD*) as well as the standard deviation

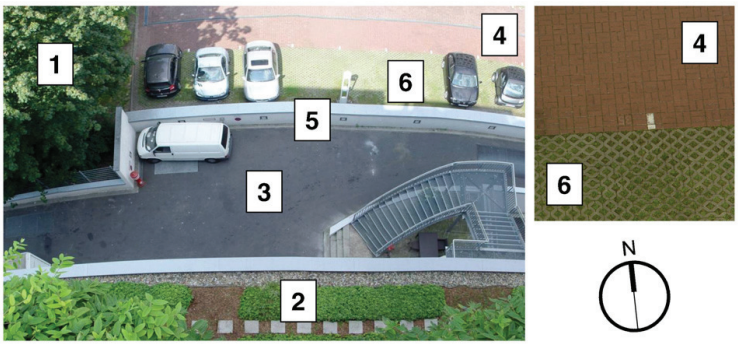

Fig. 2. Photograph showing approximately the FOV of the TIR camera (photograph courtesy of J. Rogée, Technische Universität Berlin). Description of the numbered features in the courtyard: lime tree (1), terrace with hedgerow, gravel and paving tiles (2), asphalt loading zone (3), concrete paving stones (4), wall (5) and honeycomb-type paving stones with grass (6).

of difference (*SDD*) and mean rate of change of difference (*MROCD*) provide the basis for persistence analysis.

$$MD = \overline{{}^{\uparrow}\Delta E(\overline{x}_i, t)} \tag{3}$$

$$SDD = \sigma({}^{\uparrow}\Delta E(\overline{x}_i, t)) \tag{4}$$

$$MROCD = \overline{\frac{\delta}{\delta t}({}^{\uparrow}\Delta E(\overline{x}_i, t))} \tag{5}$$

The *MD* pattern indicates the presence of persistence effects, the *SDD* pattern comprises information about the intensity of a disturbance in relation to the undisturbed reference surface and the *MROCD* pattern shows if the disturbance produced a positive or negative change in upward long-wave radiation from courtyard surfaces. The overbar in Eqs. (3) and (5) denotes the temporal average. A more detailed discussion concerning the temporal variability of selected areas of interests (AOI) follows in the Discussion section.

There are some assumptions underlying this approach. First, we disregard the spectral range discrepancy. The CNR1 pyrgeometer is a broadband (3 µm to 100 µm) and the TIR camera is a narrowband measurement device. During the Stilwerk Experiment on 30th April from 13:30 to 15:30, the TIR camera system was installed on the roof for comparison between ${}^{\uparrow}E_{\mathrm{LW\_ROOF}}$ and the spatial mean of the TIR image $\langle E_{\mathrm{TST}} \rangle$ by matching both FOV approximately. Both datasets are strongly correlated ($r^2 = 0.97$) and the root mean square error (RMSE) is 4.7 W m^{-2}, which is less than the CNR1 pyrgeometer measurement accuracy (see Fig. 4). Secondly, we have to consider that measured upward long-wave radiation includes reflections from downward long-wave radiation because surface emissivity values are less than unity. The interpretation of upward long-wave radiation from low emissivity surfaces is critical in this respect e.g. from all metallic mainly car surfaces in the courtyard.

3. Results

In the results, we present spatio-temporal patterns of *MD*, *SDD* and *MROCD* for a three-hourly and a 24-hourly temporal average using a percentile visualization approach. At first, we show all radiation balance components from the CNR1 measurement device.

3.1. Radiation balance components

During the investigation period, clear sky conditions caused high downward short-wave irradiance (${}^{\downarrow}E_{\mathrm{SW\_ROOF}}$) with a maximum of 870 W m^{-2} around noon. Particularly on 4th May all four radiation

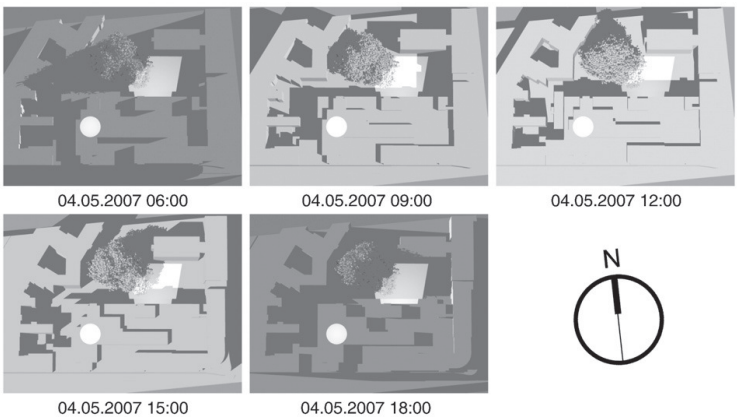

Fig. 3. Visualization of shadow in the radiative source areas for roof (circle) and courtyard (trapeze) measurements at 06:00, 09:00, 12:00, 15:00 and 18:00 on 4th May. Time specification refers to Central European Time (CET).

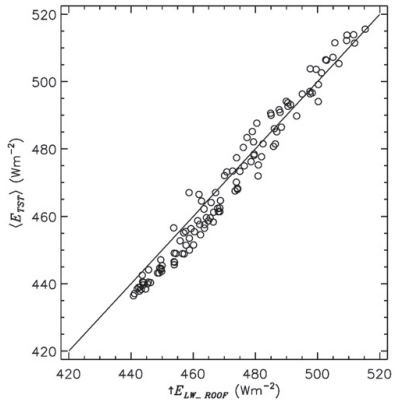

Fig. 4. Comparison between upward long-wave radiation flux densities from the roof measured by down-facing pyrgeometer and TIR camera.

components have a characteristic diurnal cycle curve (see Fig. 5). These atmospheric conditions allow for detailed analysis of the diurnal variation in upward long-wave radiation.

3.2. Spatio-temporal patterns — percentile visualization approach

Contrast within an image is based on brightness or darkness of a pixel in relation to other pixels. Modifying the contrast can enhance the ability to extract pattern information from the image. A simple way to modify contrast is to scale the pixel values within an image. Hence, we scaled the pixel values of all mean patterns (*MD*, *SDD* and *MROCD*) between the 95% percentile (maximum brightness) and the 5% percentile (minimum brightness) of the original computed mean patterns. This linear grey-scaling approach for visualization does not allow a direct comparison between the single three-hourly patterns. Furthermore, all grey-scale bars have benchmarks for the median (50%), the minimum, maximum and zero value of the computed mean pattern.

3.3. Thermal patterns of three-hourly periods

For a more detailed analysis of the different thermal regimes during day and night we present temporal mean patterns of three-hourly periods. For instance, the *MD* pattern was calculated as follows:

$$MD = \frac{1}{180}\sum_{i=1}^{180} {}^{\uparrow}\Delta E(\vec{x}_i, t). \quad (6)$$

Therefore, Fig. 6 consists of 24 patterns arranged in eight rows (A–H) which represent the temporal mean patterns of all three-hourly periods from 06:01 to 06:00 next morning. Row A shows the patterns for *MD* (left), *SDD* (middle) and *MROCD* (right) from 06:01 to 09:00 on 4th May 2007. All *MROCD* patterns illustrate the mean rate of change for $\delta t = 1$ min (Eq. (5)).

3.3.1. MD patterns of three-hourly periods

During the day, the median of the *MD* patterns is negative. The lowest three-hourly median is -123.4 W m^{-2} and belongs to the early afternoon period from 12:01 to 15:00 (Fig. 6c, left). Still after sunset the median remains negative (Fig. 6e, left). There are some areas with positive *MD* values during daytime. In the morning hours, a thermal hot spot corresponds to sunlit surfaces in the northwestern part of the courtyard in particular to the metallic car surfaces. In shadowed areas, only the hot automotive engines (Fig. 6a, left, white box) have positive *MD* values. The treetop shows a heterogeneous pattern due to the existence of both sunlit and shadowed treetop areas.

At night, all used parking spaces show lower *MD* values in contrast to the space between them. This pattern shows the influence of parked cars on the underlying surface in terms of thermal radiation. From 21:01 to 24:00, the treetop has slight positive *MD* values between 5 W m^{-2} and 24 W m^{-2}. This range probably depends on the SVF of the individual leaves and the air temperature inside the treetop. The lowest *MD* values correspond to higher situated leaves at the crown apex. This *MD* pattern can be associated with the theoretical treetop SVF distribution and is comparable to the results of the urban-park scale model experiment carried out by Spronken-Smith and Oke (1999). The patches of higher *MD* values might also indicate the influence of a higher air temperature inside the canopy. In general, air temperature is important in setting leaf temperature and therefore emission of long-wave radiation (Oke, 1987, p. 121). At night, (Fig. 6f, left) the eastern car-park area covered by concrete pavement has the highest *MD* values between 50 W m^{-2} and 55 W m^{-2}. Only the building terrace has negative *MD* values (Fig. 6f, left). At the end of the night, the median (see Fig. 6g and h, left) increased marginally from 20.9 W m^{-2} to 22.1 W m^{-2}.

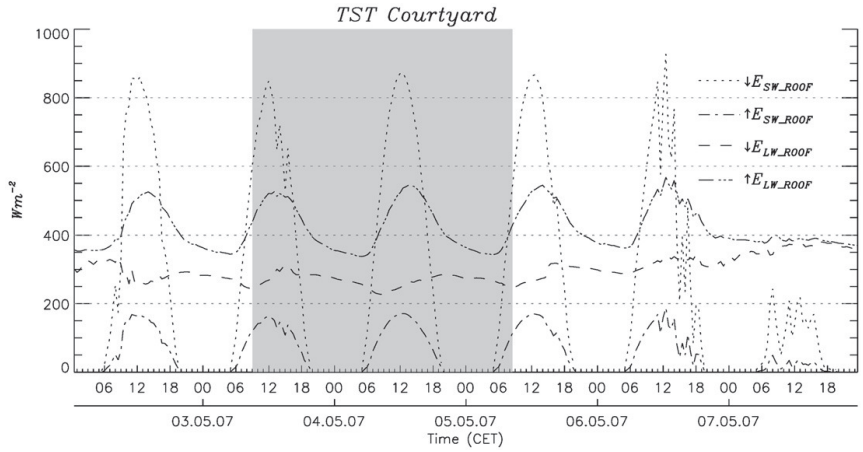

Fig. 5. All four radiation components from the CNR1 measurement device 2 m above the Stilwerk building roof (30 min average) and courtyard TST investigation period (grey box).

3.3.2. SDD patterns of three-hourly periods

High *SDD* values are the result of an alteration between direct-beam irradiance and diffuse irradiance. In the noon period from 12:01 to 15:00 formerly sunlit areas like the car-park drops into the tree shadow (Fig. 6c, middle). In the afternoon (Fig. 6d, middle) formerly shadowed surfaces like the whole terrace and the loading zone receive now direct solar irradiance. At the same time, the cars in the upper-right area drop into shadow, which caused high *SDD* values. During low Sun elevations, the median of the *SDD* patterns is generally higher, and amount to 23.1 W m^{-2} for the morning period and 25.2 W m^{-2} for the afternoon period. The highest *SDD* values correspond to sunlit metallic car surfaces. Vehicle movements also influence the *SDD* pattern. In Fig. 6c (middle, grey box) a quadratic shape shows high *SDD* values corresponding to a metallic tailboard.

At night, all *SDD* values are generally lower in comparison to the day. The loading zone and the small vertical wall exhibit the highest *SDD* values (Fig 6f, middle). Formerly used car-park spaces show higher *SDD* than the non-used spaces. Surprisingly at the end of the night, the car-park shows a contrary thermal pattern i.e. formerly used car-park spaces show lower *SDD* values (Fig. 6h, middle). Parts of the terrace, the eastern part of the car-park and the treetop have the lowest *SDD* values during the night. Some treetop branches draw attention because of higher *SDD* values (Fig. 6f, middle).

3.3.3. MROCD patterns of three-hourly periods

In particular, *MROCD* pattern interpretation has to consider the relation between courtyard and roof at the beginning of the analysed period. During the morning and noon periods negative *MROCD* values mark an alteration resulting from lower heating rates for the courtyard surfaces since the beginning of the three-hourly period. Positive *MROCD* values mark a period of higher heating rates for the courtyard surfaces. The opposite interpretation applies to the cooling period of the roof surface from 14:00 to 05:30 next morning.

Relatively sharp borders are detectable in the *MROCD* daytime patterns. In Fig. 6a, (right) one border marks the building shadow situation at the end of the period. Even roof eaves are recognisable in this pattern. During the morning period, almost 50% of the courtyard surfaces show negative *MROCD* values and accordingly minor heating

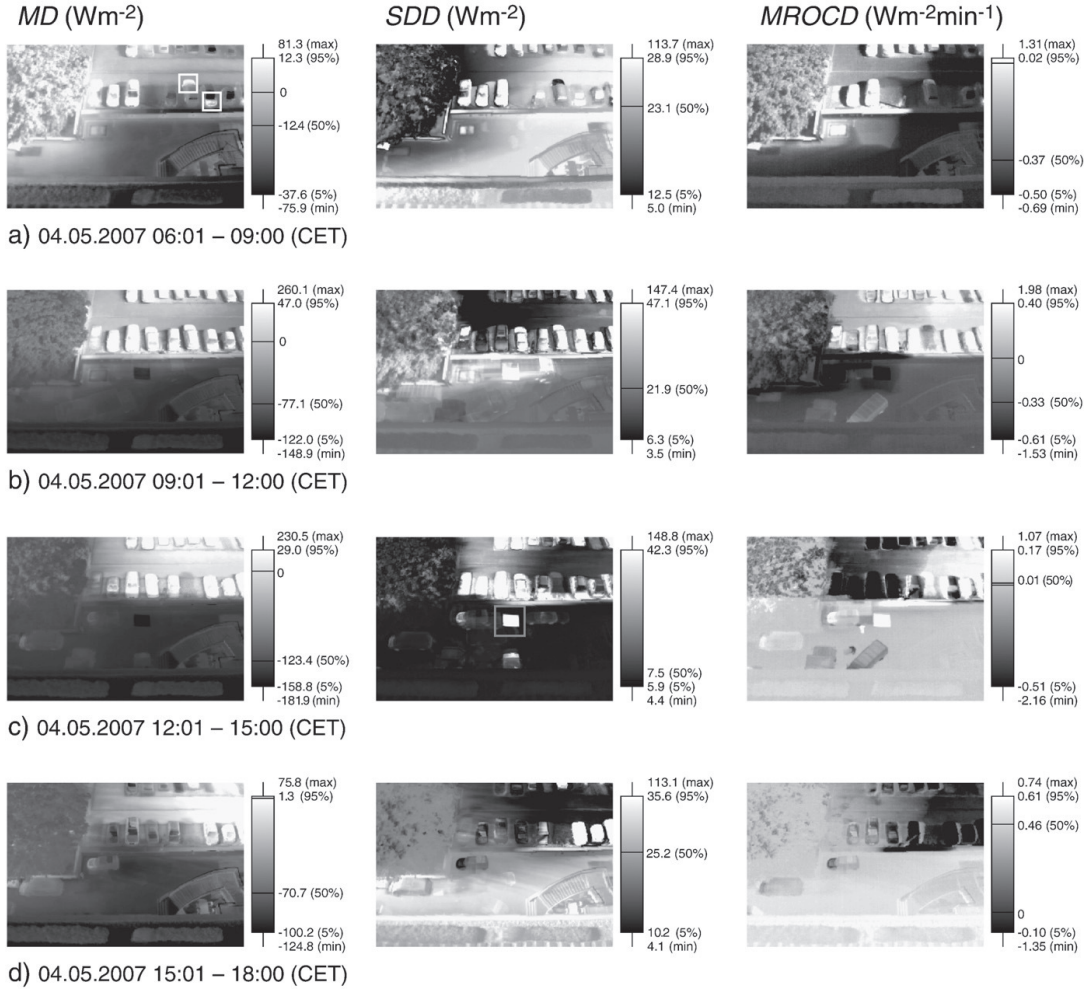

Fig. 6. Spatio-temporal patterns of mean difference (*MD*) (left column), standard deviation of difference (*SDD*) (middle column) and mean rate of change of difference (*MROCD*) (right column) between upward long-wave radiation from the courtyard and upward long-wave radiation from the roof for three-hourly periods.

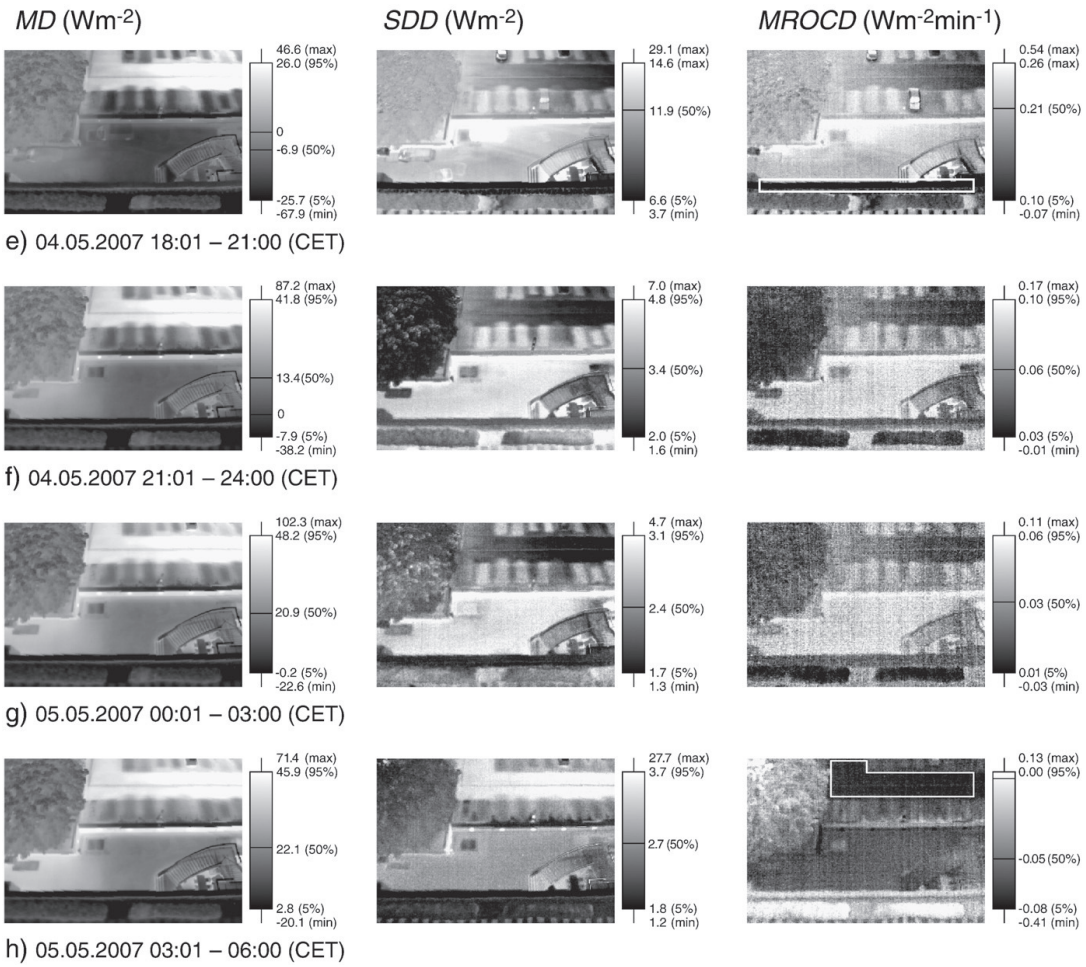

Fig. 6 (*continued*).

rates in comparison to the roof. The migration of the building shadow across the loading zone and lower parts of the treetop induces a pattern with negative *MROCD* values (Fig. 6b, right). In the afternoon the migration of shadow across the car-park (Fig. 6c and d, right) becomes apparent. In particular, car surfaces respond very strongly, if they drop into shadow. The narrow area showing the lowest *SDD* and *MROCD* values (Fig. 6e, middle and right, white box) is the metallic cover-plate of the terrace border. Later (Fig. 6f, right) the treetop and

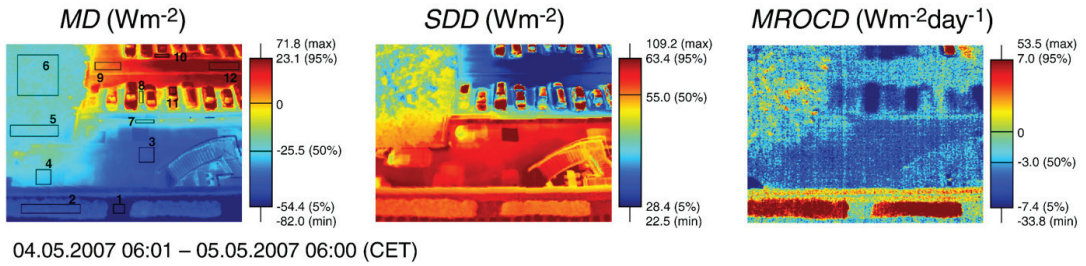

Fig. 7. Spatio-temporal patterns of mean difference (*MD*) (left column), standard deviation of difference (*SDD*) (middle column) and mean rate of change of difference (*MROCD*) (right column) between upward long-wave radiation from the courtyard and upward long-wave radiation from the roof for a 24-hourly cycle. The *MD* pattern shows the position and number of selected areas of interest (AOI) (see also Table 2).

hedgerow are able to achieve nearly similar cooling rates like the roof (*MROCD* values around zero). During 21:01 and 24:00 (Fig. 6f, right) the small wall in the courtyard has the highest *MROCD* values. The cooling rate of this vertical surface is lower in comparison to the roof due to the low SVF.

The interpretation of nighttime *MROCD* patterns is a critical issue due to essentially very low values. However, it is possible to identify different features in the courtyard. The whole car-park area covered by concrete pavers is visible as a homogenous surface structure at the end of the night (Fig. 6h, right, white box). This pattern implies a minor influence of SVF at the end of the night, because this pattern refers more to the different surface materials than to the different SVF in the courtyard. Furthermore, the *MROCD* patterns show attenuation accompanied by a decrease of the *MROCD* median and a finally slight negative *MROCD* median. The nighttime pattern from 03:01 to 06:00 is partly influenced by incident short-wave radiation from sunrise resulting in higher values for tree crown apex, but this fact does not explain the whole pattern of this three-hourly period. Hence, at the end of the night *MROCD* values could be more influenced by other processes. In the discussion, we will try to explain this result based on selected AOI and atmospheric variables.

3.4. Thermal patterns of a 24-hourly period

The 24-hourly pattern is able to show persistence effects in relation to the diurnal cycle. Fig. 7 shows *MD*, *SDD* and *MROCD* patterns for a day–night period derived from 1440 TIR images. The 24-hourly *MD* median is negative (-25.5 W m^{-2}). In addition, the 80% percentile is slightly negative (-1.4 W m^{-2}). For all selected AOI (see Fig. 7, left) the spatial averages of *MD*, *SDD* and *MROCD* are summarized in Table 2. The sunlit treetop AOI has a slight higher *MD* (-22.9 W m^{-2}) in comparison to the temporarily shadowed treetop AOI (-24.9 W m^{-2}). Even the car-park area between the parked cars and therefore situated in the car shadow has negative *MD* values (AOI 8). The car surfaces (AOI 11) and the car-park area covered by concrete paving stones (AOI 9 and AOI 12) show positive *MD* values in spite of afternoon tree shadow. In this thermal pattern, a hot spot corresponds to the eastern part of the car-park area. The whole car-park shows a slight gradient from the hot eastern to the western part. This thermal gradient is a persistence effect resulting from the history of shadow.

Table 2
Spatio-temporal average of mean difference (*MD*), standard deviation of difference (*SDD*) and mean rate of change of difference (*MROCD*) for selected areas of interests (AOI) for a diurnal cycle (4th May 06:01 to 5th May 06:00 CET), see also Fig. 7 (left) for AOI positions.

AOI number	AOI description (AOI pixel size)	*MD* (Wm^{-2})	*SDD* (Wm^{-2})	*MROCD* (Wm^{-2}day^{-1})
1	Terrace gravel (16×13)	−62.0	61.8	−0.7
2	Terrace hedgerow (81×13)	−43.9	56.3	+8.1
3	Asphalt loading zone, central (21×21	−41.3	60.6	−5.2
4	Asphalt loading zone, left (21×21)	−28.1	62.6	−4.3
5	Treetop, shadowed (66×16)	−24.9	53.7	−1.9
6	Treetop, sunlit (66×66)	−22.9	46.1	−1.4
7	Wall (26×5)	−24.3	61.9	−4.9
8	Honeycomb-type paving stones with grass (6×17)	−7.1	34.2	−4.5
9	Concrete paving stones, West (36×11)	+5.5	36.0	−3.5
10	Honeycomb-type paving stones with grass (20×5)	+21.0	25.5	−4.0
11	Car (10×10)	+22.2	52.3	−9.9
12	Concrete paving stones, East (41×11)	+28.0	31.4	−2.0

The diurnal *SDD* median (55 W m^{-2}) is higher than the three-hourly median values (Fig. 7, middle). This results from the accumulation of day and night differences between the courtyard and the roof. For instance, the asphalt loading zone and the wall show the highest *SDD* values as a consequence of completely different conditions during the day (shadow) and during the night (lower SVF) in comparison to the roof. The car surfaces show also high *SDD* values. This is a consequence of car movement and thermal performance of metallic surfaces.

The original 24-hourly *MROCD* values at 1 minute resolution were multiplied by 1440 to represent changes at the diurnal scale. Therefore, this pattern comprises spatial information about alteration in upward long-wave radiation between 06:01 and 06:00 next morning. This pattern is completely different in comparison to the 24-hourly *MD* and *SDD* patterns. It is not possible to identify features, which correspond to thermal gradients like the car-park area shown in the 24-hourly *MD* pattern (Fig. 7, left) or to the dichotomy in terms of northern sunlit and southern shadowed part.

On closer examination, the 24-hourly *MROCD* pattern shows lower values for the loading zone than for the car-park area. Furthermore, shadow due to parked cars produced the lowest *MROCD* values. Therefore, this pattern can be explained by the history of shadow. In general, we measured a slight decrease of upward long-wave radiation flux density for artificial courtyard surfaces in this 24-hourly period. Only the hedgerow on the terrace has a positive rate of change. The biomass of the vegetation is not able to store or conduct heat into ground in the same way as artificial surfaces. Air temperature is very important for modulation of vegetation surface temperature (Oke, 1987, p. 121) and upward long-wave radiation respectively. The measured air temperatures can be used to explain *MROCD* pattern for the hedgerow. We installed an air temperature sensor (Campbell CS 215) 1.3 m above the terrace and very close to the hedgerow. We measured an increase in air temperature of 1 K for this 24-hourly period from 4th May 06:01 to 5th May 06:00. This might be the reason for the positive hedgerow *MROCD* value. At roof level, the air temperature measurements showed no change. Interestingly some branches show higher *MROCD* values than the rest of the treetop. These parts are probably more influenced by turbulence processes.

4. Discussion

This section discusses the temporal variability of ${}^{\uparrow}\Delta E(\bar{x}_i, t)$ patterns and the temporal variability of ${}^{\uparrow}\Delta E(\bar{x}_i, t)$ for specific AOI in the courtyard during the TST investigation period. Furthermore, we discuss an approach to determine the surface thermal admittance using the attenuation of the thermal persistence signal.

4.1. Temporal variability of thermal patterns

A grey-scaling visualization approach using fixed minimum and maximum brightness values allows interpretation of temporal changes between the three-hourly thermal patterns. This visualization approach is critical for the night period with overall lower values because of different thermal regimes during day and night. Therefore, we considered day and night separately. For all daytime patterns (Fig. 8), the maximum brightness value represents the average of the 95% percentiles and the minimum brightness value represents the average of the 5% percentiles from all four daytime periods i.e. from 06:01 to 18:00 in Fig. 6. The same approach was applied for visualization of patterns from 18:01 to 06:00 next morning.

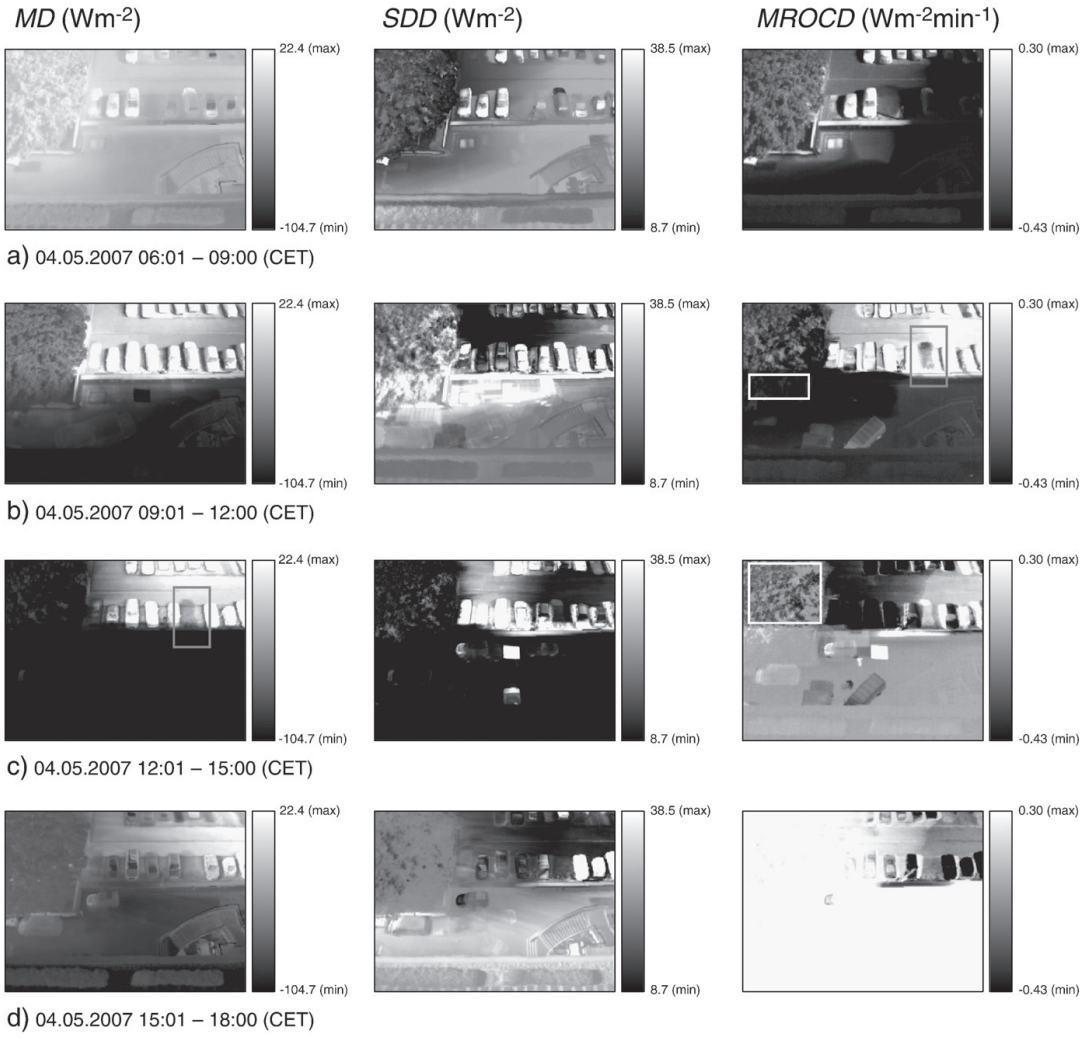

Fig. 8. Spatio-temporal patterns of mean difference (*MD*) (left column), standard deviation of difference (*SDD*) (middle column) and mean rate of change of difference (*MROCD*) (right column) between upward long-wave radiation from the courtyard and upward long-wave radiation from the roof. Visualization is based on fixed brightness values derived from the three-hourly daytime median values (06:01 to 18:00 4th May 2007 CET).

During the day, thermal hot spots in the *MD* patterns are clearly associated with sunlit car surfaces, sunlit pavements or car engines. The shadowed half of the courtyard dominates the daily *MD* patterns. After 09:00 until sunset all treetop pixels have negative *MD* values. With respect to the treetop, we can separate two phases. In the morning pattern from 09:00 to 12:00, the building shadow caused lower *MROCD* values for the shadowed treetop area than the supposed transpiration process for the sunlit crown apex (Fig. 8b, right, white box). Later on in the noon pattern from 12:00 to 15:00, the sunlit crown area shows lower *MROCD* values (Fig. 8c, right, white box).

Generally, during the night *MD* is positive because of a small SVF for the courtyard surfaces compared the roof. The influence of SVF distribution within the courtyard is remarkable for the loading zone. Between the tree and the Stilwerk building, we can expect lower SVF than for the centre of the loading zone. The *MD* patterns in Fig. 9 (left) show higher values for the area between the tree and the Stilwerk building. This result corresponds to other studies about SVF in urban areas and its influence on surface temperatures (e.g. Eliasson, 1992). The small wall shows the highest *MROCD* values (Fig. 9b, right). The restricted sky view results in an increase of *MD* during the night. For the night, the fixed brightness visualization approach shows a slight equalization tendency in the thermal patterns. For instance, the cold spots from the formerly shadowed parking spaces (Fig. 9a, left) diminish clearly but are visible at the end of the night (Fig. 9d, left). In general, the *MROCD* pattern provides insight into the spatio-temporal development of the thermal patterns. Strong changes in ${}^{\uparrow}\Delta E(\bar{x}_i, t)$ are detectable in the consecutive three-hourly *MD* patterns. For instance, an overall strong change (high brightness) dominates the *MROCD* pattern in Fig. 9a (right) whose effects are visible in the consecutive *MD* pattern (Fig. 9b, left) by overall higher values.

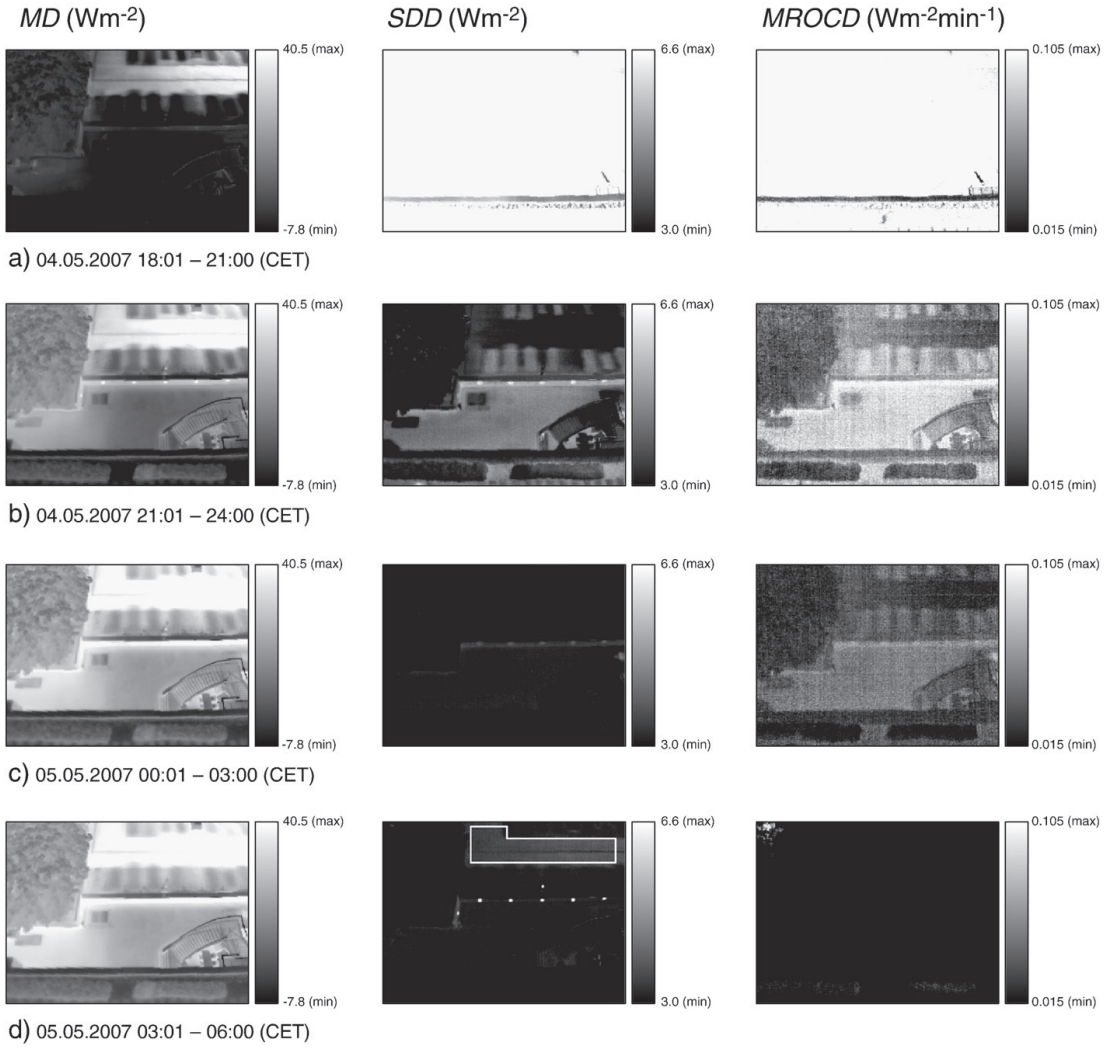

Fig. 9. Spatio-temporal patterns of mean difference (*MD*) (left column), standard deviation of difference (*SDD*) (middle column) and mean rate of change of difference (*MROCD*) (right column) between upward long-wave radiation from the courtyard and upward long-wave radiation from the roof. Visualization is based on fixed brightness values derived from the three-hourly nighttime median values (18:01 4th May to 06:00 5th May 2007 CET). The white spots in the *SDD* pattern (b, c, d) are wall lights.

4.2. Temporal variability of selected areas of interest (AOI)

Now, we discuss the temporal variability of ${}^{\uparrow}\Delta E(\vec{x}_i, t)$ for the AOI numbers 2, 5, 6, 9 and 12 from Table 2. Considerable differences show the sunlit and the shadowed vegetation AOI in Fig. 10. The range between the AOI maximum and AOI minimum data is higher for the sunlit treetop. Here alteration between sunlit and shadowed leaves produces a higher variability than for the almost shadowed hedgerow. Between 11:00 and 15:00, the graph of the shadowed treetop has the same shape like the hedgerow graph. The variability (AOI 2) is higher around 08:00 and 18:00 when the hedgerow receives direct solar irradiance. The sunlit treetop data are positively skewed in the noon period between 13:00 and 15:00. This could be a consequence of reduced leaf transpiration due to stomata closure or due to the angle between Sun and leaf orientation resulting in a higher amount of sunlit parts.

Interestingly the difference between sealed courtyard surfaces and roof does not increase during the whole night in spite of reduced SVF. Shortly after sunset around 20:00, the differences only slightly increase for all AOI. Between 02:00 and 04:00 (5th May) the differences, even slightly decrease for the concrete paving stones. The explanation for these temporal changes of difference between car-park surface and roof may be as follows. The CNR1 radiation data from the roof shows that net long-wave radiation changes from $-280\,\mathrm{W\,m^{-2}}$ at 14:00 (30 min average) to $-117\,\mathrm{W\,m^{-2}}$ at 20:00 and remains around $-70\,\mathrm{W\,m^{-2}}$ between 02:30 and 04:30. Thus, the role of net long-wave radiation in the cooling process of the roof becomes weaker. Additionally, sensible heat flux density measurements above the roof (37.5 m above street and 10.2 m above roof) show a downward sensible flux density between $39\,\mathrm{W\,m^{-2}}$ and $8\,\mathrm{W\,m^{-2}}$ after sunset (19:30 to 21:30). This period after sunset where energy is transported to the surface is also mentioned in

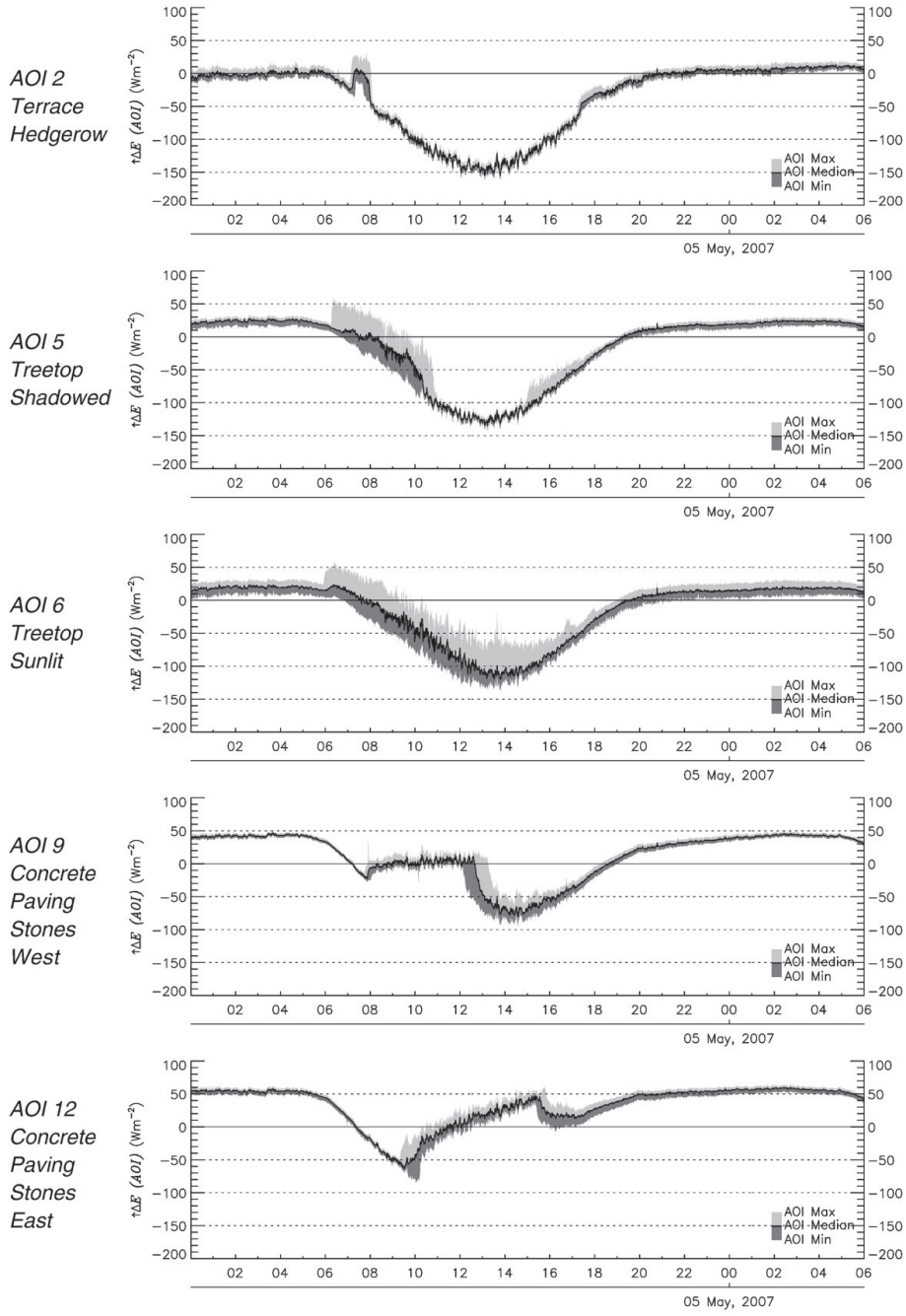

Fig. 10. Temporal variability of difference between upward long-wave radiation from areas of interest (AOI) in the courtyard and upward long-wave radiation from the roof.

Christen and Vogt (2004). Later, sensible heat flux density alternated between 9 W m^{-2} (downward) and −13 W m^{-2} (upward). Observations of local-scale sensible heat flux density in urban areas show persistence of slight upward sensible heat flux density from the warmer urban canopy layer throughout the night (Christen & Vogt, 2004; Grimmond et al., 2004; Oke, 1988). A study based on urban energy balance modelling from Harman and Belcher (2006) suggests a mechanism for this effect. They argue that the urban boundary layer

air is cooler than the surface temperature in the street canyon, because of greater downward sensible heat flux density from the urban boundary layer to the roof and higher heat capacity for street canyon surfaces and reduced SVF. The result is a slight upward sensible heat flux density from the street canyon into the urban boundary layer throughout the night (Harman & Belcher, 2006). Therefore, we suggest also a slight upward sensible heat flux density from the hotter surfaces inside the courtyard throughout the night, which influences the temporal variability of the difference between upward long-wave radiation from sealed courtyard surfaces and the roof. Also in the *SDD* pattern (Fig. 9d, middle, white box) the hotter pavement area and the wall are the only detectable features in the courtyard.

These results tend to mimic the difference between the cooling curves typical of urban and rural surfaces, especially where a rural surface is considered dry (e.g. Johnson et al., 1991; Oke et al., 1991). Another process that could influence the differences in upward long-wave radiation is the slumping of cold air from the building roof into the courtyard, which could affect the convective exchange of heat between the sealed courtyard surfaces and the atmosphere.

4.3. Derivation of surface thermal admittance by means of TST

We examined the attenuation of persistence effects for the analysis of thermal patterns and their relation to surface thermal properties. For this purpose, we look at a phenomenon, which is detectable in the noon *MD* pattern (Fig. 8c, left, grey box). One parking space appears with lower *MD* values by the shape of the formerly parked car. The departure of the car caused a persistence effect lasting over 3 h. Departure from the car-park caused a decrease in ${}^{\uparrow}E_{TST}(\bar{x}_i, t)$ which is clearly visible in the *MROCD* pattern (Fig. 8b, right, grey box). This car-shaped pattern is barely visible in the following *MD* patterns (Fig. 8d, left). Attenuation of the difference caused by temporary disturbances due to parked cars was further analysed. Difference ${}^{\uparrow}\Delta E_{\mathrm{ref}}(t)$ between temporarily shadowed and non-shadowed surfaces inside the courtyard is defined as:

$$ {}^{\uparrow}\Delta E_{\mathrm{ref}}(t) = \left\langle {}^{\uparrow}E_{TST}(\bar{x}_{\mathrm{shd}}, t)\right\rangle - \left\langle {}^{\uparrow}E_{TST}(\bar{x}_{\mathrm{ref}}, t)\right\rangle, \tag{7} $$

where $\langle {}^{\uparrow}E_{TST}(\bar{x}_{\mathrm{shd}}, t)\rangle$ is the spatial mean of the temporarily shadowed parking space and $\langle {}^{\uparrow}E_{TST}(\bar{x}_{\mathrm{ref}}, t)\rangle$ is the spatial mean of neighbouring non-shadowed reference surface. It is important to note that the considered surfaces are composed of the same material. We found several temporary persistence effects in the TIR imagery dataset. For the description of the decrease of ${}^{\uparrow}\Delta E_{\mathrm{ref}}(t)$ in the course of time, we found the following modified exponential function:

$$ {}^{\uparrow}\Delta E_{\mathrm{ref}}(t-t_0) = {}^{\uparrow}\Delta E_{\mathrm{ref}}(t_0)\exp\left(-\sqrt{\frac{t-t_0}{\tau}}\right), \tag{8} $$

where ${}^{\uparrow}\Delta E_{\mathrm{ref}}(t-t_0)$ is the difference of upward long-wave radiation flux density in the course of time after car departure, and $\Delta E_{\mathrm{ref}}(t_0)$ is the difference of upward long-wave radiation flux density between formerly shadowed and non-shadowed surface immediately after car departure. The time-constant τ is defined as:

$$ \frac{{}^{\uparrow}\Delta E_{\mathrm{ref}}(\tau)}{{}^{\uparrow}\Delta E_{\mathrm{ref}}(t_0)} = \exp(-1). \tag{9} $$

We applied a two parameter fit method to determine τ using Eq. (8) and measured TIR data. The following graphs in Fig. 11 show good agreement between computed data from Eq. (8) (grey curve) and measured TIR data (black circle) for two cases regarding concrete paving stone material.

If we compare the radiation balance of the two surfaces after car departure, then they differ only in respect to upward long-wave radiation. Therefore, we consider ${}^{\uparrow}\Delta E_{\mathrm{ref}}(t-t_0)$ as the relevant heat flux responsible for the attenuation of the persistence effect. In other words, the temporarily disturbed surface should have a higher rate of change (ROC) of surface temperature (T_s) than the reference surface close to it due to lower upward long-wave radiation. The approach summarizes the influence of further heat fluxes contributing to surface warming of the formerly shadowed surface in ΔQ_{res}, which is approximated to be constant. An appropriate thermal property governing the heating or cooling rate of a surface to a given heat flux is the thermal admittance (μ), defined by the thermal conductivity (k) and volumetric heat capacity (C) of the surface:

$$ \mu = \sqrt{kC}. \tag{10} $$

The following equation (based on Zmarsly et al., 2002, p. 57) is used for the determination of μ:

$$ \Delta Q = \frac{2A\sqrt{\Delta t}}{\sqrt{\pi}}\cdot\mu\cdot\Delta T_s + \Delta Q_{\mathrm{res}} = c\cdot\mu\cdot\Delta T_s + \Delta Q_{\mathrm{res}}, \tag{11} $$

where ΔQ is defined as the ROC of ${}^{\uparrow}\Delta E_{\mathrm{ref}}(t-t_0)$, multiplied by Δt, the constant measurement interval of 60 s. A is the active surface area set to

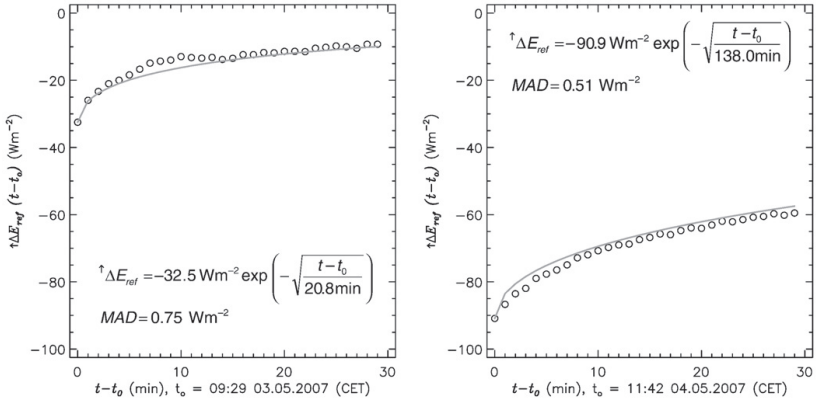

Fig. 11. Equalization of the difference between upward long-wave radiation from the temporarily shadowed car-park surface and the reference surface (concrete paving stones) close to it. Decay curves derived from exponential equations noted and based on Eq. (8). Left graph refers to case 1 and right graph refers to case 2. The *MROCD* pattern in Fig. 8b (right) corresponds to case 2. MAD is the mean absolute deviation between measured TIR data (Eq. (7)) and the data using the computed `INS;time-constant τ from Eq. (8).

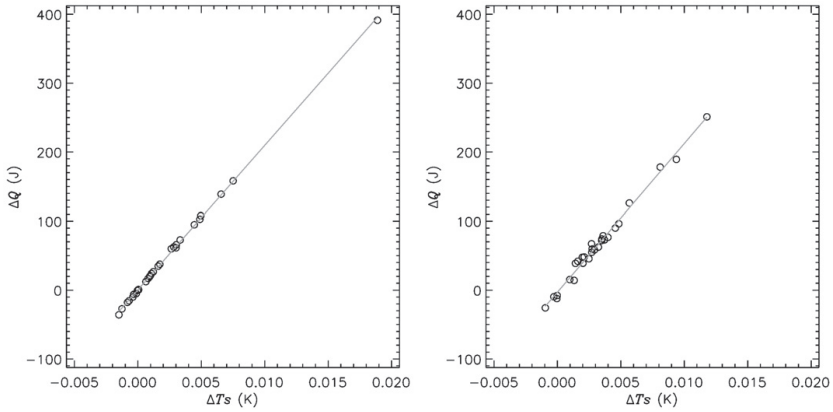

Fig. 12. Scatter plots of ΔT_s vs. ΔQ derived from TST data presented in Fig. 11. Table 3 summarizes all regression parameters of the two analysed persistence effects. Left graph refers to case 1 and right graph refers to case 2.

unity (1 m^2). ΔT_s is defined as the ROC of the difference between T_s of the formerly shadowed surface and the reference surface. T_s is derived from the original TIR data using an emissivity value of 0.95. The following graphs in Fig. 12 show scatter plots of ΔT_s vs. ΔQ for two cases.

Finally, μ is obtained from a linear regression fit using Eq. (11) and the data of the first 30 min of the persistence attenuation process. Table 3 summarizes the two analysed persistence effects. The derived thermal admittance values for dense concrete surfaces are in the range of literature values e.g. 1785 J m^{-2} $s^{-0.5}$ K^{-1} (Oke, 1987), 2349 J m^{-2} $s^{-0.5}$ K^{-1} (Stull, 1988) or 3180 J m^{-2} $s^{-0.5}$ K^{-1} (Zmarsly et al., 2002). In both cases ΔQ_{res} is very low. The higher value in case 2 could be attributed to a higher influence of sensible heat exchange at noon time.

5. Conclusion

The TIR ground-based remote sensing approach applied here is highly suitable to investigate dynamic processes within complex 3D urban structures. In addition, TST holds the possibility to assess the accuracy of 3D simulators, which produce high-resolution TIR or surface temperature scenes (Poglio et al., 2006). Further experimental studies of spatio-temporal thermal patterns need a method for handling surface emissivity at these scales. The effect of differences in atmospheric path lengths could be important for studying an extended FOV e.g. complete urban quarters by using a skyscraper as TIR camera platform.

Our findings indicate the influence of shadow on spatio-temporal patterns of upward long-wave radiation flux density from an urban courtyard. We can conclude that the history of shadow i.e. when shadow is present on the surface is important for the 24-hourly *MD* pattern. The thermal hot spot corresponds to the pavement area, which was non-shadowed between 10:00 and 15:30. The thermal cold spot corresponds to the shadowed part of the courtyard. The lime tree appears also as a cold spot due to transpiration. The 24-hourly *MROCD* pattern depends on shadow duration i.e. how long shadow has been present on the surface and on air temperature changes. The three-hourly patterns show persistence effects because of shadow, SVF distribution, surface material, human activities and turbulence characteristics of the surface–atmosphere interface. In order to prove the assumed SVF distribution in the courtyard and to make spatial correlations with thermal patterns it is possible to apply urban digital elevation models in raster format (e.g. Lindberg, 2007) or models using vector data (e.g. Teller & Azar, 2001).

Our results reveal a basic phenomenon in relation to the interpretation of nocturnal TIR images, because thermal persistence effects could continue to the night. Surfaces where shadow is present in the afternoon potentially show persistence of thermal patterns far into the night or in the case of parked cars to the next morning. With a reasonable certainty, we expect a 'nighttime bias' for these surfaces, which has to be considered e.g. in study of relations between urban morphology and nighttime thermal patterns.

The analysis of attenuation of upward long-wave radiation difference between temporarily shadowed and non-shadowed concrete surfaces inside the courtyard provides an opportunity to derive the surface thermal admittance. In order to verify this method it is necessary to carry out a controlled experiment. Further studies will address derivation of surface thermal properties from TST as well as the role of sensible heat exchange during the equalization of persistence effects.

Table 3
Fit parameters and thermal admittance of concrete paving stone material derived from the attenuation of thermal persistence effects caused by parked cars in the courtyard.

Case	Duration of disturbance (min)	R^2	$\mu_{concrete}$ (J m^{-2} $s^{-0.5}$ K^{-1})	ΔQ_{res} (J)
1	22	0.999	2395	0.35
2	269	0.989	2464	−3.03

Acknowledgements

We are especially grateful to Andreas Christen (Department of Geography and Atmospheric Science Program, University of British Columbia), who provided the procedure for radiometric correction of lens effects and made valuable comments on the manuscript. Furthermore, we gratefully acknowledge our colleges at the Chair of Climatology. Special thanks go to H. Küster, M. Otto, and J. Rogée who helped substantially in the design of the experiment and for helping to setup and maintain the meteorological measurement sites. The authors would like to thank R. Finkelnburg, F. Maussion and the reviewers for their comments, which helped to improve the quality of this paper.

References

Bruse, M., & Fleer, H. (1998). Simulating surface–plant–air interactions inside urban environments with a three dimensional numerical model. *Environmental Modelling & Software*, *13*, 373−384.
Christen, A., & Vogt, R. (2004). Energy and radiation balance of a central European city. *International Journal of Climatology*, *24*, 1395−1421.

Christen, A., Scherer, D., & Mielke, M. (2006). High frequency patterns in urban surface temperatures. *European Association of Remote Sensing Laboratories (EARSeL) — First Workshop of the Special Interest Group on Urban Remote Sensing, March 2–3 2006, Berlin, Germany*.

Chudnovsky, A., Ben-Dor, E., & Saaroni, H. (2004). Diurnal thermal behavior of selected urban objects using remote sensing measurements. *Energy and Buildings*, *36*, 1063—1074.

Eliasson, I. (1992). Infrared thermography and urban temperature patterns. *International Journal of Remote Sensing*, *13*, 869—879.

Endlicher, W., & Lanfer, N. (2003). Meso- and micro-climatic aspects of Berlin's urban climate. *Die Erde*, *134*, 277—293.

Erell, E., & Williamson, T. (2007). Intra-urban differences in canopy layer air temperature at a mid-latitude city. *International Journal of Climatology*, *27*, 1243—1255.

Grimmond, C. S. B., Salmond, J. A., Oke, T. R., Offerle, B., & Lemonsu, A. (2004). Flux and turbulence measurements at a densely built-up site in Marseille: Heat, mass (water and carbon dioxide), and momentum. *Journal of Geophysical Research Atmospheres*, *109*, D24101. doi:10.1029/2004JD004936.

Harman, I. N., & Belcher, S. E. (2006). The surface energy balance and boundary layer over urban street canyons. *Quarterly Journal Royal Meteorological Society*, *132*, 2749—2768.

Hoyano, A., Asano, K., & Kanamaru, T. (1999). Analysis of the sensible heat flux from the exterior surface of buildings using time sequential thermography. *Atmospheric Environment*, *33*, 3941—3951.

Johnson, G., Oke, T. R., Lyons, T., Steyn, D., Watson, I., & Voogt, J. (1991). Simulation of surface urban heat islands under 'IDEAL' conditions at night part 1: Theory and tests against field data. *Boundary-Layer Meteorology*, *56*, 275—294.

Kobayashi, T., & Takamura, T. (1994). Upward longwave radiation from a non-black urban canopy. *Boundary-Layer Meteorology*, *69*, 201—213.

Kottmeier, C., Biegert, C., & Corsmeier, U. (2007). Effects of urban land use on surface temperature in Berlin: Case study. *Journal of Urban Planning and Development*, *133*, 128—137.

Lagouarde, J. P., Ballans, H., Moreau, P., Guyon, D., & Coraboeuf, D. (2000). Experimental study of brightness surface temperature angular variations of maritime pine (*Pinus pinaster*) stands. *Remote Sensing of Environment*, *72*, 17—34.

Lagouarde, J. P., Moreau, P., Irvine, M., Bonnefond, J. M., Voogt, J. A., & Solliec, F. (2004). Airborne experimental measurements of the angular variations in surface temperature over urban areas: Case study of Marseille (France). *Remote Sensing of Environment*, *93*, 443—462.

Lindberg, F. (2007). Modelling the urban climate using a local governmental geo-database. *Meteorological Applications*, *14*, 263—273.

Lo, C. P., Quattrochi, D. A., & Luvall, J. C. (1997). Application of high-resolution thermal infrared remote sensing and GIS to assess the urban heat island effect. *International Journal of Remote Sensing*, *18*, 287—304.

Mertens, E. (1999). Bioclimate and city planning — Open space planning. *Atmospheric Environment*, *33*, 4115—4123.

Munier, K., & Burger, H. (2001). Analysis of land use data and surface temperatures derived from satellite data for the city of Berlin. In C. Jürgens (Ed.), *Remote Sensing of Urban Areas/Fernerkundung in urbanen Räumen Heft*, *Vol. 35*. (pp. 206—221) Regensburg: Regensburger Geographische Schriften.

Nichol, J. (2005). Remote sensing of urban heat islands by day and night. *Photogrammetric Engineering & Remote Sensing*, *71*, 613—621.

Oke, T. R. (1987). *Boundary layer climates.*New York: Methuen 435 pp.

Oke, T. R. (1988). The urban energy balance. *Progress in Physical Geography*, *12*, 471—508.

Oke, T. R., Johnson, G., Steyn, D., & Watson, I. (1991). Simulation of surface urban heat islands under 'ideal' conditions at night part 2: Diagnosis of causation. *Boundary-Layer Meteorology*, *56*, 339—358.

Poglio, T., Mathieu-Marni, S., Ranchin, T., Savania, E., & Wald, L. (2006). OSIrIS: A physically based simulation tool to improve training in thermal infrared remote sensing over urban areas at high spatial resolution. *Remote Sensing of Environment*, *104*, 238—246.

Quattrochi, D. A., & Ridd, M. K. (1994). Measurements and analysis of thermal energy responses from discrete urban surfaces using remote sensing data. *International Journal of Remote Sensing*, *15*, 1991—2022.

Rigo, G., Parlow, E., & Oesch, D. (2006). Validation of satellite observed thermal emission with in-situ measurements over an urban surface. *Remote Sensing of Environment*, *104*, 201—210.

Ruffieux, D., Wolfe, D. E., & Russel, C. (1990). The effect of building shadows on the vertical temperature structure of the lower atmosphere in downtown Denver. *Journal of Applied Meteorology*, *29*, 1221—1231.

Spronken-Smith, R. A., & Oke, T. R. (1999). Scale modelling of nocturnal cooling in urban parks. *Boundary-Layer Meteorology*, *93*, 287—312.

Stull, R. B. (1988). *An introduction to boundary layer meteorology.* Kluwer Academic Publishers 666 pp.

Sugawara, H., Narita, K., & Mikami, T. (2001). Estimation of effective thermal property parameter on a heterogeneous urban surface. *Journal of the Meteorological Society of Japan*, *79*, 1169—1181.

Sugawara, H., & Takamura, T. (2006). Longwave radiation flux from an urban canopy: Evaluation via measurements of directional radiometric temperature. *Remote Sensing of Environment*, *104*, 226—237.

Teller, J., & Azar, S. (2001). Townscope II — A computer systems to support solar access decision-making. *Solar Energy*, *70*, 187—200.

Voogt, J. (2008). Assessment of an urban sensor view model for thermal anisotropy. *Remote Sensing of Environment*, *112*, 482—495.

Voogt, J. A., & Oke, T. R. (1998). Effects of urban surface geometry on remotely-sensed surface temperature. *International Journal of Remote Sensing*, *19*, 895—920.

Voogt, J. A., & Oke, T. R. (2003). Thermal remote sensing of urban climates. *Remote Sensing of Environment*, *86*, 370—384.

Zmarsly, E., Kuttler, W., & Pethe, H. (2002). *Meteorologisch-klimatologisches Grundwissen.* Stuttgart: Ulmer 176 pp. (in German).

Appendix C: Spatial and temporal variability of urban tree canopy temperature during summer 2010 in Berlin, Germany

Meier, F. and Scherer, D. (2010): Spatial and temporal variability of urban tree canopy temperature during summer 2010 in Berlin, Germany.

Status: Submitted to Theoretical and Applied Climatology
Manuscript number: TAAC-D-11-00003

Own contribution:

- TST data acquisition
- Meteorological data collection
- Processing of TST data and meteorological data
- Tree data acquisition and processing
- Sealing data acquisition and processing
- Compilation of tree crown mask
- Analysis and interpretation of experimental results
- Preparation of manuscript with all figures and tables and subsequently revision of the manuscript after comments and improvements of co-author

Spatial and temporal variability of urban tree canopy temperature during summer 2010 in Berlin, Germany

Fred Meier and Dieter Scherer

Technische Universität Berlin, Department of Ecology, Chair of Climatology, Rothenburgstraße 12, D-12165 Berlin, Germany

Phone: 0049-30-314-71496

Fax: 0049-30-314-71355

E-mail: fred.meier@tu-berlin.de

Abstract

Trees form a significant part of the urban vegetation. Their meteorological and climatological effects at all scales in urban environments make them a flexible tool for creating a landscape oriented to the needs of an urban dweller. This study aims at quantifying the dependency of spatio-temporal patterns of canopy temperature (T_C) and canopy-to-air temperature difference (ΔT_C) on meteorological conditions, tree-specific (physiological) and urban site-specific characteristics. We observed T_C and ΔT_C of 56 individual urban trees using a high-resolution thermal-infrared (TIR) camera and meteorological measurements in the city of Berlin, Germany. The TIR camera recorded one image per minute over a period of two months from 1st July to 31st August 2010. Our results show that ΔT_C depends on tree genus, leaf size, degree of sealing around the tree and atmospheric conditions especially atmospheric vapour pressure deficit (*VPD*). The average diurnal course of ΔT_C shows a consistently positive value for all trees. *Populus* showed lowest daytime ΔT_C but highest nighttime ΔT_C. *Acer* showed maximum ΔT_C with one individual reaching more than 8 K at eight days in July and one day in August. Trees surrounded by high amounts of sealed surfaces consistently showed higher ΔT_C in spite of smaller leaf size. During high *VPD* (45 hPa) and T_a (36 °C) tree canopy temperature varied between 39 °C for park trees and 42 °C for city square trees. The tree-specific T_C in response to the urban environment is essential for comprehensive research concerning the energy and water balance of individual trees. With knowledge from these studies, it is then possible to evaluate and optimise the benefits of trees in cities.

Keywords: urban climate, urban trees, time-sequential thermography, thermal-infrared remote sensing, canopy temperature, leaf size, sealing, leaf-to-air temperature difference

1. Introduction

From previous studies about urban vegetation in particular urban trees, we know that trees produce distinct meteorological and climatological effects at all scales in urban environments (Heisler 1986; Oke 1989; Voogt and Oke 1997). This includes the influence of tree cover on the local-scale surface energy balance (Grimmond et al. 1996) and the reduction of canopy air temperature in comparison to the built environment by evapotranspiration and shadowing. However, the cooling effect differs from site to site and during the day (Souch and Souch 1993; Spronken-Smith and Oke 1998; Upmanis et al. 1998; Shashua-Bar and Hoffman 2000; Potchter et al. 2006; Bowler et al. 2010). Trees reduce surface temperatures (Hoyano 1988; Robitu et al. 2006; Shashua-Bar et al. 2009; Meier et al. 2010a), the building energy use (Rosenfeld et al. 1995; Akbari et al. 2001) and help to improve human thermal comfort by modifying the human energy balance (Mayer and Höppe 1987; Brown and Gillespie 1990; Streiling and Matzarakis 2003; Thorsson et al. 2004; Gulyás et al. 2006). Trees also modify the wind field in street canyons. This is important in relation to dispersion processes of pollutants (Gromke and Ruck 2007; Litschke and Kuttler 2008).

However, there are only few studies regarding the spatial and temporal variation of canopy temperature of urban trees and their response to the urban environment (Montague and Kjelgren 2004; Mueller and Day 2005). According to previous field studies, urban vegetative evapotranspiration is affected by advection and edge effects i.e. the oasis or clothesline effect because of strong surface heterogeneity in urban environments (Oke 1979; Hagishima et al. 2007). The experiment of Heilman et al. (1989) showed how building walls affect water use by adjacent shrubs, at which the long-wave radiation emitted by the walls appeared the major factor but cumulative water use was greatest for shrubs grown away from the wall. Kjelgren and Montague (1998) revealed that trees over asphalt had higher leaf temperatures than those over non-sealed areas resulting in higher water loss or stomatal closure depending on tree species. A study from Basel, Switzerland, based on thermal-infrared (TIR) imagery obtained during a single helicopter flight, showed that tree canopy temperatures at noon are species-specific and depend on location, leaf size and stomatal conductance (Leuzinger et al. 2010). There have been no studies, which characterize canopy temperature over a wide range of trees, sites and atmospheric conditions in an urban environment, beyond those that have investigated temporal dynamics of several individual trees at different sites (e.g. Montague and Kjelgren 2004) or one-time canopy temperature of more than 400 trees (Leuzinger et al. 2010).

The objective of this study is to estimate spatio-temporal variability of canopy temperature (T_C) and canopy-to-air temperature difference ($\Delta T_C = T_C - T_a$) of individual trees in an urban environment.

We aim to quantify the dependency of spatio-temporal patterns of T_C and ΔT_C on meteorological conditions, tree-specific (physiological) characteristics and urban site-specific characteristics. State-of-the-art TIR cameras mounted on towers or high-rise buildings allow a simultaneous sampling of spatial and temporal changes of canopy temperatures by recording time series of thermal images. We will refer to this as time-sequential thermography (TST, Hoyano et al., 1999). The obtained TST data cover a period of 62 days from 1st July to 31st August 2010. On the long-term perspective, our experimental setup aims to provide basic data on species-specific canopy temperature and ΔT_C in urban environments in order to compare different years. In detail, we address the following questions:

1.) Are there differences in terms of ΔT_C between and within the observed crowns in our study area and if so, how is the magnitude during an average diurnal cycle?

2) How does ΔT_C depend on atmospheric conditions, genus-specific variables and what influence has the location of the tree within the city?

In the next section, we describe the study site, our experimental setup, the survey of tree data and pre-processing steps of TST data. Section 3 presents the observed spatio-temporal patterns of ΔT_C and their relation to meteorological conditions during the measurement period, the influence of leaf size, trunk diameter and location within the city. The discussion section give answers to the above-mentioned questions under consideration of previous studies by other authors related to tree canopy temperatures.

2. Materials and Methods

2.1 Study site and experimental setup

The study site is located in the city of Berlin, Germany, (52°27'N, 13°19'E) in the south-western Steglitz-Zehlendorf district. The city structure in the examined area (Fig. 1) is characterized by a high amount of vegetation, five to six-storey block development with courtyards and mature trees, low-rise residential houses, street trees, one park with mature trees and a playground, villas with gardens and one isolated high-rise building. The study is conducted under the umbrella of the urban climate research program 'Energy eXchange and Climates of Urban Structures and Environments' (EXCUSE) that focuses on quantification of energy, momentum and mass exchange processes in the urban boundary layer. The research infrastructure includes a measurement platform on top of a

high-rise building and comprises a TIR camera system (7.5-14.0 µm, 320 x 240 pixels, VarioCam head, InfraTec GmbH). The fixed field of view (FOV) of the TIR camera covers an area of approximately 0.3 km^2. Technical specifications of the TIR camera system are summarised in Meier et al. (2010a, Table 1). Within the FOV, we measure continuously air temperature T_a and relative humidity *RH* (HMP45A, Vaisala) and downward short-wave radiation ${}^{\downarrow}E_{SW}$ (Starpyranometer 8101, Schenk GmbH) at a height of 22.5 m above ground, while wind velocity and wind direction are measured at a height of 23 m above ground at the same location using a cup anemometer and vane (Lambrecht GmbH). The measurement frequency is 5 sec and for further analysis, we used the 30 min averages. Vapour pressure deficit (*VPD*) was calculated as the difference between saturation vapour pressure using Magnus formula and actual vapour pressure derived from *RH* and T_a measurements. A tipping-bucket rain gauge measured precipitation at 0.1 mm resolution.

2.2 Thermal remote sensing data

During routine operation, the TIR camera system captures one image per minute and is oriented towards northwest (325°) and inclined by 59° from the nadir angle. Therefore, main parts of the observed crowns are oriented towards southeast. We expect different T_C for unseen areas of the crown resulting from effective thermal anisotropy (Lagouarde et al. 2000; Voogt and Oke 2003). Hence, we analyse a directional canopy temperature and not the complete canopy temperature representing the three-dimensional (3-D) crown surface.

The pre-processing and correction of TIR images comprise four steps. At first, radiance is converted into a brightness temperature T_b using firmware calibration parameters and case temperature under the assumption that the surface is a Lambertian blackbody. The camera is equipped with a wide-angle lens. This lens produce radiometric and geometric distortion, which are corrected in step two and three. Finally, an atmospheric correction is applied that accounts for spatial variability of line-of-sight (LOS) geometry due to the 3-D character of the examined urban environment and the oblique view. The method uses spatially distributed LOS geometry parameters, atmospheric profile data derived from meteorological measurements in the FOV and the radiative transfer model MODTRAN^{TM}5.2 (Berk et al. 2005). The reader is referred to the work of Meier et al. (2010b) for further details on radiometric, geometric and atmospheric corrections. For this study, we used cloud data from the WMO station 10381 Berlin-Dahlem that allowed us to apply the atmospheric correction procedure for cloudy conditions. However, we only used TIR data during no rain conditions and cloud base heights exceeding 330 m above ground. Under consideration of these meteorological conditions and functional deficiencies of the camera system, we could analyse

64860 single TIR images (2162 half-hourly averages) representing 72.6 % of the two months measurement period.

We applied the Stefan-Boltzmann law (δ = Stefan-Boltzmann constant) assuming an emissivity (ε) of 0.97 for the canopy surface (Campbell and Norman 1998) in order to derive T_C. Further, we account for reflected downward long-wave radiation ($^{\downarrow}E_{LW}$) measured on top of the high-rise building (Eq. 1).

$$T_b^4 \cdot \delta = T_C^4 \cdot \varepsilon \cdot \delta + (1-\varepsilon) \cdot {}^{\downarrow}E_{LW} \qquad (1)$$

A detailed consideration of reflected long-wave radiation originated from other parts than the sky (walls, roofs, ground surface) is not yet possible due to unknown view factors for the tree pixels and not TIR-scanned surrounding surfaces. Due to the oblique view, the sensor-target distance varies between 150 m for selected trees in the foreground and 500 m for selected trees in the background of the image. Thus, the spatial resolution of one pixel varies between 0.5 and 1.8 m. The spatial resolution exceeds typical leaf size values and in fact, T_C is a spatial integral over a lot of leaves and partly branches. Therefore, one T_C pixel already represents a part of the tree foliage. We use the median value of ΔT_C derived from all tree-specific crown pixels in order to describe the canopy-to-air temperature difference for one single crown. The spatial variability within the observed crown is defined as the difference between the 95 % and 5 % percentiles of ΔT_C. Although, we measured T_a in a height of 22.5 m above ground (white circle in Fig. 1), air temperature differences between the locations of tree canopies can be expected. This aspect is beyond the scope of this study.

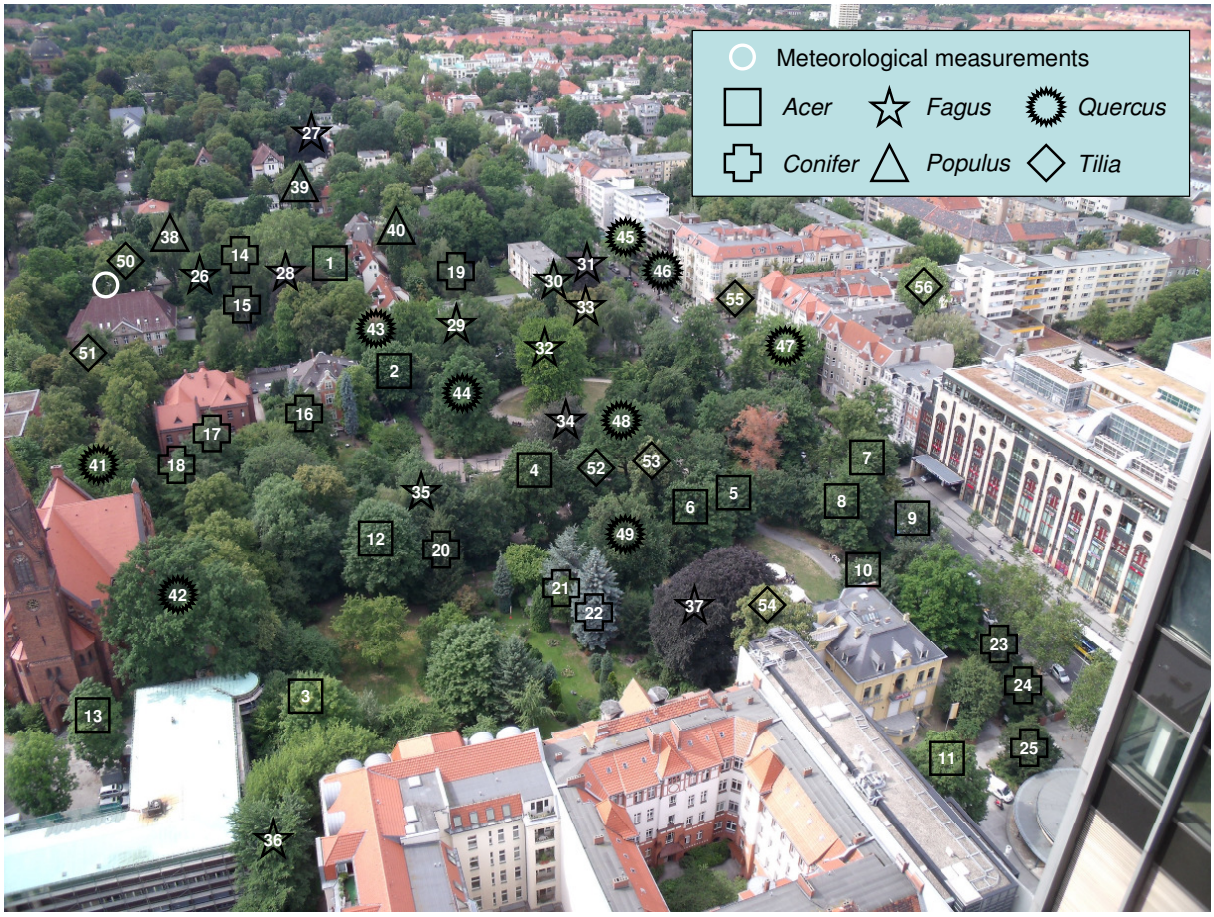

Fig. 1 Photograph taken from the high-rise building that captures the study site, field of view (FOV) and viewing direction (northwest) of the TIR camera. The symbols indicate tree genus and the numerals are used to indicate individual trees in the text

2.3 Tree data

We selected 56 individual trees and compiled a tree crown mask based on photographs from the high-rise building and TIR images. Every crown could be clearly separated from other surfaces surrounding the tree. Fig. 1 shows the FOV of the TIR camera and all selected crowns, which represent approximately 30 % of all trees inside the FOV. We estimated leaf size, trunk circumference at breast height (1.3 m above ground), tree height, habit, crown diameter and identified the genus and species of selected trees. Among these, we found *Acer platanoides*, *Acer pseudoplatanus*, *Acer campestre*, *Fagus sylvatica*, *Populus nigra*, *Quercus robur*, *Tilia spec.* and various conifers (e.g. *Taxus baccata*, *Pinus sylvestris*, *Larix europaeus, Abies procera*). We henceforth refer to the genus only and we sorted all conifers into one group. For 42 broadleaf trees, we measured the leaf size of 20-50 leaves per tree using a leaf area meter (Li-Cor Model 3100). In

order to estimate the influence of tree-specific location within the city, we computed the mean degree of sealing around the trunk in a square of 50 by 50 m. This area is oriented towards southeast taking into account the viewing direction of the camera i.e. 10 m towards north and west and 40 m towards south and east respectively. For this purpose, we used the sealing map of Berlin that is available in a 2.5 m raster format (Senate Department for Urban Development 2007).

3. Results

This section starts with an overview of spatio-temporal patterns showing the variability within a single crown and the spatial distribution of minimum, mean and maximum ΔT_C. Then we present the influence of atmospheric conditions, tree-specific and site-specific parameters on the spatio-temporal variability of ΔT_C. All time specifications refer to Central European Time (CET) and the end of the 30-min averaging period.

3.1 Spatio-temporal patterns

The tree mask and corresponding tree genus including the total number of TIR pixels per genus is presented in Fig. 2a. In order to facilitate interpretability we show spatio-temporal patterns of minimum, mean and maximum surface-to-air temperature difference for every pixel of the whole TIR image based on Eq. 1 (Fig. 2g, 2h, 2i).

The mean spatial variability within a single crown varies between 0.4 and 1.2 K whereas eight *Acer* trees have values more than 1 K (Fig. 2b). The maximum spatial variability varies between 1.9 and 6.5 K. *Tilia* (No. 55) located near the crossroad shows the maximum value (Fig. 2c).

The mean ΔT_C pattern shows that all trees have a positive canopy-to-air temperature difference (Fig. 2e). We can separate three clusters. These are the city square cluster, the park cluster and trees close to residential houses or close to streets. The conifer *Taxus baccata* (No. 25) located at the city square (lower right corner in Fig. 1) shows the overall highest mean ΔT_C value of 2.9 K. *Fagus* and *Quercus* show the lowest mean values between 1.3 and 1.5 K. These cold trees belong to the park cluster. *Populus* (No. 39, 40) and *Fagus* (No. 36) have mean ΔT_C values comparable to the park trees in spite of their locations close to buildings.

The minimum ΔT_C pattern (Fig. 2d) reveals that negative ΔT_C values occurred. These values were measured at night. It is particularly noticeable that *Acer* (No. 3, 5, 10) exhibited the absolute minimum ΔT_C, which is contrary to the mean and maximum ΔT_C patterns. The upper crown parts of *Acer* No. 3 and No. 10 reach exactly the adjacent building roof edges. This might be influencing the

cooling process of the crown, because during the night building roofs have the lowest surface-to-air temperature difference (Fig. 2g).

The maximum ΔT_C pattern (Fig. 2f) shows a similar pattern like the mean ΔT_C pattern whereas *Acer* consistently exhibited values greater than 7 K. Several trees outside the park cluster stayed relatively cool e.g. *Populus* (No. 38, 39, 40) and *Quercus* (No. 41, 42). The absolute maximum ΔT_C of 8.9 K was measured for *Acer* (No. 11). Building roofs showed maximum surface-to-air temperature differences of more than 40 K (Fig. 2i).

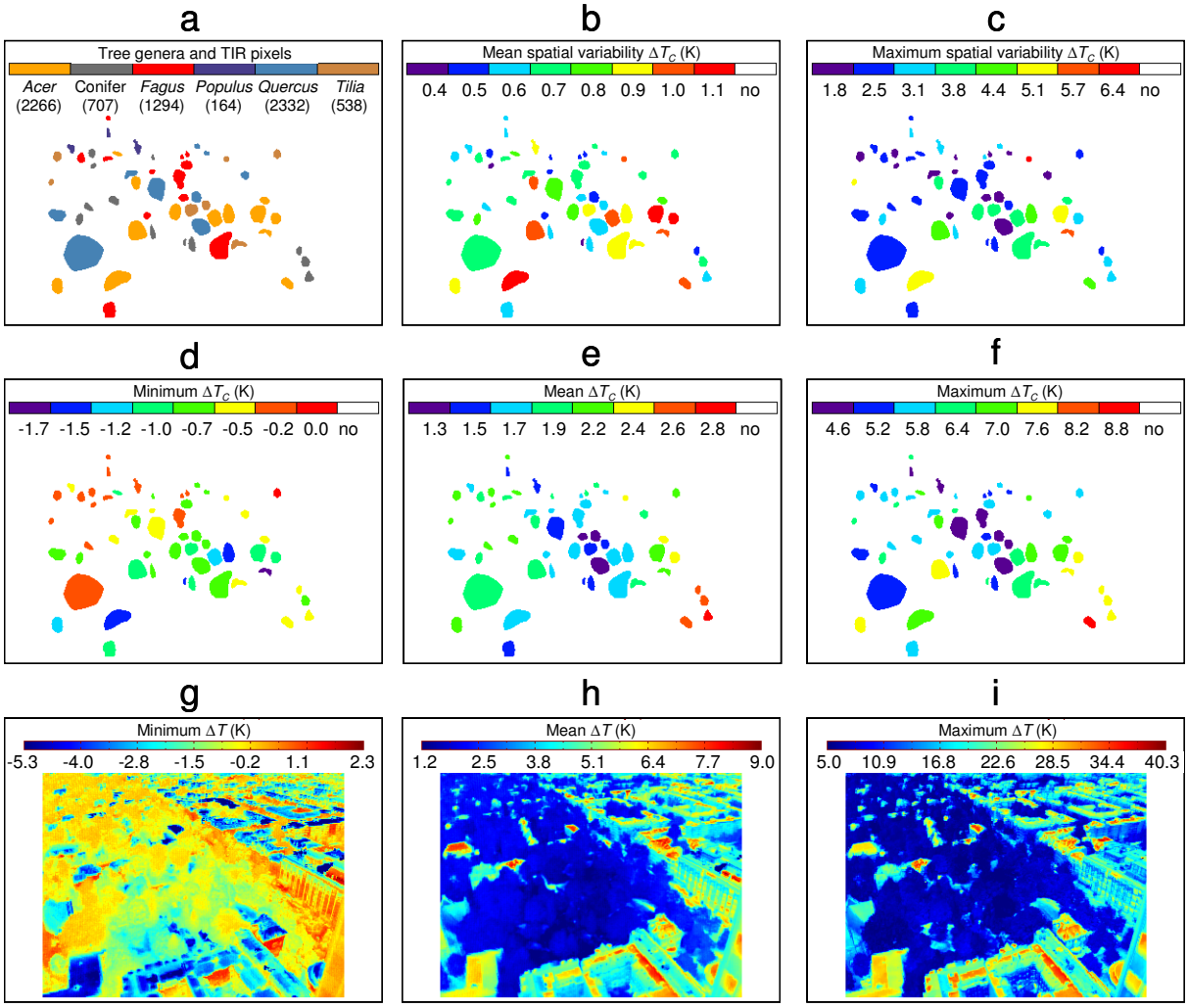

Fig. 2 Tree mask and corresponding tree genus inclusive total number of TIR pixels per genus (**a**), mean and maximum spatial variability within a crown (**b**, **c**), minimum, mean and maximum canopy-to-air temperature difference (ΔT_C) (**d**, **e**, **f**), minimum, mean and maximum surface-to-air temperature difference (ΔT) (**g**, **h**, **i**)

3.2 Influence of atmospheric conditions

3.2.1 Meteorological boundary conditions during the study period

Daily means of T_a, *VPD*, wind speed and daily sums of precipitation are depicted in Fig. 3, which also shows daily means of ΔT_C derived from all 56 crowns and the measured maximum and minimum ΔT_C during the day. Especially the first and middle part of July was very hot and dry leading to persistent high values of ΔT_C, T_a and *VPD*. On July 11, the daily mean of T_a exceeded 30 °C and the daily mean of *VPD* reached 27 hPa. The daily means of ΔT_C were between 0.6 and 3.3 K whereas the maximum ΔT_C reached more than 8 K for eight days in July and only for one day in August. The minimum ΔT_C (-1.5 K) was measured at 7th July during the night.

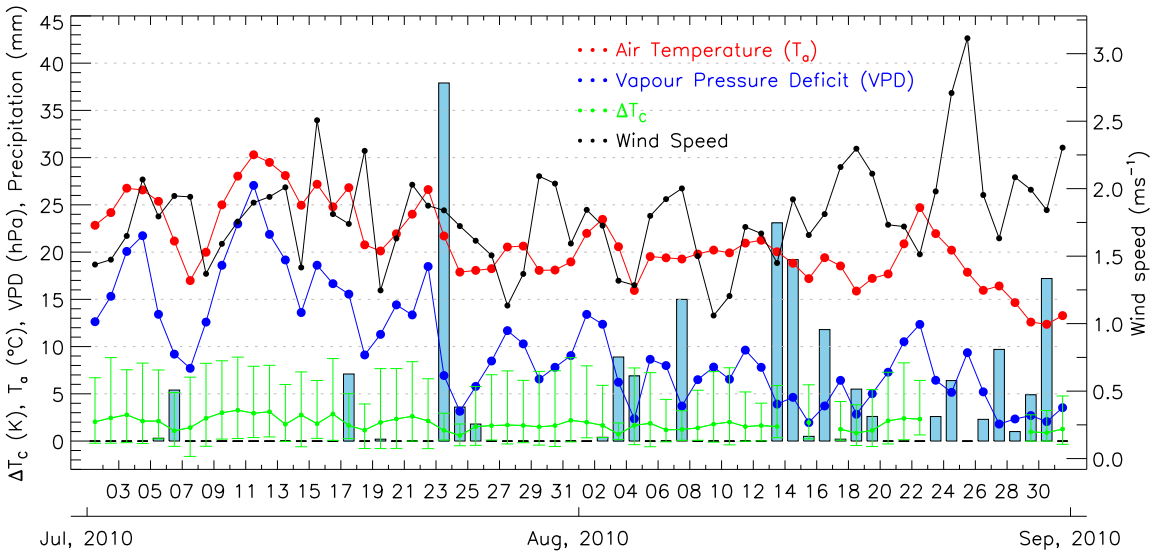

Fig. 3 Temporal variation of daily air temperature (T_a), vapour pressure deficit (*VPD*), wind speed, precipitation, mean canopy-to-air temperature difference (ΔT_C) of all crowns and daily maximum and minimum ΔT_C

Table 1 summarises meteorological conditions during June, July and August 2010. The table contains the corresponding long-term values (standard period 1961-1990, 2 m above ground) recorded at the climate station Berlin-Dahlem, Albrecht-Thaer-Weg (Chmielewski and Köhn 1999), which is situated at a distance of 1.5 km to the northwest of the study site. The June values are included in order to show meteorological conditions and particularly the very low amount of precipitation (6.4 mm) before the study period. During July, T_a and *VPD* exceeded the long-term means about 4.6 K and 7.4 hPa respectively.

Table 1 Monthly means of air temperature (T_a) and vapour pressure deficit (*VPD*), monthly sums of downward short-wave radiation ($^{\downarrow}E_{SW}$) and precipitation in comparison to climate data for the 1961-1990 period measured at the climate station Berlin-Dahlem, Albrecht-Thaer-Weg (Chmielewski and Köhn 1999)

	June	July	August
T_a (°C)			
2010	18.4	23.1	18.5
1961-1990	17.1	18.5	18.0
$^{\downarrow}E_{SW}$ (MJ m-2)			
2010	652.2	660.6	421.7
1961-1990	532.7	521.5	446.4
VPD (hPa)			
2010	10.1	14.9	6.5
1961-1990	7.0	7.5	6.7
Precipitation (mm)			
2010	6.4	55.2	138.3
1961-1990	70.0	53.0	64.0

3.2.2 Average diurnal course

The average diurnal course reveals that during the whole day ΔT_C remained positive (Fig. 4). During the night, ΔT_C was relatively constant between 0.4 and 1.8 K. At noon, ΔT_C was between 1.6 and 5.2 K. The maximum range between the individual trees amounts to 4 K and was observed at 13:00. In the morning, the course of ΔT_C shows some similarity to the course of $^{\downarrow}E_{SW}$. Both show a steep increase until 10:00. The median line of the box plots in Fig. 4 has a plateau like shape between 10:00 and 12:00 followed by a stepwise decrease until sunset. If we look at the 75 % percentile, ΔT_C starts to decrease one hour before noon because of increasing T_a with a slightly higher positive rate of change. The time of maximum ΔT_C does not coincide with the time of maximum T_a and the time of maximum T_C. At 13:00, mean tree canopy temperature reached its maximum value of 28.3 °C. During this time, the curve has the shape of a small hump. This could be attributed to the course of the incoming solar radiation that shows a small depression at 12:00 and 14:30. The next peak in the curve of T_C is present at 16:00. This coincides with diurnal maxima of T_a and *VPD*.

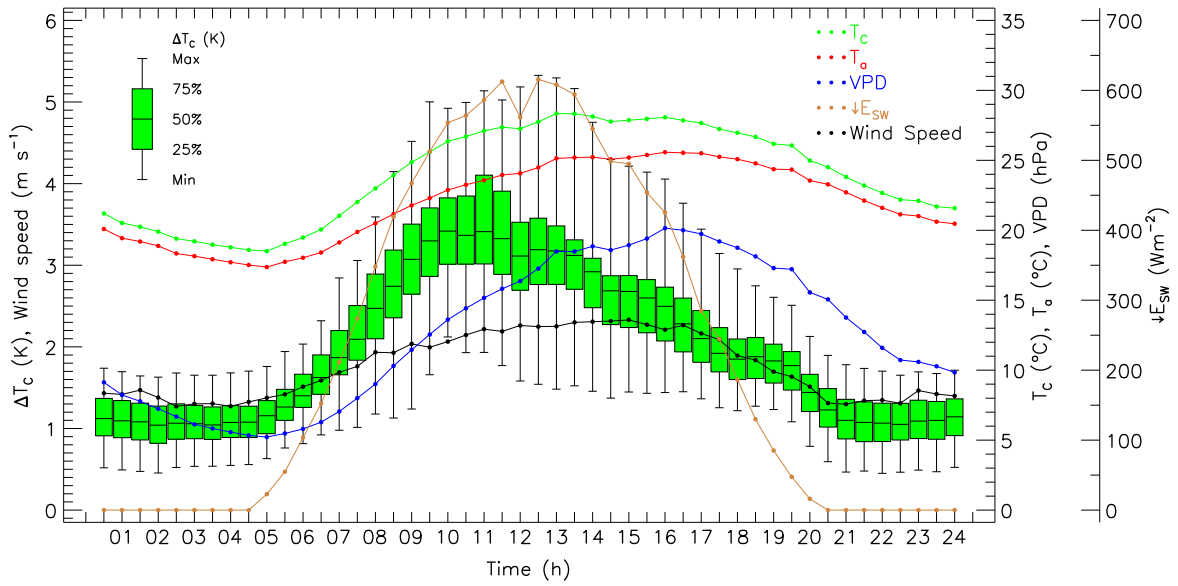

Fig. 4 Average diurnal course of mean canopy temperature (T_C), canopy-to-air temperature difference (ΔT_C) distribution for all 56 trees (box plots), wind speed, air temperature (T_a), vapour pressure deficit (*VPD*) and downward short-wave radiation ($^{\downarrow}E_{SW}$) based on 30-min averages from 1st July to 31st August 2010

3.2.3 Influence of downward short-wave radiation

The analysis to what extent trees show differences in their response to atmospheric conditions focuses on the daytime situation. The idea is to analyse the variability of ΔT_C under prevailing high $^{\downarrow}E_{SW}$ (12:30) or *VPD* (16:00) conditions in accordance to the average diurnal course as depicted in Fig. 4. The next section refers to the influence of *VPD*.

The linear correlation coefficients (r^2) between $^{\downarrow}E_{SW}$ and ΔT_C at 12:30 show clear differences between trees in the study area especially between *Populus* and *Acer* trees (Fig. 5, left). In the correlation pattern, all *Acer* trees have high values of up to 0.87 (No. 9) and *Populus* trees have the lowest values. The spatial distribution of the slope of the regression line (Fig. 5, right) depicts higher values for *Acer* trees. This pattern reveals that *Acer* trees (No. 8, 9, 10, 11) and conifer (No. 24) surrounded by a high degree of sealing are more sensitive to $^{\downarrow}E_{SW}$. High albedo surfaces and walls surrounding these trees can increase the intercepted reflected short-wave radiation.

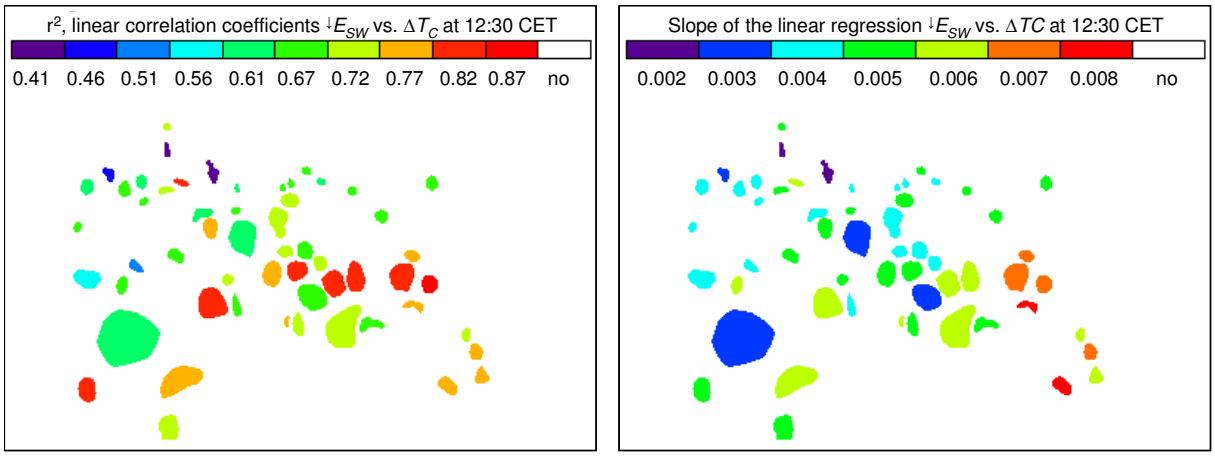

Fig. 5 Relation between downward short-wave radiation ($^{\downarrow}E_{SW}$) and canopy-to-air temperature difference (ΔT_C), spatial distribution of linear correlation coefficients r^2 (**left**) and slope of the regression line (**right**) based on 30-min averages at 12:30 from 1st July to 31st August 2010

3.2.4 Influence of vapour pressure deficit

The maximum *VPD* at 16:00 was 47.1 hPa (11th July). The day before and after this day exhibited *VPD* above 45.0 hPa. The minimum *VPD* was 5.2 hPa. The relationship between *VPD* and ΔT_C can be described by a third-order polynomial function (Fig. 6). This function provides reasonably strong fits of data with r^2 values ranging from 0.81 (*Acer* and *Quercus*) to 0.88 (conifers). The ΔT_C curves of all trees have their minimum around 10 hPa with the exception of *Populus*. The minimum ΔT_C of *Populus* developed around 15 hPa. Concerning the response to high *VPD*, the maximum ΔT_C is located around 41.0 hPa for all trees, whereas only the conifer ΔT_C exceeds 5 K. However, standard deviations of ΔT_C (Fig. 6) indicate higher values for single trees. Conifer No. 25 reached the highest afternoon ΔT_C value (6.7 K) at 9th July.

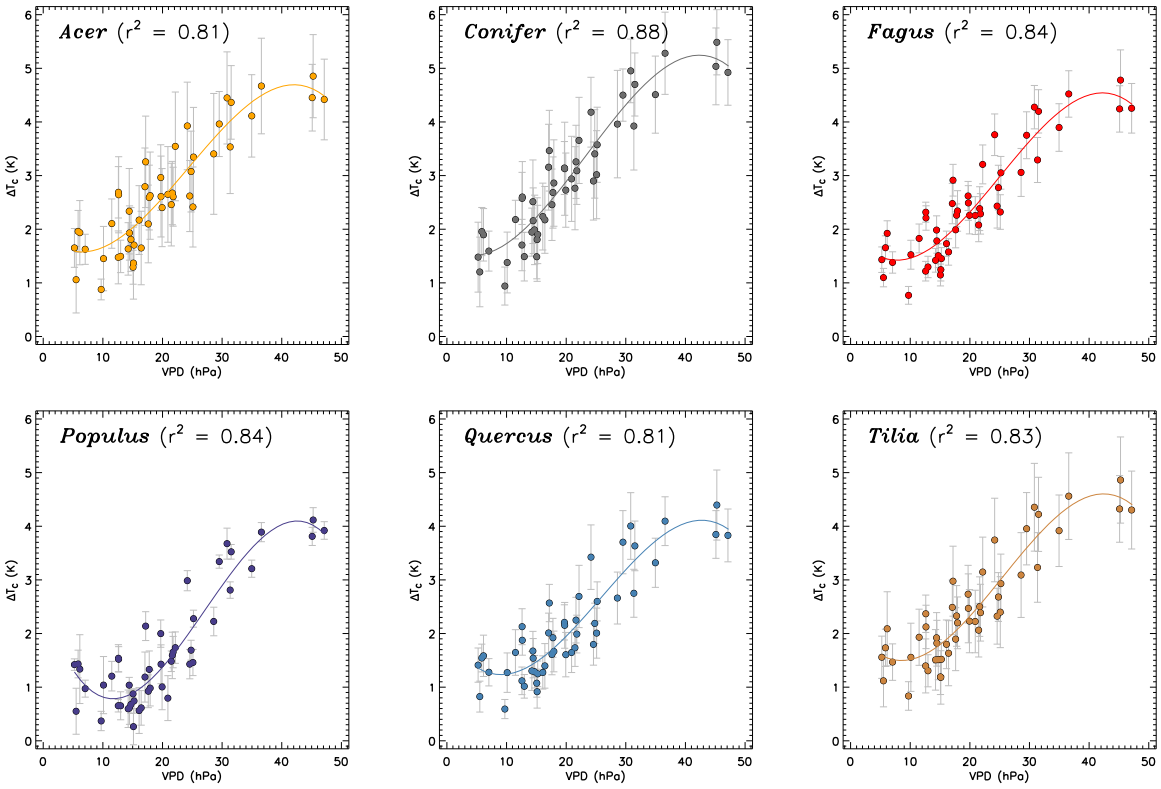

Fig. 6 Relation between vapour pressure deficit (*VPD*) and mean genus-specific canopy-to-air temperature difference (ΔT_C) based on 30-min averages at 16:00 from 1st July to 31st August 2010. Vertical error bars indicate ± spatial standard deviations of ΔT_C derived from all measured trees of the genus

3.2.5 Influence of wind speed and wind direction

The influence of wind speed or wind direction is hardly detectable via two-dimensional scatter plots. Hence, we analysed the variation of mean ΔT_C (all trees) via 3-D scatter plots at 12:30 and 16:00. For high amounts of ${}^{\downarrow}E_{SW}$ (> 800 W m^{-2}), an increase in wind speed caused no remarkable reduction of ΔT_C (Fig. 7a). Only wind speeds higher than 3 m s^{-1} reduced the mean ΔT_C at high levels of global radiation. The 3-D scatter plots also show that the highest mean ΔT_C values at noon arise during very dry and sunny weather conditions (Fig 7b). The influence of high wind speeds diminishes for high *VPD* conditions (>25 hPa) (Fig. 7c). This strong relation between ΔT_C and *VPD* answers also the question on the relation between wind direction and ΔT_C. Very dry southeastern winds leads to high ΔT_C values. Consistently lower ΔT_C values appear when moist air from the northwest reached the study area (Fig. 7d).

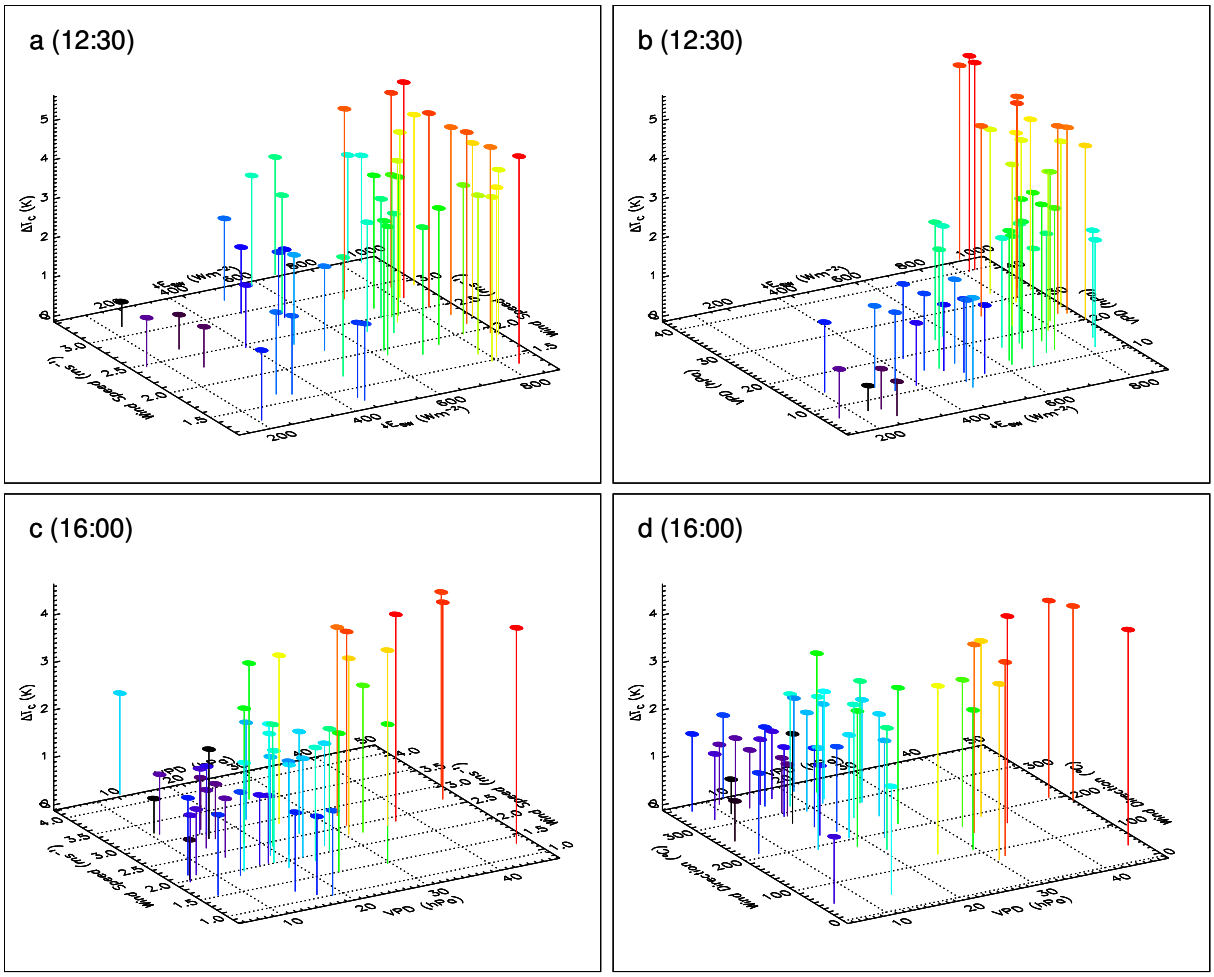

Fig. 7 Influence of downward short-wave radiation ($^{\downarrow}E_{SW}$) and wind speed on mean canopy-to-air temperature difference (ΔT_C) at 12:30 (**a**), influence of $^{\downarrow}E_{SW}$ and vapour pressure deficit (*VPD*) on mean ΔT_C at 12:30 (**b**), influence of *VPD* and wind speed on mean ΔT_C at 16:00 (**c**) and influence of *VPD* and wind direction on mean ΔT_C at 16:00 (**d**) from 1st July to 31st August 2010

3.3 Influence of tree-specific parameters

3.3.1 Average diurnal course of genus-specific canopy temperature

The mean genus-specific canopy temperature during the average diurnal course reveals clear differences between genera (Fig. 8). During the day, *Populus* had the lowest canopy temperature and ΔT_C remained below 2 K except for the morning period between 08:00 and 10:00. *Quercus* exhibited the second lowest temperature during the day. *Acer* had the highest canopy temperature between 08:00 and 15:00. In the afternoon conifers showed the highest T_C. *Tilia* and *Fagus* show a similar thermal behaviour and can be classified between *Quercus* and conifers. The fluctuations in the T_C curves are strongly linked to changes in $^{\downarrow}E_{SW}$ (see Fig. 4). The maximum T_C appears at 13:00

except for *Populus*. After this maximum, T_C decreases until 14:30. A secondary maximum is visible at 16:00, at the same time as T_a and *VPD* show their maxima. Now *Populus* reaches its absolute daily maximum. Only *Acer* shows no increase between 14:30 and 16:00.

This wavelike behaviour is also apparent in the average diurnal course of ΔT_C but the daily maxima are displaced due to the dependency of T_a. Especially *Acer* shows a greater deviation from T_a. The course of *Populus* is nearly similar to the course of T_a and only here the maximum ΔT_C was measured in the morning around 09:00.

During the night, we can only see small differences between the genera as already described by the box plots in Fig. 4. The range of the mean genus-specific ΔT_C amounts to 0.5 K. However, absolute values indicate the complete contrary situation in comparison to the daytime. *Populus* shows the highest ΔT_C and *Acer* reached the lowest ΔT_C values.

We computed the difference between maximum and minimum genus-specific ΔT_C (Fig. 8, bottom) in order to describe the variability of ΔT_C within a genus. The highest within genus variability show *Acer* and conifers in particular in the morning and afternoon period. *Fagus* reached also values above 2 K between 08:30 and 09:30.

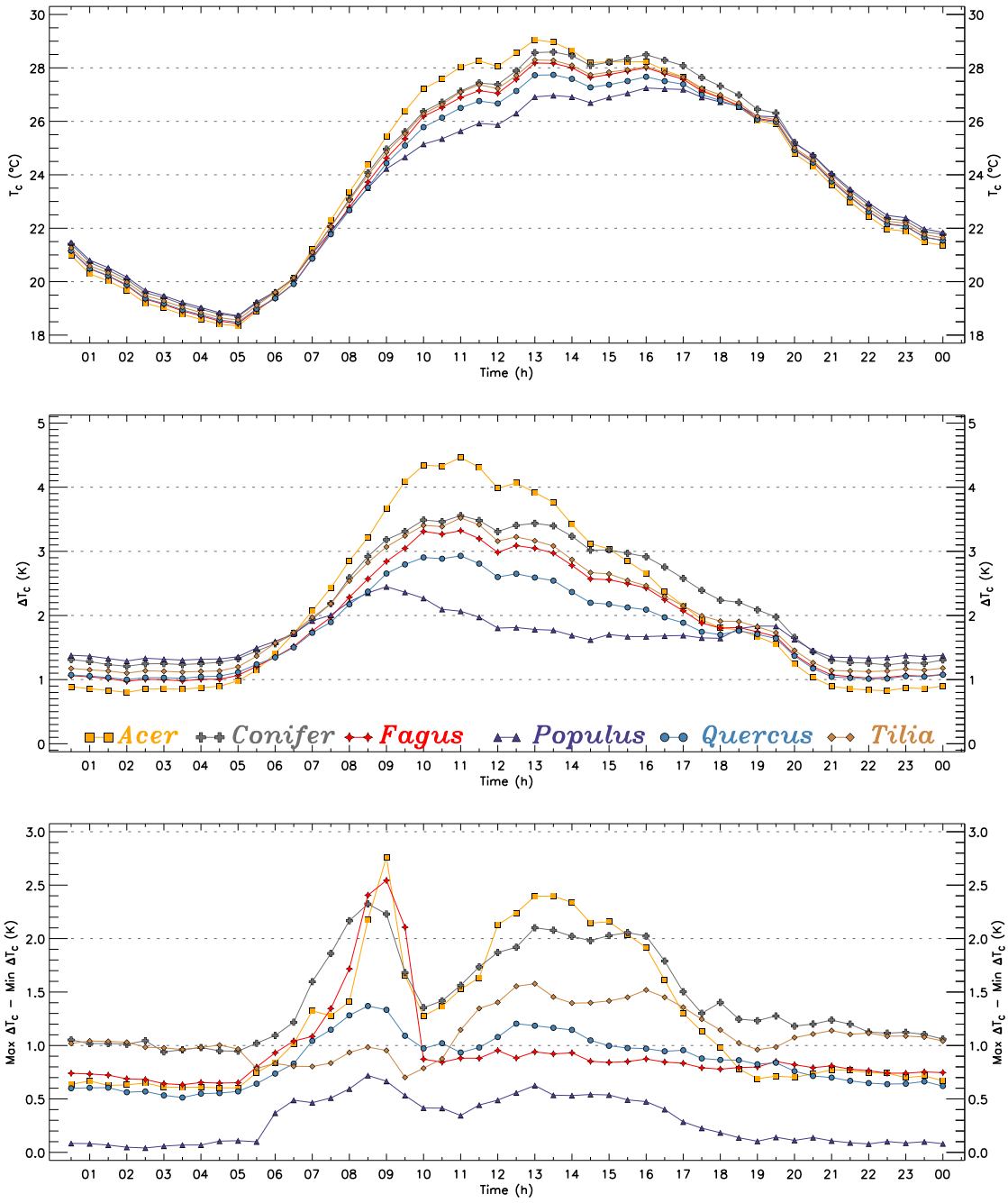

Fig. 8 Average diurnal course of mean genus-specific canopy temperature (T_C) (**top**), canopy-to-air temperature difference (ΔT_C) (**middle**) and difference between maximum and minimum ΔT_C (**bottom**) based on 30-min averages from 1st July to 31st August 2010

3.3.2 Influence of leaf size and trunk circumference

The leaf size of the examined deciduous trees was between 18.4 cm^2 (*Populus*, No. 39) and 138.4 cm^2 (*Acer*, No. 8). *Acer* trees showed the highest standard deviation of leaf size (up to 82 cm^2).

Trees with smaller leaves had generally lower ΔT_C during daytime (Fig. 9, left). The maximum variability of ΔT_C for trees having similar leaf size is about 2 K.

During the night, small leaves especially *Populus* are slightly warmer than big leaves but the regression analysis yields a very low correlation between the two parameters (Fig. 9, right).

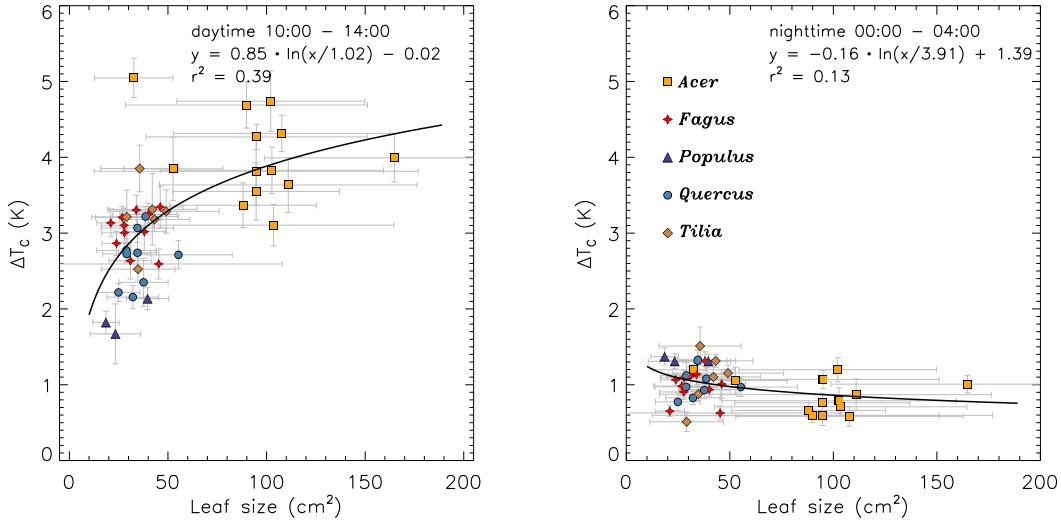

Fig. 9 Relation between leaf size and canopy-to-air temperature difference (ΔT_C) averaged for daytime (**left**) and nighttime (**right**). Horizontal error bars indicate ± standard deviations of leaf size. Vertical error bars indicate ± spatial standard deviations of ΔT_C within the crown

Further, we analysed the relation between ΔT_C and trunk circumference as a surrogate for tree height that varies approximately between 10 and 35 m. We prefer to use the measured trunk circumference because we only made a rough estimate of tree height. The trunk circumference is between 0.85 and 3.9 m. During the day, some trees with larger circumferences show a slightly lower ΔT_C (Fig. 10, left). The linear dependence is visible for *Fagus* (r^2=0.35), *Quercus* (r^2=0.14), *Tilia* (r^2=0.17) and *Populus* but not for conifers. Only *Acer* shows higher ΔT_C values for larger circumferences (r^2 = 0.19). However, the linear regression analysis yields only moderate correlations. During the night, small trees like *Acer* appear slightly cooler but the dependence is scarcely visible (Fig. 10, right).

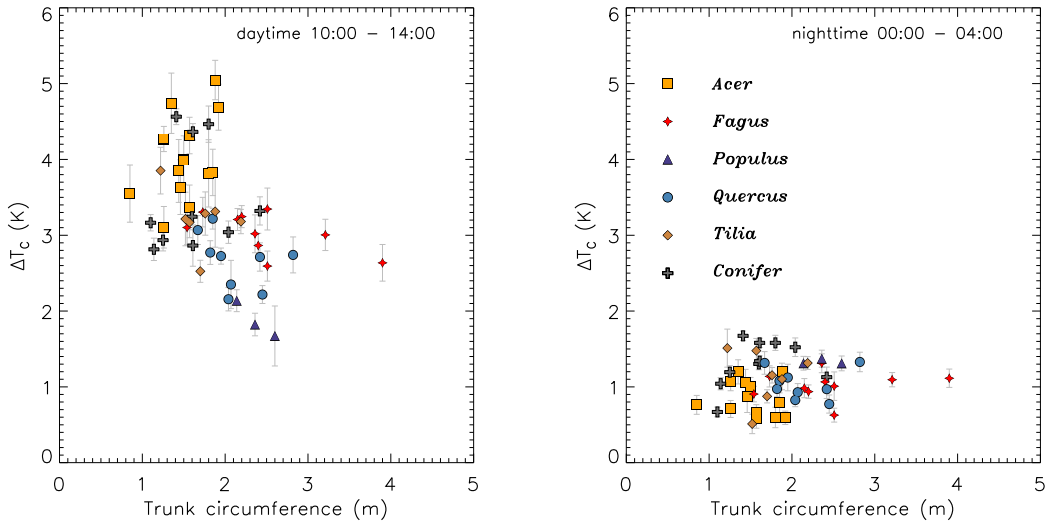

Fig. 10 Relation between trunk circumference at breast height and canopy-to-air temperature difference (ΔT_C) averaged for daytime (**left**) and nighttime (**right**). Vertical error bars indicate ± spatial standard deviations of ΔT_C within the crown

3.4 Influence of site-specific characteristics

The spatio-temporal patterns of ΔT_C presented in Fig. 2 already show a relation between the specific urban location of the tree and its thermal behaviour in form of the described clusters. Now, we use the average degree of sealing around the tree as a quantitative descriptor representing the influence of urban structures on its thermal behaviour. During day and night, we measured higher crown temperatures for all trees surrounded by a higher degree of sealing (Fig. 11). For all genera, linear regression lines and coefficients of determination are depicted except for *Populus* (only three individuals). An additional second-order regression line is shown for conifers (Fig. 11 left, $r^2 = 0.9$). *Acer* trees and conifers show higher ΔT_C than other trees at high levels of sealing whereas for conifers the relation between degree of sealing and ΔT_C is weak for locations under 70 % degree of sealing.

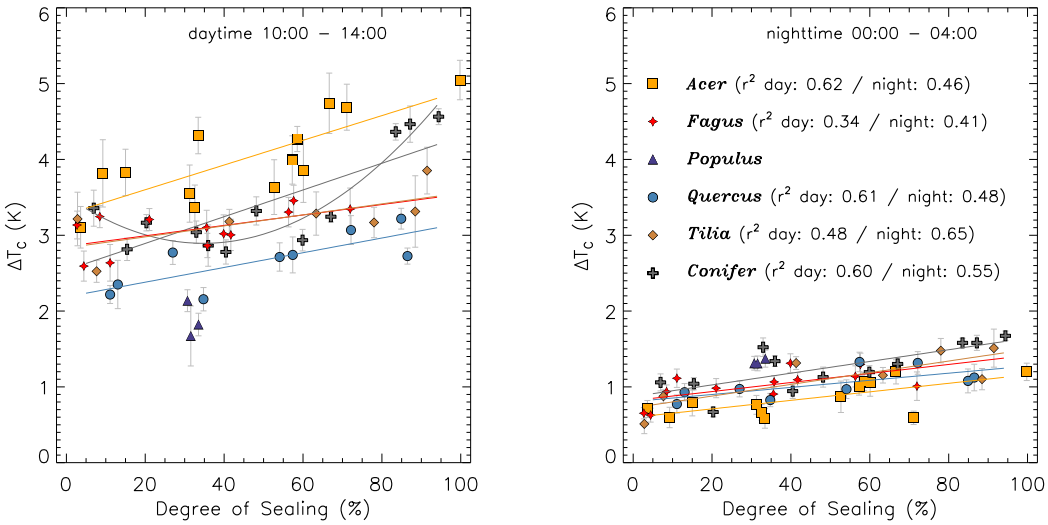

Fig. 11 Relation between degree of sealing around the tree and canopy-to-air temperature difference (ΔT_C) averaged for daytime (**left**) and nighttime (**right**). Vertical error bars indicate ± spatial standard deviations of ΔT_C within the crown

4. Discussion

There are differences in terms of ΔT_C of up to 4 K at 13:00 and up to 1.8 K at night as shown in the average diurnal cycle (Fig. 4) as expected and shown in previous studies (Leuzinger et al. 2010). In the study of Leuzinger et al. (2010), *Acer platanoides* showed maximum ΔT_C of 5 K. In our study, *Acer* trees also had the highest ΔT_C with an average noon value of 4 K. However, the absolute maximum ΔT_C of 8.9 K was measured for the city square tree No. 11 that is *Acer campestre* characterized by smaller leaves in comparison to *Acer platanoides*. *Populus* (Körner et al .1979) and *Quercus* (Leuzinger and Körner 2007) reach high stomatal conductance values. Therefore, at ample water supply conditions, we expect high transpiration rates and lower ΔT_C values for these trees as indicated in the mean diurnal course of these two genera (Fig. 8).

The observed variability of ΔT_C within the crown varied on average between 0.4 and 1.2 K whereas *Acer* showed generally higher values and the maximum range was 6.5 K (*Tilia* No. 55). In a mature forest, observed variability was between 6 K for *Larix* and 11.8 K for *Tilia* (Leuzinger and Körner 2007). In the forest study, the TIR camera was installed directly above the canopy resulting in a higher geometrical resolution, which provides more details of canopy structure like branching, leaf area density or sunlit and shadowed areas. In cities, buildings and isolated trees produce huge

shadow patterns especially at low sun elevations. We observed maximum within crown variability between 07:00 and 10:30 indicating the influence of sunlit-shadow patterns. Methods using temperature variability within a canopy as an indicator of plant water stress as suggested by Fuchs (1990) need information on the 3-D building structure in order to use these methods in urban areas.

The dependence of boundary layer thickness on leaf size and leaf shape as the lobed form of *Quercus* leaves influence the heat and mass exchange by turbulence between leaf and atmosphere (Schuepp 1993). The partly lower canopy temperatures for *Populus*, *Quercus, Tilia* and *Fagus* can be attributed to differences in leaf size. The thin flattened petioles of *Populus* cause leaves to flutter. This behaviour also reduces the boundary layer resistances (Grace 1978). If a leaf is cooler than air temperature then the greater rate of convective heat exchange, causes the smaller leaf to be nearer to air temperature than the larger leaf as described in the example in Campbell and Norman (1998). However, the average diurnal course shows only positive ΔT_C values for all trees and in spite of this observation, the larger leaves of *Acer* are nearer to air temperature at night.

The relation between leaf size and ΔT_C is superimposed by the influence of the tree-specific location within the city. This effect produces differences of up to 2 K for *Acer* trees having similar leaf size (Fig. 9, left). The leaf size of Acer No. 11 is rather small (33 cm^2) but this tree showed maximum ΔT_C during the study. Previous studies analysed the effect of urban ground cover on tree microclimate (Whitlow et al. 1992) and leaf temperatures (Kjelgren and Montague 1998; Montague and Kjelgren 2004; Mueller and Day 2005). Our study confirms that trees over sealed surfaces exhibit consistently higher canopy temperatures due to interception of upward long-wave radiation from non-vegetative surfaces having higher surface temperatures as depicted in Fig. 2. For the day and night situation, we can distinguish between cold trees, mainly located in the centre of the park and in gardens of low residential areas, and relatively hot trees surrounded by a high amount of sealing e.g. at the city square. Higher leaf temperature enhances the leaf-to-air vapour pressure deficit and the relevance of stomatal control on transpiration (Kjelgren and Montague 1998; Celestian and Martin 2005). However, for short periods building shadow can reduce tree canopy temperature (Meier et al. 2010a). The interception of long-wave radiation during the night is one explanation for the observed nighttime temperature excess especially for the *Populus* canopy, which has predominantly vertical orientated leaves (Kucharik et al. 1998) causing a low sky-view factor and more interception of long-wave radiation in comparison to canopies having horizontally orientated leaves. Canopy structure and leaf angle distribution explain lower temperatures of *Acer* during night under the assumption of more horizontally or spherical oriented leaves. The sensitivity

of *Acer* trees in relation to ${}^{\downarrow}E_{SW}$ is consistent with this leaf orientation. An interpretation of small differences in nighttime ΔT_C is complicated because air temperature is measured at one location at a height of 22.5 m whereas the height of some trees is lower. Small trees especially *Acer* trees show lower nighttime temperatures (Fig. 10, right). Spronken-Smith and Oke (1998) analysed thermal imagery of urban parks and their surroundings, where roofs were also cooler than tree canopies during the night. Besides the magnitude of nighttime temperature variability, it would be interesting to ask whether a greater respiration due to higher nighttime canopy temperature in urban environments contributes to a decline in net photosynthesis or not.

The observed relationship between ΔT_C and *VPD* (Fig. 6) indicates for *Populus* the classical feedback mechanism of stomatal control depending on leaf water content that allows maintaining high rates of transpiration as long as supply of water is sufficient (Körner 1985). All other trees show an increase in ΔT_C at lower *VPD* indicating the feedforward mechanism of stomatal control as a response to increasing *VPD* in order to conserve soil water (Körner 1985). The hydraulic architecture of trees (ring-porous vs. diffuse-porous) is able to influence stomatal regulation of transpiration in response to high *VPD* environments (Bush et al. 2008). However, in order to confirm differences in stomatal regulation of transpiration we need more information on the variation of tree-specific stomatal conductance, which was not measured during the study. During extreme high *VPD* (45 hPa) and T_a (36 °C) in the afternoon at 10th, 11th and 12th July, canopy temperature varied between 39 °C (park trees) and 42 °C (city square trees) corresponding to long-wave radiation emissions between 522 and 543 W m^{-2}. Hence, a high portion of absorbed incoming radiation (${}^{\downarrow}E_{SW}$ = 478 and ${}^{\downarrow}E_{LW}$ = 415 W m^{-2}) is dissipated by long-wave radiation.

5. Conclusions

The obtained TIR remote sensing data in combination with meteorological measurements enabled us to analyse canopy-to-air temperature differences of 56 individual urban trees belonging to different genera over a period of two summer months. Our results reveal clear differences between tree genera and strong spatial variability. However, a simple separation between cool (*Populus*) and hot trees (*Acer*) for instance to tackle adverse effects of the urban heat island disregard the nighttime situation, have to consider water supply (Whitlow et al. 1992) and positive outcomes of shadow due to an optimised canopy architecture (Heisler 1986).

This study reveals that buildings and surface cover influence the radiation budget of tree canopies. One frequently discussed way to reduce the radiative input in urban areas is the white roof concept promoting the use of high albedo materials. This concept would decrease tree interception of long-wave radiation emitted from buildings and ground surfaces but at the same time, it would increase absorption of reflected short-wave radiation from surrounding surfaces especially for high trees above roof level. The magnitude of this effect depends on the degree of sealing around the tree but a deeper understanding requires information on the complete 3-D radiation exchange including the thermal data of all surrounding surfaces and detailed view factors for the crowns. In this context, the combination of TST, meteorological observations and 3-D radiative exchange and energy balance models adapted to the complex urban environment e.g. DART EB (Gastellu-Etchegorry 2008) would be helpful.

On the long-term perspective, we are planning to build up a complete tree inventory in the FOV of the TIR camera. Recently we equipped five trees with sap flux sensors in order to analyse linkages between canopy temperature and transpiration (stomatal response) in different urban settings and under various atmospheric conditions.

The tree-specific canopy temperature in response to the urban environment is essential for comprehensive research concerning the energy and water balance of individual trees. With knowledge from these studies, it is then possible to evaluate and optimise the benefits of trees in urban environments e.g. in order to tackle adverse effects of the urban heat island.

Acknowledgements

We would like to thank Petra Grasse (Freie Universität Berlin, Institute of Meteorology) for providing the cloud data and Jörn Welsch (Senate Department for Urban Development, Urban and Environmental Information System) for providing the sealing map dataset. We are especially grateful to Albert Polze, Britta Jänicke and Marco Otto who helped substantially in the tree data collection and analysis.

References

Akbari H, Pomerantz M, Taha H (2001) Cool surfaces and shade trees to reduce energy use and improve air quality in urban areas. Sol Energy 70: 295-310

Berk A, Anderson GP, Acharya PK, Bernstein LS, Muratov L, Lee J, Fox MJ, Adler-Golden SM, Chetwynd JH, Hoke ML, Lockwood RB, Cooley TW, Gardner JA (2005) MODTRAN5: a reformulated atmospheric

band model with auxiliary species and practical multiple scattering options. Proceedings SPIE, 5655: 88-95

Bowler DE, Buyung-Ali L, Knight TM, Pullin AS (2010) Urban greening to cool towns and cities: A systematic review of the empirical evidence. Landscape Urban Plan 97: 147-155

Bush SE, Pataki DE, Hultine KR, West AG, Sperry JS, Ehleringer JR (2008) Wood anatomy constrains stomatal responses to atmospheric vapor pressure deficit in irrigated, urban trees. Oecologia 156:13-20

Campbell GS, Norman JM (1998) An introduction to environmental biophysics. Springer, New York

Celestian SB, Martin CA (2005) Effects of parking lot location on size and physiology of four southwest landscape trees. J Arboric 31:191-197

Chmielewski FM, Köhn W (1999) The long-term agrometeorological field experiment at Berlin-Dahlem, Germany. Agric For Meteorol 96: 39-48

Fuchs M (1990) Infrared measurement of canopy temperature and detection of plant water stress. Theor Appl Climatol 42:253-261

Gastellu-Etchegorry J (2008) 3D modeling of satellite spectral images, radiation budget and energy budget of urban landscapes. Meteorol Atmos Phys 102:187-207

Grace J (1978) The turbulent boundary layer over a flapping Populus leaf. Plant Cell Environ 1:35-38

Grimmond CSB, Souch C, Hubble MD (1996) Influence of tree cover on summertime surface energy balance fluxes, San Gabriel Valley, Los Angeles. Clim Res 6:45-57

Gromke C, Ruck B. 2007 Influence of trees on the dispersion of pollutants in an urban street canyon – experimental investigation of the flow and concentration field. Atmos Environ 41:3387 - 3302

Gulyás Á, Unger J, Matzarakis A (2006) Assessment of the microclimatic and human comfort conditions in a complex urban environment: Modelling and measurements. Build Environ 41:1713-1722

Hagishima A, Narita K, Tanimoto J (2007) Field experiment on transpiration from isolated urban plants. Hydrol Processes 21:1217-1222

Heisler, GM (1986) Effects of individual trees on the solar radiation climate of small buildings. Urban Ecol 9:337-359

Heilman JL, Brittin CL, Zajicek JM (1989) Water-use by shrubs as affected by energy exchange with building walls. Agric For Meteorol 48:345-357

Hoyano A (1988) Climatological uses of plants for solar control and the effects on the thermal environment of a building. Energy Build 11:181-199

Kjelgren R, Montague T (1998) Urban tree transpiration over turf and asphalt surfaces. Atmos Environ 32:35-41

Körner C, Scheel JA, Bauer H. (1979) Maximum leaf diffusive conductance in vascular plants. Photosynthetica 13:45-82

Körner C (1985) Humidity responses in forest trees - precautions in thermal scanning surveys. Arch Meteor Geophy B 36:83-98

Kucharik CJ, Norman JM, Gower ST (1998) Measurements of leaf orientation, light distribution and sunlit leaf area in a boreal aspen forest. Agric For Meteorol 91:127-148

Lagouarde JP, Ballans H, Moreau P, Guyon D, Coraboeuf D (2000) Experimental study of brightness surface temperature angular variations of maritime pine (*Pinus pinaster*) stands. Remote Sens Environ 72:17-34

Leuzinger S, Vogt R, Körner C (2010) Tree surface temperature in an urban environment. Agric For Meteorol 150:56-62

Leuzinger S, Körner C (2007) Tree species diversity affects canopy leaf temperatures in a mature temperate forest. Agric For Meteorol 146:29-37

Litschke T, Kuttler W (2008) On the reduction of urban particle concentration by vegetation - A review. Meteorol Z 17:229-240

Mayer H, Höppe P (1987) Thermal comfort of man in different urban environments. Theor Appl Climatol 38: 43-49

Meier F, Scherer D, Richters J (2010a) Determination of persistence effects in spatio-temporal patterns of upward long-wave radiation flux density from an urban courtyard by means of Time-Sequential Thermography. Remote Sens Environ 114: 21-34

Meier F, Scherer D, Richters J, Christen A (2010b) Atmospheric correction of thermal-infrared imagery of the 3-D urban environment acquired in oblique viewing geometry. Atmos Meas Tech Discuss 3: 5671–5703. doi:10.5194/amtd-3-5671-2010

Montague T, Kjelgren R (2004) Energy balance of six common landscape surfaces and the influence of surface properties on gas exchange of four containerized tree species. Sci Hortic 100: 229-249

Mueller EC, Day TA (2005) The effect of urban ground cover on microclimate, growth and leaf gas exchange of oleander in Phoenix, Arizona. Int J Biometeorol 49:244-255

Oke, T. (1979) Advectively-assisted evapotranspiration from irrigated urban vegetation. Bound-Lay Meteorol 17:167-173

Oke TR (1989) The micrometeorology of the urban forest. Philos Trans R Soc London, Ser B 324:335-349

Potchter O, Cohen P, Bitan A (2006) Climatic behavior of various urban parks during hot and humid summer in the mediterranean city of Tel Aviv, Israel. Int J Climatol 26:1695–1711

Robitu M, Musy M, Inard C, Groleau D (2006) Modeling the influence of vegetation and water pond on urban microclimate. Sol Energy 80:435-447

Rosenfeld AH, Akbari H, Bretz S, Fishman BL, Kurn DM, Sailor D, Taha H (1995) Mitigation of urban heat islands - materials, utility programs, updates. Energy Build 22:255-265

Senate Department for Urban Development (2007) Berlin digital environmental atlas 01.02 impervious soil coverage (sealing of soil surface). Data base: Urban and Environmental Information System (UEIS)

Shashua-Bar L, Hoffman ME (2000) Vegetation as a climatic component in the design of an urban street - An empirical model for predicting the cooling effect of urban green areas with trees. Energy Build 31:221-235

Shashua-Bar L, Pearlmutter D, Erell E (2009) The cooling efficiency of urban landscape strategies in a hot dry climate. Landscape Urban Plan 92:179-186

Souch CA, Souch C (1993) The effect of trees on summertime below canopy urban climates: a case study. Bloomington, Indiana. J Arboric 19:303–312

Spronken-Smith RA, Oke TR (1998) The thermal regime of urban parks in two cities with different summer climates. Int J Remote Sens 19:2085-2104

Streiling S, Matzarakis A (2003) Influence of single and small clusters of trees on the bioclimate of a city: A case study. J Aboric 29: 309-316

Schuepp PH (1993) Tansley Review No. 59 Leaf boundary-layers. New Phytol 125: 477-507

Thorsson S, Lindqvist M, Lindqvist S (2004) Thermal bioclimatic conditions and patterns of behaviour in an urban park in Göteborg, Sweden. Int J Biometeorol 48: 149-156

Upmanis H, Eliasson I, Lindqvist S (1998) The influence of green areas on nocturnal temperatures in a high latitude city (Göteborg, Sweden). Int J Climatol 18: 681-700

Voogt JA, Oke TR (1997) Complete urban surface temperatures. J Appl Meteorol 36: 1117-1132

Voogt JA, Oke TR (2003) Thermal remote sensing of urban climates. Remote Sens Environ 86:370-384

Whitlow TH, Bassuk NL, Reichert DL (1992) A 3-year study of water relations of urban street trees. J Appl Ecol 29:436-450

Appendix D: High-frequency fluctuations of surface temperatures in an urban environment

Christen, A., Meier, F. and Scherer, D. (2010): High-frequency fluctuations of surface temperatures in an urban environment.

Status: Submitted to Remote Sensing of Environment
Manuscript number: RSE-D-10-00873

Own contribution:

- TST data acquisition
- Meteorological data collection
- Photo documentation and 3-D model visualization
- Decomposition scheme (with co-authors)
- Derivation of 3-D surface data (height, azimuth, zenith)
- Literature review about the use of TST in urban and vegetation studies
- Interpretation of experimental results
- Analysis of atmospheric effects on temperature fluctuations
- Preparation of manuscript parts concerning the experimental setup and mean temperature patterns

High-frequency fluctuations of surface temperatures in an urban environment

A. Christen[(1)*], F. Meier[(2)], D. Scherer[(2)]

[(1)] Department of Geography, / Atmospheric Science Program University of British Columbia, 1984 West Mall, Vancouver, BC, V6T 1Z2, Canada

[(2)] Technische Universität Berlin, Department of Ecology, Chair of Climatology, Rothenburgstraße 12, D-12165 Berlin, Germany

[*] Corresponding author. E-mail address: andreas.christen@ubc.ca (A. Christen)

Abstract

It has been occasionally observed that surface temperatures of land-atmosphere interfaces fluctuate on scales of a few seconds to several minutes. It has been discussed and speculated that these variations are a response to high-frequency dynamics of turbulent heat exchange in the atmosphere. This study presents an attempt to resolve such fluctuations using time-sequential thermography (TST) from a ground-based platform in an urban environment. The contribution discusses a scheme to decompose measured apparent radiance converted to surface temperatures in a TST dataset into fluctuating, high-frequency (< 20 min) and long-term mean (>20 min) parts. The scheme is applied to a set of four TST runs (day/night, leaves-on/leaves-off) recorded from a 125 m high platform above a complex urban environment in the city of Berlin, Germany. Fluctuations in surface temperatures of different urban facets are measured and related to possible sensor errors, effects along the line of sight (LOS), and surface properties (material and form). Although sensor noise is shown to be a significant source of error, a number of relationships were found that link fluctuations to the surface energy balance: (1) Surfaces with surface temperatures that were significantly different from the air temperature experienced the highest fluctuations. (2) With increasing surface temperature above (below) air temperature, surface temperature fluctuations experienced a stronger negative (positive) skewness. (3) Surface materials with lower thermal admittance (lawns, vegetation) showed higher fluctuations of surface temperature than surfaces with high thermal admittance (walls, roads). (4) The emergence of leaves showed a measurable impact on high-frequency thermal behavior where the leaves caused surface temperatures to fluctuate more compared to a leaves-off situation. (5) In many cases, observed fluctuations were coherent across several neighboring pixels. The evidence from (1) to (5) suggests that atmospheric turbulence might be a significant control of fluctuations at scales < 20 min. The study underlines the potential of using high-frequency thermal remote sensing in energy balance and turbulence studies at complex land-atmosphere interfaces. Using high sampling frequencies in TST observations might allow for the extraction of information on the dynamic response of the surface energy balance to atmospheric turbulence, thermal admittance of surface materials and/or potential visualization of turbulent motions.

Keywords: Surface temperatures, Sensible heat flux, Thermal admittance, Thermal anisotropy, Thermal infrared, Thermal remote sensing, Time sequential thermography, Turbulence, Urban energy balance, Urban environment, Urban vegetation.

1. Introduction

1.1 Fluctuations of surface temperatures at land-atmosphere interfaces

The surface energy balance (Monteith and Unsworth, 2008) controls surface temperatures of land-surfaces. Surface temperatures vary as a consequence of radiative input and output (Q^*), changes in subsurface conduction of heat (Q_G) and changes in sensible (Q_H) and latent heat exchange (Q_E) with the atmosphere. Radiative input is relatively constant on short time periods (< 1 hr) the exceptions being sky conditions with broken clouds and situations underneath plant canopies where sun flecks cause rapid changes in short-wave irradiance (Chazdon, 1988). However, at higher-frequencies, in the order of seconds to minutes, surface temperatures are expected to respond to the turbulent sensible and latent heat flux densities in the atmosphere. The instantaneous wind field of atmospheric turbulence and the resulting changes of laminar boundary layer thickness are expected to control temperature fluctuations and cause them to respond to atmospheric heat surplus or deficits (carried by turbulent eddies) on the same length and time scales as the atmospheric motions themselves.

Paw U et al. (1992) operated a directional infrared thermometer at a nominal frequency of 10 Hz over a maize canopy and identified ramp structures in the surface temperature signal of the crop that were significantly correlated with simultaneously measured fluctuations in air temperature above the canopy. The magnitude of surface temperature ramps was, however, significantly smaller than the air temperature ramps. The ramps in the surface temperature signal reflect the abrupt replacement of progressively warmed (or cooled) near-surface air with well-mixed cool (warm) air from aloft driven by coherent eddies in the turbulent flow. Ballard et al. (2004) measured high-frequency fluctuations of directional thermal radiance in a grass canopy at 1 sec to 5 min intervals and hypothesized that turbulent mixing plays a dominant role in explaining their high-frequency traces.

Surface temperature fluctuations due to turbulent exchange might be small, and are expected to depend on the surface material's thermal properties and the efficiency of the atmospheric turbulence to exchange heat through the laminar and turbulent boundary layers. The latter process is driven by atmospheric dynamics, which are in turn controlled in part by the surface's form (roughness).

Our hypothesis is that surface temperature fluctuations on various facets of an urbanized land atmosphere-interface might be driven by the high-frequency dynamics of the instantaneous surface-atmosphere exchange.

For longer integration periods (> 20 min to 2 hr), we suggest that spatial differences in mean surface temperature between facets, and trends in mean surface temperature are controlled by different radiative input and conductive storage fluxes which, in turn, are controlled by surface material (albedo, thermal properties) and form (orientation, sky view factor, solar geometry, porosity). At higher frequencies (< 20 min), however, surface temperature fluctuations can be expected to follow the discussed dynamic effects of wind (i.e. turbulent exchange). Separating the spatial field of measured surface temperatures conceptually into a mean (trend) and a fluctuating (high-frequency) part could therefore assist us in quantifying the forcing processes acting on different time scales.

1.2 The use of time sequential thermography (TST)

State-of-the-art thermal infrared (TIR) cameras allow a simultaneous sampling of spatial and temporal changes of surface temperatures by recording a time series (t) of thermal images ($\mathbf{x} = x,y$). We will refer to this as time-sequential thermography (TST, Hoyano et al., 1999). TST is typically restricted to fixed ground-based platforms with a directional field of view (FOV), as sensors on airborne or satellite platforms do not provide enough temporal repetition and/or geometric resolution to resolve small-scale and short-term changes that are potentially caused by a turbulent atmosphere.

1.2.1 TST in urban environments

TST in previous research on urban surfaces was mostly motivated by either (i) the potential to infer thermal properties of the urban surface, (ii) to determine terms of the surface energy balance or (iii) to analyze building-environment heat transfer. Most studies reported in the peer-reviewed literature use TST to resolve spatial differences in mean temperature and warming and cooling rates from hourly to diurnal time steps. Hoyano et al. (1999) uses TST runs of buildings over 24-h recorded at one-minute intervals to infer sensible heat flux density of individual building facets. Sugawara et al. (2001) and Chudnovsky et al. (2004) used fixed TIR cameras on top of high-rise buildings (> 100m) that were operated at intervals of 5 min and 60 min to estimate thermal properties of urban surface facets at the neighborhood scale. Meier et al. (2010a) used TST recorded at 1 min intervals to investigate thermal dynamics in an urban courtyard over two days and used the attenuation of thermal persistence effects (e.g. shadow) in order to derive surface thermal admittance. All studies cited above analyzed and discussed temporal variation on time scales typically larger than those of turbulent length scales.

1.2.2 TST in vegetation studies

In non-urban ecosystems, TST has been applied to study temporal and spatial variations in surface temperatures of grassland (e.g. Shimoda and Oikawa, 2008, TST at 5 min intervals) or the estimation of biomass heat storage (e.g. Garai et al. 2010, TST at 2 min intervals). Higher-frequency analysis has been used in the laboratory to study stomatal regulation and transpiration of individual leaves (e.g. Jones, 1999, TST at 1 min intervals). Leuzinger and Körner (2007) investigate thermal regulation of leaf-temperatures in a forest canopy using TST at 5 s intervals. They observed fluctuations in leaf temperatures up to 2 K that remained entirely unexplained, but also concluded that the unexplained fluctuations correlated poorly against measured wind speed. They do not rule out that wind causes the observed fluctuations but argue that the actual turbulent patterns experienced by the sampled trees may have deviated substantially from their single-point anemometer. Ballard et al. (2004) used TST to study grass surface temperatures at 1.3 m above the canopy at a 20 sec interval and report that a 'rapid effect of cooling from the wind is easily noticeable' in their TST runs.

The specific objectives of the current contribution are to (i) present a scheme to decompose a signal of measured apparent surface temperatures by time-sequential thermography into a high-frequency fluctuating and a long-term mean part, (ii) to apply the decomposition scheme to a set of time-sequential thermography runs from a complex urban environment that is composed of many different facets and surface materials, (iii) to quantify surface temperature fluctuations of the different urban facets and relate them to possible instrumental error sources, effects along the line of sight (LOS) and surface properties (material and form).

To simplify the discussion, in this contribution we will use the term 'temperature' and the symbol T for 'apparent surface temperatures' with a surface emissivity of $\varepsilon = 1.0$. If we refer to air temperature, or corrected surface temperatures, this will be explicitly noted.

2. Methods

2.1 Experimental set-up

To address objectives (ii) and (iii), this contribution builds upon data sampled by a TIR camera that recorded temperature fluctuations in a relatively complex urban setting. We use data from an urban environment because this provides the opportunity to simultaneously sample a large spectrum of various land-surface materials and three-dimensional (3-D) form (height above ground, slope, and azimuth) under the same meteorological forcing.

2.2.1 Thermal camera

The thermal infrared (TIR) camera used in this study is a VarioCAM® head (Infratec GmbH, Dresden, Germany) that was operated at 1 Hz. The camera uses an uncooled microbolometer focal plane array (320 x 240 pixels) that is thermally stabilized with a Peltier element. It is recording the signal at a resolution of 16 bit (thermal resolution 0.08 K at 30°C) with an accuracy of 2 %. The spectral range of the camera's sensitivity is between 7.5-14.0 µm. The camera's aperture is protected by a polyethylene foil with an estimated transmissivity of τ_{foil} = 0.75 in the sensitive range, which is considered in the radiance-to-temperature conversion. The array is protected by an encapsulation (IP 65) and the camera is enclosed in an environmental enclosure that also hosts a ventilation and heating system to avoid strong temperature fluctuations. During operation, case temperature was continuously monitored. Every 6 seconds all microbolometer elements were homogenized (shutter) and the camera case temperature was stored in order to use the optimized radiance-to-temperature calibration parameters and to avoid drift effects. The calibration parameters for the camera system were determined by the manufacturer using blackbody temperatures. The resulting time-series were corrected in post processing for geometry (lens distortion) and for lens vignetting / narcissus effects before any further post processing steps. Both corrections are described in detail in Meier et al. (2010b).

2.1.2 Field of view

The TIR camera was installed on top of an isolated high-rise building overseeing part of the city of Berlin, Germany (52.4556ºN, 13.3200ºE, WGS-84). The camera was mounted on a boom at a height of 125 m above ground level 3 m off the roof's edge. The original FOV of the camera is 64° by 50° and covers an area of approximately 0.3 km^2. Because of the geometric correction, the FOV in the analysis was cropped to 57º by 44º. TST runs were recorded with a fixed FOV oriented towards Northwest (325°) and inclined by 59° from the nadir (FOV ranges between 36.3 and 81.8º from the nadir). Due to the oblique view, the sensor-target distance varies between 125 and 700 m (median 234 m), which corresponds to a geometric resolution between 0.5 and 2.5 m for the instantaneous field of view (IFOV) of 3.6 mrad.

Urban cover and form in the FOV is documented in Figure 1. The underlying terrain has a gentle slope of about 1º from the foreground (SE, 42 m a.s.l.) to the image background (NW, 65 m a.s.l). The FOV is characterized by a high fraction of urban vegetation and contrasting building densities. Five to six- story buildings enclosing courtyards dominate the upper right (Northern part). The center and the left hand side (South) include a park with mature trees and detached low and mid-rise

residential houses. Figure 1c shows modeled buildings and ground elevation in the camera's field of view (in absence of vegetation and small-scale elements). The dataset was calculated from a 3-D building vector model format (Kolbe 2009) in combination with a digital ground model (DGM). The building model and the DGM combined results into a digital surface model (DSM), which will be further used in the analysis.

Trees found in the FOV are dominantly deciduous that include *Acer platanoides*, *Acer pseudoplatanus, Fagus sylvatica, Populus nigra, Quercus robur, Tilia spec.* The FOV also shows a few evergreen trees (approx. 10% of all trees, *Taxus baccata, Pinus sylvestris, Abies procera*). Tree height varies between 10 and 30 m. Figures 1a and b show the contrasting surface of the leaves-on and leaves-off situation.

2.1.3 Climate measurements

Downward short-wave $\downarrow E_{SW}$ and long-wave radiation $\downarrow E_{LW}$ (CM3, and CG 3, Kipp & Zonen, Delft, Netherlands), air temperature T_{air} and relative humidity RH (HMP45A, Vaisala, Vantaa, Finland) are measured on top of the isolated high-rise building. Additionally a fast anemometer/thermometer (USA-1, Metek GmbH, Elmshorn, Germany) and hygrometer (Li-7500, Licor Inc., Lincoln, NK, USA) were operated at the same location. Within the FOV,at a horizontal distance of 300 m from the high-rise building (52.4568ºN, 13.3161ºE, WGS-84), T_{air} and RH were measured at ground level (2 m) underneath a relatively open tree canopy and 3.5 m above an exposed 19 m pitched roof (both HMP45A, Vaisala, Vantaa, Finland). Wind velocity / direction (Lambrecht GmbH, Göttingen, Germany) was measured 4 m above the same roof.

2.1.4 TST Runs

In April 2009, four 80 min runs were recorded at 1 Hz. The weather conditions during the four runs and for the preceding 24 hours are summarized in Table 1. Two of the runs, D1 and N1 are from early April when leaves of the deciduous trees have not yet emerged ('leaves-off') and hence more ground and building walls are visible. The second set, runs D2 and N2, ('leaves-on'), is from late April 2009 when leaves emerged and a closed canopy formed over the park. All runs were recorded under cloudless skies. Daytime runs are characterized by high downward short-wave radiation with averages of 634 (D1) and 780 (D2) W m^{-2}. The wind velocity was relatively low and ranged between 2.3 and 2.6 ms^{-1} at 23 m a.g.l, and between 1.6 and 2.9 ms^{-1} at 125 m a.g.l.

2.2 Analysis of TST data

2.2.1 Decomposition schemes

The TST runs of $T(\mathbf{x},t)$ were decomposed in post processing using spatial and temporal averaging operators with the goal to separate high-frequency fluctuations in temperatures from the mean patterns and trends.

A temporal averaging operator is written using an overbar. For example, the temporal average of the temperature $T(\mathbf{x},t)$ of a single pixel in the image is $\overline{T}(\mathbf{x})$:

$$\overline{T} = \frac{1}{N}\sum_{t=0}^{N} T(t) \tag{1}$$

A spatial average is written using angle brackets, so the average temperature of a spatial subset or the entire image is $\langle T \rangle$:

$$\langle T \rangle = \frac{1}{N}\sum_{\mathbf{x}=0}^{N} T(\mathbf{x}) \tag{2}$$

This short-hand notation is in accordance with the common notation in atmospheric turbulence theory (Raupach and Shaw, 1982), although it should be noted that the spatial averaging operator in this application does not equally weight surface areas due to the distorted image geometry (IFOV vs. distance) and so this term is not equal to the spatially averaged complete surface temperature as defined by Voogt and Oke (1997).

We define departures at a time step t from the temporal average using the prime-symbol

$$T'(t) = T(t) - \overline{T} \tag{3}$$

In analogy we suggest a dot-in-a-box symbol ($\boxdot$) to denote the deviation of a pixel at location $\mathbf{x}$ from the spatial average of a region or an entire image:

$$T^{\boxdot}(\mathbf{x}) = T(\mathbf{x}) - \langle T \rangle \tag{4}$$

The time-sequential thermography images were decomposed following two schemes; firstly according to the inner-temporal outer-spatial scheme:

$$T(\mathbf{x},t) = T'(\mathbf{x},t) + \overline{T}^{\boxdot}(\mathbf{x}) + \langle \overline{T} \rangle \tag{5}$$

The left hand side is the instantaneous temperature as measured by the thermal camera. $T'(\mathbf{x},t)$ is the temporal departure of the instantaneous temperature of a pixel from its (temporal) average temperature. We call this term *ftrend*. *ftrend* quantifies how the temperature of a pixel compares to its own long-term average temperature and is a function of both time and space. The second term, $\overline{T}^{\boxdot}(\mathbf{x})$, is the spatial departure of the temporally averaged temperature of a pixel from the entire spatiotemporal average of the time-sequence. We call this term *mpattern*. *mpattern* is a 2D image

(describing the entire run) that shows the pixel's temperature anomaly, i.e. if a pixel is on average warmer or cooler than the entire image. The last term in Eq. (5), $\langle\overline{T}\rangle$, is the spatiotemporal average of the time-sequential images, which is a single scalar that denotes the average temperature of the entire run of all pixels. We name the last term *mtotal.* All terms and their respective names are summarized in Table 2.

In analogy, we can also form an inner-spatial outer-temporal decomposition:

$$T(\mathbf{x},t) = T^{\boxdot}(\mathbf{x},t) + \langle T\rangle'(t) + \overline{\langle T\rangle} \tag{6}$$

The left hand side is again the instantaneous temperature image, similar to (5). $T^{\boxdot}(\mathbf{x},t)$ is the spatial departure of the instantaneous temperature of a pixel from the spatial average of the instantaneous image. We name this term *fpattern*. *fpattern* tells us how the temperature of a pixel compares to the temperature of spatially separated pixels at the same time. *fpattern* is also a function of time and space. The second term in Eq. (6), $\langle T\rangle'(t)$, is the temporal departure of the spatial average temperature of an instantaneous image from the spatiotemporal average of the time-sequence. We call this term *mtrend*. This is a time series with a single value per time step. It tells us if an image is generally warmer or cooler than the entire time-sequence, and hence will typically show the warming/cooling trend of the entire time sequence. As calibration is applied every 6 seconds, part of the signal in *mtrend* is expected to come from the drift of the entire microbolometer focal plane array. By subtracting *mtrend*, errors from sensor drift could be partially reduced. The last term in Eq. (6) again is the spatiotemporal average of the time-sequential images, i.e. *mtotal*. Note that by definition of an average it follows $\overline{\langle T\rangle} = \langle\overline{T}\rangle$.

Combining Eq. (5) and (6) gives:

$$T'(\mathbf{x},t) + \overline{T}^{\boxdot}(\mathbf{x}) + \langle T\rangle = T^{\boxdot}(\mathbf{x},t) + \langle T\rangle'(t) + \overline{\langle T\rangle} \tag{7}$$

As the spatiotemporal average is the same in both cases, Eq. (7) simplifies to:

$$T'(\mathbf{x},t) + \overline{T}^{\boxdot}(\mathbf{x}) = T^{\boxdot}(\mathbf{x},t) + \langle T\rangle'(t) \tag{8}$$

By combining the two averaging schemes, we can form a total fluctuating component, which is the deviation from both, the spatial and temporal average. This term will be called *ftotal*.

$$ftotal = T(\mathbf{x},t) - \overline{T}^{\boxdot}(\mathbf{x}) - \langle T\rangle'(t) - \overline{\langle T\rangle} \tag{9}$$

Based on Eq. (5) and (6), *ftotal* can be rewritten as

$$ftotal = T^{\boxdot}(\mathbf{x},t) - \overline{T}^{\boxdot}(\mathbf{x}) = T'(\mathbf{x},t) - \langle T\rangle'(t) \tag{10}$$

ftotal can be considered as the high-frequency fluctuation of a pixel from the spatiotemporal mean. It has long-term warming (or cooling) removed as it shows only the deviation from its own average

temperature. Further *ftotal* eliminates changes in temperature that affect the entire image. Hence, this term is very useful as it eliminates instrumental effects (shutter) that can affect the entire microbolometer focal plane array.

It is important to note that the scheme introduced here, and the interpretation of the terms, assumes that the FOV is much larger than the spatial scale of expected high-frequency fluctuations – in other words, the characteristic scale of the FOV must be larger than the integral turbulent length scale expected to cause fluctuations. Under those assumptions, a mean trend (warming or cooling) or instrumental effects only affect the average temperature of the image.

2.2.2 Integral statistics

From each of the decomposition terms introduced in 2.2.1, temporal and/or spatial statistical parameters can be calculated (except for *mtotal*, which is a scalar). The temporal statistics of *ftotal* are notably useful. The temporal standard deviation of *ftotal* is defined as

$$\sigma'_{ftotal}(\mathbf{x}) = \sqrt{\overline{\left(T'(\mathbf{x},t) - \langle T\rangle'(t)\right)^2}} \tag{11}$$

and results in an image that quantifies for each pixel (**x**) the integral variability of the temperature fluctuation over a given time period. Note that the prime above the sigma indicates that this is the *temporal* standard deviation of *ftotal* (as there is also an instantaneous spatial standard deviation which is not used). Similarly a temporal skewness of the temperature fluctuations can be defined:

$$Sk'_{ftotal}(\mathbf{x}) = \overline{\left(\frac{T'(\mathbf{x},t) - \langle T\rangle'(t)}{\sigma'_{ftotal}}\right)^3} \tag{12}$$

These statistics will be used to quantify the fluctuations and are correlated against thermal, material and urban form parameters. In the current study, all integral statistics (σ'_{ftotal}, Sk'_{ftotal}) were calculated for a time period of 20 min. σ'_{ftotal}, and Sk'_{ftotal} of four 20 min blocks where then averaged in each run (80 min). 20 min was considered to be short enough to exclude a significant influence by the diurnal course of differential warming and cooling of surfaces, yet long enough to include effects of turbulent exchange of larger eddies.

Similarly, statistics can be applied to a spatial field in order to quantify spatial variability. Note that the FOV of the camera does not allow an unbiased sampling and so effects of view geometry and thermal anisotropy (Voogt and Oke, 1998) will limit the practical use of the spatial statistics. The spatial standard deviation of *mpattern,* for example, is defined as

$$\sigma^{\boxdot}_{mpattern} = \sqrt{\langle \overline{T}^{\boxdot 2}(\mathbf{x})\rangle} \tag{13}$$

Note that the dot-in-a-box symbol above the sigma indicates that the term is a spatial standard deviation. And similarly for the spatial skewness of *ftotal*:

$$Sk^{\square}_{mpattern} = \left\langle \left(\frac{\overline{T}^{\square}(\mathbf{x})}{\sigma^{\square}_{mpattern}} \right)^3 \right\rangle \quad (14)$$

2.2.3 Spectral analysis

To quantify the temporal scale of fluctuations in more detail, a Fourier transform was applied to the entire 80 min of *ftotal* in each run. All pixels were transformed into temporal spectral energies in 16 different logarithmically spaced bands, using a standard fast Fourier transform, after applying a linear detrending to the time series (Stull, 1988). This resulted in images (**x**) of the spectral densities in different bands.

2.2.4 Spatial coherence

To quantify the spatial scale (spatial extent) of temperature fluctuations in the image, cross-correlations of the temperature time-series (*ftotal*) were calculated between neighboring pixels:

$$C'_{ftotal}(\mathbf{x},\mathbf{r}) = \frac{\overline{(T'(\mathbf{x},t) - \langle T\rangle'(t))\,(T'(\mathbf{x}+\mathbf{r},t) - \langle T\rangle'(t))}}{\sigma'_{ftotal}(\mathbf{x}) \quad \sigma'_{ftotal}(\mathbf{x}+\mathbf{r})} \quad (15)$$

C'ftotal will indicate if neighboring pixels, displaced by a distance **r**, experience similar fluctuations in their time series of *ftotal*. *C'ftotal* is useful to quantify any spatial coherence in fluctuations, and to assess if any observed coherence relates to surface materials, surface form and/or sensing element geometry (potential effects of calibration / shutter). Practically, for each pixel, the correlation to its neighboring pixels (displaced by **r)** was calculated for cardinal directions (left, up, right, down) and the average correlation in all 4 directions is shown. *C'ftotal* was calculated for **r** = 1, 2, 4, 8 and 16 pixels over periods of 20 min. Note that the actual distance on the ground varies between 0.5 and 2.5 m per pixel displacement due to the oblique sensor view. *C'ftotal* ranges between 1 (perfect spatial correlation) to -1 (perfect negative correlation) and 0 indicates no correlation with fluctuations of nearby pixels.

2.3 Surface classification and 3-D data

All pixels in the FOV were manually classified by visual (subjective) analysis of rectified (oblique) photos from the camera's location, with the help of the 3-D building model and aerial photos. Four overarching form-based *facet categories* were identified – (a) roofs, (b) walls, (c) ground and (d) trees. The categories were further separated based on their facet material into *material classes*. Roofs were separated into classes 'tile', 'tar', 'metal' and' 'gravel'; walls into 'brick' and 'painted' (painted stone or concrete); ground into 'road' (impermeable) and 'lawns'; and trees into

'deciduous' and 'evergreen' (Figure 1d, Table 3). Pixels were only classified if they contained the same surface material across the pixel. To avoid neighboring effects, all masks were cropped (eroded) using a 3x3 neighborhood maximum filter. For trees, crown areas were classified but not stems. Only trees that were easily identifiable in the leaves-on runs were included. 284 pixels (0.4 % of the FOV) were removed from further analysis because they contained either low-emissivity materials or A/C and heat venting systems with significant anthropogenic release. The removed areas are listed as 'excluded' in Figure 1d and are not used in any reported statistics or visualizations. 45.4% of all pixels in the FOV were classified into one of the masks. The remaining 54.6% are either pixels with mixed materials, part of the high-rise building's facade in the lower right foreground (excluded) or areas that had fine structure and were eroded by the 3 x 3 filter (in the background).

Each TST pixel is linked to the corresponding DSM via 3-D geometrical transformations used in computer graphics (Foley and van Dam, 1984), ground control points, and the interior and exterior orientation parameters of the camera. Further details are described in Meier et al. (2010b). The combination of FOV and DSM attributes a height above ground, a slope and an azimuth to each building pixel (roof or wall). Vegetation is not resolved in the DSM, so information on tree crown geometries is not available.

3. Results

We will report temperature fluctuations in relation to facet materials (subsection 3.1), to height above ground (section 3.2) and azimuth (thermal anisotropy, subsection 3.3).

3.1 Effects of surface materials

3.1.1 Mean temperatures

Spatial differences in mean temperatures are not the focus of this study, yet they are presented where essential for understanding the magnitude of temperature fluctuations. The mean temperatures of urban vegetation in the FOV are discussed in Meier et al. (2011, submitted).

The average spatiotemporal temperatures (*mtotal*) for all four runs are summarized in Table 4. *mtotal* is significantly above air temperature (at 2 m) in the daytime runs (D1 and D2), and slightly below air temperature in the nocturnal runs (N1 and N2).

The spatial temperature anomaly (*mpattern*) is shown as images in Figure 2 for all four runs. Figure 3 shows statistics of *mpattern* conditionally sampled for each of the facet materials. In the daytime runs (D1 and D2), trees, lawns and shadowed surfaces like selected walls experience the lowest

average temperatures. In contrast, roofs, sunlit walls and street surfaces show highest average temperatures - some tar and metal roofs reach more than 40 °C at an air temperature of 16.7 °C. The distribution of *mpattern* ($Sk^{\square}_{mpattern}$) in D1 and D2 is positively skewed towards higher temperatures (Table 4). The daytime median values for *mpattern* of several roof types range between +5 and +8.5 K in the leaves-off and between +6.8 and +11 K in the leaves-on run. Trees show lowest temperatures of all material classes, and are close to, yet above, air temperatures.

During the night (N1 and N2), roofs and lawns show lowest temperatures, and are typically 1 – 2.5 K below air temperature. In contrast, wall and road surfaces are warmest and 1 - 2 K above air temperature. Trees are closest to air temperature. *mpattern* in the FOV is negatively skewed ($Sk^{\square}_{mpattern}$, Table 4), indicating that there are more extreme departures form *mtotal* for cooler surfaces.

3.1.2 Integral standard deviation of temperature fluctuations

Integral standard deviation of σ'_{ftotal} is shown as images (**x**) for all runs in Figure 4 and statistics for the different facet material classes are summarized in Figure 5. In both daytime runs (D1, D2), metal roofs show the highest σ'_{ftotal} of all surface materials (Label 1 in Figure 4) and show temperature fluctuations that are nearly twice as strong as for any other observed material. Tile, tar and gravel roofs show intermediate σ'_{ftotal} (Label 2). Figure 5 illustrates for run D2 how different roof materials stratify σ'_{ftotal} into metal > gravel > tar > tile, which is not observed in D1. In both daytime runs, painted (stone and concrete) walls have lowest σ'_{ftotal} (Label 3), followed by brick walls. Fluctuations on vegetation pixels are intermediate (Label 4), and comparable to those on non-metal roofs. Figure 4 illustrates how σ'_{ftotal} of deciduous trees (in the park) changes from the leaves-off situation (D1), where mostly fluctuations on the ground (lawns) are visible, to higher fluctuations of the trees' crowns in the leaves-on situation (D2). Note that coniferous trees have not changed their relative signature compared to other materials (Figure 5, D1 and D2). In both runs, lawns show highest σ'_{ftotal} of all vegetated areas (Label 5). Special cases are roads where traffic lanes are characterized by a high σ'_{ftotal} (label 6).

At night (N1, N2), the only surfaces with noticeable elevated $\sigma'_{ftotal,}$ are lawns (Label 7) and trees in N2. Again, a clear difference between the leaves-off (N1) and leaves-on (N2) situation is evident in the park where trees in N2 are set apart from the rest of the image (Label 9). Selected roofs (metal, gravel) experience slightly higher fluctuations than the rest of the image. In Figure 4, walls are visible as areas that have a lower $\sigma'_{ftotal,}$ than the average of the image (Label 8).

Figure 6 shows time series of sample pixels representing each of the classes. Temperature fluctuations over 60 min for the runs D1 and N1 are plotted at 1 Hz and compared to air temperature at 5 min intervals. The graph clearly illustrates the fundamental differences between day (D2) and night (N2). A wide range of temperatures characterizes the daytime situation and significant fluctuations at multiple frequencies in all traces, while during night temperatures are uniform, and fluctuations show rather small-scale (high-frequency) variations only.

3.1.3 Spectral analysis of temperature fluctuations

Figure 7 summarizes spectral energies of temperature fluctuations (*ftotal*) for different bands of the Fourier transform of each pixel (**x**). The selected images range over three orders of magnitude, between periods of P = 5 seconds to about P = 500 seconds (columns). At the highest frequencies (P = 5 sec), the spectral energy of the images is rather uniform across them, exceptions being lanes on roads where vehicles move (Label 1) and paths in the park where pedestrians walk (Label 2). Note that roads are partially obscured by leaves that emerged in runs D2 and N2 and so traffic is not as easily visible as in D1 and N1. Also noticeable are border effects, i.e. pixels on building edges or between contrasting surfaces are characterized by higher energy – in particular in run D2. Runs N1 and N2 reveal a radial pattern, with lower spectral energies in the center of the image compared to the corners.

At intermediate frequencies (P = 50 sec) spectral energies of *ftotal* show significant differences between D1 and D2. In particular, foliage on trees with large leaves in D2 causes an increase in spectral energy of *ftotal* (Label 3) compared to other materials and the leaves-off situation, where only a few conifers and lawns (Label 4) stand out. A similar pattern is observed during night, with tree crowns in the center of the park showing larger spectral energies (Label 3 in N2), although overall energy in the fluctuations is lower.

At low frequencies (P = 500 sec), spectral energies reveal a more complex pattern, with gradients across objects. For example, trees in D2 show a clear difference between the south-facing and north-facing parts of crowns (Label 5). Highest fluctuations are observed for metal roofs (Label 6). During the night, fluctuations are weak, and only a few tree crowns (label 5) and lawn patches (Label 7) stand out with higher fluctuations.

Figure 8 shows ensemble spectra of temperature variations (*ftotal*) for different facet categories in 16 logarithmically spaced bands from 1 sec to 1 hr. The curves shown are median values of each category. All spectra show a relative minimum around 30 sec (50 sec at night), and a peak in the range 2 min to 10 min. Spectra stratify into different surface categories above ~30 sec, with highest fluctuations for lawns and trees. Notable is the convergence of the spectra between trees and lawns

from the leaves-off situation (D1) to the leaves-on situation (D2), where the two classes overlap. On the high-frequency end (right), all materials converge below 10 with increasing energy, the exception being roads, which stay above any other category throughout the high-frequency end at day.

3.1.4 Coherence of fluctuations

Figure 9 visualizes the spatial coherence C'_{ftotal} of all runs and Figure 10 summarizes ensemble statistics of C'_{ftotal} sorted by material class. C'_{ftotal} was calculated based on Equation 15 and quantifies how well the temperature fluctuations of a pixel correlate with its neighbors at a distance of $\mathbf{r} = 2$ pixels. Strongest spatial correlation is found on metal roofs (e.g. Label 1), followed by tar roofs. But also vegetated surfaces show a significant C'_{ftotal} that reveals the form of individual crowns and lawn patches (lawns - Label 2, deciduous tree crowns - Label 3 in Figure 9). Walls (e.g. Label 4) or roads show little cross-correlation. During the night, most surfaces are not well correlated, with the exception of clearly visible lawn patches in the park (Label 2) Similar patterns have been observed for distances of $\mathbf{r} = 1$, 4, 8 and 16 pixels (not shown).

3.2 Effects of urban form

3.2.1 Mean temperatures vs. height above ground

Figure 11 shows average temperatures and temperature fluctuations as a function of height above ground for walls and roofs. The height above ground was extracted for all pixels from the 3-D city model (Section 2.3). Only data from the leaves-off situation is shown in Figure 11 to reduce possible interference with vegetation. During the day, temperatures (*mpattern*) of walls and roofs are significantly above air temperatures and generally increase with height (Figure 11a). During the night, temperatures decrease with height. Although lower walls stay significantly warmer than air temperatures, the difference between surface and air temperature is reduced with height. Roofs are all significantly cooler than air temperatures, and their temperature generally decreases with height (Figure 11d).

As the 3-D building model does not include vegetation, Figure 12 is used to illustrate height dependence of temperature for vegetation. Figure 12 shows representative time traces of temperature fluctuations (*ftotal* + *mpattern*) for three selected pixels from a single, free-standing tree at three different heights above ground (3 m, 7 m and 14 m). This conifer (*Abies procera*) is seen entirely by the camera at an off-nadir angle of approximately 52º. The time traces illustrate that mean temperatures (*mpattern*+*mtotal*) during day are – in contrast to roofs - decreasing with height

from 22.0ºC at 3 m to 21.6ºC at 7 m and 21.1ºC at 14 m. During the day (D2), tree crowns with leaves are more than 10 K cooler than roof surfaces at approximately the same height above ground. At night, the tree crowns are approximately 2K warmer than roofs.

3.2.2 Temperature fluctuations vs. height above ground

Temperature fluctuations on walls are small. Nevertheless, during both the daytime (Figure 11b) and nighttime (Figure 11e) a small increase of σ'_{ftotal} with height can be seen. Skewness Sk'_{ftotal} increases from more negative numbers on lower walls to values close to zero in the middle and higher part of walls. Such a trend is not observed for roofs, where effects of slope are likely included. For the tree shown in Figure 12, fluctuations increase with increasing height above ground: σ'_{ftotal} = 0.26 K at 3 m, σ'_{ftotal} = 0.43 K at 7 m and σ'_{ftotal} = 0.60 K at 14 m.

3.3 Effects of thermal anisotropy

Microscale temperature patterns created by the 3-D urban surface structure, as well as by the thermal properties of urban surfaces, lead to directional variations of long-wave emittance. This directional variation is termed effective thermal anisotropy (Voogt and Oke 2003). The application of TIR remote sensors from a fixed FOV to the determination of surface temperatures is complicated by effective thermal anisotropy (Lagouarde et al. 2004). The term 'effective' is used in order to indicate that anisotropy arises because of surface structure and temperature patterns, rather than the non-Lambertian behaviour of individual facets (Voogt 2008).

Figure 13 shows the effects of the effective anisotropy on mean temperatures and fluctuations. The rectangular street grid in the FOV is aligned along 120º / 300º and 30º / 210º respectively. Most building walls and roofs have therefore an azimuth of 30º (NNE), 120º (ESE), 210º (SSW) or 300º (WNW). Walls with an azimuth towards WNW are hidden in the current FOV and not sampled by the camera (which points towards 325º). These walls are therefore not represented in Figure 13. However, the camera can tangentially see roofs with an azimuth of around 300º that have a gentle slope. This applies mostly to the foreground.

While most NNE-facing walls are slightly below air temperature in the daytime runs, walls facing ESE and SSW are 3–6 K warmer than air temperatures (Figure 13a). For roofs, NNE-facing facets are coolest and SSW-facing facets are warmest. A similar pattern is found for D2. The nighttime runs (N1, N2) do not show any directional variability of roofs, while north facing walls are about 1.5 K cooler in the evening than south facing ones (not shown). Temperature fluctuations expressed as σ'_{ftotal} do not change significantly with azimuth for walls (Figure 13b). Roofs show a clear

anisotropy in the magnitude of fluctuations, where highest fluctuations are found on SSW facing roofs and lowest on NNE facing roofs.

4 Discussions

Observed fluctuations in temperature (*ftotal*) will be discussed in the context of instrumental effects of the microbolometer array in the camera (section 4.1), effects along the line of sight (LOS) by the intervening turbulent atmosphere and moving objects (section 4.2), and the energy balance at the surface itself (sections 4.3).

4.1 Fluctuations caused by the microbolometer array

Instrumental effects that could cause the temperature signal to fluctuate are either signal noise of the microbolometer focal plane array (subsection 4.1.2), or changing temperature gradients (signal drift) across the array as the array progressively warms up or cools down (subsection 4.1.2).

4.1.1 Signal noise

The inter-pixel signal noise of the array was not determined directly, but manufacturer specifications provide estimates of 0.08 K at 30ºC (Infratec, 2005). The 1% percentile with the lowest σ'_{ftotal} in each image is twice this value, and 0.16 K, 0.16 K, 0.15 K and 0.15 K in the four runs D1, D2, N1, and N2 respectively. Although the 1% percentile with the lowest σ'_{ftotal} is not equal to the noise of the array, it can be considered as an upper limit if the pixels do not experience any other error sources and are working representatively for the array. These values correspond to approx. 40 - 50% of the average σ'_{ftotal} in the daytime runs and 70-75% of the average σ'_{ftotal} in the N1 and N2 runs. This means that random inter-pixel noise of the array is a serious, if not dominant, effect that possibly causes most of the variation leading to σ'_{ftotal}. It is therefore questionable, if 'true' fluctuations at the surface in the night runs can be resolved. Nevertheless, sensor noise should not relate to any specific surfaces in the FOV. Based on the results presented, noise dominates fluctuations in the high-frequency part ($P < 30$ sec), where ensemble-averaged spectra of all facet classes converge, and surface effects cannot be separated anymore (see Figure 8). Despite this noise, the presented images σ'_{ftotal} (Figure 4) clearly demonstrate that differences in σ'_{ftotal} between materials and facets (e.g. Figure 5) can be resolved as well as that spectra at $P > 30$ sec separate materials into different energies. We argue that this would not be observed if the noise of the array was the only process affecting σ'_{ftotal}.

4.1.2 Differential warming of the array

The effect of differential warming across the array is expected to be eliminated constantly by the internal calibration (shutter), but might add additional high-frequency noise below the frequency of the shutter. This effect might cause more variability on the corners of the array compared to its thermally more stable center. Indeed, N1 and N2 runs show a radial pattern with slightly lower σ'_{ftotal} in the center compared to the corners (Figure 4). To quantify the magnitude of this effect, a linear regression of σ'_{ftotal} vs. distance to center pixel was calculated for all pixels classified as trees. Although other effects could cause temperatures of trees to fluctuate, it can be assumed that the 'true' surface temperature of a large sample of trees should not show any dependence as a function of the distance from image center of a sufficiently large FOV. Trees have been chosen because they are spatially abundant across the FOV and their small-scale 3-D structure ensures that form and material effects (such as azimuth) are minimized, as well as sample objects (trees) are reasonably often repeated across the FOV. Linear regressions were performed for regions of increasing distances from the center (bin width of 10 pixels between 0 and 200 pixels from the center). The regressions indicate an average increase of σ'_{ftotal} by 0.047 K (N1, $r^2 = 0.86$), and 0.028 K (N2, $r^2 = 0.82$) respectively from the image center to the corners, which corresponds ~20% of the signal of σ'_{ftotal} during the night. The effect is more evident in the spectral analysis (Figure 7, N1 and N2) where the radial effect is clearly seen at a period of 5 seconds (the shutter equalizes fluctuations > 30 sec). During the daytime, this effect is not directly visible and derived regressions are not significant. Stronger thermal anisotropy effects likely superimpose the signal (south vs. north side of trees on opposite sides of image). Based on the nighttime quantification, the effect of differential warming in the daytime runs is estimated to be not more than 10% of the (higher) signal of σ'_{ftotal}.
Patterns in the cross-correlation functions C_{ftotal} that relate to the image geometry could be a further indicator of fluctuations caused preferably in certain regions of the image (e.g. corners). Although interesting patterns are revealed by C_{ftotal} (section 3.1.4 and Figure 9), none of the patterns show a dependence on distance from image center or in any specific direction across the array. Hence it must be assumed that part of the fluctuations originate from processes either along the line of sight or at the surface.

4.2 Effects along the line of sight (LOS)

4.2.1 Absorption in a turbulent atmosphere

To estimate the effect of air temperature and humidity fluctuations along the LOS, an atmospheric radiative transfer model (MODTRAN 5.2, Berk et al .2005) was combined with the sensor's known

spectral sensitivity (see Meier et al., 2010b for details). Using measured standard deviations of temperature and humidity fluctuations (see section 2.1.3 and Table 2), an upper limit of the effect of a turbulent atmosphere was estimated as follows: The maximal error is considered as the difference between modeled atmospheric absorption for two temperatures that were offset by σ_{air} at absolute air temperature T_{air}. The estimated effect of air temperature fluctuations along the median path length of 234 m is 0.018 K for N1 and 0.012 K for N2. During day, due to a strongly convective atmosphere, stronger fluctuations of T_{air} are observed that cause maximum fluctuations of 0.068 K and 0.073 K for D1 and D2, respectively. This corresponds in all cases to less than 10% of the measured signal of σ'_{ftotal}. Note that the calculation assumes that air temperatures will change instantaneously along the entire line-of-sight as expressed by σ_{air}. However, realistically temperature variations (eddies) will cause the spatially integrated value of σ_{air} along the LOS to be much smaller than the single-point measurement of σ_{air}. Similarly, the effect of humidity fluctuations was estimated as the difference between modeled atmospheric absorption for the same temperature, but different absolute humidity (offset by $\sigma_{\rho v}$, see Table 2) at the measured absolute humidity ρ_v. Effects of humidity fluctuations along the path are in all cases are < 3% of measured σ'_{ftotal}.

4.2.2 Moving objects

The approach presented in this study assumes that all objects in the FOV are fixed and not moving. However, in an urban environment cars and pedestrians (which are usually warmer) trace temperature signals that are either directly resolved or cause sub-pixel variation. Higher order moments, and the spectral analysis at high-frequencies (Figure 7 at P = 5 sec) indeed indicate extreme values along road lanes that are attributable to moving traffic. In addition, ensemble spectra of road surface temperatures are higher in the range of 1 – 30 sec compared to any other surfaces (Figure 8).

Further, wind could cause flexible objects to move, an effect which is most likely restricted to trees. A displacement, even in the sub-pixel scale, would change the signal emitted from pixels and can also alter the geometry of surface objects. Tree movement was not monitored, but studies indicate that at the observed wind speed of ~ 2.5 m/s, the unimodal swaying of typical coniferous trees is less than 1 m at 15 m height (Schindler et al. 2010).

4.2.3 Swaying of camera platform

Finally, the camera itself (mounted on a 3m boom) or the entire high-rise building might sway relative to the ground. This would lead pixels that are on strong mean gradients (such as edges) to

show higher σ'_{ftotal} due to contamination by neighboring pixels. Evidence for this effect is observed in Figure 4 (D2) and Figure 7 (D2, and N1, most clearly visible at 5 sec). To quantify this error, an edge detection filter was applied to calculate the spatial standard deviation of *mpattern* in a 3 x 3 neighborhood (σ_{3x3}), which is an indication of the sharpness of nearby 'edges'. σ_{3x3} was then compared to the temporal σ'_{ftotal} on a pixel-by-pixel basis. For the entire image, there is positive relationship between σ_{3x3} and σ'_{ftotal} with slopes of 0.008 K K^{-1} (r^2 = 0.01) in D1, 0.044 K K^{-1} (r^2 = 0.32) in D2, 0.025 K K^{-1} (r^2 = 0.07) in N1, and 0.009 K K^{-1} (r^2 = 0.03) in N2. These relationships are estimated to explain 2.6% of σ'_{ftotal} in D1, 6.4% in D2, 9.0% in N1, and 1.6% in N2. This matches the visual interpretation of the images, where runs D2 and N1 are more affected by this error. While wind speed was similar during the two daytime and the two nighttime runs, wind direction was changing from along the boom (view direction, 325º in D1 and N2) to perpendicular in N1 and N2 (Table 1). A perpendicular wind is expected to cause more lateral swaying of the boom and/or building and hence more displacement. If the same procedure is applied only to the masked areas that are at least 1 pixel away from any facet edge, the explained error is reduced to 1.2% (D1), 4.5% (D2), 4.7% (N1) and 0.7% (N2) of σ'_{ftotal} because sharp edges are excluded.

4.3 Effects of the surface energy balance

Although all the effects discussed above can explain a significant part of the observed total variation of σ'_{ftotal}, none of the effects can explain the *differences* observed *between material classes* or the observed relations with height and azimuth of the urban form. Those differences must be an effect of the surface energy balance of the corresponding facets. It was hypothesized that net all-wave radiation, Q^*, boundary-layer and aerodynamic resistances (r_b and r_a), subsurface heat storage (expressed as thermal admittance), as well as potentially water availability, control the magnitude and spectral characteristics of both the mean temperature and the temperature fluctuations of a facet.

4.3.1 Radiation and shadowing

In runs D1 and D2, surfaces situated higher above the ground received more direct short-wave radiation for a longer period over the morning which explains that the spatial temperature anomaly (*mpattern*) is significantly above air temperature for roofs and higher walls (Figure 11a). In contrast, lower surfaces are more likely in shadow and are below or at air temperature. During the night, the influence of a reduced sky-view factor on the long-wave radiation exchange is suitable to explain higher temperatures of lower walls compared to higher walls (Figure 11d). Notable are extraordinarily warm walls in narrow courtyards (foreground in Figure 2, N1 and N2) and walls in

the denser part of the city (Figure 2, upper right). As urban form does not change over 20 min, sky-view factor and solar access can explain mean temperatures and warming/cooling rates, but not fluctuations.

In the daytime runs, moving shadows, however, can create temperature fluctuations on a range of scales. The thermal effect of shadows and accompanied reduced or increased solar irradiance is not a strictly high-frequency phenomenon. Depending on the duration of shadowing, the scale of the object causing shadows, and the change in short-wave radiation, the persistence of shadow effects varies from several minutes to hours (Meier et al., 2010a). Shadows reduce the difference between surface and air temperatures, hence it is expected that shadowed parts of the FOV show lower fluctuations due to turbulent exchange. This is illustrated in Figure 13, where north facing roofs and walls have lower mean temperatures and also less temperature fluctuations σ'_{ftotal}.

4.3.2 Reflectivity

Most materials studied have emissivities < 1.0 and part of the signal in the apparent surface temperature might be caused by reflection of fluctuating radiance from nearby objects or the sky. As large fluctuations of the long-wave emittance (originating from nearby objects, the sky or the long-wave part of the direct solar irradiance) are not expected, an error from reflection is likely small. The only exception could be a non-Lambertian behavior of a surface (e.g. metal roof) in combination with a changing solar position over 20 min. Evidence for this effect however, was not found in the current dataset.

4.3.3 Turbulent heat transfer

Figure 14 plots fluctuations (σ'_{ftotal}) against mean temperature (*mpattern*) for five overarching categories (roofs, walls, roads, lawns, trees). For D1 and D2 clear positive relationships between mean temperature and fluctuations develop - the warmer a surface (the higher the difference to air temperature) the higher are the observed temperature fluctuations (σ'_{ftotal}). Temperatures of surfaces that are significantly warmer than air temperature are more affected by turbulent exchange. If cooler air from the atmosphere is mixed towards the surface, it will cause stronger fluctuations at the surface, and part of the sensible heat is transferred into the air, which cools the surface. Interestingly, the different categories in Figure 14 show varying slopes (vegetation shows a steeper slope, roofs intermediate, walls do not show a clear relation). This could suggest that material properties such as thermal admittance, but also water availability, and potentially form factors (laminar boundary layer thickness) may play an important role (see section 4.3.4). The role of water availability is evident in the temperatures of vegetated surfaces that transpire, which are on average

(D1) and (D2) lower than roofs (Figure 3). This is in agreement with Leuzinger et al. (2010) who found in an urban environment at similar latitude daytime differences in temperatures of ~20K between roofs and trees. Observed fluctuations change most dramatically with increasing difference to air temperature for trees and lawns compared to artificial materials that have no Q_E during D1 and D2. The separation in Figure 14 can in part be attributed to the fact that not only sensible heat flux, but also latent heat flux causes fluctuations at high frequencies (note the significant vapor pressure deficit in the runs, Table 1).

Over rough surfaces, turbulent exchange is intermittent. This means that a few events (e.g. cool, dry and downward moving eddies) that occur in a short time are responsible for the majority of the sensible heat flux during day. If intermittency is observed, the facet's temperature will experience a negative skewness ($Sk'_{ftotal} < 0$), because negative temperature departures caused by cool (downward moving) eddies are infrequent. The opposite would be expected for surfaces that are below air temperature (i.e. positive Sk'_{ftotal}) because positive temperature departures are driving the exchange, but are infrequent. This pattern of skewness is expected because air is thermally better mixed than surfaces, and the range of observed surface temperatures of the urban surface is much larger than the range in air temperature. Figure 15 illustrates Sk'_{ftotal} as a function of mean temperature (*mpattern*) and in relation to air temperature. In daytime runs (D1, D2), most materials (lawns and roofs, to some extent also trees) do indeed show decreasing (i.e. more negative) skewness with increasing departure from air temperature. Walls do not show a clear trend of Sk'_{ftotal} with temperature. Roads show a positive Sk'_{ftotal}, likely due to contamination by 'warm' moving vehicles (see section 4.2.2). During the night, in particular tree and lawn surfaces show positive Sk'_{ftotal} when below air temperature, and negative Sk'_{ftotal} when above. Another notable detail is the height dependence of the skewness of wall temperature fluctuations - walls below 10 m show a more negative Sk'_{ftotal} compared to walls that are higher and where $Sk'_{ftotal} \approx 0$. This implies that fewer turbulent eddies mix down to the base of the urban canopy and cool the walls (both day and night). This is in agreement with profile measurements of turbulent exchange that show downward directed exchange dominates sensible heat exchange in the lower canopy (Christen et al., 2007). Interestingly, nocturnal roofs do not show the postulated increase of skewness with decreasing temperature, yet are generally characterized by a slightly positive Sk'_{ftotal} as expected. It is likely that the less fluctuating wind at roof level creates a regime of efficient mixing that exchanges energy more constantly with the atmosphere.

4.3.4 Thermal admittance

Why are the slopes of σ'_{ftotal} vs. mean temperature (*mpattern*) in Figure 14 not similar for different categories? This could be explained by subsurface heat conduction, namely the different thermal admittance of surface materials. A facet with a high thermal admittance (e.g. walls or roads) 'absorbs' any heat flux caused/enabled by turbulent exchange quickly and efficiently, and as a consequence surface temperatures, do not change dramatically. Facets with a low thermal admittance (e.g. leaves, porous lawn canopies) however, respond to a change in turbulent sensible heat flux with a significant surface temperature change (or latent heat flux).

Figure 16 shows the relationship between thermal admittance μ and spectral energy at P = 73 sec, the range where spectra start to significantly diverge between materials (Figure 8). Values for thermal admittance are taken from the literature describing the thermal properties of building materials (Oke, 1981; Spronken-Smith and Oke, 1999, Berge et al., 2009) and of vegetation (Byrne and Davis, 1980; Jones, 1992; Jayalakshmy and Philip, 2009). Where several estimates exist in these sources, the horizontal error bars in Figure 16 indicate the range of values reported. A relationship between temperature fluctuations and thermal admittance is evident in the two graphs (D1 and D2), resulting in higher fluctuations on materials with lower thermal-admittance - although the level of fluctuations is different (which is also influenced by radiative and turbulent exchange).

4.3.5 Spatial scale of turbulent exchange fluctuations

The spatial coherence of fluctuations expressed by C'_{ftotal} (Figure 9 and 10) indicates that the spatial scale of fluctuations is more evident on surfaces that experience significant fluctuations. It is likely that there is a relatively constant sensor noise across the microbolometer array on which the energy balance effects (as other error sources) are superimposed. Therefore it is not surprising that for pixels where (uncorrelated) sensor noise is dominant, and actual fluctuations expected from the energy balance are small (high thermal admittance materials), C'_{ftotal} is close to zero. However, if fluctuations are dominantly caused by the surface energy balance, then C'_{ftotal} is expected to be higher (closer to 1) as turbulent eddies exist on a range of scales, and some will affect neighboring pixels at the same time. It is clear that the spatial and temporal resolution of the system limits the information that can be extracted on the scales explicitly resolved, and temperature fluctuations caused by small eddies (less than ~1 m) will not be resolved. Nevertheless it is surprising to see how clearly the different surfaces separate in C'_{ftotal} . In particular the lawn surfaces, with an excellent response due to their lower thermal admittance, show spatially coherent patterns, suggesting that large coherent eddies (30 sec to several minutes) control most of the exchange of

heat over a rough surface as reported from traditional fast anemometry (e.g. Roth and Oke, 1993; Feigenwinter and Vogt, 2005, Christen et al., 2007).

5. Conclusions

This contribution presents an approach to separate a time-sequential thermography (TST) dataset into mean and fluctuating signals. The proposed decomposition scheme was applied to surface temperatures from four TST datasets over 80 min. The chosen FOV was an urban surface composed of many different facets (roofs, walls, trees, lawns, roads). Facets in the FOV experienced fluctuations in surface temperature that related to surface materials and form. The observed relationships can be summarized as follows:

- Surfaces that experience strongest surface temperature fluctuation are significantly warmer (cooler) than air temperature. Surfaces that are closer to air temperature show less fluctuation (see Figure 14).
- With increasing temperature of a surface above air temperature, fluctuations show a stronger negative skewness. There is also some evidence for the opposite case, where surfaces with surface temperature below air temperature show a more positive skewness. This is explained by large turbulent eddies that cause sensible heat to be exchanged between a more uniformly mixed atmosphere and a thermally patchy surface.
- Surface materials with lower thermal admittance (lawns, vegetation) show higher fluctuations in surface temperature than surfaces with high thermal admittance (walls, roads) (see Figure 16). Leaf emergence of deciduous trees between runs shows a measurable impact on high-frequency thermal behavior. The emerged leaves cause surface temperatures to fluctuate more compared to a leaves-off situation.
- The spatial coherence of fluctuations suggests the relevant scale of atmospheric turbulence might be significantly larger than the geometric resolution of the image (0.5 to 2.5 m).

It has been shown that a significant part of the fluctuations in apparent surface temperatures are caused by sensor noise, sensor calibration effects, and other complicating factors (changes in atmospheric transmission, small lateral movements of the camera due to wind, moving objects). Nevertheless, the key findings let us conclude that the effect of turbulent exchange of sensible heat

between different urban facets and the atmosphere on the surface temperature signal can be measured in the time-traces of most materials.

Clearly, there are spatial and temporal constraints that limit the study to processes inside the spatiotemporal scale the field observation was designed for. The smallest fluctuations observable with the current geometric resolution were 0.5 m (in the foreground). However, more recent work (Christen and Voogt, 2010) has demonstrated that significant temperature fluctuations can happen at much smaller scales (10 cm). An upper spatial limit is the scale of the entire FOV. The effect of large-scale boundary layer eddies that could change surface temperatures of the entire image are filtered by the decomposition scheme and are not visible either.

Further, the temporal scale of resolved fluctuations is limited. Although the nominal operation frequency was 1 Hz, spectral analysis indicates that highest frequencies are significantly contaminated by sensor noise. In this range, the temperature resolution of the sensor and sensor effects formed a severe limitation. In particular in the nocturnal runs, where the thermal structure of the atmosphere and the absent short-wave irradiance are expected to cause smaller surface temperature fluctuations, a separation of sensor effects from energy balance effects is impossible for most surfaces – except metal roofs and lawns.

Nevertheless, the current study underlines the potential of using high-frequency thermal remote sensing in energy balance and turbulence studies at complex land-atmosphere interfaces. Using high sampling frequencies in TST observations allows for the extraction of information on the dynamic response of the surface energy balance to atmospheric turbulence, thermal admittance of surface materials and/or potentially visualizes turbulent motions. This is possible in complex canopies such as urban environments where a direct measurement of fluxes and/or turbulent exchange in a spatial context is otherwise not possible, yet information on turbulent exchange is in demand for applications in dispersion modeling, air pollution and weather forecasts, as well as climate-sensitive urban design.

Acknowledgements

The infrastructure and the experimental part of this study were funded through "Energy eXchange and Climates of Urban Structures and Environments (EXCUSE)" supported by the Technical University of Berlin (Scherer). Part of the data analysis and computing infrastructure was supported by NSERC Discovery Grant #342029-07 (Christen).

References

Ballard J.R., Smith, J.A., Koenig G.G., 2004. Towards a high temporal frequency grass canopy thermal IR model for background signatures. *Proceedings SPIE.* 5431, 251 -259.

Berge B., Butters C, Henley F., 2009. The Ecology of Building Materials. 2nd Edition. Architectural Press, 427 pp.

Berk, A., Anderson, G. P., Acharya, P. K., Bernstein, L. S., Muratov, L., Lee, J., Fox, M. J., Adler-Golden, S. M., Chetwynd, J. H., Hoke, M. L., Lockwood, R. B., Cooley, T. W. & Gardner, J. A. (2005). MODTRAN5: a reformulated atmospheric band model with auxiliary species and practical multiple scattering options. *Proceedings SPIE*. 5655, 88-95.

Byrne G. F., Davis J. R., 1980. Thermal Inertia, thermal admittance and the effect of layers. *Remote Sensing of Environment*. 9, 295-300.

Chazdon R.L., 1988. Sunflecks and their importance to forest understorey plants. *Advances in Ecological Research*. 18, 1-63.

Christen A., van Gorsel E., Vogt R. 2007. Coherent structures in urban roughness sublayer turbulence. *Int. J. Climatol.* 27, 1955-1968.

Christen A., Voogt J. A. 2010. Inferring turbulent exchange processes in an urban street canyon from high-frequency thermography. Recorded presentation of the 19th Symposium on Boundary Layers and Turbulence, August 2 - 6, Keystone CO, USA.

Chudnovsky, A., Ben-Dor, E., Saaroni, H, 2004. Diurnal thermal behavior of selected urban objects using remote sensing measurements. *Energy and Buildings*. 36, 1063–1074.

Feigenwinter C., Vogt R., 2005. Detection and analysis of coherent structures in urban turbulence. *Theor. Appl. Climatol.* 81, 219–230.

Foley, J. D. and van Dam, A., 1984. Fundamentals of interactive computer graphics, in: The Systems Programming Series, 1 edition, Addison-Wesley Publishing Company, Reading.

Garai, A., Kleissl, J., Smith, S. G. L., 2010. Estimation of biomass heat storage using thermal infrared imagery: application to a walnut orchard. *Boundary Layer Meteorology*. 137, 333-342.

Kolbe, T. H., 2009. Representing and Exchanging 3-D City Models with CityGML. In: Lee, J. & Zlatanova, S. (Ed.). Lecture Notes in Geoinformation and Cartography, Springer Berlin Heidelberg, pp. 15-31.

Hoyano, A., Asano, K., Kanamaru, T., 1999. Analysis of the sensible heat flux from the exterior surface of buildings using time sequential thermography. *Atmospheric Environment*. 33, 3941-3951.

Infratec 2005. Operating instruction for VarioCAM® head. InfraTec GmbH, Gostritzer Straße 61-63, 01217 Dresden, Germany.

Jayalakshmy M. S., Philip J., 2010. Thermophysical properties of plant leaves and their influence on the environment temperature. *International Journal of Thermophysics.* 31, 2295–2304.

Jones H. G., 1992. Plants and microclimate – A quantitative approach to environmental plant physiology. 2nd ed., Cambridge University Press. Cambridge UK., 428 pp.

Jones, H. G., 1999. Use of thermography for quantitative studies of spatial and temporal variation of stomatal conductance over leaf surfaces. *Plant Cell and Environment*. 22, 1043-1055.

Lagouarde, J. P., Moreau, P., Irvine, M., Bonnefond, J. M., Voogt, J. A., Solliec, F., 2004. Airborne experimental measurements of the angular variations in surface temperature over urban areas: Case study of Marseille (France). *Remote Sensing of Environment*. 93, 443–462.

Leuzinger S., Körner C., 2007. Tree species diversity affects canopy leaf temperatures in a mature temperate forest. *Agricultural and Forest Meteorology*. 146, 29-37.

Leuzinger S., Vogt R., Körner C. 2010. Tree surface temperature in an urban environment. *Agricultural and Forest Meteorology.* 150, 56-62.

Meier F., Scherer D., Richters J., 2010a. Determination of persistence effects in spatio-temporal patterns of upward long-wave radiation flux density from an urban courtyard by means of Time-Sequential Thermography. *Remote Sensing of Environment*. 114, 21-34.

Meier F., Scherer D., Richters J., Christen A., 2010b. Atmospheric correction of thermal-infrared imagery of the 3-D urban environment acquired in oblique viewing geometry. *Atmos. Meas. Tech. Discuss.* 3, 5671-5703. doi:10.5194/amtd-3-5671-2010 (under review for *Atmos. Meas. Tech.*).

Meier F., Scherer D., 2011. Spatial and temporal variability of urban tree canopy temperature during summer 2010 in Berlin, Germany. (in preparation).

Monteith J. L., Unsworth M. H. 2008. Principleas of environmental physics. 3rd ed. Academic Press. 418 pp.

Oke T. R., 1981. Canyon geometry and the nocturnal heat island: comparison of scale model and field observations. *J. Climatol.* 1, 237-254.

Paw-U K.T., Brunet, Y., Collineau, S., Shaw, R.H., Maitani, T.; Qiu, J., Hipps, L. 1992. On coherent structures in turbulence above and within agricultural plant canopies. *Agricultural and Forest Meteorology*. 61, 55-68.

Raupach M.R. and Shaw R.H., 1982. Averaging procedures for flow within vegetation canopies. *Boundary-Layer Meteorology*. 22, 79-90.

Roth M., Oke T. R., 1993a. Turbulent transfer relationships over an urban surface. I. Spectral characteristics. *Q J Roy Meteorol Soc.* 119, 1071–1104.

Schindler D., Vogt R., Fugmann H., Rodriguez M., Schonborn J. and Mayer H. 2010. Vibration behavior of plantation-grown Scots pine trees in response to wind excitation. Agricultural and Forest Meteorology. 150, 984-993.

Shimoda S., Oikawa T., 2008. Characteristics of canopy evapotranspiration from a small heterogeneous grassland using thermal imaging. *Environmental and Experimental Botany*. 63, 102-112.

Spronken-Smith R. A., Oke T. R., 1999. Scale Modelling of Nocturnal Cooling in Urban Parks. *Boundary-Layer Meteorology*. 93, 287-312.

Stull R. B. 1988. An introduction to boundary layer meteorology. Kluwer Academic Publishers, Dordrecht. 670 pp.

Sugawara, H., Takamura, T., 2006. Longwave radiation flux from an urban canopy: Evaluation via measurements of directional radiometric temperature. *Remote Sensing of Environment*. 104, 226–237.

Voogt, J. A., 2008. Assessment of an urban sensor view model for thermal anisotropy. *Remote Sensing of Environment*. 112, 482–495.

Voogt, J.A., Oke T. R., 1997. Complete urban surface temperatures. *Journal of Applied Meteorology*, 36, 1117-1132.

Voogt, J. A., Oke, T. R., 1998. Effects of urban surface geometry on remotely-sensed surface temperature. *International Journal of Remote Sensing*. 19, 895–920.

Voogt J.A., Oke, T.R., 2003. Thermal remote sensing of urban climates. *Remote Sensing of Environment*. 86, 370-384.

Table 1: Weather conditions during the four runs. Standard deviations of air temperature and humidity are based on 10Hz measurements averaged over 10 minutes.

			Day		**Night**	
Run			**D1**	**D2**	**N1**	**N2**
			Leaves-off	Leaves-on	Leaves-off	Leaves-on
Date			2009-04-07	2009-04-20	2009-04-06	2009-04-20
Time		CET	11:00-12:20	11:48-13:08	20:37-21:57	21:00-22:20
Short-wave incoming	80 min average	W m^{-2}	634	780	0	0
	Preceeding 24h total	MJ m^{-2} day^{-1}	19.5	25.8	22.2	25.8
Long-wave incoming	80 min average	W m^{-2}	317	286	292	269
	Preceeding 24h total	MJ m^{-2} day^{-1}	25.6	23.2	24.4	23.4
Wind	23 m	m s^{-1}	2.6	2.3	2.3	2.4
	125 m	m s^{-1}	1.6	1.8	2.9	2.9
Wind direction	23 m	º from N	125	66	96	39
Air temperature	2 m	ºC	20.4	16.7	12.5	11.8
	125 m	ºC	18.8	16.3	13.1	12.4
Std. Dev.	*125 m*	*K*	*0.63*	*1.12*	*0.19*	*0.15*
Relative humidity	2 m	%	49.8	36.7	60.1	52.6
	125 m	%	47.5	24.5	57.2	41.8
Std. Dev.	*125m*	*g m^{-3}*	*0.0063*	*0.0061*	*0.0047*	*0.0043*

Table 2: Summary of terms used in the decomposition scheme.

Term	Name	Dimensions	Description
$\langle\overline{T}\rangle = \overline{\langle T\rangle}$	*mtotal*	Scalar	Spatial-temporal average of the time-sequence.
$\overline{T}^{\boxdot}(\mathbf{x})$	*mpattern*	2D array	Spatial anomaly of the average temperature of a pixel from the spatial-temporal average of the time-sequence.
$\langle T\rangle'(t)$	*mtrend*	1D array	Temporal departure of the average temperature of an instantaneous image from the spatial-temporal average of the time-sequence.
$T^{\boxdot}(\mathbf{x},t)$	*fpattern*	3D array	Spatial departure of the instantaneous temperature of a pixel from the average temperature of the the instantaneous image.
$T'(\mathbf{x},t)$	*ftrend*	3D array	Temporal anomaly of the instantaneous temperature of a pixel from the average temperature of that pixel.
$T^{\boxdot}(\mathbf{x},t) - \overline{T}^{\boxdot}(\mathbf{x})$ $T'(\mathbf{x},t) - \langle T\rangle'(t)(\mathbf{x})$	3D array	*ftotal*	Spatio-temporal departure of a pixel from both, the spatial and temporal mean.

Table 3: Manual classification of surfaces in the field of view.

Surface	n (pixels)	% of FOV	No. of contiguous areas	Median slope
Roof-Tile	4955	6.5%	45	34
Roof-Gravel	1535	2.0%	15	0
Roof-Tar	1806	2.4%	16	30
Roof-Metal	1776	2.3%	2	11
Wall-Painted	4304	5.6%	37	90
Wall-Brick	2664	3.5%	23	90
Ground-Roads	1675	2.2%	21	1
Ground-Grass	1406	1.8%	10	2
Trees-Deciduous	12662	16.5%	33	
Trees-Coniferous	1797	2.3%	13	
Excluded	284	0.4%	4	
Unclassified	41936	54.6%		

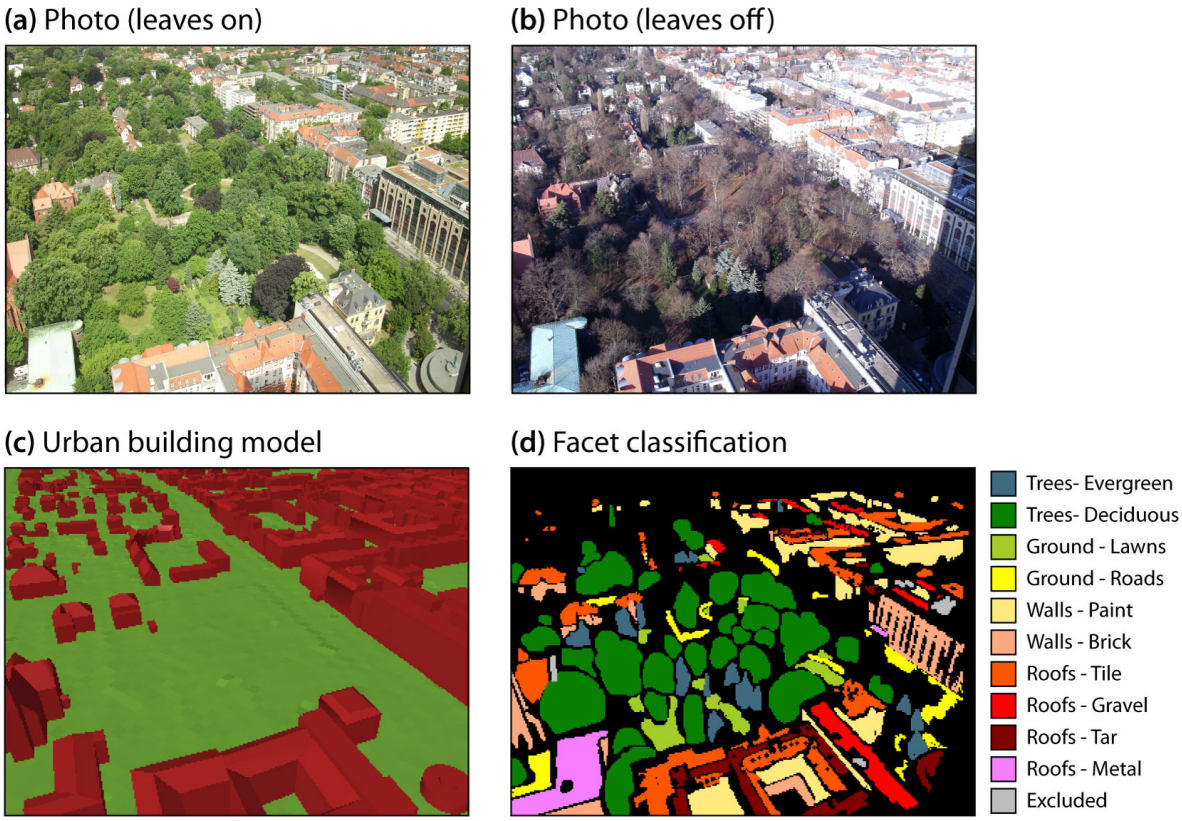

Figure 1: Field of view of thermal camera for (a) leaves on, (b) leaves off, (c) digital building model and (d) surface classification.

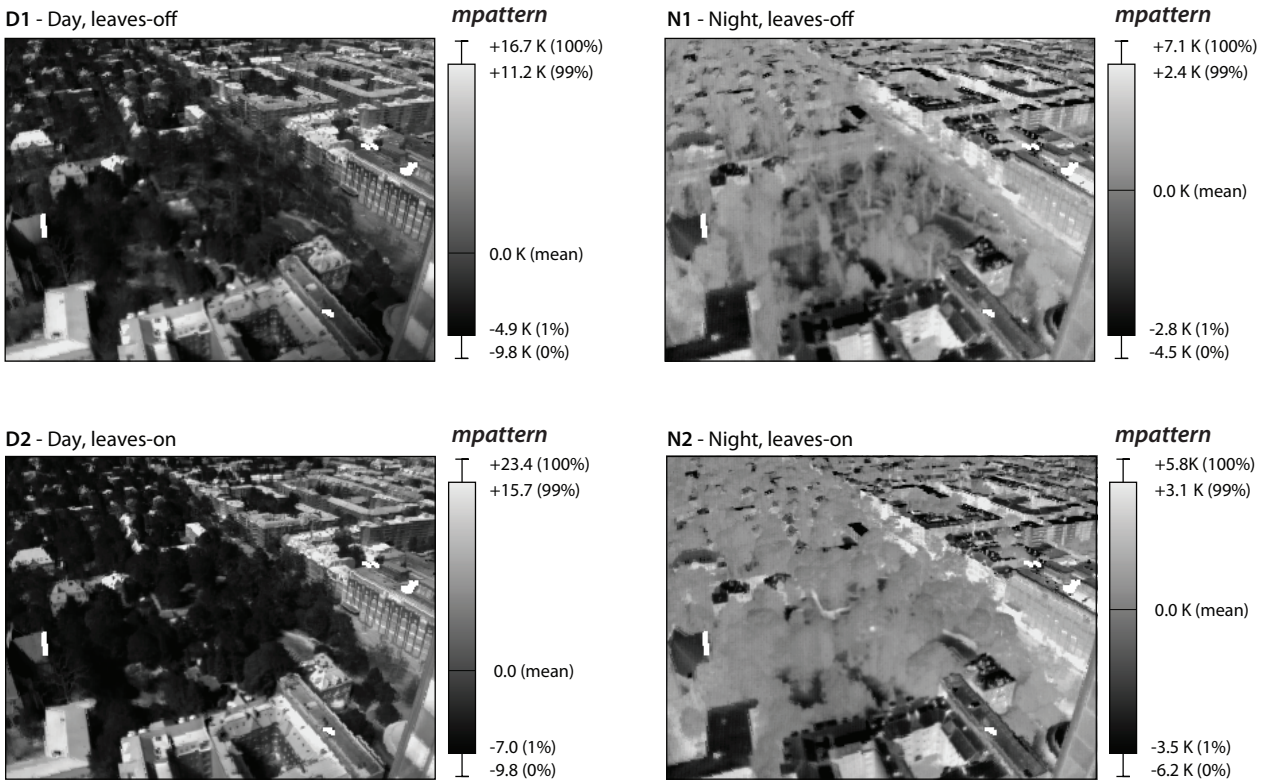

Figure 2: Spatial temperature anomaly (mpattern) of all four runs. The visualization uses a linear grey scale between the 1 and 99th percentile in each image. Pixels drawn in white have been excluded from analysis.

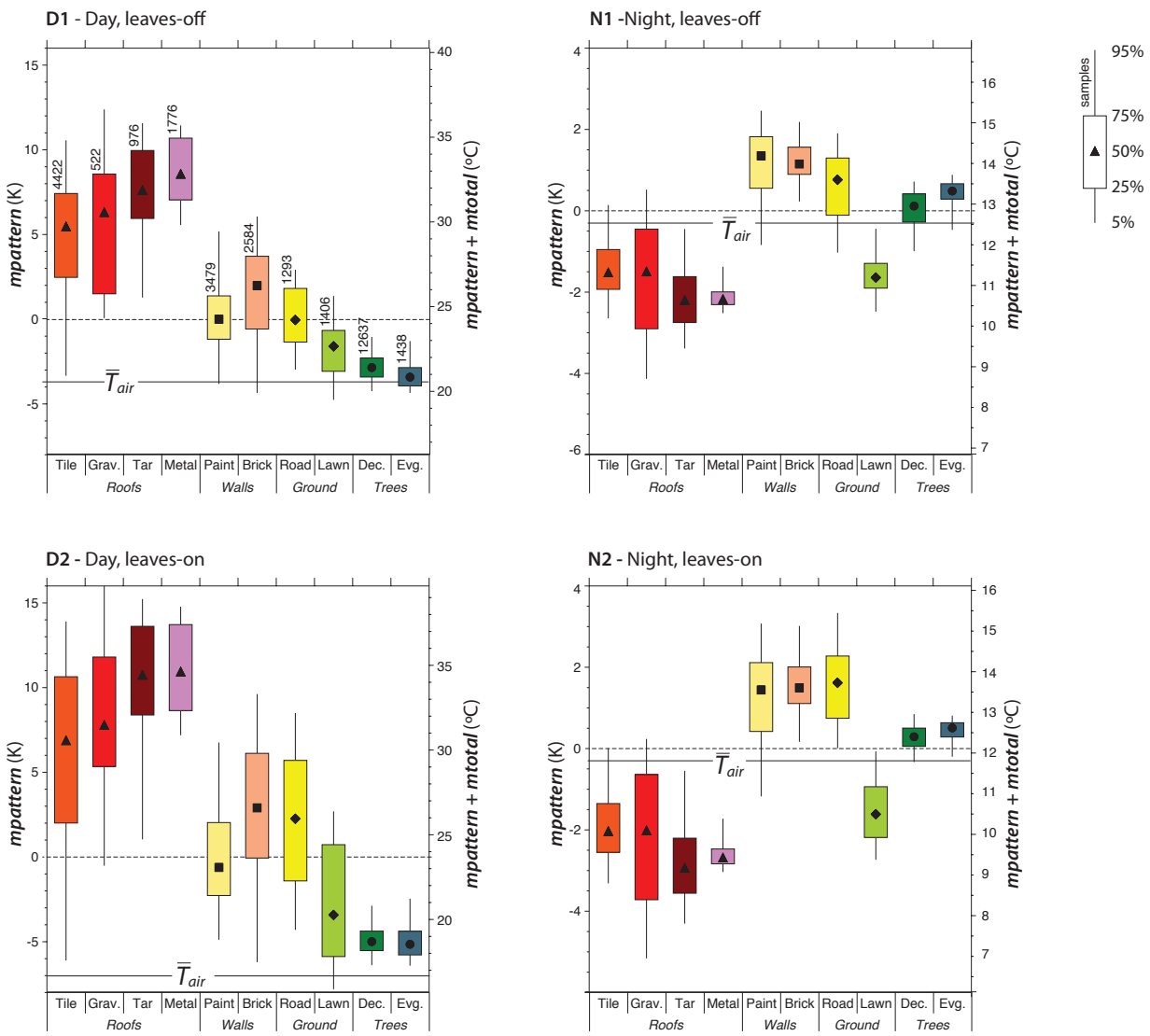

Figure 3: Ensemble averages of spatial temperature anomaly (mpattern) sorted by facet materials in all four runs. The numbers in the upper left graph indicate the number of pixels included in each class and are the same for all four runs.

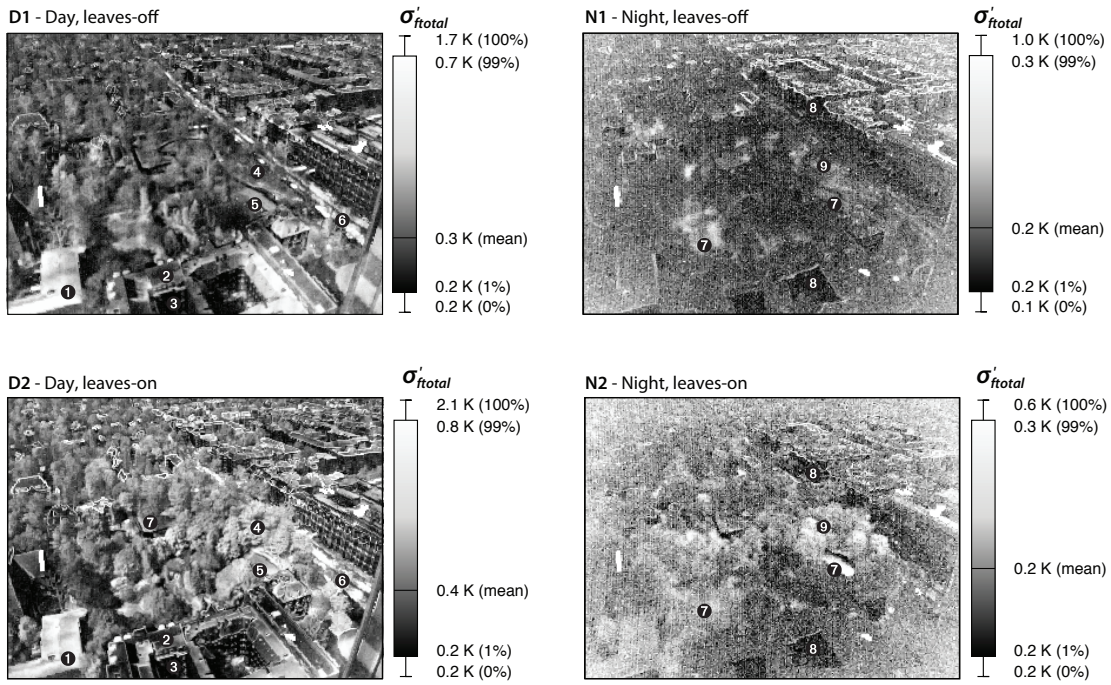

Figure 4: Average standard deviation of temperature fluctuations (σ'ftotal) over 20 min visualized for all four runs. The visualization uses a non-linear grey scale between the 1 and 99th percentile in each image. Pixels drawn in white have been excluded from analysis. For labels 1 to 9 see text.

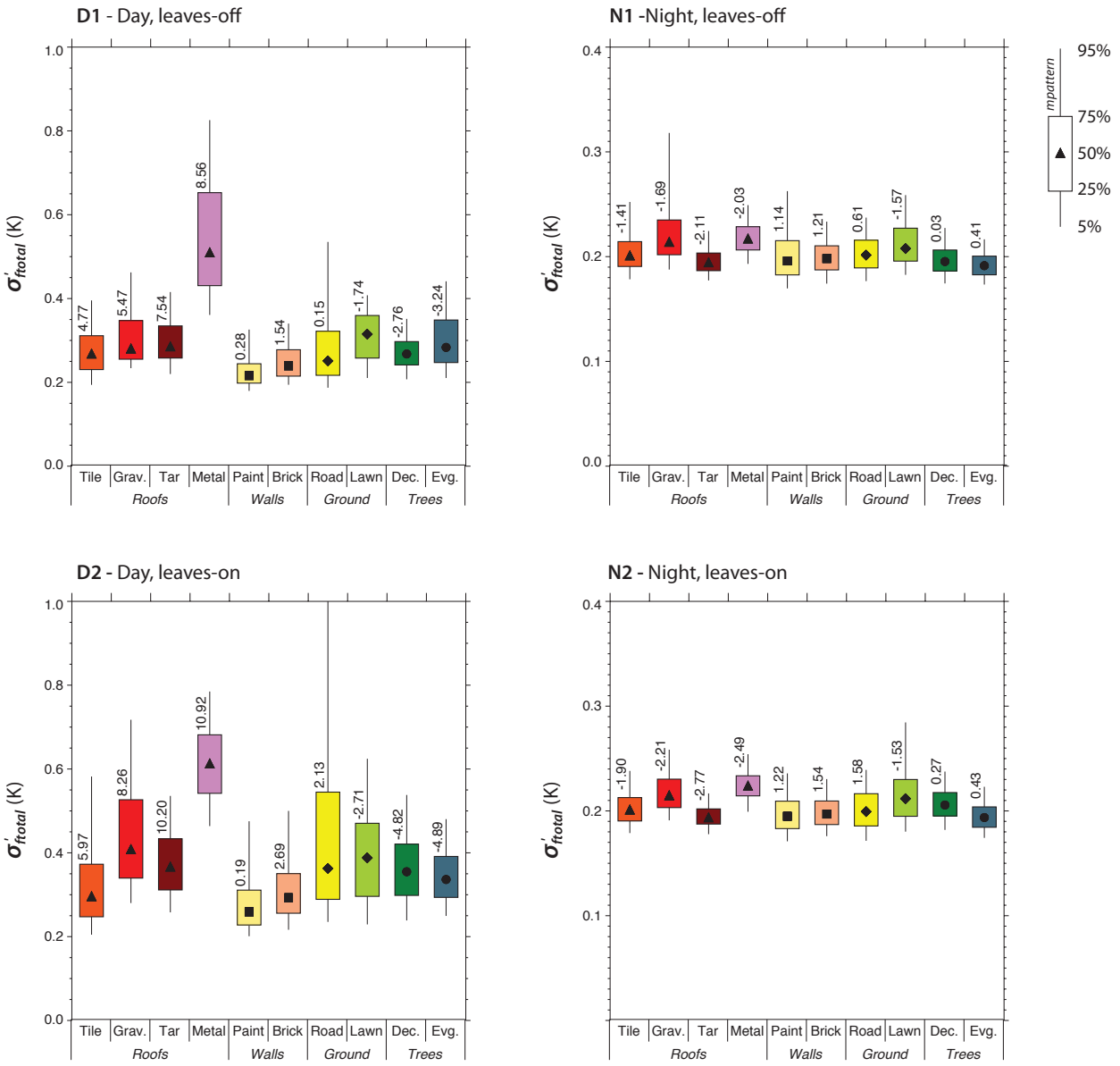

Figure 5: Ensemble averages of the standard deviation of temperature fluctuations (σ'ftotal) sorted by facet materials in all four runs. The numbers in the upper left graph correspond to the median mtotal of each class. The numbers of samples are similar to Figure 3.

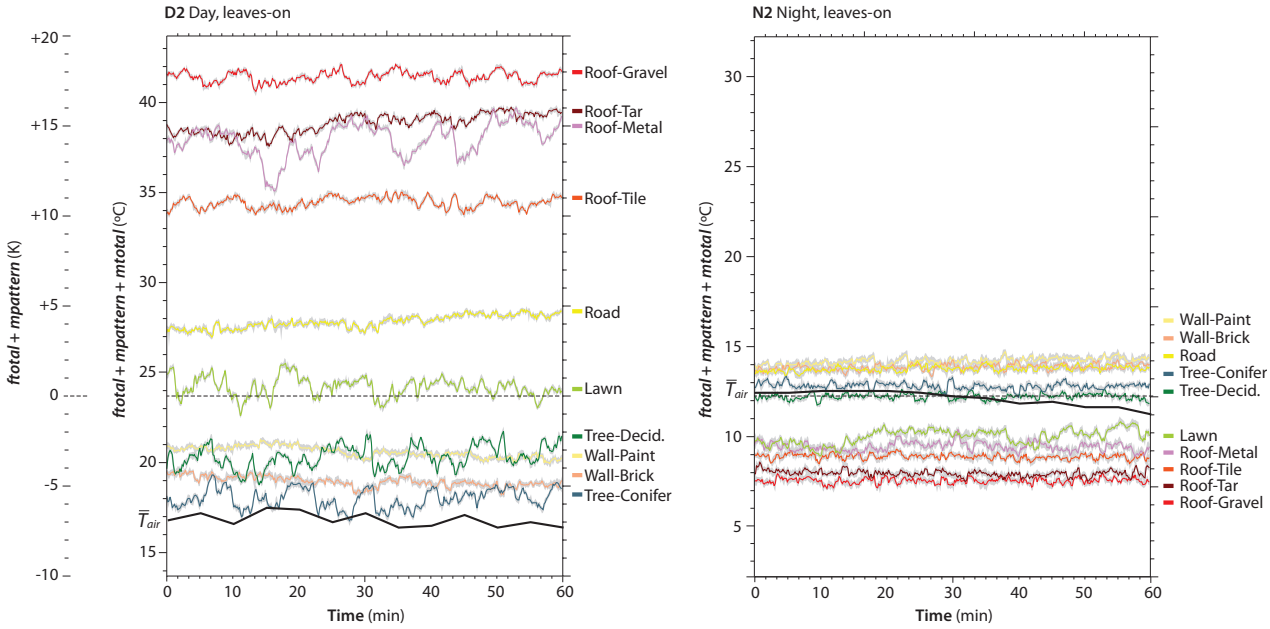

Figure 6: Sample time series of temperature fluctuations during 60 min of a day (D2) and a night (N2) of selected pixels representing typical behaviour for the facet material classes. All pixels are exposed to direct solar irradiance. Values are expressed relative to the anomaly (ftotal + mpattern, left axis - which is common for both graphs) and absolute temperature (ftotal + mpattern + mtotal, individual in both graphs)

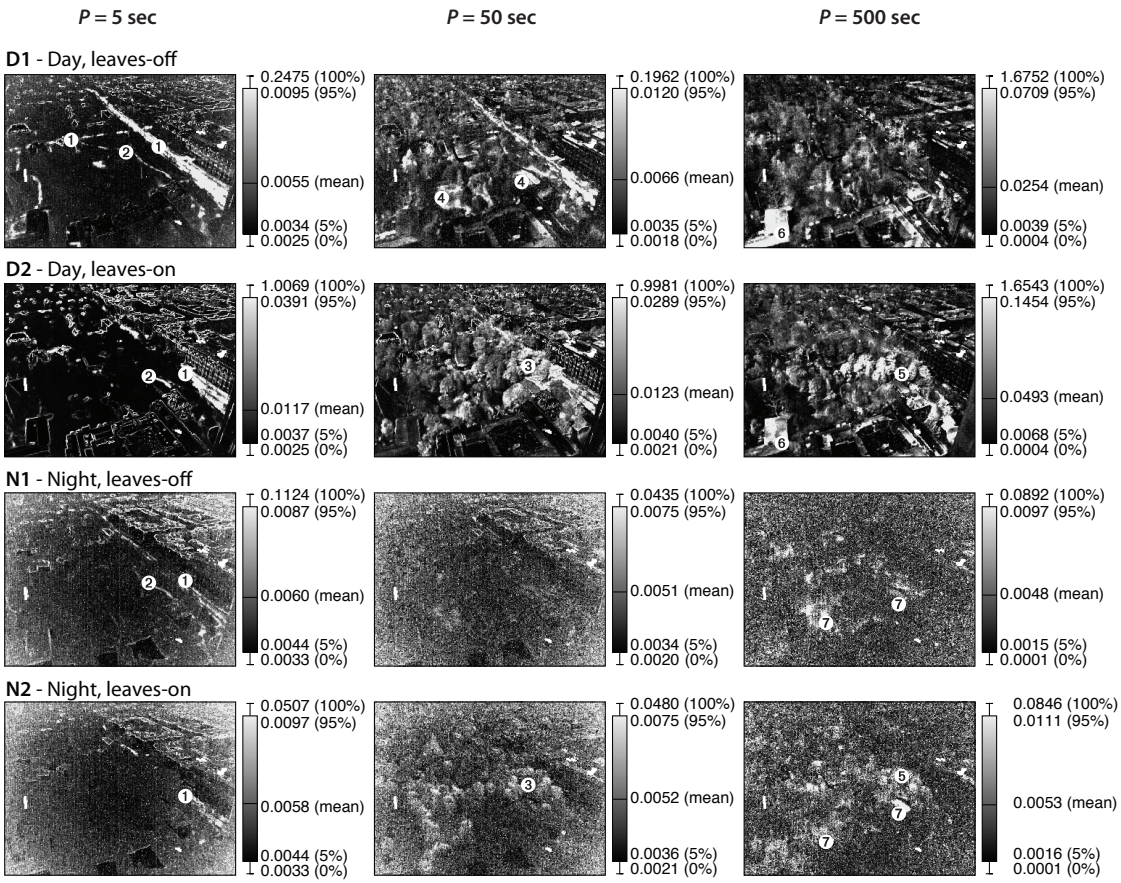

Figure 7: Normalized spectral energies f S(f) of temperature fluctuations (ftotal) for all runs (rows) for three selected different bands with period P = 5, 50 and 500 sec (columns). The visualization uses a linear grey scale between the 1 and 99th percentile in each image. Pixels drawn in white have been excluded from analysis. For labels 1 – 7 see text.

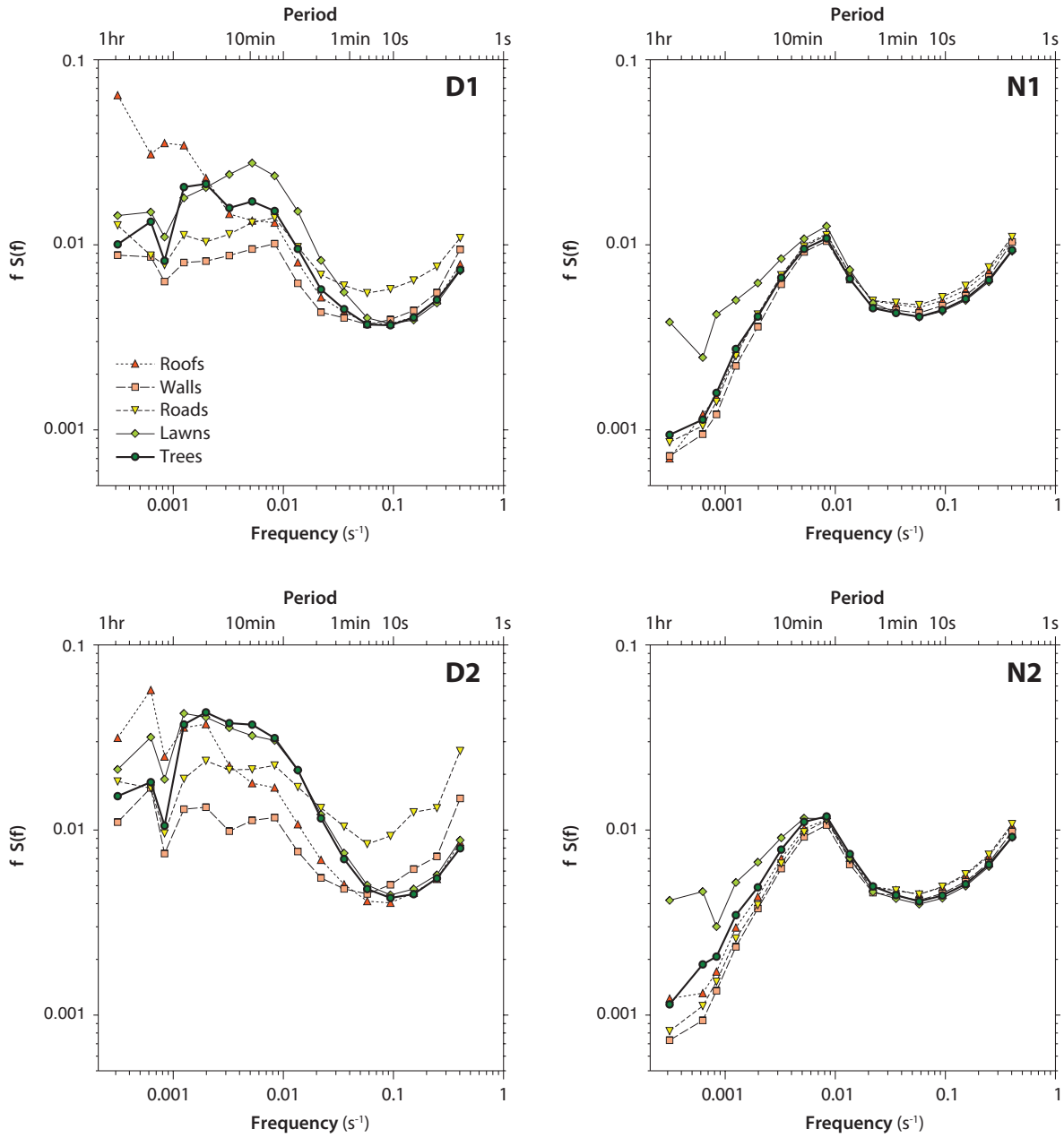

Figure 8: Ensemble averaged spectral energy S(f) of temperature fluctuations (ftotal) for all pixels, multiplied by frequency f. The spectra have been classified into five main facet categories.

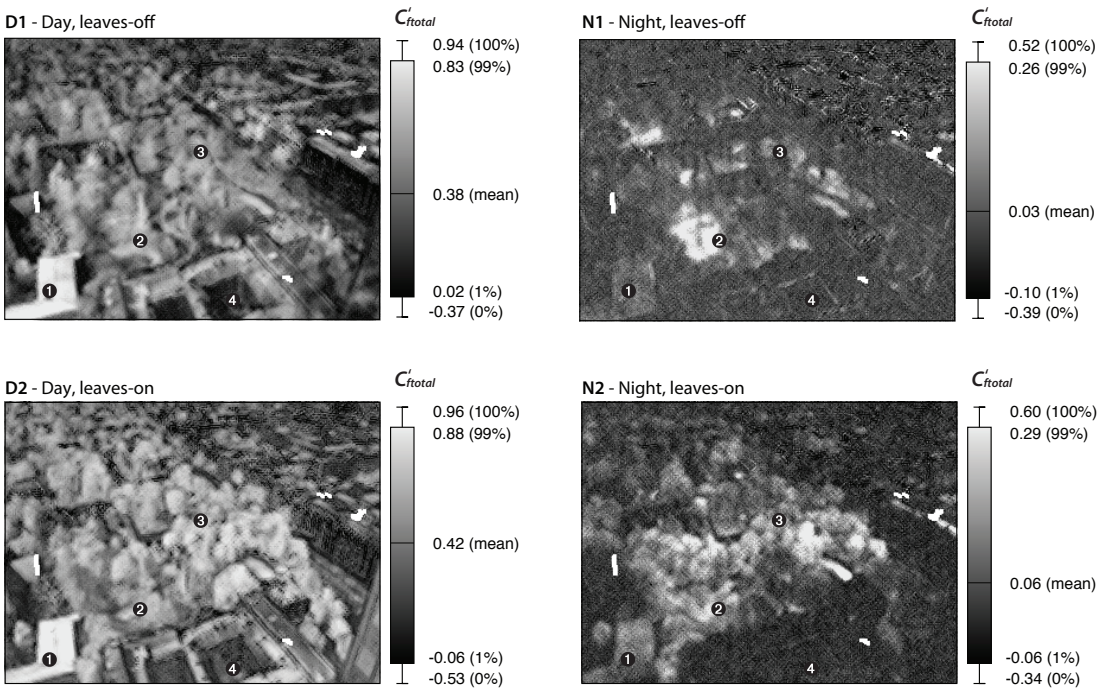

Figure 9: Spatial coherence C'ftotal of temperature fluctuations at r = 2 pixels over 20 min. The visualization uses a linear grey scale between the 1 and 99th percentile in each image. Pixels drawn in white have been excluded from analysis. For labels 1 to 5 see text.

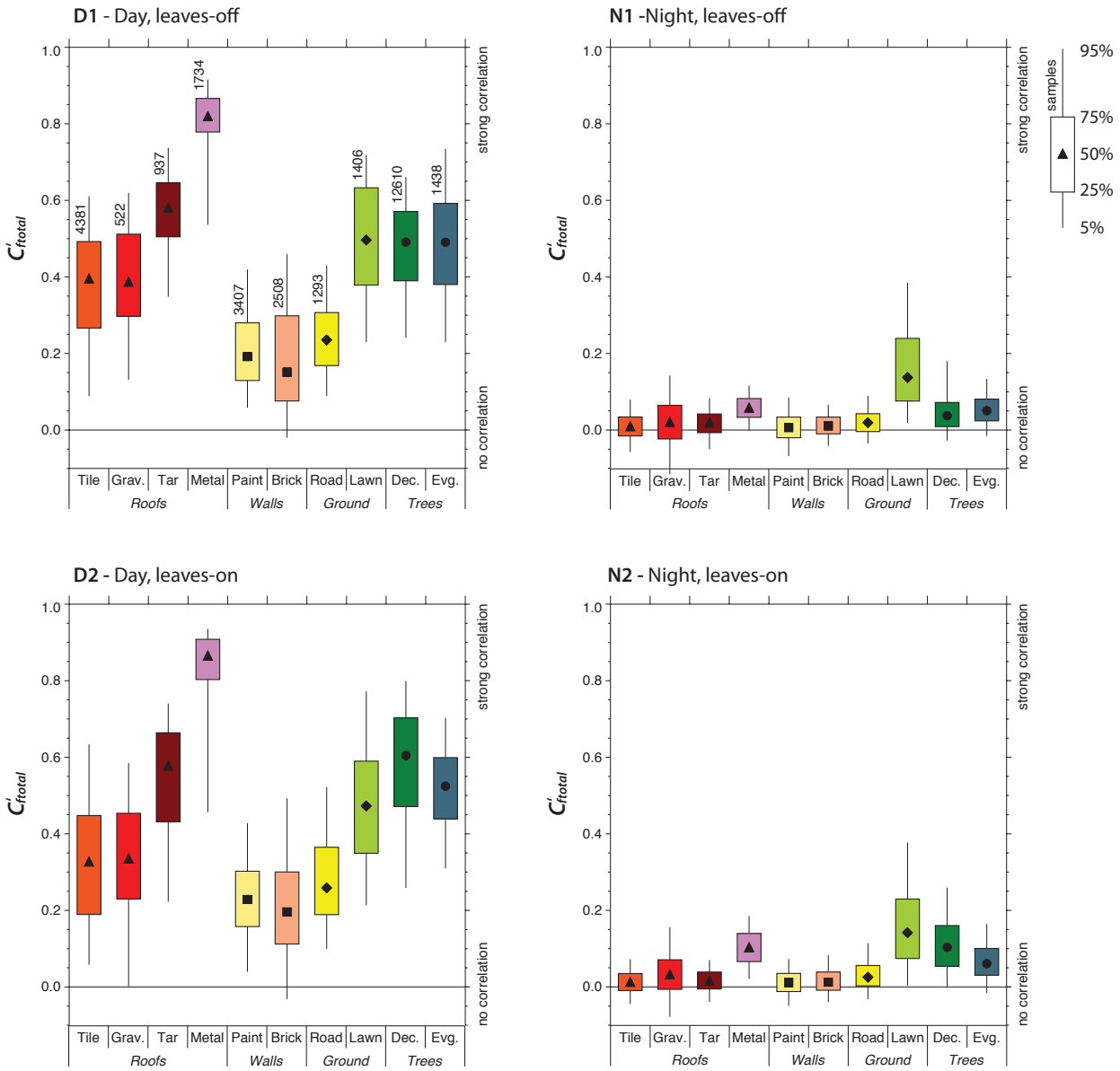

Figure 10: Ensemble averages of the spatial coherence at r = 2 pixels (C'ftotal) sorted by facet materials in all four runs. The numbers in the upper left graph indicate the number of pixels included in each class and are the same for all four runs.

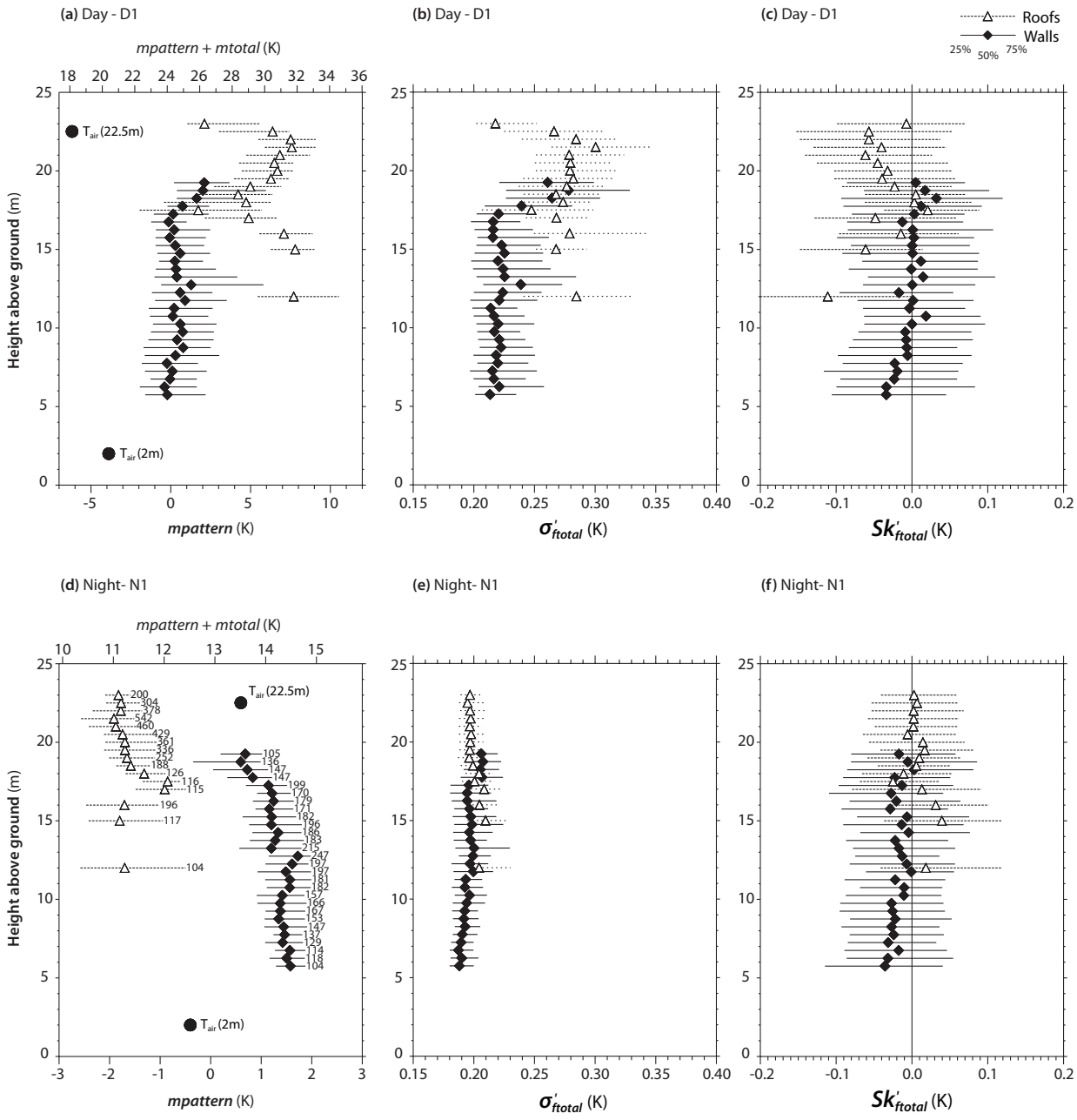

Figure 11: Height dependence of (a, d) spatial temperature anomaly (mpattern), (b, e) standard deviation of temperature fluctuations (σ'ftotal) and (c, f) skewness of temperature fluctuations (Sk'ftotal) of walls (brick and paint) and roofs (all materials except metal) the two leaves-off runs (D1 and N1). Numbers in figure (e) are the numbers of pixels considered in each class, and are the same for all other figures. Only classes with more than 100 pixels are shown.

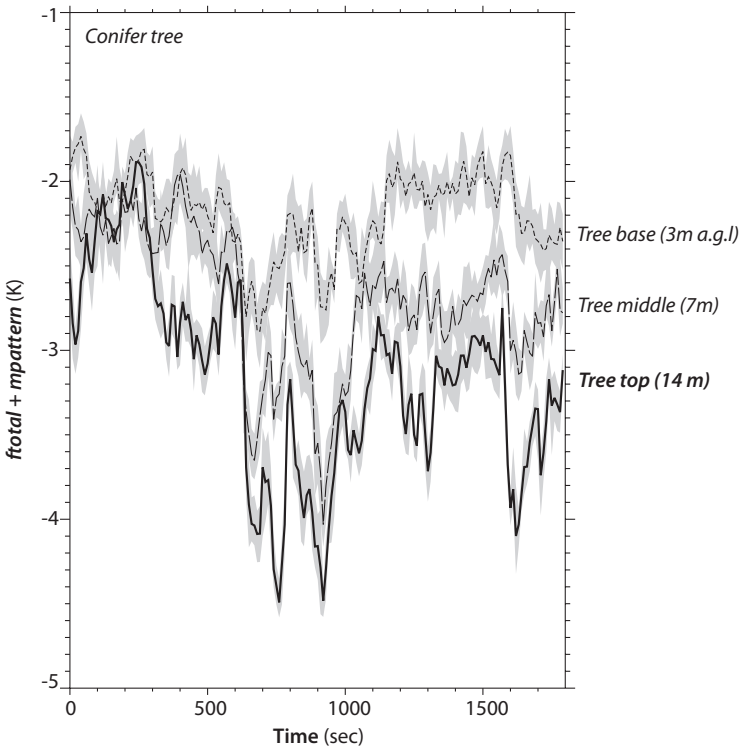

Figure 12: Instantaneous temperature fluctuations (ftotal + mpattern) of three selected pixels on different height on a conifer tree over 30 min. Data from the daytime, leaves-off run (D1).

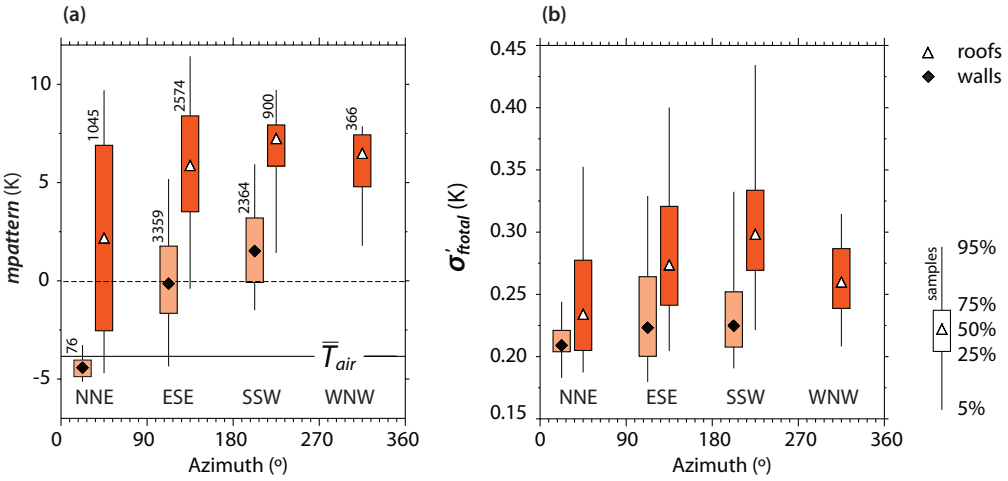

Figure 13: Dependence of (a) spatial temperature anomaly (mpattern) and (b) standard deviation of temperature fluctuations (σ'ftotal) of walls and roofs as a function of geographic azimuth. Numbers in (a) refer to the number of pixels included in the analysis. All data are from run D1 (roofs < 15° slope and metal roofs excluded).

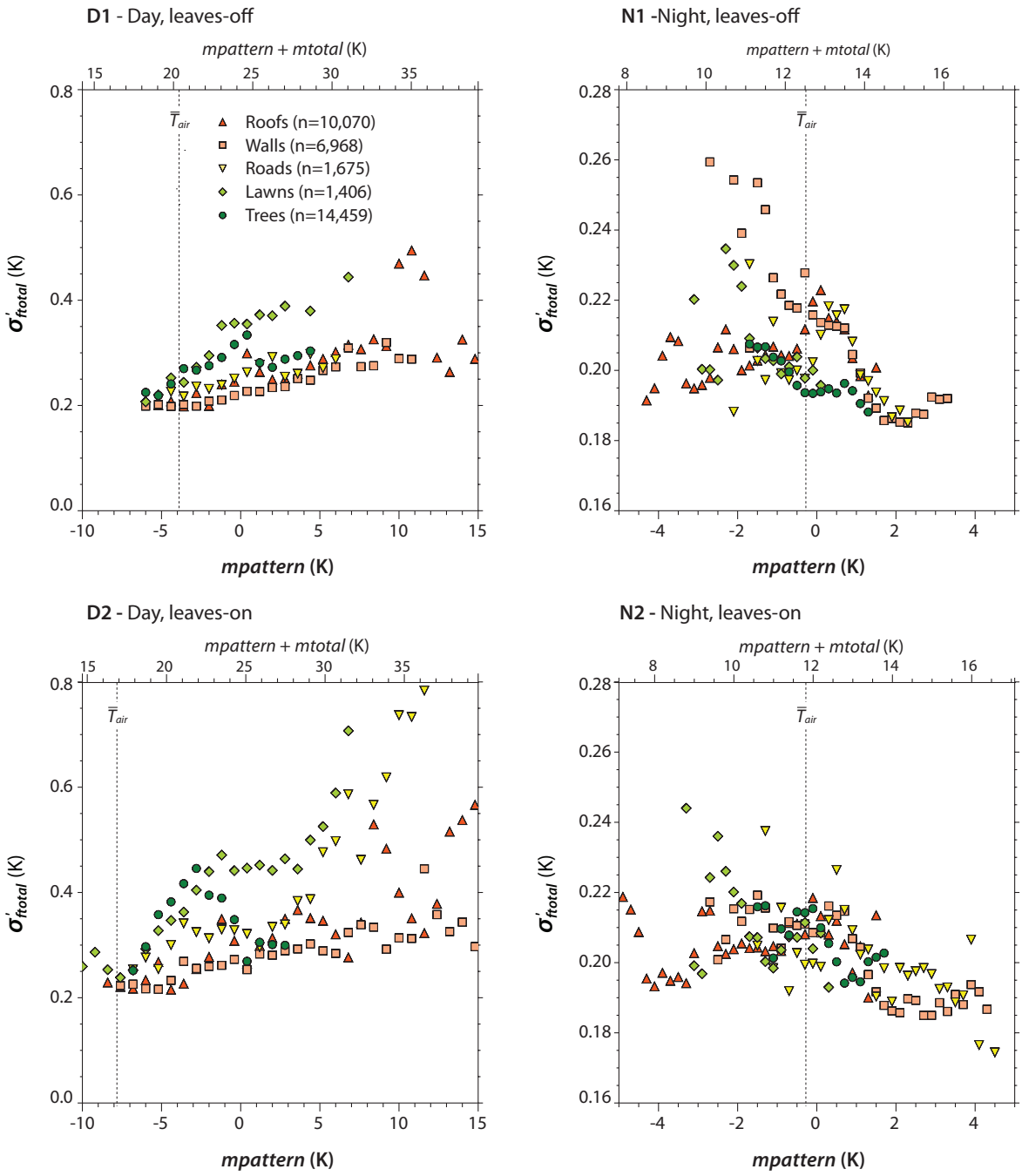

Figure 14: Standard deviation of temperature fluctuations (σ'ftotal) as a function of spatial temperature anomaly (mpattern) for all pixels classified into four facet categories (roofs, walls, lawns, roads and trees).

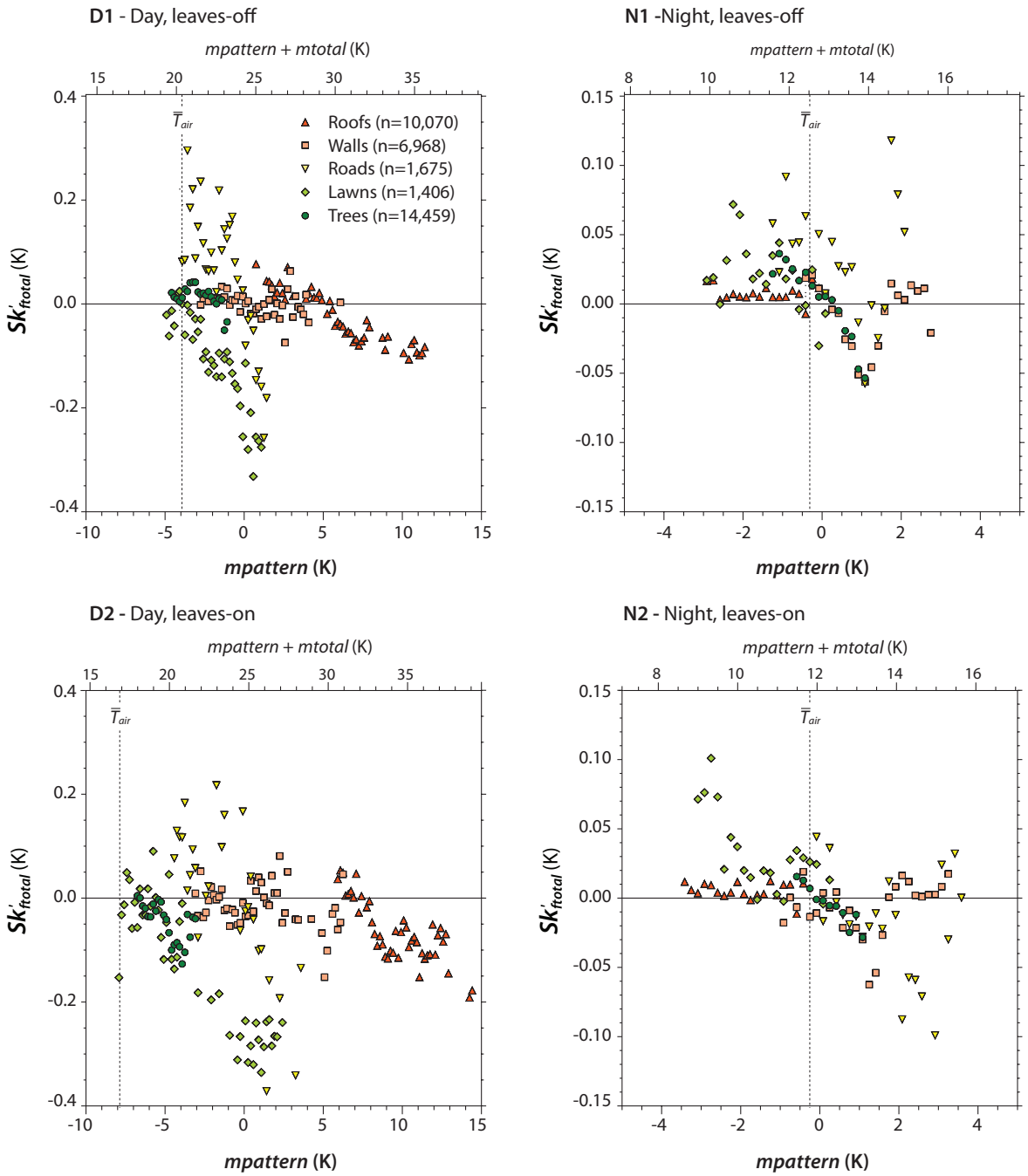

Figure 15: Skewness of temperature fluctuations (Sk'ftotal) as a function of temperature anomaly (mpattern) for all pixels classified into the four main facet material categories (roofs, walls, lawns, roads and trees).

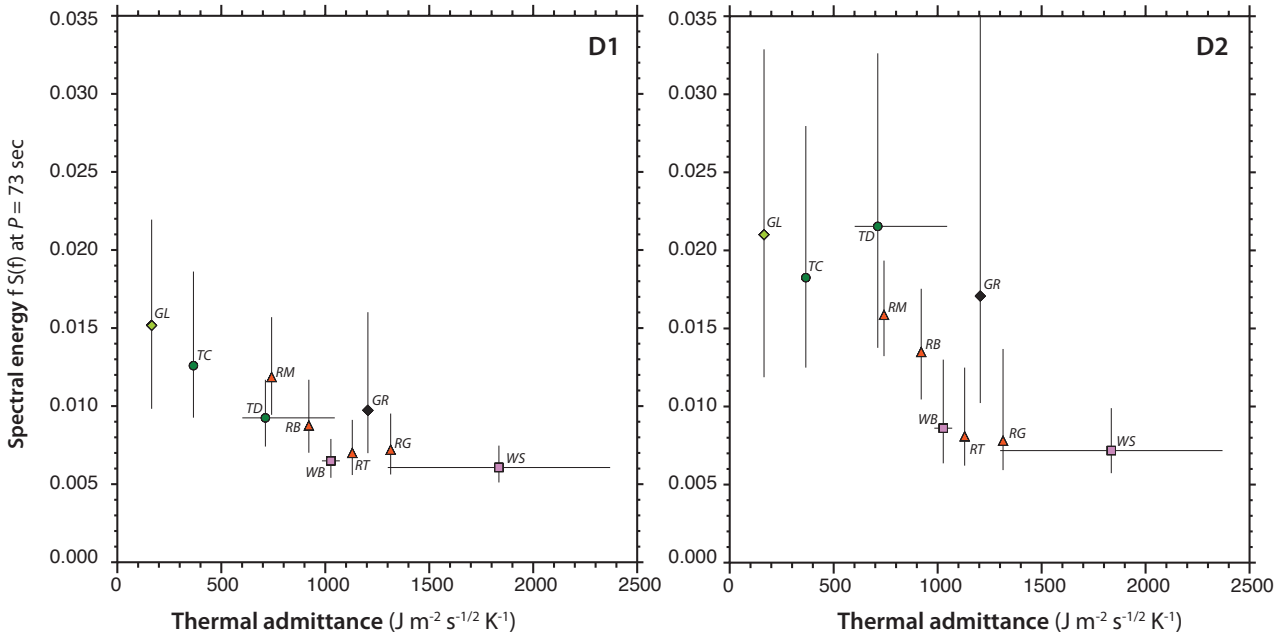

Figure 16: Ensemble averaged spectral energy of temperature fluctuations (ftotal) at P = 73 sec as a function of literature values for thermal admittance μ of different facet materials. Vertical error bars denote the 25 and 75th percentiles of all pixels in the given material class. Horizontal error bars, if given, refer to the range of values provided in the literature. Legend: RT = Roofs - clay tiles, RG = Roofs gravel, RB = Roofs bitumen / tar, RM = Roofs metal, WB = Walls brick, WS = Walls stone / paint / concrete, GL = Ground-lawns, GR = Ground-roads, TD - Trees deciduous, TC - Trees evergreen.